Exploring actinide chemistry: uranyl detection and thorium catalysis

by

Charmaine Dawn Tutson

A dissertation submitted to the Graduate Faculty of
Auburn University
in partial fulfillment of the
requirements for the Degree of
Doctor of Philosophy

Auburn, Alabama
May 6, 2017

Key Words: Uranyl, thorium, catalysis, detection

Approved by

Anne Gorden, Chair, Associate Professor of Chemistry and Biochemistry
Edward Parish, Professor of Chemistry and Biochemistry
German Mills, Professor of Chemistry and Biochemistry
Christopher J. Easley, Associate Professor of Chemistry and Biochemistry

Abstract

In a world where there is a strong need to improve our means of producing energy to sustain our ever expanding population with low green-house emissions, nuclear power offers sustainability and low greenhouse emissions, but needs appropriate measures to be taken to harness its power and minimalize its environmental impact. The presence of the common contaminant, uranyl, a dioxy cation of 6+ uranium with an overall 2+ charge, needs to be readily identified, thus, the ability to chelate very specifically these metal ions has applications in the nuclear energy production, remediation, and waste disposal fields. Along with this, the ability to extract uranyl from environmental media, aqueous and soil matrices, would aide in clean-up. The ease of preparing salen ligands and their ability to form stable metal complexes, coupled with the fluorescence of 2-quinoxalinol allows for the synthesis of a variety of salen 2-quinoxalinol ligands capable of serving as metal chelators for uranyl.

The first portion of this work focused on developing solid phase extractors for uranyl by loading the salen 2-quinoxalinol ligands onto a solid substrate and exploring its ability to extract uranyl from aqueous samples. The second portion explored the ability of imidazole derived ligands, a common by-product produced during the synthesis of the salen 2-quinoxalinol derived ligands, to serve as chemosensors for uranyl. Expanding our fundamental knowledge of the 5-f elements is a growing area of research. Elucidating the chemical properties of these atoms allows for increased application in the nuclear field through helping the clean-up process by separating common lanthanides from present actinides, as well as in other areas of chemistry by finding ways to harness these properties in new and developing areas of research. Here, we explore the use of thorium nitrate as a simple actinide salt catalyst for the oxidative coupling of *ortho*-phenylenediamine to produce 2,3-diaminophenazine. The presence of the lone pairs on the

amine groups of *ortho*-phenylinediamine and the pi-orbitals of the double bonds lead us explore

other derivatives containing lone pairs or pi orbitals to determine if thorium nitrate was capable

of coupling them.

believe in myself. Dr. Pamela Leggett-Robinson, you allowed me to conduct my first research project during ROCKETS and I have not forgotten the guidance you gave me during that time. I'm sure the third floor of Armstrong Hall still despises us for the cabbage, but it was worth it. Dr. Albert Russell, I cannot fathom the words to thank you enough, not only for being my mentor, but for being my friend. From the conversations about science to the ones about life, you've proven time and time again that you have my best interest at heart.

To my amazing parents, Theodore and Victoria Tutson, I would not be who I am or where I am without your love, guidance, but most importantly, your support. You all allowed me to chase this dream without questioning my motive or sanity. I am forever grateful and consider myself blessed to call you my parents. Tyrone, my favorite brother, thank you for the random calls that let me know you were proud of me. Those meant more to me than you'll ever know and kept me going at times. Shangerial, my favorite sister and possibly the greatest influence in my life, thank you! For always being there and believing in me when I didn't believe in myself. To my boys Desmond and Cornelius, I began this journey to show you guys that you can be anything you want to be and have been here long enough to welcome two nieces, Madeline and Blake. You all are my motivation and I hope this shows you to shoot for the stars. To my best friend Shemariah, I don't know what I would have done without your constant reminder of how proud of me you were and encouragement. You are the best friend I could have ever asked for. Dr. Ricquita Pollard, your pep talks were constantly needed and I would have not made it without them. To my amazing roommates and friends, Juanica and Tommie, you all were there during the valleys and mountains and I am forever indebted to you all. Your friendship means the world to me. Dr. Kristy Crews, thank you for giving me a role model to follow. Dr. Jessica Crumbley, we started this ride together and your friendship has sustained me

through many difficult moments. I am so thankful I asked you for directions on the first day.

Peedy, you were a little late to the party, but thank you for your support during this process.

Khalifa Jordan, thank you for your belief and slight encouragement during this process.

To my former labmates: Dr. Branson Maynard, Dr. Kushan Weeirasairi, Dr. Mike Devore, and Chasity Ward, thank you for the talks, whether scientific or personal. To my current labmates: Nick Klann, Julie Niklas, Clay Black, and Ethan Hiti, thank you for your insight and good luck. To my girls Maya West and Emily Hardy, your friendship was so vital to during my matriculation at Auburn. Our time in lab was comforting and the conversations were endless. To my undergraduates, Thomas Moreland, Sara Payne, and Ryan Yates, thank you for your help and friendship. Good luck with your endeavors.

There are so many people I feel are responsible and played a role in reaching my educational goals and I say thank you. Antonio Hayes, Gerald T., Jakiel Sanders, Brandon Williams, Carly Engel, The Phenoms of 40-Tude (Karen Robinson, my Sweet 16, I remember those nights in the library) and anyone else that sent a text, well wish, or congratulations: THANK YOU! To the amazing chemistry office staff that answered my million questions: Mrs. Lynn Walker, Mrs. Carol Nixon, Mrs. Kiley Coan, and of course, my bff Mrs. Lavonne Howard, thank you! Dr. Duin, although I broke a few instruments of yours, you still welcomed me to continuously use them, thank you.

I'd like to dedicate this dissertation to the memory of my amazing grandmother, Patricia Ann Bird, who was so proud of me, but passed away during my pursuit.

Table of Contents

List of Tables

List of Figures

List of Illustrations

List of Abbreviations

EPA   Environmental Protection Agency

ICP   Inductively Coupled Plasma

ICP-MS   Inductively Coupled Plasma Mass Spectrometry

[XA$_2$]   4,5-bis(2,6-diisopropylanilido)-2,7-di-*tert*-butyl-9,9-dimethylxanthene

BDPP   2,6-bis(2,6-diisopropylanilidomethyl)pyridine dianion

DPEPhos   (diphenylphosphinophenyl)ether

DME   1,2-dimethoxyethane

Th(sal)$_4$ tetrakis(salicylaldehydato)thorium(IV)

Th(TTA)$_4$ tetrakis(thenoyltrifluoroacetonato)thorium(IV)

ETAM   N,N'-diethyl-2,3-dihydroxyterephthalamide

Me$_3$BnN   trimethylbenzylammonium;

DOTA   1,4,7,10-tetraazacyclododecane-1,4,7,10-tetraacetic acid

DTPA   diethylenetriaminepentaacetic acid

TAM   6,19-bis(2-((2,3-Dihydroxy-4-((2-methoxyethyl)carbamoyl)benzoyl)amino)ethyl)-
12,13,25,26-tetrahydroxy-2,10,15,23-tetraoxo-3,9,16,22-tetraaza-6,19-
diazoniatricyclo[22.2.2.2^{11,14}]triaconta-1(26),11,13,24,27,29-hexaene dichloride tetrahydrate

BMMim   1-butyl-2,3-dimethylimidazolium

Th(pyOS)4(dmf)   dimethylformamidetetrakis(1-oxo-2-thiopyridinato) Thorium(IV)

HOPO   hydroxypyridinone

1,2-HOPO 1-hydroxy-2(1*H*)-pyridinone

3,2-HOPO 3-hydroxy-2(1*H*)-pyridinone

3,4-HOPO 3-hydroxy-4(1*H*)-pyridinone

H$_2$IDA   iminodiacetic acid

H$_3$NTA   nitrilotriacetic acid

H$_4$EDTA   ethylenediaminetetraacetic acid

DHPTA   1,3-diamino-2-hydroxypropane-N,N,N',N'-tetraacetic acid

HEDTA   (2-hydroxyethyl)ethylenediaminetriacetic acid

HEIDI   N-(2-hydroxyethyl)iminodiacetic acid

NTP   nitrilitripropionic acid

CIT   citric acid;

1,3,5-tCPBA   1,3,5-tri(4'-carboxylphenyl) benzoic acid

H$_3$TPO   tris-(4-carboxylphenyl)phosphineoxide

DPO   cis-ethylenebis-diphenylphosphine oxide

TFA   trifluoroacetic acid

MeOH   Methanol

EtOH   Ethanol

acac   acetylacetonate

HBP   2-(2'-hydroxyphenyl)benzimidazole

HBYP   2-(1H-benzimidazol-2-yl)phenol

TMAC   4-(trimethyl ammonium chloride)acetamide-2-(1H-naphtho[2,3-d]imidazole-2-yl)phenol

OLEDs   Organic Light Emitting Diodes

Salqu   salen 2-quinoxalinol derivatives

2-Qu   2-quinoxalinol

HL   Heterogeneous Ligand

BR   Bare Resin (M-PVA)

Sal   2-(1*H*-imidazo[4,5-b]phenazin-2-yl)phenol derivatives

Salq   2-(1*H*-imidazo[4,5-b]quinoxalin-2-yl)phenol derivatives

Salph 2-(2-hydroxyphenyl)-1*H*-benzimidazole derivatives

OPD   *ortho*-phenylenediamine

DAP   2,3-diaminophenazine

Chapter 1: Introduction

Since the coining of the term "radioactivity" by Pierre and Marie Sklodowska Curie in 1898, after Henri Becquerel's initial reported results of uranium materials emitting radiation, efforts have been made to investigate elements possessing this property.[1] By definition, radionuclides are atoms with enough energy in the nucleus to make them unstable, thus resulting in the potential to emit energy as either an alpha or beta particle or as gamma radiation.[1] It is known that all discovered elements have radionuclides, such as tritium with hydrogen, and all elements heavier than lead are radioactive.[2] The heavy elements of interest explored here are thorium and uranium, belong to chains of successive decay. Both of these have radionuclides that have been explored for their chemical and physical characteristics.

Radioactive is a term that has ignited fear in people since the dropping of the first atomic bomb in 1945, in which a uranium-based weapon was used on the city of Hiroshima .[3] This fear solidified by the dropping of a second weapon on Nagasaki, the accident that left Chernobyl desolate, and the natural disaster in Fukushima,[3, 4, 5] the negative aspects of radioactive elements somewhat overshadow the positives of characteristics these elements possess that could be applied. The actinide series consists of 15 elements that are all radioactive, and these possess a wide range of chemistry applications that have not been extensively studied, especially as compared to the transition metals. A recent search (December 2016) of the Cambridge Crystallographic Data Center resulted in a total of 699,104 structures, 349,066 are structures containing transition metals and 5,721 containing the actinides uranium, thorium, neptunium, and plutonium. Of the 5,721 actinide structures, 4,799 are uranium structures and all the rest the actinides are the remaining 10%. Thus, this group of elements is relatively underexplored, and yet, they offer unique characteristics such as the ability to undergo spontaneous or induced

fission. It is safe to say that delving deeper and expanding our fundamental knowledge of these elements offers opportunity to widen our chemical scope and change the outlook on radioactive elements. These projects explore a means of changing the view of nuclear power as a way to protect our environment from potential contaminants like uranyl, as well as exploring the abilities of thorium as a catalyst, its coordination environment, and unique chemistry.

Projects I and II: Detection of Uranyl in the Environment

Aside from its use in weapons, uranium has other characteristics that have been exploited of since its discovery in pitchblende by Martin Heinrich Klaproth in 1789.[1] With a density that is almost 60 times higher than lead, uranium has a density of 18.95 g/cm^3 and lead has one of 11.35 g/cm^3, the aerospace industry has taken advantage of this, and it is used as a counterbalance on their airplanes.[6,7] Along with the high density, before the Cold War reduced availability of uranium, uranium was used as an additive in glazes used to coat the glassware that was produced by companies such as Fiestaware.[8] It is widespread knowledge that the main use for uranium is as a fuel source for nuclear power. As it stands, the dependence of the United States and the world on fossil-fueled energy has - and will continue to leave - an irreversible effect on the environment. According to the Environmental Protection Agency, the key greenhouse gases emitted by human activity are carbon dioxide, methane, nitrous oxide, and fluorinated gases, with them accounting for 80.9-, 10.6-, 5.9-, and 2.6%, respectively.[9] These gases are emitted via agricultural activities, waste management, industrial processes, and the main culprit, fossil fuels.[10] According to the EPA, fossil fuels produce 81% of the energy consumed in the United States, which also spews CO_2 into the atmosphere.[11] One means to get away from this is to increase the use of nuclear power as the energy source. To date, 8.5% of the United States'

energy is supplied by nuclear reactors and civilian nuclear reactors are responsible for about 11% of the world's energy production according to the World Nuclear Association.[11]

Nuclear power is such an attractive energy source because it is a low-greenhouse gas emitter with most of its emissions occurring during construction, and it is a high yielding source compared to a smaller land footprint.[11] In regards to being high yielding, according to the Department of Energy, one ton of natural uranium produces energy equivalent to 16,000 tons of coal or 80,000 barrels of oil, both of which are high greenhouse gas emitting sources.[11] A majority of emissions occur during the building of the nuclear facilities and is minimalized upon the completion of the plant; however, along with the minute amount of green-house gases emitted into the environment, the possibility of nuclear facilities leaking contaminants into the environment is still an issue that looms large in the public consciousness.[11] Keeping this in mind, although means of detecting uranium in aqueous and soil samples has been developed, but there remain challenges in developing direct, real-time, on-site methods of detection.

Issues with current detection methods

Radiation Source Identification

A quick and easy way to detect uranium in the environment is through the use of the Geiger counter.[12] This hand-held device is used to measure ionizing radiation such as alpha- and beta-particles, and gamma rays.[13] With low-costs and easy of portability, the Geiger counter would seem to be the best way to go when identifying the presence of radionuclides, however, there are limitations associated with this method. The major limitation is the fact that Geiger counters, although robust, cannot differentiate between radiation sources. Therefore, the

presence of beta, or gamma-emitters is measured the same.[12] A separate specialized counter is required for detecting alpha emissions.[13] With actinides possessing the ability to emit all three types of radiation,[1] and some isotopes being exclusively alpha emitters, being able to identify the type of radiation is imperative to identifying the element.

Matrix Interference

Inductively Coupled Plasma Mass spectrometry, ICP-MS, is an elemental determination technique capable of analyzing trace amounts of elements using inductively coupled plasma as an ionization source coupled with another analytical techniques such as mass spectrometry, but one could also use emission spectroscopy or optical emission spectrometry.[14] Compared to other methods, like Graphite Furnace Atomic Absorption Spectroscopy, ICP-MS has equal or lower detection methods and higher throughput. The high temperature of the plasma source allows for the analysis of complexed samples without much interference from the matrix of the sample; however, due to the possibility of the presence of elements in the matrix that can cause two major interferences, actinides have to be isolated prior to measurements.[15] The first type of interference is known as isobaric interferences occurs when samples contain equal massed isotopes of different elements, such as the presence of ^{232}Th and ^{232}U or ^{238}U and ^{238}Pu. The second type of interference is known as polyatomic interference in which multiple elements equate to the same mass as other elements, such as ^{238}U^{1}H and ^{239}Pu or ^{238}U and ^{237}Np^{1}H. The best results occur when the actinides are separated into individual fractions, requiring lengthy sample preparation. Lengthy sample preparation and initial purification steps are recurring issues with many of these analytical techniques.[16,17]

Chemosensors

Issues associated with current analytical techniques have inspired researchers to explore other means of detecting and identifying actinides. One method is through the use of chemosensors, a molecule that convalently or non-covalently reacts with an analyte to produce a detectable change and increase overall sensitivity of detection.[18] This change can be visible to the naked eye, such as with a colorimetric sensor, in which a color change occurs after the introduction of the analyte.[19] Another detectable change is through the coupling of chemosensors with other analytical techniques such as Ultra-Violet Visible Spectroscopy, a method that offers high sensitivity, selectivity, and convenience.[20] In this way the detectable change is visible in the spectra of the chemosensor before and after interaction with the analyte, in which a bathochromic or hypsochromic shift is detected. This is a result of a change in electron density in the complex.[21] Common actinide chemosensors will be explored in chapters 2 and 3 when the projects associated with the detection of uranyl via the use of salen derived ligands is discussed.

The synthesis of the salen 2-quinoxlinol ligand can result in three products, two of which are shown in Scheme 1.1. In the first project, the disubstituted salen 2-quinoxalinol derived ligands are covalently bonded to a polymer substrate, poly(vinyl)alcohol to produce a heterogeneous detection method for 2+ metal ions. The use of a physical substrate was explored to move towards a uranyl detector that mimics litmus papers and other dip-stick analytical methods, in which the paper or stick is impregnated with the sensor for real-time sensing. After loading the ligand onto the polymer support, the heterogeneous detector was subjected to agitation with metal 2+ cations and analyzed via UV-Vis, fluorimetry, and microfluorimetry.
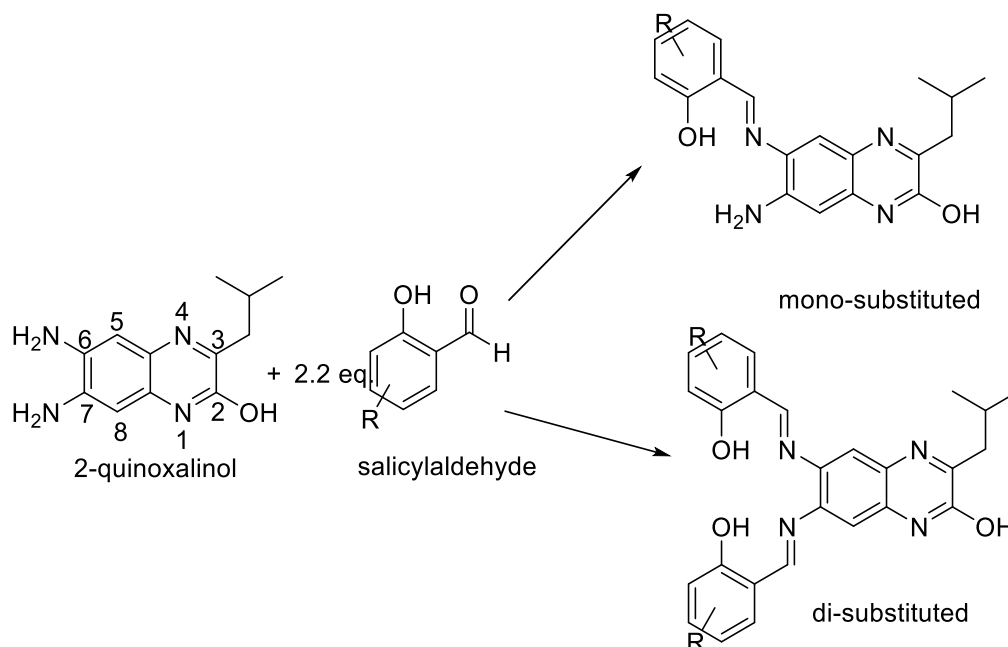
Scheme 1.1 The general synthesis of the mono- and di-substituted salen 2-quinoxalinol ligands.

The second project utilizes a byproduct of the salen ligand synthesis, imidazole. With the formation of the mono-substituted salen 2-quinoxalinol, a competition between the intermolecular reaction of the mono-substituted ligand and the salicylaldehyde to produce the desired product, the di-substituted ligand, versus the intramolecular reaction to produce a side product known as the imidazole, Scheme 1.2. For many years, this product was not purified and isolated as being of interest. This changed when a crystal structure of a derivative was isolated and characterized. Subsequently, the imidazole products have been characterized as bidentate sensors.
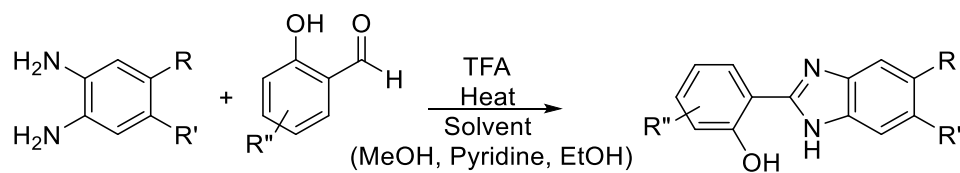
Scheme 1.2 General conditions for the formation of the imidazole product.

Project III: Thorium and its Catalytic Abilities

Although it is the most abundant radioactive element found in nature, thorium has a unique chemistry that has remained relatively unexplored.[22] The Th(IV) ion has been demonstrated to possess the ability to reach multiple coordination numbers from 4 to 15, thus allowing it to coordinate a wide-range of ligands with potential in numerous applications. [23] This ability of thorium to coordinate a wide-range of ligands results in an inability to predict its coordination geometry. Along with this, thorium is relatively underexplored when compared to uranium. Thus, an increase in the fundamental knowledge of its chemical reactivity is warranted. Here, we explore multiple thorium (IV) coordination environments and unique flexible coordination geometry using a chronological and numerical approach to compare complexes described in the literature, ranging from 1971-2016. This allows us insight to explore its catalytic properties.

The potential for covalency offered by thorium and the involvement of the d-orbital in bonding, as well as the high Lewis acidity, the propensity to remain in the +4 oxidation state, and large ionic radii it possesses, results in very unusual reactivity.[24,25,26,27] In the nine-coordinate environment, it was found that Th(IV) has an ionic radius of 1.09 Å, making it the largest stable tetravalent metal ion.[28] Because it is so prevalent naturally, thorium possesses desirable characteristics that make it of interest to the civilian nuclear fuel industry.[24] Much of the research dedicated to developing a more complete understanding of thorium chemistry is the result of an interest in sequestering actinide ions, whether as a fuel source in itself or as a surrogate to Pu(IV) in nuclear waste separation studies.[29]

As the focus here is ligand covalent coordination chemistry with oxo- aza- or soft donors and thorium coordination environments, a list of explored complexes can be seen in Table 1.1, a

few noteworthy areas of exploration will not be discussed, including, 1) research mimicking or pertaining to naturally occurring minerals such as zeolites[30]; 2) research based strictly on organometallic compounds[31] and 3) thorium ionic compounds.[32]

Table 1.1. The Th(IV) complexes explored.

Entry Number	Complex	Coord. #	idealized geometry	ref
3	BDPPTh(CH$_2$SiMe$_3$)$_2$	5	square pyrimidal	12
4	XA$_2$Th(CH$_2$SiMe$_3$)$_2$	5	square pyrimidal	12
5	Th(BDPP)$_2$	6	distorted tetrahedron	12
6	BDPPThCl$_2$(dme)	7	pentagonal bipyramidal	12
7	XA$_2$ThCl$_2$(dme)	7	pentagonal bipyramidal	12
8	{N[o-NCH$_2$P^{i}Pr$_2$)C$_6$H$_4$]$_3$}Th[Co(CO)$_3$].	7	trigonal bipyramidal	16
9	Th(C$_7$H$_5$O$_2$)$_4$	8	dodecahedron	21
10	Na$_4$[Th(C$_6$H$_4$O$_2$)$_4$·21H$_2$O	8	trigonal-faced dodehedra	23
11	Th(C$_8$H$_4$F$_3$O$_2$S)$_4$	8	dodecahedron	24
12	Th[(CH$_3$)$_2$CHN(O)O(O)C(CH$_3$)$_3$]$_4$	8	cubic	26
13	Th[(CH$_3$)$_2$CHN(O)O(O)CH$_2$C(CH$_3$)$_3$]$_4$	8	dodecahedron	26
14	[Th(C$_5$H$_7$O$_2$)$_4$]$_2$·C$_6$H$_5$NH$_2$	8	square antiprism	31
15	[Me$_3$BnN]$_4$[Th(ETAM)$_4$]	8	between the bicapped trigonal prismatic and trigonal dodecahedron	33
17	Th**TAM**K$_4$·(DMF)$_2$·(MeOH)$_2$·THF,	8	novel	37
18	Th$_2$I$_5$[κ^2(O,O')-μ-O(CH$_2$)$_2$OCH$_3$]$_3$(DME)	8	bicapped trigonal pyramidal	39
19	Th$_4$(μ$_4$-O)(μ-Cl)$_2$I$_6$[κ^2(O,O')-μ-O(CH$_2$)$_2$OCH$_3$]$_6$	8	distorted tetrahedron	39
20	[BMMim]$_2$-[Th$_3$(PO$_3$)$_4$(H$_2$P$_2$O$_7$)$_3$]	8	square antiprism	42
21	Th(pyOS)4(dmf)	9	monocapped square antiprism	43
22	(C$_5$H$_4$NO$_2$)$_4$(H$_2$O)Th	9	amonocapped Archimedean antiprism and the D_{3h} tricapped trigonal prism	44
26	Th(3,2-HOPO)·H$_2$O	9	distorted monocapped square-antiprismatic	47
27	(NMe$_4$)$_4$[Th(ETAM)$_3$MeOH]$_2$	9	dimer	33
28	[Th(NTA)(H$_2$NTA)(H$_2$O)·H$_2$O	9	capped square antiprismatic	49
29	[Th(EDTA)(H$_2$O)]·H$_2$O	9	capped square antiprismatic	49
30	Na$_4$[Th$_6$O$_2$(hedta)$_6$]·28H$_2$O	9	distorted monocapped square-antiprismatic	52
31	[Th(C$_9$O$_6$NH$_{12}$)-(H$_2$O)(NO$_3$)]·2.5H$_2$O	9	distorted monocapped square antiprismatic geometry.	52
32	[Th$_2$Al$_8$(OH)$_{14}$(H$_2$O)$_{12}$(C$_6$O$_5$NH$_8$)$_4$](NO$_3$)$_6$·57H$_2$O	9	distorted monocapped antiprismatic	52
33	(C$_4$N$_2$H$_{12}$)[Th$_2$Fe$_2$(OH)$_2$(H$_2$O)$_2$(C$_6$O$_7$H$_4$)$_2$(C$_6$O$_7$H$_5$)$_2$]·5H$_2$O	9	distorted monocapped antiprismatic	52
35	[C$_7$H$_{11}$N$_2$]$_5$[Th$_2$(1,3,5-tCPBA)$_2$Cl$_6$]·Cl	9	muffin-type	53
36	[C$_9$H$_{17}$N$_2$][Th(TPO)Cl$_2$]·18H$_2$O	9	irregular muffin-type	59
37	[NH$_4$]$_2$[Th(NO$_3$)$_6$]	12	irregular icosahedron	60
38	[Th(HIDA)$_2$(C$_2$O$_4$)]·H$_2$O	10	bicapped square antiprismatic	49
39	Th(NO$_3$)$_2$-DPO·(NO$_3$)$_2$	10	distorted bicapped square antiprism	61
40	[Th(TPO)(OH)(H$_2$O)]·8H$_2$O	10	spherical sphenocorona	59

Five to Seven Coordinate Complexes

Dialkyl Thorium Complexes

Interest in thorium coordination chemistry is not solely limited to actinide sequestration or waste remediation. Emslie[33] and co-workers were investigated non-carbocyclic

organoactinide complexes for their potential in organometallic catalysis. This group was interested in sufficiently thermal stable Th(IV) dialkyl complexes that could accommodate thorium's size and containing robust structural elements[34]. Successful preparations of 5-, 6- and 7-coordinate thorium complexes began with the synthesis rigid and planar NON-donor, 4,5-bis(2,6-diisopropylanilido)-2,7-di-*tert*-butyl-9,9-dimethylxanthene [XA₂] and the isolation of the thermally unstable lithium salt McConville's 2,6-bis(2,6-diisopropylanilidomethyl)pyridine dianion, BDPP, followed by subsequent reactions to get the 5- (**3-4**), 6- (**5**), and 7- (**6-7**)coordinate complexes, respectively (Scheme 1.3).
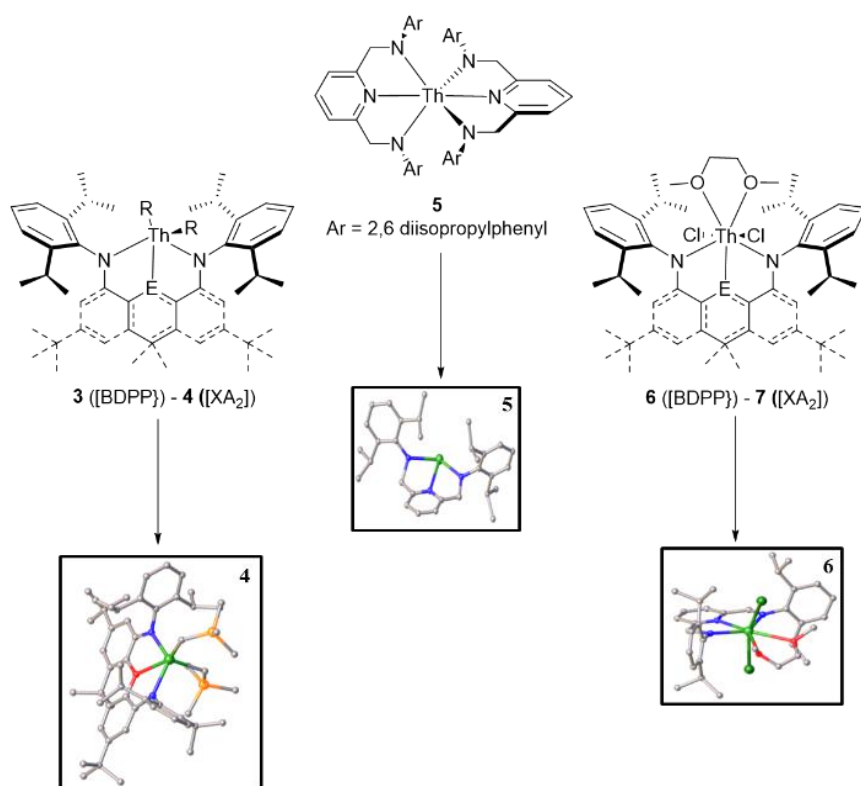
Scheme 1.3. Synthesis of Thorium complexes **3**-**7**.

9

Although proposed for potential catalytic properties, the results garnered very interesting unusual coordination environments for thorium(IV) based on the bulkiness of the ligands. Through the reaction of $Li_2[BDPP]$ and $Na_2[XA_2]$ with $[ThCl_4(dme)_2]$ in benzene at 0 °C or in toluene at room temperature, respectively, resulted in the unusual 7-coordinate Th(IV) dichloride complexes **6** and **7**. The ^{1}H NMR spectra supports the presence of symmetric pentagonal bipyramidal products through shifts representative of one molecule of symmetrically coordinated dme, a 1,2-dimethoxyethane, and a lone C*H*Me$_2$ signal. The pentagonal bipyramidal geometry was confirmed through single crystals of complex **6**·2toluene and shows the two chloride anions in the apical positions with an angle of 156.38(10)° for [Cl(1)-Th-Cl(2)] and Th-Cl bond lengths of 2.698(3) and 2.686(3) Å. The Th-O$_1$ and Th-O$_2$ bond lengths are 2.674(8) and 2.724(8) Å, respectively. The bite angle of the O$_1$-Th-O$_2$ is 59.9(2)°. Structure 6 also contained two bite angles, N$_1$-Th-N$_2$ and N$_2$-Th-N$_3$, with values of 65.2(3)° and 64.3(3), respectively. The bite angles – that is - the angle between the coordinating atom-metal-coordinating atom that is formed when a ligand coordinates a metal center, is of interest because this angle is one end of a triangle formed where the base is the ligand linker. Thus, the bite angle plays a role in the final coordination geometry of the metal center. This is of interest here because Thorium has such a flexible coordination geometry, that we have observed a range of bite angles from 42.05° to 156.38°. In this particular example, the Xray diffraction characterization demonstrates the BDPP, 2,6-bis(2,6-diisopropylanilidomethyl)pyridine dianion ligand is planar, and the binds to the Th^{4+} center through the comparatively short Th-N$_{anilido}$ bonds with lengths of 2.305(9) and 2.321(8) Å.

Reacting complexes **6** and **7** with 2 equivalents of $LiCH_2SiMe_3$ afforded the base- and salt-free 5-coordinate dialkyl thorium(IV) complexes, **3** and **4**, respectively. Variable temperature ^{1}H and ^{13}C NMR spectra confirmed the identity of these complexes. At 60 °C, Th*C*H$_2$ and C*H*Me$_2$ shifts

were observed, with the ThCH_2 at -0.32 ppm for **5** or -0.17 ppm for **4** on the ^{1}H NMR spectra

and 89 ppm for **3** or 97 ppm for **4**. Cooling the complexes to -80 °C produced two distinct

CH_2SiMe_3 groups, two CHMe$_2$ signals, and ligand backbone resonances that support the loss of

top-bottom symmetry. The authors, Emslie et al., were thus able to produce the first structurally

characterized thorium dialkyl complex supported by a multidentate non-carbocyclic ancillary

through the growth of single crystals of **6**·toluene that shows a square pyramidal geometry

distorted in the square plane due to the rigidity of the ligand.[33] NMR analysis showed that the

alkyl groups were not identical, and this was confirmed from the crystal structure featuring one

alkyl group is located in the NON plane and the other is directly above the plane. Two

interesting observations found in the crystal structure of **4** are 1) the Th-O bond length [2.534(3)

Å] is similar to previous reports of coordinated dme and this is surprising since a diaryl ether is

thought to be a far less effective donor than dme[35] and 2) the Th-C-Si bond angles of 127.6(3)°

and 126.8(3)° are significantly larger than other observed sp^3-hybridized carbon atoms; this has

been attributed to α-agostic C-H-Th interactions.[36] The bite angle between the two carbon atoms

and the thorium metal center is 112.0° and an average bond distance of 2.4755 Å. The average

bond angle of the O-Th-N atoms in complex **4** was calculated to be 62.93° and Th-N bond

lengths were an average of 2.3015 Å. Both [BDPP] 5- and 7- coordinate complexes were used to

synthesize 6-coordinate Th(IV) complex **5**; with the [XA$_2$] complexes resulting in no reaction.

Solution NMR in d_5-bromobenzene between 20 and -35 °C supports the formation of a

symmetrical product with only one CHMe$_2$ environment. Structural characterization using small

molecule X-ray diffraction crystallography reveals that **5** forms a distorted tetrahedron geometry

with four amido donors and the two N$_{pyridine}$ directed toward the edges of the tetrahedron to form

the 6-coordinate complex. Complex 5 has an average bite angle between the thorium center and

the nitrogen atoms was calculated to be 63.80° and the bond lengths ranged from 2.368 to 2.615 Å.

The N[o-NHCH$_2$P^{i}Pr$_2$)C$_6$H$_4$]$_3$ Ligand

The need for a greater understanding of the electronic structure and ability to form chemical bonds of actinides led Arnold and co-workers to probe the formation of bonds between actinides and transition metals.[37] With the idea that more in depth knowledge of the fundamental properties of metal-metal bonds involving 5f elements would aide in the separation of actinides from other present fission products in the nuclear fuel cycle.[38] The dearth of f-block element metal-metal bonds compared to non f-block elements is due, in large part, to the limited synthetic routes available to form such bonds.[39] Arnold et al. took advantage of the hard/soft donor system facilitated by the N[o-NHCH$_2$P^{i}Pr$_2$)C$_6$H$_4$]$_3$ ligand to bind the hard actinides to the soft transition metals.[40] This was achieved via UV irradiation of the 8-coordinate heterobimetallic complex {N[o-NCH$_2$P^{i}Pr$_2$)C$_6$H$_4$]$_3$}Th[Co(CO)$_4$], Scheme 1.4A, to produce a unique 7 coordinate complex {N[o-NCH$_2$P^{i}Pr$_2$)C$_6$H$_4$]$_3$}Th[Co(CO)$_3$], **8**, possessing a Co-Th bond - the first of its kind. The Th(IV) center is trigonal bipyramidal, Scheme 1.4B, and the Co-Th bond length is 3.0771(5) Å. The average Th-N bond length was calculated to be 2.405 Å, resulting in an average bite angle of 65.68°. The Th-P bonds averaged a length of 3.194 Å and had a bite angle of 96.62°.
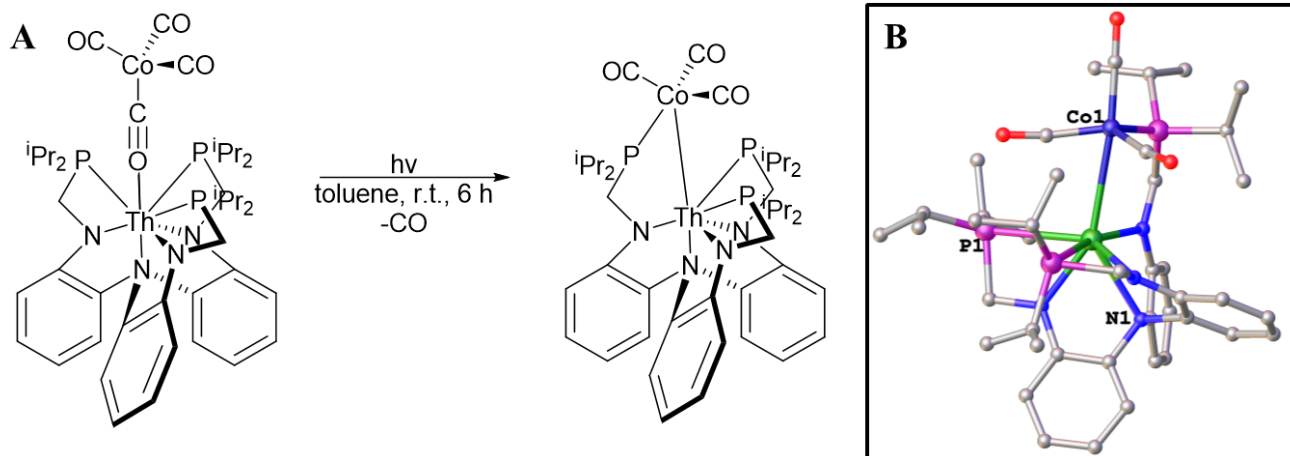
Scheme 1.4. A) The synthesis of complex **8**, {N[o-NCH$_2$P^{i}Pr$_2$)C$_6$H$_4$]$_3$}Th[Co(CO)$_3$]. B) Seven coordinate complex **8** illustrating the Co-Th bond. Both images are generated from the Cambridge Crystallographic Database [37].

Eight Coordinate Complexes

Tetrakis(salicylaldehydato)thorium(IV) Complex

Complexes that possess an eight-coordinate Th(IV) center are quite common and feature primarily bi- and tetra-dentate ligands. In the early stages of structural characterization using single crystal X-ray crystallography, most reported thorium complexes featured 9-coordinate thorium with 8 coordinating oxygen atoms and a solvent molecule occupying the 9th coordination site.[41] In fact, prior to 1976, only the β-diketone and dithiocarbamate complexes showed 8-coordinate complexes until Rickard and Hill[42] synthesized and determined the structure of tetrakis(salicylaldehydato)thorium(IV), Th(sal)$_4$, **9**. The authors sought to take advantage of the idea that an asymmetric chelating ligand could help stabilize the dodecahedron (D$_{2d}$) solid-state geometry as preferred relative to a potential square antiprism (D$_{4d}$) geometry through the

13

ordering of different donor atoms into non-equivalent sets of sites. It was determined that the

eight O-atoms lie along the *m* edges in a dodecahedron geometry with an approximate D_{2d}

symmetry. The phenolate oxygen atoms occupy the B sites and the aldehyde oxygen atoms

occupy the A sites, with M-A/B distances of 2.520 and 2.315 Å, respectively.[41] Recall that a

perfect dodecahedron contains A and B sited with θ_A and θ_B angles, both at 45°, Scheme 1.5.

Variation from this idealized dodechedron results in distorted dodecahedra, such as the square

antiprismatic.[42]
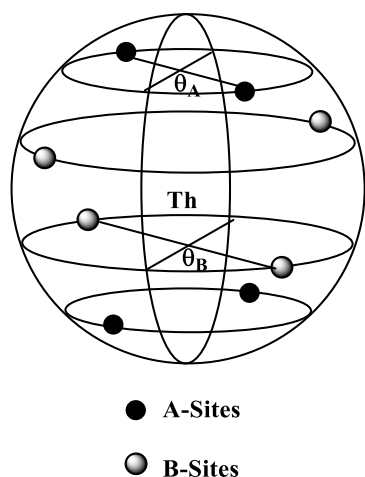
Scheme 1.5. The A- and B-sites of a dodecahedron.

Tetrakis(catecholato) thorate Complex

The coordination of tetravalent actinides is of keen interest in part due to the concept of

using Th(IV) as a structural model for Pu(IV), based on thorium's lower radioactivity, similar

ionic radius, and relative ease of characterization. Highly selective ligands that could be used in

the case of an accidental exposure or plutonium poisoning arose from studies that demonstrated

that plutonium is moved and stored by the iron transport and storage compounds, transferrin and

ferritin, in mammals. Model systems based on siderophores-naturally occurring iron sequestration compounds produced in marine bacteria - have been the basis for designing actinide sequestering agents.[43] An ongoing project in the Raymond laboratories was inspired by the design and characterization of such agents.[44] Mimicking iron (Fe^{3+}) sequestering agents in bacteria, in which three bidentate catechol ligands coordinate iron, the group employed four catechol ligands to coordinate the tetravalent thorium metal center. The tetrakis(catecholato) thorate (**10**), $Na_4[Th(C_6H_4O_2)_4 \cdot 21H_2O$, synthesized in 1978 was the first case of structural analysis for these types of chelators with Th using single-crystal X-ray diffraction. This compound featured a trigonal-faced dodecahedron (D_{2d}) geometry with a bond length ratio of 1.00, $\theta_A = 37.9°$ and $\theta_B = 75.4°$. The Th-O bond lengths are nearly identical, with Th-O_1 = 2.418(3) Å and Th-O_2 = 2.412(3) Å, with a bite angle of 66.798°.[44]
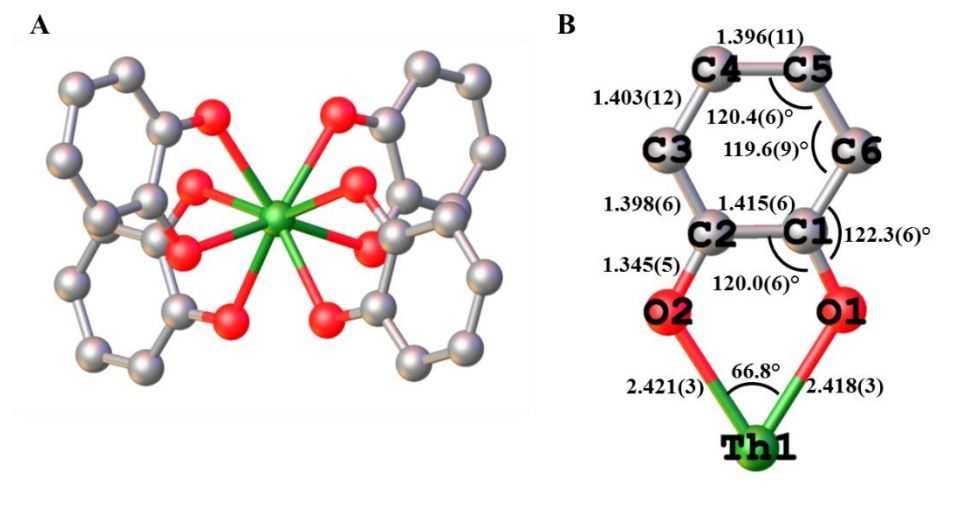
Figure 1.1. A) Complex **10** ($Na_4[Th(C_6H_4O_2)_4 \cdot 21H_2O$). B) Schematic diagram of the Th(IV) catecholate coordination geometries with the average bond distances and angles. Both images generated from the Cambridge Crystallographic Database [44].

Tetrakis(thenoyltrifluoroacetonato)thorium(IV) Complex

Interest in the properties of Th(IV) chelated with β-diketones lead Lenner[46] and Lindqvist to synthesize tetrakis(thenoyltrifluoroacetonato)thorium(IV), **11**, Th(TTA)$_4$, to determine the effect of an asymmetric ligand on the coordination of thorium (IV). Crystals were grown from an aqueous solution of Th(NO$_3$)$_4$.5H$_2$O with a benzene solution of HTTA. The structure consists of an 8-coordinate distorted dodecahedron, with four of the bidentate ligands coordinated to the Th center with a Th-O bond with an average length of 2.397 Å and an average bite angle of 69.575 Å. Each of the four ligands serve as the leg of the two perpendicular trapezoids of the dodecahedron, with the angle between the trapezoids measuring at 94.5°, versus the ideal 90°, Figure 1.2. The TTA ligand is relatively planar aside from the fluorine atoms and the thienyl rings; the plane of the ligand is folded over the line of the oxygen atoms, with the thorium atom over this line resulting in an average of 13.68° for the fold of Th(TTA)$_4$. The molecule is propeller like, with all the CF$_3$ groups on the same side of the plane and the thienyl groups on the other side of the plane, Figure 1.3.[4]
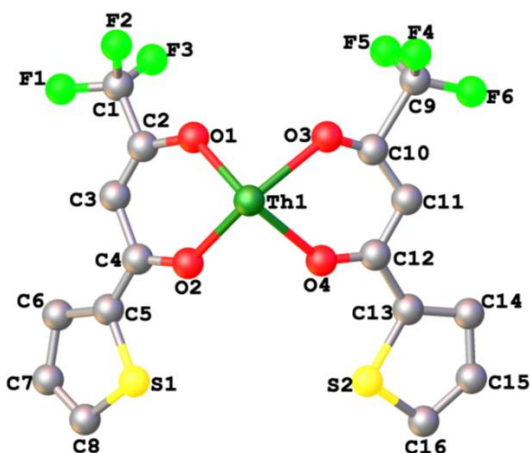
Figure 1.2. The spectroscopic picture of the tetrakis(thenoyltrifluoroacetonato)thorium(IV) molecule **11**, Th(TTA)$_4$. . Image generated from the Cambridge Crystallographic Database [46].
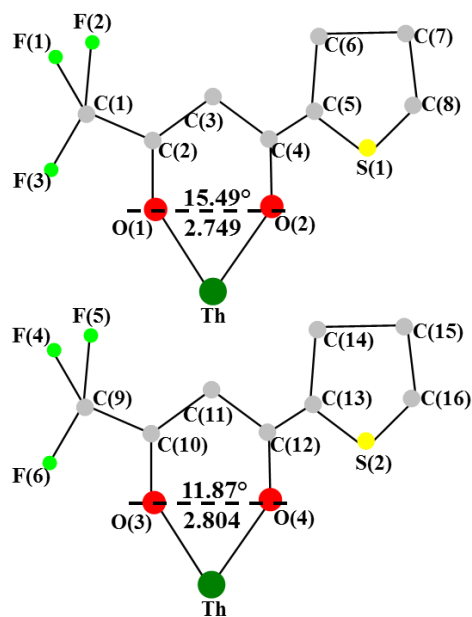
Figure 1.3. The geometry of the two independent TTA ligands from **11** [46].

Hydroxymate Thorium Complexes

Again inspired by the iron-transport biomimetic approach[47] to design tetravalent actinide

ligands, Raymond and co-workers prepared hydroxyamate complexes with thorium(IV).[48] A

positive attribute of these ligands is that they can be used as an archetype or analog of a

macrochelate without the steric or solubility issues associated with macrochelates.[49] Prior to this

point in 1980, such complexes had not been structurally characterized, although quantitative

analysis and solvent extraction studies of hydroxamic acids with actinides had been reported.[49]

The colorless complexes, $Th[(CH_3)_2CHN(O)C(O)R]_4$, where $R = C(CH_3)_3$ or $CH_2C(CH_3)_3$, as

shown in Figure 1.4, were both soluble in hydrocarbons, but displayed very different

coordination geometries.[27] The stereochemistry constraints placed on the complex, **12**, from the

tert-butyl substituents force the ligand to form a geometry around the thorium(IV) center that is

nearly cubic (S_4). The neopentyl substituted complex, **13**, was found to have a dodecahedron (D_{2d}) geometry. In both complexes, the $Th-O_N$ bond is shorter than the $Th-O_C$, for complex **12**, the bonds were 2.357(3) Å and 2.492(3) Å, respectively; for complex **13**, the bonds averaged 2.36(1) Å and 2.46(2) Å, respectively. Complex **12** was found to have a bite angle of 62.329° and complex **13** had bite angles ranging from 62.867° to 63.673° with an average of 63.228°. The authors attribute this to the unsymmetrical nature of the hydroxamate ligand and the localization of the charge on the oxygen atom that is bound to nitrogen. The aforementioned dodecahedral (D_{2d}) geometry of complex **13** was thought to give the maximum stability required for selective tetravalent actinide sequestration.[51]
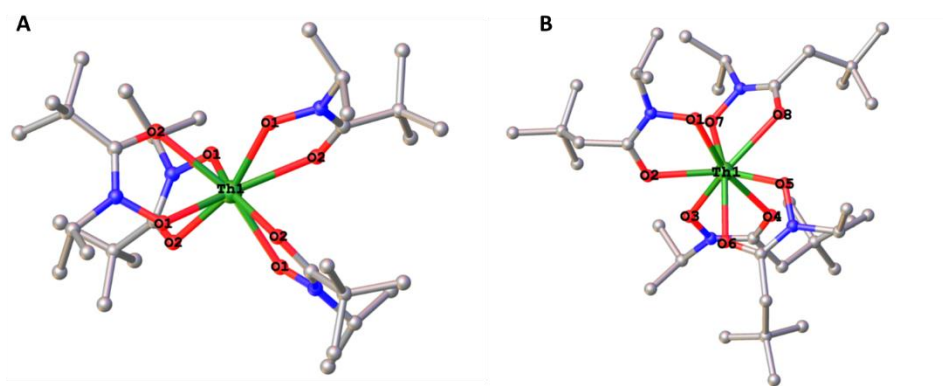
Figure 1.4. A) Complex $Th[(CH_3)_2CHN(O)O(O)C(CH_3)_3]_4$ **12** with hydrogen atoms omitted for clarity. B) A view of complex $Th[(CH_3)_2CHN(O)O(O)CH_2C(CH_3)_3]_4$ **13**. Both images generated from the Cambridge Crystallographic Database [58].

Tetrakisacetylacetonate aniline Thorium Complex

With an interest in thorium tetrakisacetylacetonate ammonia and aniline compounds, $2ThA_4 \cdot NH_3$ and $2ThA_4 \cdot C_6H_5NH_2$, as synthesized by Blitz[52] lead Smith and co-workers[53] to

synthesize the adduct of thorium(IV) tetrakisacetylacetonate with aniline, **14**. Smith *et al.* proposed to determine three things: 1) whether the nitrogen was within the thorium coordination sphere; 2) whether a hydrogen bonded structure was formed; or 3) whether they were clathrates like the benzene adduct previously reported by Lenner.[54] To do this, thorium tetrakisacetylacetonate (abbreviated ThA_4) and aniline were reacted in hot ether, and subsequently cooled to produce crystals. Analysis of the resulting solids revealed two independent ThA_4 molecules. As shown in figure 1.5, the complexes were found to have antiprism coordination and the aniline, while clatharate without hydrogen-bonding to the complex, still has an effect on some of the ligand planes. The planes of the two ligands open to include the aniline that lies between them. This observation is supported by the mean dihedral angle, *D*, of 42.05° versus the $D = 27.9°$ for the ligands opposite the aniline.[53] The median bond lengths between the Th_1 and oxygen atoms was 2.41 Å and a median bite angle of 69.70°. The second thorium atom possessed bite angles ranging from 67.6° to 71.1° with an average of 69.98° and Th2-O bond lengths that averaged 2.385 Å.
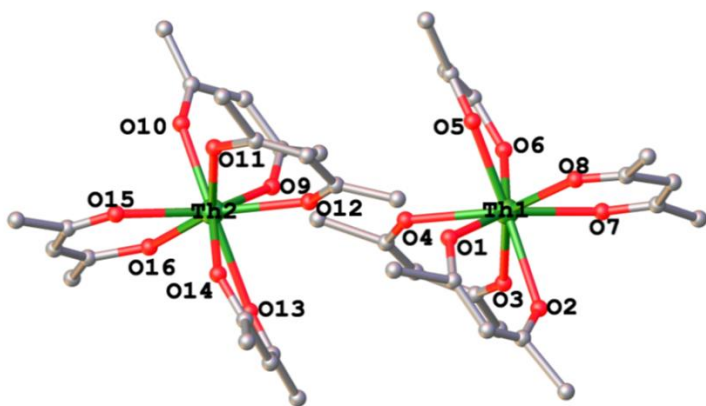
Figure 1.5. The two ThA_4 molecules of **14**. The image was generated from the Cambridge Crystallographic Database [53].

Catecholamide-based Thorium Complex

The need to reduce the volumes of radioactive fission materials and spent fuels requiring long-term storage in geological repositories has been a hot topic for the nuclear energy industry.[55]   Following the biomimetic approach that proved that hard metal ions, such as actinide(IV) ions, have a preference for oxygen donor ligands,[56] Raymond et al.[55] synthesized ligands for actinide sequestration. The authors were interested in thorium(IV) complexes due to it being considered a good analogue for Pu(IV) as a result of its similar radii, coordination number, and oxidation state.[36] With the knowledge that catecholate-based ligands can be used to chelate Fe(III), they sought to design catecholamide-based ligands for binding. The ligand N,N'-diethyl-2,3-dihydroxyterephthalamide (ETAM) was synthesized and coordinated to Th(IV). The authors were able grow crystals of two thorium(IV) complexes: 1) the 8-coordinate [Me$_3$BnN]$_4$[Th(ETAM)$_4$], **15**, where Me$_3$BnN = trimethylbenzylammonium and 2) a dimer, **27**, (NMe$_4$)$_4$[Th(ETAM)$_3$MeOH]$_2$, with both metal centers possessing a coordination number of 9 that will be discussed in the later sections. The coordination geometry of complex **15**, Figure 1.6, was not clear, but it was determined to be between that of an ideal bicapped trigonal prismatic (C$_{2v}$) and the ideal trigonal dodecahedron, although somewhat closer to geometry of the dodecahedron. The thorium(IV) metal center and the oxygen of complex **15** were found to have a median bond length of 2.414 Å and bite angles that range from 63.9° to 65.06°, with an average bite angle of 64.63°.[55] (Of interest, to date, the structural characterization of the Pu(IV) analog of this complex has not been reported.)
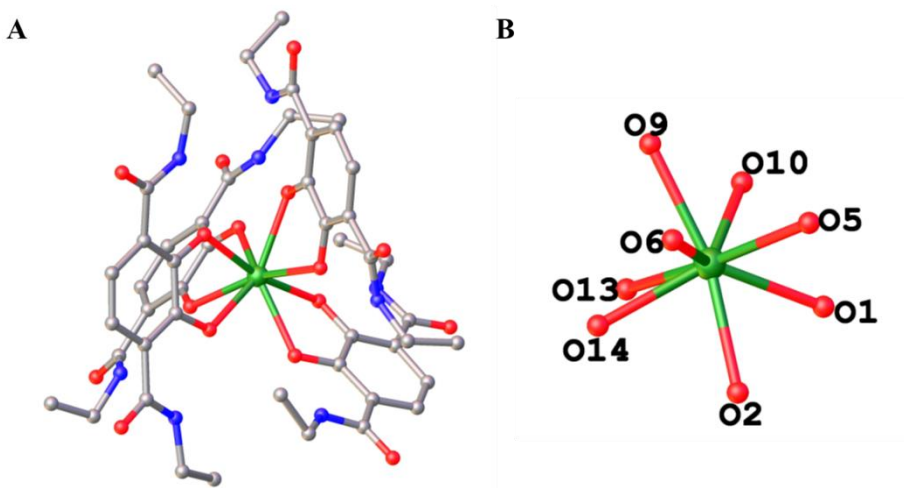
Figure 1.6. a) The OLEX diagram of [Me₃BnN]₄[Th(N,N'-diethyl-2,3-dihydroxyterephthalamide)₄] **15**. b) The isolated coordination geometry of the 8-coordinate Th(IV) ion in **15**. Both images generated from the Cambridge Crystallographic Database [55].

Terephthalamide-based Thorium Complex

Another concept has peaked interest in thorium(IV) coordination chemistry, that of its possible use in radiotherapy, in which the α-particle emitter [227]Th is complexed to a ligand that can covalently linked to a biomolecule to enable targeted radiation delivery.[58] A high thermodynamic stability and rapid coordination kinetics is required to be appropriate for such a task. Previously proposed macrocycles have either high stability and slow rates or vice-versa, such as the case with 1,4,7,10-tetraazacyclododecane-1,4,7,10-tetraacetic acid, DOTA, and diethylenetriaminepentaacetic acid, DTPA. The structure of these as the Th(IV) complexes have not as yet been reported. Raymond et al.[59] designed and synthesized a novel macrocyclic octadentate ligand that incorporated terephthalamide, 6,19-bis(2-((2,3-Dihydroxy-4-((2-methoxyethyl)carbamoyl)benzoyl)amino)ethyl)-12,13,25,26-tetrahydroxy-2,10,15,23-tetraoxo-

21

3,9,16,22-tetraaza-6,19-diazoniatricyclo[22.2.2.2^{11,14}]triaconta-1(26),11,13,24,27,29-hexaene dichloride tetrahydrate, (TAM) binding units and chelated it to thorium(IV). The synthesis and structure of the ligand, **16**, can be seen in Figure 1.7. The ligand incorporates the thermodynamic stability of a macrocycle with the desired rapid kinetics of linear ligands and fulfilling the required coordination number of thorium(IV), 8. The authors were able crystallize the complex, Th**TAM**K$_4$·(DMF)$_2$·(MeOH)$_2$·THF, Figure 1.8, **17**. This was analyzed and found to have a novel inner coordination environment between the ideal bicapped trigonal prism and an ideal trigonal dodecahedron (D$_{2d}$). Complex **17** possessed an average Th-O bond length of 2.41 Å that resulted in an average bite angle of 64.95°.
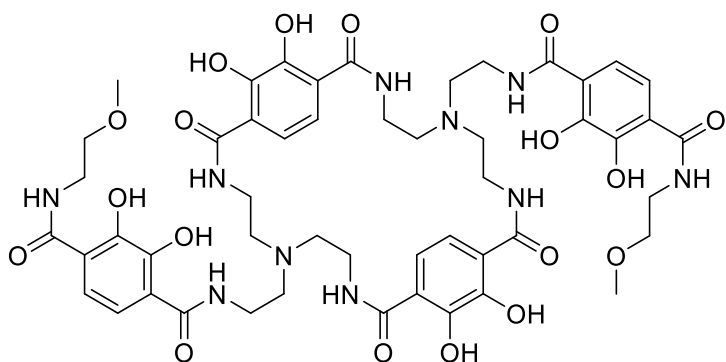
Figure 1.7. Macrochelate TAM derived ligand **16** [59].
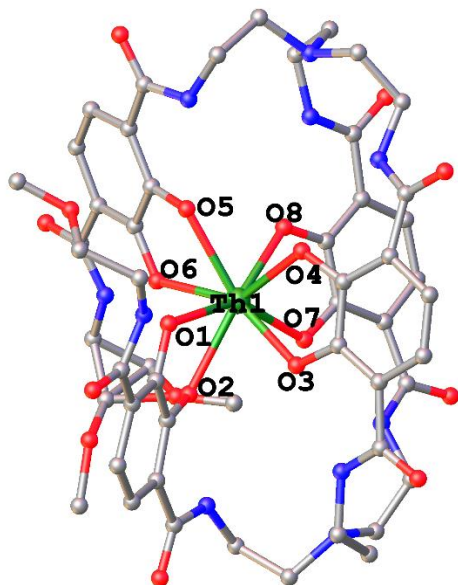
Figure 1.8. Complex **17** with potassium ions, solvent molecules, and hydrogens omitted for clarity. The image was generated from the Cambridge Crystallographic Database [59].

Di- and Tetranuclear Thorium Complexes

The soluble actinide-halide complexes are regularly explored due to them being possible starting materials for other compounds[60] lead Kiplinger et al. to begin developing methods that did not require thorium metal as a starting material.[60] This was done in prior reports[60b] through the reaction of $ThCl_4(DME)_2$, where DME = 1,2-dimethoxyethane, and trimethylsilyl iodide via complete halide exchange to give $ThI_4(DME)_2$. The halide exchange product can then react with excess DME to give the dinuclear thorium complex, $Th_2I_5[\kappa^2(O,O')-\mu-O(CH_2)_2OCH_3]_3(DME)$, **18**. During the halide exchange, if the reaction does not go through complete exchange, the production of a mixed-halide compound occurs, yielding $ThCl_{4-x}I_x(DME)_2$. This mixed-valent compound then spontaneously reacts with DME in methylene chloride to give the tetranuclear

thorium(IV) μ_4-oxo cluster, $Th_4(\mu_4$-$O)(\mu$-$Cl)_2I_6[\kappa^2(O,O')$-μ-$O(CH_2)_2OCH_3]_6$, **19**. Figure 1.9 shows the dinuclear cluster, **18** with its two different thorium(IV) metal ions that are bridged by three alkoxide-ether ligands that are a result of the cleavage of DME C-O bonds. The compound had Th-$O_{alkoxide}$ bond lengths that averaged 2.360(7) Å and Th-I bond length was 3.1384(8) Å. The Th-O_{ether} and DME coordinated molecule had distances of 2.577(7) Å and 2.538(7) Å, respectively, both of which are representative of dative bonds as supported by literature.[62] The angle between the Th_1-O-Th_2 atoms was 100.8(3)°, which was similar to the alkoxide bridge in complex **19**.
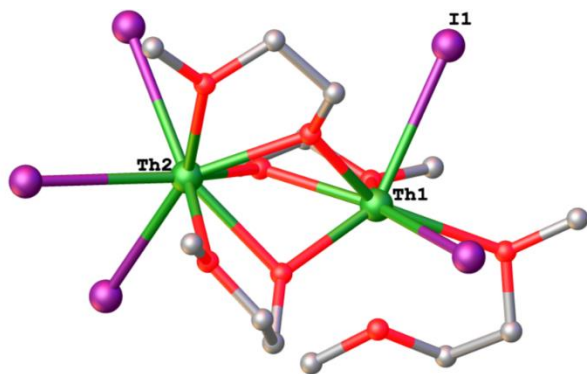
Figure 1.9. Complex **18**, $Th_2I_5[\kappa^2(O,O')$-μ-$O(CH_2)_2OCH_3]_3$(DME). The image was generated from the Cambridge Crystallographic Database [61].

Complex **19** contains a rare μ_4-O atom that coordinates to the four Th(IV) atoms and is one of two tetranuclear μ_4-oxo complex that has been characterized via X-ray crystallography.[63] The four thorium atoms were a pair of two different thorium metal ions, Figure 1.10, all of which are bonded to the central oxo-bridge, O1. The Th-Th distances were found to range from 3.6309(9) – 4.1623(5) Å, with the shorter distance being shorter than those reported in literature, 3.7431(9) Å, but the longer distance was longer than the other reported 4.0031(6) Å.[57] The

24

average bond angle for Th_1-O1-Th_1 and Th_2-O1-Th_2 were found to average 98.4(5)°, with the

Th_1-O1-Th_2 angle averaging 115.355(13)°. The Th-O bond lengths of 2.391(7) Å for the Th_1-O1

bond and the Th_2-O1 had a bond length of 2.409(7) Å, resulting in a distorted tetrahedral

geometry.
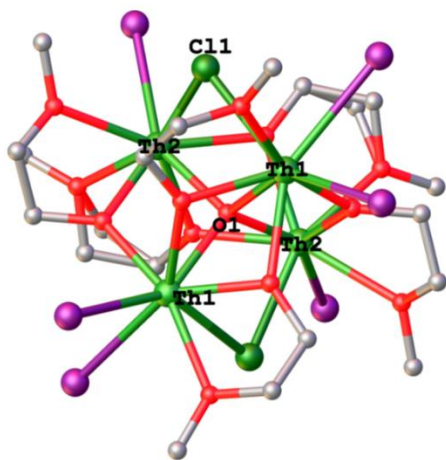
Figure 1.10. Complex **19**, the μ4-oxo tetranuclear complex, μ4-oxo cluster, Th4(μ4-O)(μ-Cl)2I6[κ2(O,O')-μ-O(CH2)2OCH3]6. The image was generated from the Cambridge Crystallographic Database [61].

Phosphite-based Ligands

Early reports of thorium (IV) coordination complexes focused on the structural

characterization of the synthesized complexes with the stated key goal being structures as

archetypes for the improvement of rational design for selective tetravalent actinide extractants.

The desire for a highly selective ligand for incorporation into an electronic or chemical sensor is

still very relevant today. Wang et al.[64] reported the first thorium open-framework compound with mixed-valent phosphite and pyrophosphate ligands that demonstrated the ability of being highly stable in aqueous solutions in acidic and basic pH, 1-14. The complex, $[BMMim]_2$-$[Th_3(PO_3)_4(H_2P_2O_7)_3]$, ThP-1 (**20**), where BMMim = 1-butyl-2,3-dimethylimidazolium, was found to crystallize in the centrosymmetric cubic space group and adopted a square antiprism coordination, as part of an open-framework resembling metal-organic framework 5 (MOF-5). The crystal structure, Figure 1.11, shows that the coordination sphere contains four oxygen atoms provided by four different distinct phosphite ligands with the other four oxygen atoms provided by two separate pyrophosphate ligands; however, with each phosphate ligand bridging three adjacent thorium centers a Th_6P_8 cluster is formed resulting in an overall octahedral geometry.[64] The $Th-O_1$ and $Th-O_2$ bond lengths were 2.395 and 2.416 Å, respectively. The O_1-$Th-O_2$ bite angle 76.8°.
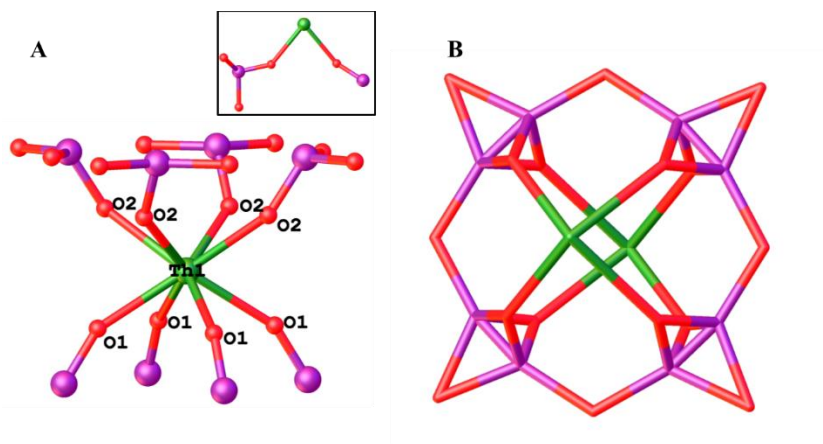
Figure 1.11. a) The Th(IV) cation of **20 -** [1-butyl-2,3-dimethylimidazolium]$_2$-$[Th_3(PO_3)_4(H_2P_2O_7)_3]$. b) The hexanuclear clusters achieved by the phosphite ligands. The thorium atoms are in green, the oxygen atoms in red, and the phosphate atoms are in purple. Both images generated from the Cambridge Crystallographic Database [64].

Nine Coordinate Thorium Complexes

Thiopyridine-based Thorium Complex

An investigation on the complexes of actinide ions led Viagto et al. to probe the complex dimethylformamidetetrakis(1-oxo-2-thiopyridinato) Thorium(IV), Th(pyOS)4(dmf).[65] Taking advantage of the large ionic radii of Thorium, the authors prepared and structurally characterized the complex, **21**, Th(pyOS)4(dmf), producing a nine-coordinated Th(IV). Eight of the donor atoms were from four bidentate ligands and a dimethylformamide solvent molecule, Figure 1.12, resulting in a distorted monocapped square antiprism. The complex possessed Th-S bonds that averaged 2.965 Å and Th-O bonds that averaged 2.424 Å. These bond lengths resulted in bite angles that averaged 73.0°, 75.26°, and 70.41°, for the O-Th-O, S-Th-S, and O-Th-S bite angles, respectively.
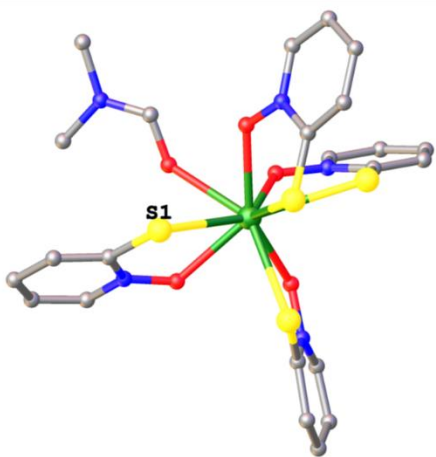
Figure 1.12. Complex **21**, Th(pyOS)4(dmf). Image generated from the Cambridge Crystallographic Database [65].

1-oxy-2-pyridonate

Raymond et al.[66] prepared and described a nine-coordinate $(C_5H_4NO_2)_4(H_2O)Th$, **22**,

between thorium(IV) and bidentate 1-oxy-2-pyridonate $(C_5H_4NO_2^-)$ structure.[66] This structure

revealed a primary coordination sphere around the thorium(IV) metal center completed with 8

oxygen atoms from the four bidentate 1-oxy-pyridonate ligands and a single coordinated water

molecule along the C_2 axis of the metal center. The average bond length between Th^{IV} and the

ligand O atoms is 2.44 Å, and that between Th^{IV} and the water O atom is 2.52 Å. This results in

an average bite angle of 64.671° and a geometry that resembles a D_{3h} tricapped trigonal prism,

but is actually an intermediate C_{2v} symmetry pathway between the C_{4v} monocapped Archimedean

antiprism and the D_{3h} tricapped trigonal prism, as you can see in Figure 1.13. The authors

attribute this difference in geometry between this and the 9-coordinate tetrakis(tropolonato)(N,N-

dimethylformamide)thorium(IV) complex reported by Day in 1970[67] as due to an asymmetric

charge distribution in the oxypyridinone ligand, as compared with the more symmetric

tropolonate.
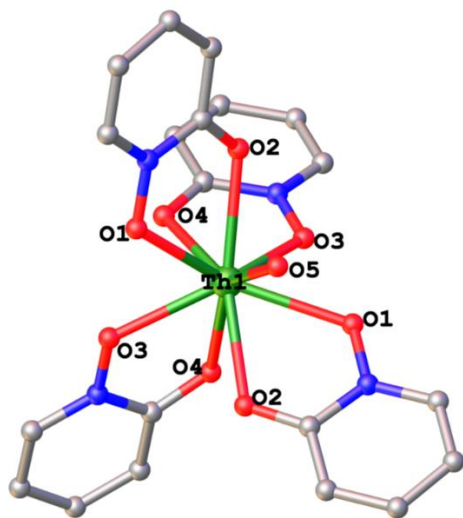
Figure 1.13. The nine-coordinate complex $(C_5H_4NO_2)_4(H_2O)Th$ **-22** with the view normal to the plane along the pseudo-C_3 axis. The image is generated from data in the Cambridge Crystallographic Database [66].

Hydroxypyridinone Ligands

Due to its chemical toxicity as a heavy metal, the need to sequester thorium, whether *in vivo* or in the environment, is of concern in applying thorium as nuclear fuel. Ligands containing hydroxypyridinone (HOPO) chelating units have been found effective in animals for the decorporation, the removal of radioactive materials absorbed in the body, of Th(IV) and other actinides.[68] To compare and contrast the ability of HOPO-based ligands with Th(IV),[69] three hydroxypyridinone isomers were synthesized and characterized as Th(IV) complexes: **23**) 1-hydroxy-2(1*H*)-pyridinone, **24**) 3-hydroxy-2(1*H*)-pyridinone, **25**) 3-hydroxy-4(1*H*)-pyridinone, abbreviated 1,2-HOPO, 3,2-HOPO, and 3,4-HOPO.[69] All three ligands were synthesized to add an amide linkage to be used as a point of attachment prepare a multidentate ligand.

All three ligands were subjected to complexation with Th(IV) and demonstrated to have different optimal binding pH ranges. Reaction of the 3,2-HOPO to prepare a Th(IV) complex produced crystals that were analyzed using XRD. The complex, Th(3,2-HOPO)·H_2O, **26**, was determined to be nine-coordinate, with the ninth coordination spot being occupied by an amide oxygen. This amide oxygen is readily displaced by a liquid water molecule in water and forms an infinite linear coordination polymeric structure with a distorted monocapped square-antiprismatic geometry. The average Th-$O_{phenolic}$ is 2.405(8) Å and the average length of the Th-O_{oxo} bond is 2.524(11) Å, resulting in average bite angle of 63.21°. When compared to the crystal structure of the metal free ligand, the geometry of both structures are nearly identical, leading to the idea that the ligands might serve as metal chelators.[69]
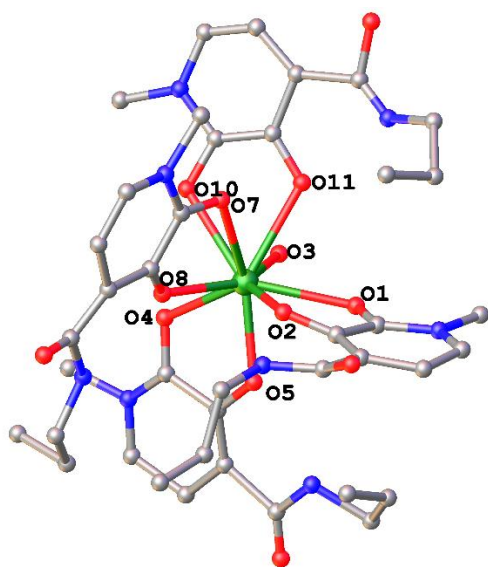
Figure 1.14. Structure of complex **26** Th(3-hydroxy-2(1*H*)-pyridinonate)$_4$, view is down from the cap of the monocapped square antiprism, C_{2v} geometry. The image was generated from the Cambridge Crystallographic Database [69].

N,N'-diethyl-2,3-dihydroxyterephthalamide Ligand

Work conducted by the Raymond lab in which the ligand N,N'-diethyl-2,3-dihydroxyterephthalamide (ETAM) was coordinated to Th(IV) resulting in the formation of an 8-coordinate complex, **15**, produced an addition structure, the bimetallic complex **27**.[55] This 9-coordinate complex was obtained by the synthesis of Th[ETAM}$_4$ where the addition of an excess thorium resulted in a bimetallic species Th$_2$[ETAM]$_6$. This structure, shown in Figure 15a, has four complexes per unit cell and crystallizes in $P2_1/c$ space group. Two of the three TAM ligands bind to the thorium(IV) with the catecholate oxygen atoms, while the third TAM ligand binding as a bridge to the second Th(IV) center, with the amide ortho to the oxygen oriented to allow the carbonyl oxygen to bind the second Th(IV) center, Figure 1.15b. Prior examples of TAM complexes show this amide oxygen pointing away from the metal, allowing the amide proton to hydrogen bond the deprotonated, coordinating catecholate oxygen. The average bond lengths between the thorium metal center and the oxygen atoms was 2.45375 Å, resulting in an average bite angle of 68.125°.[55]
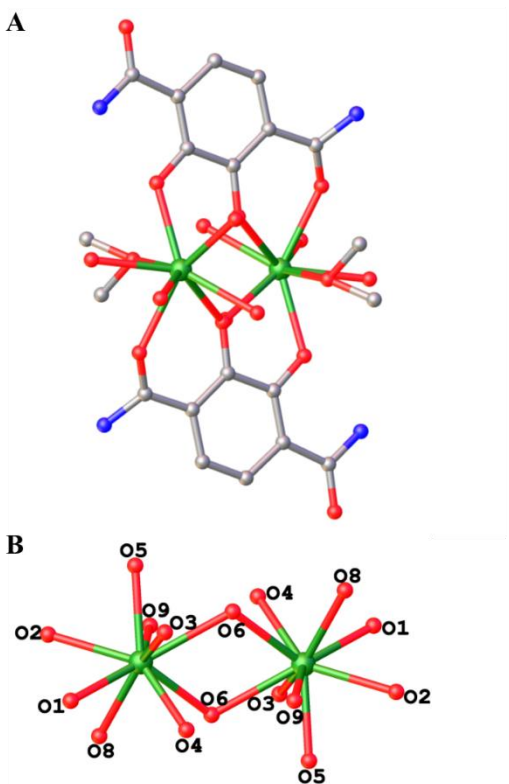
Figure 1.15. a) The ORTEP diagram of complex **27** – (Th$_2$(N,N'-diethyl-2,3-dihydroxyterephthalamidate)$_6$). b) The coordination geometry of the Th(IV) metal centers as seen in complex **27**. Both images have been generated from the Cambridge Crystallographic Database [55].

Aminopolycarboxylate-based Ligands

  Another proposed means of actinide sequestration is through the binding of tetravalent actinides with ligands from the aliphatic aminopolycarboxylate family. These have been characterized primarily in solution studies or with uranium.[70] Until Thuèry[71] investigated the ability of aminocarboxylate ligands on chelating thorium(IV) ions, only one metal complex with aminocarboxylate ligands had been structurally characterized and reported.[72] In this

32

investigation, Thuèry complexed Th(IV) with three common ligands: 1) iminodiacetic acid (H$_2$IDA), which formed a 10-coordinate complex, and two 9-coordinated complexes with 2) nitrilotriacetic acid (H$_3$NTA), 3) ethylenediaminetetraacetic acid (H$_4$EDTA). All three complexes were produced under hydrothermal conditions.[71] The 10-coordinate complex, **38**, is discussed in the 10-coordinate section. The first 9-coordinate complex, [Th(NTA)(H$_2$NTA)(H$_2$O)·H$_2$O], **28**, has an asymmetric unit that is comprised of two ligands in different states of protonation, Figure 1.16. One ligand is trianionic and chelates the metal ion though one nitrogen atom, three oxygen atoms, and two carboxylate groups are bridging bidentate. The Th-O bond lengths average 2.41(3) Å, while the Th-N bond distance was reported at 2.799(2) Å, with average bite angles of 79.51° and 62.24°, respectively. The Th-O$_{H2O}$ bond length is equal to 2.564(2) Å. The resulting structure is most closely a capped square antiprismatic (D$_{4d}$) geometry. The second ligand is monoanionic and has two monodentate carboxylate groups coordinated to it, as well as, one uncoordinated carboxylic acid arm, and a central ammonium group.[71]
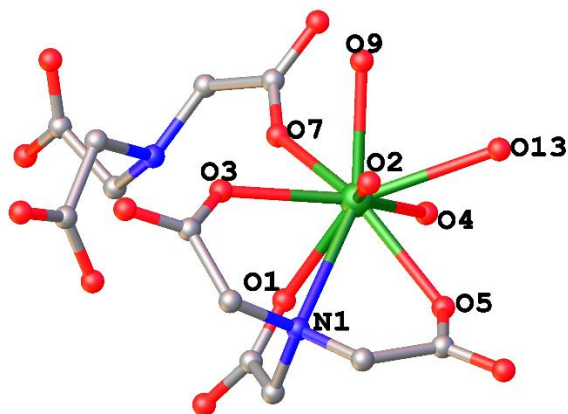
Figure 1.16. Structure of complex [Th(NTA)(H$_2$NTA)(H$_2$O)·H$_2$O], **28** with the carbon-bound hydrogens omitted. This image generated from the Cambridge Crystallographic Database [71].

The second 9-coordinate complex, **29**, [Th(EDTA)(H$_2$O)]·H$_2$O, is the second Th(IV)-EDTA complex to be characterized crystallographically, Figure 1.17. This complex has an asymmetric unit with the Th(IV) ion coordinated by four oxygen atoms and two nitrogen atoms from the EDTA^{4-} anion, two carboxylate oxygen atoms from neighboring molecules, and an aqua ligand to give a capped square antiprismatic (D$_{4d}$) coordination environment. The Th-O bond length averages 2.41(3) Å and the Th-N bond lengths average 2.727(13) Å. The average O-Th-N bite angle was calculated to 63.208° and the N-Th-N bite angle is 66.95°.
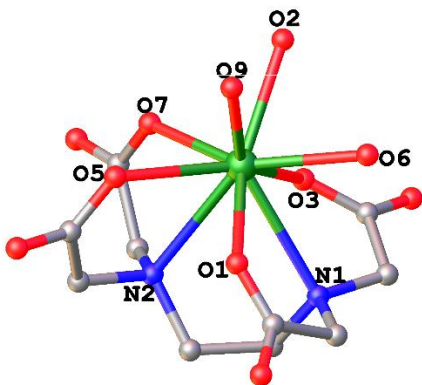
Figure 1.17. Structure of complex **29 -** [Th(EDTA)(H$_2$O)]·H$_2$O, with the carbon-bound hydrogens omitted for clarity. The figure has been generated from the Cambridge Crystallographic Database [71].

Polycarboxylate-based Ligands

The ability of Th(IV) to form polynuclear species after undergoing hydrolysis and condensation can have an effect on the transportation of radionuclides in the environment.[73] Forbes et al.[74] took an interest in understanding the effect that condensation and chelation have on each other in the environment when polynuclear clusters are formed. To enhance their understanding, the group used five polycarboxylates, shown in Figure 1.18, to form ternary and binary Th(IV) and other metal centered complexes. Four of the synthesized complexes contained 9-coordinate Th(IV) metal centers, while two formed polynuclear complexes.
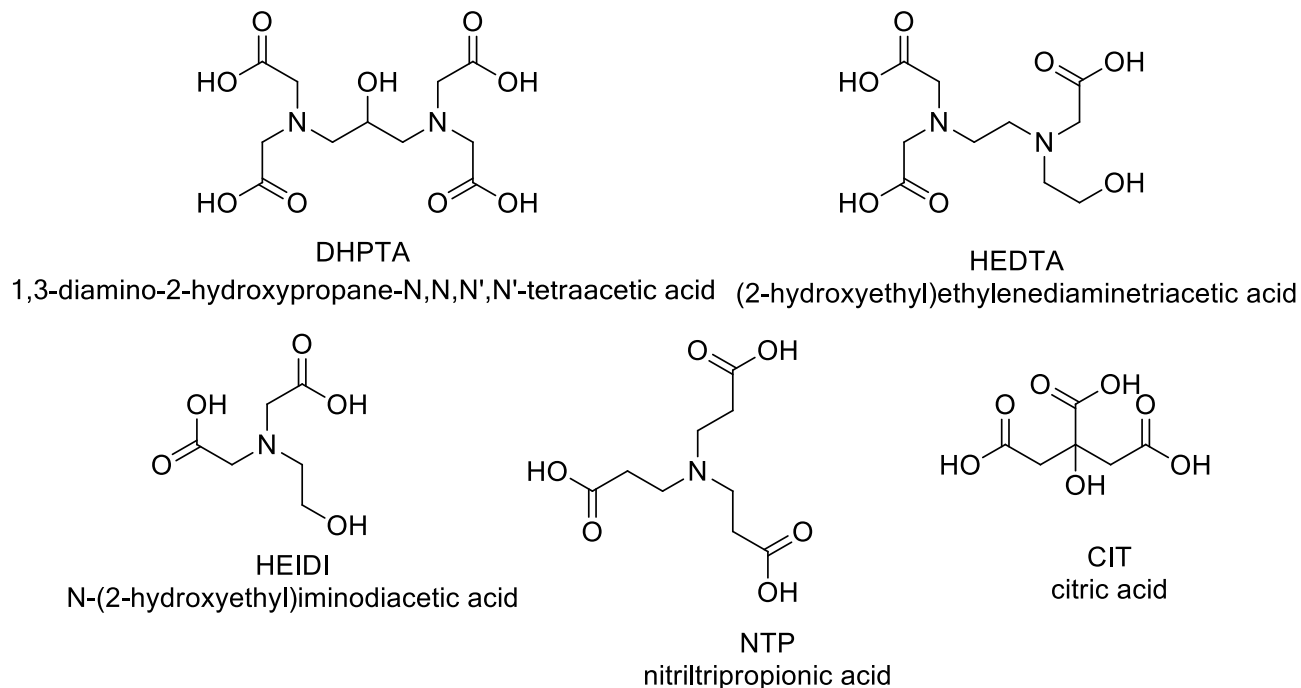
Figure 1.18. Ligands used to complex Th(IV) [74].

The first complex, Th$_6$hedta (with hedta being 2-hydroxyethyl)ethylenediaminetriacetic acid), characterized showed two trimeric Th(IV) cores that were linked via the HEDTA ligand to form a hexameric molecular species with an overall formula of Na$_4$[Th$_6$O$_2$(hedta)$_6$]·28H$_2$O, Figure 20, **30,** Figure 1.19 inset. Each of the Th(IV) cations in the trimeric core is coordinated by seven O atoms and two N atoms forming an overall distorted monocapped square antiprismatic (most closely D$_{4d}$) coordination geometry with Th-O bonds ranging from 2.322(7)-2.516(8) Å. The Th-N bonds averaged 2.784(7) Å. The O-Th-O bite angle is 68.1(2)° and the bite angle between the thorium atom and the nitrogen atoms was 66.3(3)°. This hexameric species is a result of the free O atom of the carboxylate group on the HEDTA ligand coordinating to the Th(IV) cation of the neighboring trimeric unit. Further analysis showed that

there are four unique Na^+ cations present to balance the negative charge of the cluster,
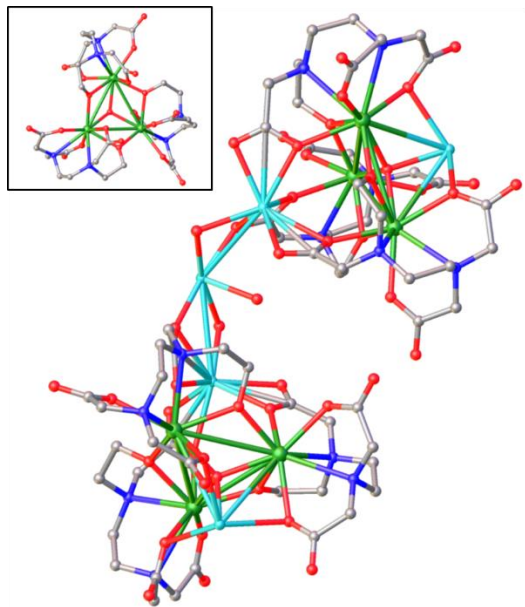
$[Th_6O_2(hedta)_6]^{4-}$.[74]

Figure 1.19. Inset: The trimeric unit of complex **30 -** $Na_4[Th_6O_2(hedta)_6]\cdot 28H_2O$. The H_2O molecules have been omitted for clarity. The hexameric form of complex **30 -** $Na_4[Th_6O_2(hedta)_6]\cdot 28H_2O$. The H_2O molecules have been omitted for clarity. Both images generated from the Cambridge Crystallographic Database [74].

Utilizing the NTP, nitriliproprionic acid, ligand, the second nine-coordinated Th(IV) structure was synthesized and characterized. The complex, **31**, Th(NTP), Figure 1.20a, was obtained during the synthesis of a heteronuclear NTP complex with Al(II), however, the intended heteronuclear species was not isolated. Instead, 2-D sheets of $[Th(C_9O_6NH_{12})$-$(H_2O)(NO_3)]\cdot 2.5H_2O$, Figure 1.20b, resulted. Each Th(IV) cation is coordinated by nine O

atoms with bond lengths ranging from 2.337(5)-2.592 Å, resulting in an average bite angle of 66.86(7)° and a distorted monocapped square antiprismatic geometry (most closely resembling D_{4d} geometry).
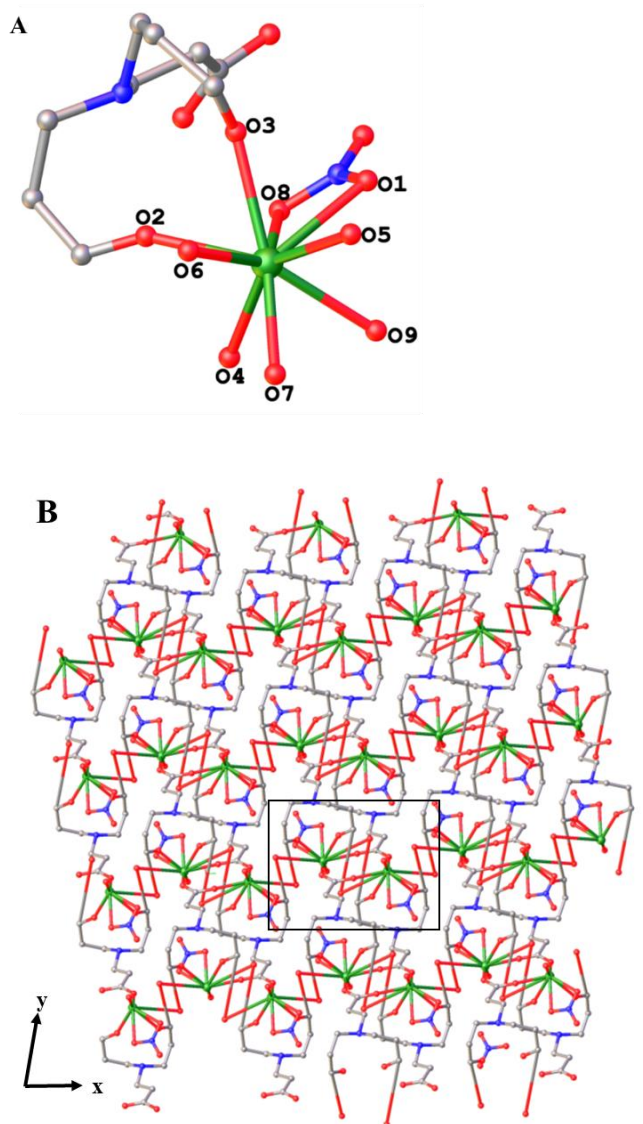
Figure 1.20. a) One NTP ligand and one nitrate anion bonding to the Th(IV) ion in complex **31-**[Th(C_9O_6NH_{12})-(H_2O)(NO_3)]·2.5H_2O. The 2D sheets of complex **31 -** [Th(C_9O_6NH_{12})-(H_2O)(NO_3)]·2.5H_2O. Both images generated from the Cambridge Crystallographic Database [74].

The primary stated overall goal of this work was the isolation of novel heteronuclear complexes. This was achieved with the third complex, in which the HEIDI ligand (N-(2-hydroxyethyl)iminodiacetic acid) was used to complex both Th(IV) and Al(III), Th_2Al_8HEIDI, **32**. This complex was synthesized through the chelation of a hexameric Al(III) core complex and the HEIDI ligand, resulting in two mixed-metal dimeric complexes Figure 1.21. Specifically, two ligands can chelate the Th(IV) and Al(III) cations in a tetradentate manner via the carboxylate, hydroxyl, and amine functional groups of the ligand. Additional water adducts were found to coordinate either metal to complete the coordination sphere and are bridged through the deprotonated hydroxyl group. The overall molecular formula for the complex is $[Th_2Al_8(OH)_{14}(H_2O)_{12}(C_6O_5NH_8)_4](NO_3)_6 \cdot 57H_2O$. The Th(IV) metal centers form distorted monocapped antiprismatic coordination spheres with Th-O bond distances ranging from 2.383(3)-2.640(3) Å and elongated Th-N bonds, with Th_1-N possessing a value of 2.776 Å and Th_2-N a value of 2.781 Å.[74] The average N-Th-O bite angle was calculated to be 63.68°.
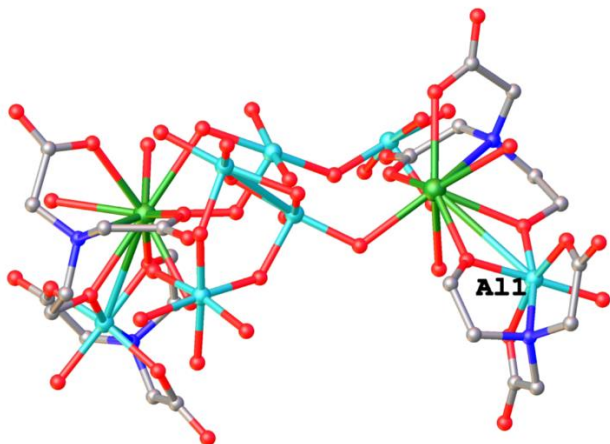
Figure 1.21. The Al atoms forming the central core of complex **32**. ([Th$_2$Al$_8$(OH)$_{14}$(H$_2$O)$_{12}$(C$_6$O$_5$NH$_8$)$_4$](NO$_3$)$_6$·57H$_2$O). This image generated from the Cambridge Crystallographic Database [74].

These authors also successfully synthesized a Th(IV)/Fe(III) heteronuclear complex, Th$_2$Fe$_2$cit (**33**), utilizing the citrate (CIT). The complex resulted in the coordination of Fe(III) cation by six CIT as ligands, with two of the Fe(III) cations being bridged through two central O atoms that are also coordinated to a Th(IV) cation to give a tetramolecular species, Figure 1.22. The Th(IV) coordination sphere is completed by the chelation of the CIT ligand and an additional water molecule, with the Th-O bond lengths ranging from 2.387(3)-2.563(2) Å, resulting in a bite angle of 66.85°. The overall formula for the complex is (C$_4$N$_2$H$_{12}$)[Th$_2$Fe$_2$(OH)$_2$(H$_2$O)$_2$(C$_6$O$_7$H$_4$)$_2$(C$_6$O$_7$H$_5$)$_2$]·5H$_2$O.
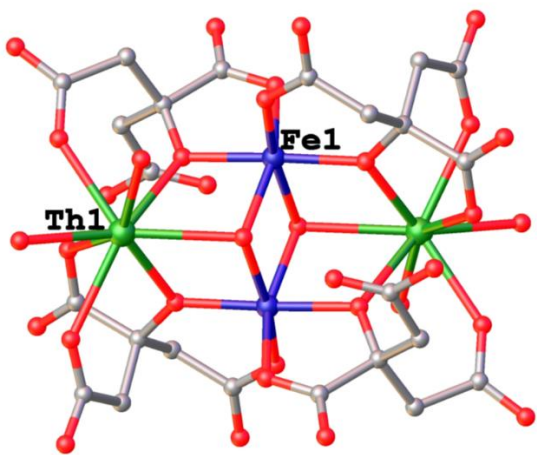
Figure 1.22. Structure of complex **33**. The image was generated from the Cambridge Crystallographic Database [74].

Carboxylphenol-based Ligand

The ability of low-valent, i.e. III and IV, actinides and their similarities to the coordination chemistry of lanthanides, in which the geometry is based on ligand repulsion inspired Wang et al.[75] to synthesize three Th(IV) complexes. Of the three complexes, one was crystallized and determined structurally to be a nine-coordinate Thorium(IV) complex. The complex was coordinated by 1,3,5-tri(4'-carboxylphenyl) benzoic acid (1,3,5-tCPBA), **34**, Figure 1.23.
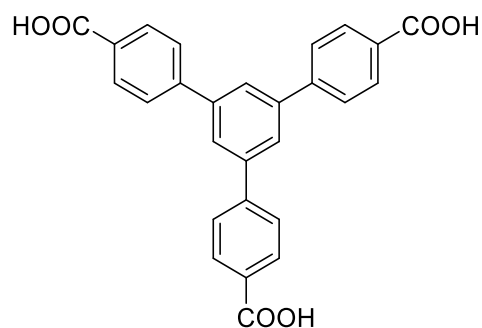
Figure 1.23. The 1,3,5-tri(4'-carboxylphenyl) benzoic acid (1,3,5-tCPBA) ligand (**34**) used by Wang et al. [75].

Single crystal X-ray diffraction of the resulting compound $[C_7H_{11}N_2]_5[Th_2(1,3,5\text{-}tCPBA)_2Cl_6]\cdot Cl$, **35**, revealed that the compound crystallizes in the monoclinic $C2/c$ space group. This complex coordination environment was unique in comparison to other nine-coordinate Th(IV) complexes. The compound is comprised of flat layers with a single Th(IV) metal center bonding to three 1,3,5-tCPBA ligand, resulting in a range of 2.435(11)-2.566(9) Å for the Th-O bond distances, Figure 1.24, resulting in an average bite angle of 52.53°. To satisfy the nine-coordination sites, three chloride anions are bounded to the Th(IV) and result in three unique bond lengths, 2.787(4), 2.775(5), and 2.856(4) Å.
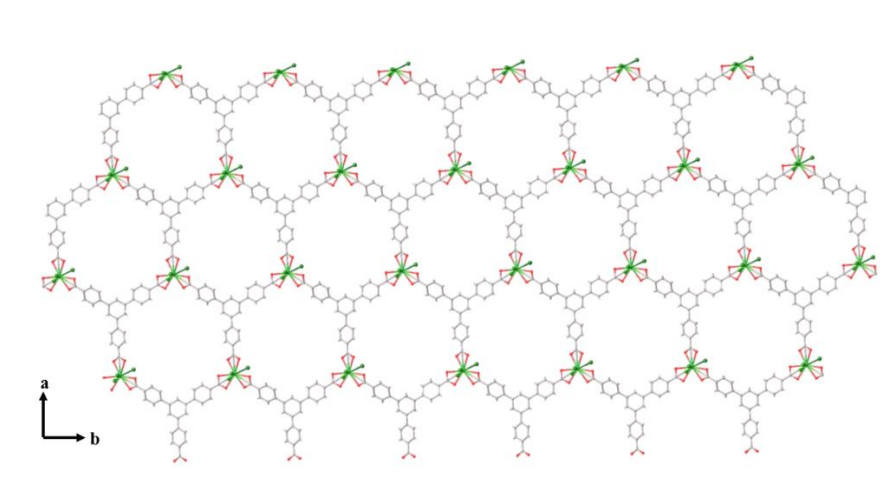
Figure 1.24. The flat layers of the single Th(IV) metal center from complex **35,**
[$C_7H_{11}N_2$]$_5$[Th$_2$(1,3,5-tCPBA)$_2$Cl$_6$]·Cl. This image generated from the Cambridge
Crystallographic Database [75].

Many published nine-coordinate Th(IV) complexes report a square antiprismatic
(D_{4d})(example Figure 1.19) or trigonal prism geometry (C_{2v}) (example Figure 1.15),[76] due to
each coordination geometry containing a set of three vertices related by a three-fold
pseudosymmetry axis. With a set of 5 more vertices related by a collinear pseudosymmetry axis
and a vertex sitting on the axis, (See Figure 1.25), the appropriate geometry for complex **35** can
be described as "muffin-type", as defined by Alvarez and Ruiz-Martinez.[77] Couple this with the
Th(IV) cation sharing the same equatorial plane as the neighboring Th(IV) cation, which is then
linked to six more Th(IV) cations via the ligand units results in graphene-like layers that contain
hexagonal (6,3)-honeycomb-like motifs.[75]

Figure 1.25. The "muffin type" coordination environment of complex **35,** [$C_7H_{11}N_2$]$_5$[Th$_2$(1,3,5-tCPBA)$_2$Cl$_6$]·Cl. Defined as such as it does not fit into a clearly defined Archimedean geometry. This figure has been generated from the Cambridge Crystallographic Database [75].

Phosphineoxide-based Ligand

The potential applicability of metal-organic frameworks, MOFs, to molecular recognition, gas storage, and catalysis has inspired many research groups to explore the characterization of these compounds.[78] It has been shown that the stability of the MOFs can be heavily influenced by the charge density of the metal cation, and this hypothesis is strongly supported by the fact that the high valent metal based MOFs exhibit high thermal stability and water resistance.[79] With interest in the use of Th[232] nuclear fuels, the need to develop an understanding of the solid state characteristics Th(IV) is vital[25,80] Albrecht-Schmitt et al.[81] synthesized and characterized two 3D Th(IV) frameworks with tris-(4-carboxylphenyl)phosphineoxide (H$_3$TPO, Figure 1.26). The first of these, complex **36,** [$C_9H_{17}N_2$][Th(TPO)Cl$_2$]·18H$_2$O, was synthesized from ionothermal conditions and, the second, **40**, was produced from a solvothermal reaction with Th(NO$_3$)$_4$ to give [Th(TPO)(OH)(H$_2$O)]·8H$_2$Oand will be discussed further later below.
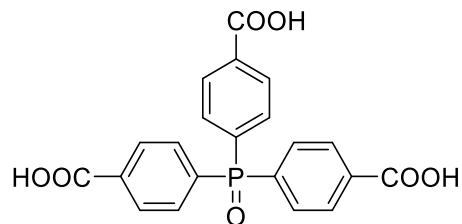
Figure 1.26. The structure of H_3TPO [81].

Complex, **36**, crystallizes in the unusual orthorhombic space group $P2_12_12$. The asymmetric unit has one Th(IV) center, one 1-butyl-2,3-dimethylimidazolium cation, one TPO unit, and two terminal chloride atoms, Figure 1.27. With six oxygen atoms from the three independent chelating carboxylate groups, which is considered rare, one phosphine oxygen atom, and two terminal chloride atoms, the resulting Th(IV) center is nine-coordinate. The Th-O bond distances range from 2.371 – 2.568(7) Å with an average bite angle of 52.27° and the geometry can be described as an irregular "muffin" shape ,[77] as might be more typically seen in lanthanide complexes. The Th_2 binuclear subunit come from the two adjacent Th(IV) atoms in the [*ab*] plane being double-bridged by two TPO units with the coordination sites of the chelating carboxylate oxygen and phosphine oxygen atoms. These binuclear units connect to four neighboring binuclear units to form a (4, 4) layer in the [*ab*] plane, which are further bridged by the TPO to form the 3-D framework. The steric bulk of the triphenyl phosphine is likely the source of the irregular geometry.
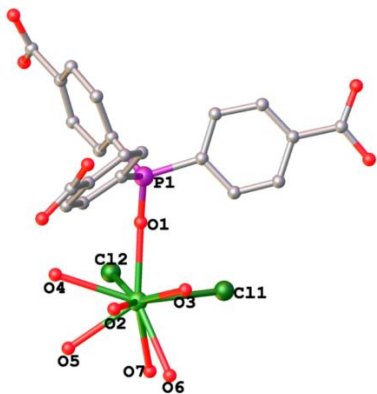
Figure 1.27. The coordination environment of complex **36**. Image constructed from the Cambridge Crystallographic Database [81].

Ten or Greater Coordinate Thorium Complexes

Bis(ammonium)hexanitratothorium(IV) Complex

The role of nitrate complexes in the separation chemistry of actinides led Spirlet et al.[82] to synthesize 12-coordinate bis(ammonium)hexanitratothorium(IV). The authors prepared the complex from the reaction of thorium nitrate with ammonium nitrate in stoichiometric proportions in a highly acidic (10 M) nitric acid solution. The resulting complex, **37**, $[NH_4]_2[Th(NO_3)_6$, possesses 12 coordinated O atoms from six bidentate nitrate ions, with Th-O bond distances ranging from 2.545(6) – 2.608(5) Å. The coordination environment is an irregular icosahedron (C2v). The authors also synthesized the Pu analog of the complex, is isostructural to the Th(IV) complex and can be seen in Figure 1.28.
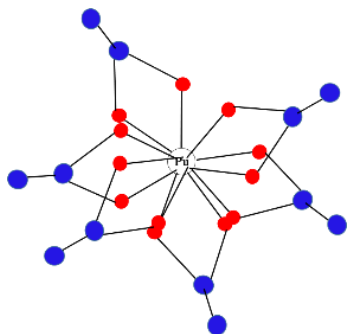
Figure 1.28. The reported isostructural Pu(IV) complex ([NH$_4$]$_2$[Pu(NO$_3$)) is analogous to complex **37** [NH$_4$]$_2$[Th(NO$_3$) [82].

Aminocarboxylate-based Ligands

A renewed interest in the elimination of thorium from living organisms led Thuèry to investigate the ability of aminocarboxylate ligands in the coordination of Th(IV) ions.[71] Thuèry complexed Th(IV) with three ligands, two of which were discussed in prior sections and the third was iminodiacetic acid (H$_2$IDA). All three complexes were produced under hydrothermal conditions. The 10-coordinate complex, [complex [Th(HIDA)$_2$(C$_2$O$_4$)]·H$_2$O (HIDA = iminodiacetic acid), **38**, Figure 1.29, showed that the metal center was coordinated by two carboxylate groups from two HIDA⁻ anions, two oxygen atoms from two different HIDA⁻ anions and two oxalate ligands that were formed *in situ*. The ten-coordinate environment resulted in a bicapped square antiprismatic geometry. The bond lengths between the thorium center and oxygen atoms of carboxylate atoms are 2.59(3) and 2.411(3) Å. The bridging oxalate ligand forms Th-O bonds with a length of 2.491(6) Å and the average bite angle was calculated to be 60.02°.
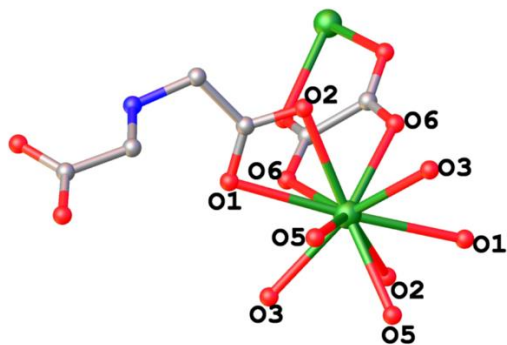
Figure 1.29. Structure of complex [Th(HIDA)$_2$(C$_2$O$_4$)]·H$_2$O **38**. Image constructed from the Cambridge Crystallographic Database [71].

Diphenylphosphine Oxide Ligands

The diverse nature of Th(IV) coordination ability coupled with a need for a greater understanding of it led Biros and co-workers[83] to study complexes containing Th(IV) coordinated to a rigid, bidentate phosphine oxide ligand. Such ligands have been proposed previously in solution-solution extractions for actinides with trivalent actinides.[84] The authors used the same cis-ethylenebis-diphenylphosphine oxide, DPO, ligand to study seven different Th(IV) complexes that are all 10 or more in coordination number. The different complexes arise from the different crystal growing environments.[83]

The first complex, Th(NO$_3$)$_2$-DPO·(NO$_3$)$_2$, **39a**, was grown via slow vapor diffusion of benzene into a concentrated solution of the complex dissolved in methanol resulted in a 10-coordinated, asymmetric Th(IV) complex that crystallized in the triclinic space group P1. Figure 1.30, is comprised of 1:3 Th(NO$_3$)$_2$-ligand complex with two outer sphere nitrate anions and resembles a distorted bicapped square antiprism with the bidentate nitrato groups in the apical positions, with Th-O bonds ranging from 2.394 – 2.641 Å.[83] This complex has an average bite angle

associated with thorium atoms bound to oxygen atoms of the nitrate anions is 48.42° and those phosphine oxide ligand was calculated to average 70.02°.
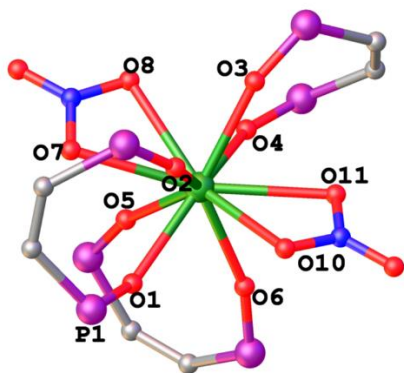

Figure 1.30. Coordination environment of complex **39a** Th(NO$_3$)$_2$-DPO·(NO$_3$)$_2$, where DPO is cis-ethylenebis-diphenylphosphine oxide (C$_{26}$H$_{22}$P$_2$O$_2$), grown via slow vapor diffusion of benzene. Image constructed from the Cambridge Crystallographic Database [83].

Obtaining crystals from diffusion of carbon tetrachloride vapors into a concentrate solution of the complex in non-coordinating chloroform resulted in complex **39b** shown in Figure 1.31, which, crystallized in the monoclinic space group P21/n. Like **39a**, this complex is a 10-coordinate 1:3 Th(NO$_3$)$_2$-ligand complex with two outer sphere nitrate anions, however, a carbon tetrachloride solvent molecule is also present. The Th-O bond distances range from 2.3857 to 2.6497 Å, these distances form an average bond angle of 48.62° for the oxygen atoms on the nitrate groups and 68.95° for oxygen atoms on the phosphine oxide molecules. [83]
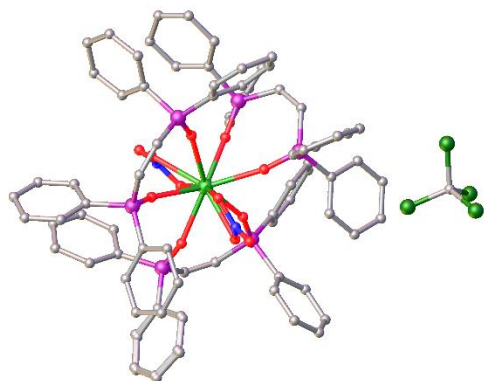
Figure 1.31. Coordination environment of complex **39b** prepared from thorium nitrate and the tetraphenyl bis diphenylphosphine oxide and grown from the vapor diffusion of carbon tetrachloride into the solution of complex in chloroform.. Image constructed from the Cambridge Crystallographic Database [83].

Probing the other metal-ligand stoichiometries and solution behavior of the aforementioned complex (**39b**) resulted in the synthesis of one 12-coordinate and one 10-coordinate complexes. To do this, the authors prepared a concentrated mixture of $Th(NO_3)_4$ hydrate and DPO in methanol in a 1:1 stoichiometric ratio and placed the methanol mixture in a refrigerator for 72 hours. The solved structure corresponds to the orthorhombic space group *Pbca* and the asymmetric unit, **39c**, showed both the 10- and 12-coordinate Th(IV) complexes, Figure 1.32, along with two ordered molecules of methanol. The 1:2 metal-ligand complex is the ten coordinate environment and bears three bidentate nitrato groups that results in the an overall charge of +1, with Th-O bond distances ranging from 2.342 – 2.627 Å. The 1:1 complex is twelve coordinate and bears five bidentate nitrato groups, which results in an overall charge of -1, with Th-O bond distances ranging from 2.360 – 2.656 Å. In both complexes, all eight counter-ions are bound directly to the Th(IV) center. With an average bite angle between Th_1

and the nitrato oxygen atoms calculated to be 49.06° and those on the phosphine oxide average 73.00°, giving the 1:2 complex a distorted bicapped square antiprism (D_{4d}) geometry. The average bite angle between the Th2 atom and the nitrato oxygen atoms is 48.66° and the oxygen atoms of the phosphine oxide form a bite angle of 68.22°, resulting in an icosahedron geometry.
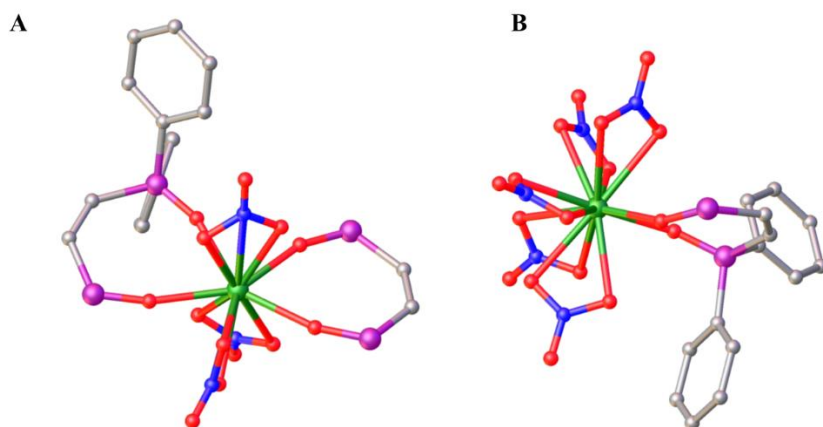

Figure 1.32. The A) 10- and B) 12-coordinate environments of complex **39c**. Image constructed from the Cambridge Crystallographic Database [83].

Crystallizing complex **39d** in methanol via vapor diffusion, with diisopropylether as the co-solvent, resulted in a 1:3 metal-ligand complex that crystallized in the triclinic space group P1 and has an epoxide in place of the alkene, Figure 1.33.[83] There are three ligands and two nitrato groups bound in a bidentate manner to the 10-coordinate Th(IV). The complex resembles a distorted bicapped square antiprism (D_{4d}) geometry with the inner sphere nitrato groups occupying the apical positions and the three ligands occupy the equatorial positions. The epoxide bearing ligand is bound with the oxygen atoms perpendicular to the nitrates, which is

51

assumed to be stabilized by the electrostatic interactions between the epoxide oxygen and the nitrato nitrogen. The Th-O bond distances range from 2.377(3) – 2.642 (3) Å, resulting in average bite angles of 48.86° and 69.76° between the nitrato oxygen atoms and the thorium atom, as well as, the phosphine oxide oxygen atoms, respectively.
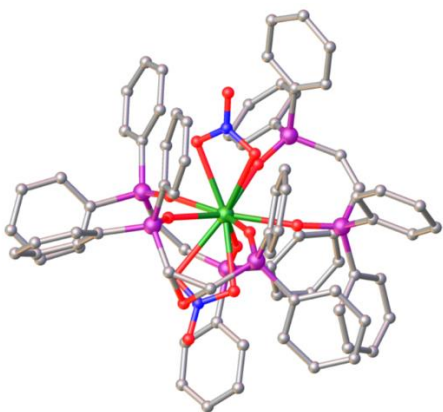

Figure 1.33. The coordination environment of complex **39d**. Image constructed from the Cambridge Crystallographic Database [83].

Three additional complexes came from efforts to reproduce the epoxide bearing complex, **39d**, by dissolving **39** in methanol and increasing stepwise the amount of epoxidation occurring in the solution. In each case, 1, 2, or 3 equivalents of t-BuOOH was added to the mixture, before stirring for one hour at room temperature and vapor diffusion in benzene or iPr$_2$O. The tBuOOH did not result in epoxides on any of the bound ligands, but did result in two 1:3 metal-ligand complexes. These polymorphs differed only in the amount and location of the solvent in the crystal lattice. The Th-O bond distances in the ten coordinate structures range from 2.413(4) – 2.700(4)Å for **39e** and 2.391(3) – 2.663 Å for **39f**.[83] The packing of the two complexes reveals a

difference between the two complexes, although both bear three bidentate ligands and two bidentate nitrato groups. Complex **39e** has one outer sphere nitrate ion, three methanol molecules, and one water molecule, whereas, **39f** has one ordered outer sphere nitrate ion and two methanol molecules. The third complex showed that there were two different Th(IV)-ligand complexes in one asymmetric unit, which was solved in the triclinic space group P1. The first complex the thorium(IV) is bound to two bidentate nitrato atoms, two bidentate ligands, one monodentate ligand, and one water molecule. In the second complex with a 1:3 metal-ligand ratio, the Th(IV) is similar to that of complex **39a**. The first Th(IV) metal center is ten-coordinate is in a distorted antiprism geometry.

Thorium-Oxygen Metal-Organic-Frameworks

In one unusual case, the applicability of metal-organic-frameworks to the fields of molecular recognition and gas storage, inspired Albrecht-Scmitt et al. explore the three-dimensional Th(IV) frameworks in reference 60. One of the complexes they synthesized, **40**, crystallized in the centrosymmetric triclinic space group of P1 with a 3-D framework of dimers the [Th_2O_{18}], the thorium-oxygen subunit. The asymmetric unit contains one crystallographically independent, ten-coordinate Th(IV) ion, as shown in Figure 1.34. Two μ_2-bridging oxygen atoms from two bridging hydroxyl groups, two oxygen atoms from two bidentate bridging carboxylate groups, four oxygen atoms form two chelating carboxylate groups, one phosphine oxygen atom, and one terminal oxygen atom as a water molecule complete the inner coordination sphere. This complex, Figure 34, adopts a coordination geometry that can be described as a spherical sphenocorona, as described by Ruiz-Martinez and Alvarez[85] in 2009. There are two planes, with a square plane defined by O1, O2, O3 and O6.

53

The second plane is a pentagonal plane defined by O4, O5, O7, O8, and O9. Overall, the resulting 12 coordinate polyhedron contains 22 edges and 14 faces of 12 triangles and 2 squares. The Th-O bond distances range from 2.34 – 2.69 Å and the complex has a bite angle of 69.0(4)°.[81]
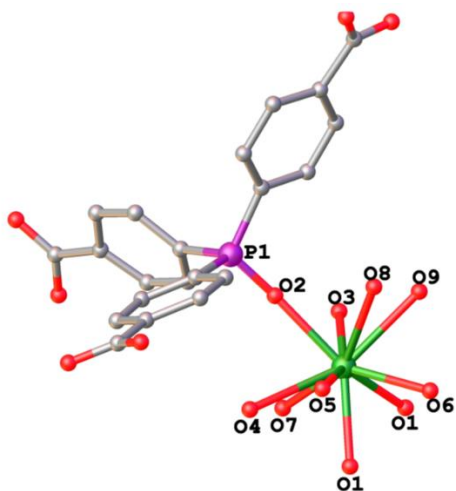

Figure 1.34. The coordination environment of complex **40** [81].

The aforementioned complexes are examples that show the complex nature of Th(IV) and the binding geometries it can obtain. The ability of thorium to coordinate in different geometries and a wide-range of coordination numbers results in the difficulty to predict its preferred geometry and convolutes efforts to model it via computational methods. Even with the difficulties associated with predicting their geometry, Th(IV) complexes afford untapped possibilities of catalysis, MOF's that can be used for molecular recognition and magnetic molecules, and a potential means to sequester a fuel source, which would lead one to believe that delving further into this underexplored area would be beneficial. To our knowledge, this is the

first review of its kind that was prepared comparing coordination numbers and metal center environment rather than a specific type of ligand binding Th(IV).[86] This is further proof that elucidating the chemical capabilities of thorium is pertinent to expanding our knowledge of the element, this is why we have explored the catalytic capabilities of thorium as a simple salt.

References

1. Friedlander, G.; Kennedy, J. W.; Macias, E. S.; Miller, J. M. Nuclear and radiochemistry; John Wiley & Sons: New York, 1981; pp 1.

2. Cheremisinoff, N. P. Pollution control handbook for oil and gas engineering; John Wiley & Sons; New York, 2016; pp 1207.

3. Gosling, F. G. The Manhattan project: making the atomic bomb; Office of Scientific and Technical Information, DOE: Oak Ridge, TN, 1999.

4. Rich, Motoko. *The Lonely Towns of Fukushima. The New York Times*, March 10, 2017, A4.

5. United Nations Scientific Committee on the Effects of Atomic Radiation. UNSCEAR 1988 Report: Annex D, Exposures from the Chernobyl accident.

6. Hammond, C. R. The handbook of chemistry and physics: The elements. CRC press, 2000; pp 16, 31.

7. Gallacher, T. D. Boeing use of depleted uranium counterweights in aircraft; Technical report for Oak Ridge National Laboratory Exposure Assessment Group: Oak Ridge, TN, August 1994.

8. Schneider, S.; Kocher, D. C.; Kerr, G. D.; Schofield, P. A.; O'Donnell, F. R.; Mattsen, C. R.; Cotter, S. J.; Bogard, J. S.; Wiblin, C. Systematic radiological assessment of exemptions for source and byproduct materials; NUREG-1717; U.S. Nuclear Regualtory Commission: Washington, D.C. 2001.

9. Inventory of U.S. greenhouse gas emissions and sinks: 1990-2014, EPA 430-R-16-002; U.S. Environmental Protection Agency, U.S. Government Printing Office: Washington, DC. 2016, pp 8.

10. Inventory of U.S. greenhouse gas emissions and sinks: 1990-2014, EPA 430-R-16-002; U.S. Environmental Protection Agency, U.S. Government Printing Office: Washington, DC. 2016, pp 9-15.

11. Inventory of U.S. greenhouse gas emissions and sinks: 1990-2014, EPA 430-R-16-002; U.S. Environmental Protection Agency, U.S. Government Printing Office: Washington, DC. 2016, pp 19.

12. Rutherford, E.; Geiger, H. Electrical method of counting the number of particles from radioactive substances, Proceedings of the Royal Society of London, London, England, December, 1908; Harrison and Sons.

13. Knoll, G. F. Radiation detection and measurement. John Wiley and sons; New York, 3rd Ed.; pp 104.

14. Wolf, R. E. What is ICP-MS?; United States Geological Services, U.S. Government Printing Offices: Washington, DC. 2015.

15. Hang, W.; Zhu, L.; Zhong, W.; Mahan, C. J. Anal. At. Spectrom. 2004, *19*, 966-972.

16. Truscott, J. B.; Jones, P.; Fairman, B. E.; Evans, E. H.; Anal. Chim. Acta. 2001, *433*, 245/253.

17. Guerin, N.; Nadeau, K.; Potvin, S.; Hardy, J.-M.; Lariverie, D. Radioanal. Nucl. Chem. 2013, *295*, 1803.

18. Wang, B.; Anslyn, E. V. Chemosensors: principles, strategies, and applications. John Wiley and sons, New Jersey, 2011; pp 1.

19. Wang, B.; Anslyn, E. V. Chemosensors: principles, strategies, and applications. John Wiley and sons, New Jersey, 2011; pp 276.

20. Skoog, D. W.; Holler, F. J.; Crouch, S. Fundamentals of analytical chemistry, 8th Ed.; Thomson Learning Brooks Cole: Belmont, CA. 2004.

21. Kaur, N.; Kumar, S. Tetrahedron 2011, 67, 9233.

22. Bailar, J. C., Jr.; Emeleus, H. J.; Nyholm, Sir R.; Troyman-Dickenson, A. F. Comprehensive Inorganic Chemistry, Vol. 5, Actinides; Pergamon Press: New York, N.Y. 1973.

23. Examples: a) Torapava, N.; Persson, I.; Eriksson, L.; Lundberg, D. Inorg. Chem. 48 (2009) 11712-11723. b) Manhas, B. S.; Trikha, A. K. J. Inorg. Nucl. Chem. 43 (1981) 305-307. c) Xiao, C-L.; Wang, C-Z.; Mei, L.; Zhang, X-R.; Wall, N.; Zhao, Y-L.; Chai, Z-F.; Shi, W-Q. Dalton Trans. 44 (2015) 14376-14387. d) Arnold, J.; Gianetti, T. L.; Kashtan, Y. Nature, 6 (2014), 554-554.

24. Burns, C.J.; Neu, M.P.; Boukhalfa, H.; Gutoxski, K.E.; Bridges, N.J.; Rogers, R.D. Chapter 3.3: The Actinides. In Comprehensive Coordination Chemistry II; Parkin, G. F. R., Ed.; Elsevier Ltd.: San Diego, 2004; Vol. 3, p 189.

25. Petit, L.; Joubert, L.; Maldivi, P.; Adamo, C. J. Am. Chem. Soc. 128 (2006) 2190-2191.

26. a) Edwards, P. G.; Parry, J. S.; Read, P. W. Organometallics 14 (1995) 3649-3658. b) Korobkov, I.; Gambarotta, S. Organometallics 23 (2004) 5379-5381.

27. Walensky, J. R.; Martin, R. L.; Ziller, J. W.; Evans, W. J. Inorg. Chem. 49 (2010), 10007-10012.

28. Shannon, R. D. Acta Crystallogr., Sect. A 32 (1976) 751-767.

29. Natrajan, L. S.; Swinburne, A. N.; Andrews, M. B.; Randall, S. Heath. Coord. Chem. Rev. 266-267 (2014) 171-193.

30. a) Wilson, R. E.; Skanthakumar, S.; Knope, K. E.; Cahill, C. L.; Soderholm, L. Inorg. Chem. 47 (2008), 9321-9326. b) Wickleder, M. S.; Fourest, B.; Dorhout, P. K. Thorium. In The Chemistry of the Actinide and Transactinide Elements. Morss, L. R.; Edelstein, N. M.; Fuger, J., Ed.; Springer: The Netherlands, 2006; Vol. 3; p 52.

31. a) Cantat, T.; Graves, C. R.; Jantunen, K. C.; Burns, C. J.; Scott, B. L.; Schelter, E. J.; Morris, D. E.; Hay, P. J.; Kiplinger, J. L. J. Am. Chem. Soc. 130 (2008) 17537-17551. b) Rehe, D.; Kornieko, A. Y.; Emge, T. J.; Brennan, J. G. Inorg. Chem. 55 (2016) 6961-6967. c) Behrle, A. C.; Castro, L.; Maron, L.; Walensky, J. R. J. Am. Chem. Soc. 137 (2015) 14846-14849. D) Behrle, A. C.; Kerridge, A.; Walensky, J. R. Inorg. Chem. 54 (2015) 11625-11636. d) Batrice, R. J.; Fridman, N.; Eisen, M. S. Inorg. Chem. 55 (2016) 2998-3006. e) Daly, S. R.; Piccoli, P. M. B.; Schultz, A. J.; Todorova, T. K.; Gagliardi, L.; Girolami, G. S. Angew. Chem. 49 (2010) 3379-3381. f) Blake, P. C.; Lappert, M. F.; Taylor, R. G. Inorg. Chim. Acta. 139 (1987) 13-20. g) Bell, N. L.; Maron, L.; Arnold, P. L.. J. Am. Chem. Soc. 137 (2015) 10492-10495.

32. a) Maynard, B. A.; Lynn, K. S.; Sykora, R. E.; Gorden A. E. V. Inorg. Chem. 52 (2013) 4880-4889. b) Wilson, R. E..; Skanthakumar, S.; Burns, P. C.; Soderholm, L. Angew. Chem. 46 (2007) 8043-8045. c) Torapava, N.; Lundberg, D.; Persson, I. Eur. J. Inorg. Chem. 2011 (2011) 5273-5278. d) Smiles, D. E.; Wu, G.; Kaltsoyannis, N.; Hayton, T. W. Chem. Sci. 6 (2015) 3891-3899.

33. Cruz, C. A.; Emslie, D. J. H.; Harrington, L. E.; Britten, J. F.; Robertson, C. M. Organometallics 26 (2007) 692-701.

34. a) Emslie, D. J. H.; Piers, W. E.; Parvez, M. Dalton Trans. 12 (2003) 2615-2620. b) Tsurgi, H.; Matsuo, Y.; Yamagata, T.; Mashima, K. Organometallics 23 (2004) 2797-2805.

35. a) Rabinovich, D.; Scott, B. L.; Nielson, J. B.; Abney, K. D. J. Chem. Crystallogr. 29 (1999) 243-246. b) Korobov, I.; Gambarotta, S.; Yap, G. P. A. Angew. Chem., Int. Ed. 42 (2003) 4958-4961.

36. a) Fendrick, C. M.; Mintz, E. A.; Schertz, L. D.; Marks, T. J. Organometallics 3 (1984) 819-821. b) Clark, D. L.; Grumbine, S. K.; Scott, B. L.; Watkin, J. G. Organometallics 15

(1996) 949-957. c) Bruno, J. W.; Smith, G. M.; Marks, T. J.; Fair, C. K.; Schultz, A. J.; Williams, J. M.   J. Am. Chem. Soc. 108 (1986) 40-56.

37. Ward, A. L.; Lukens, W. W.; Lu, C. C.; Arnold, J. J. Am. Chem. Soc. 136 (2014) 3647-3654.

38. a) Arnold, P. L.; Turner, Z. R.; Katsoyannis, N.; Pelekanaki, P.; Bellabaraba, R. M.; Tooze, R. P. Chem.-Eur. J. 16 (2010), 9623-9629. b) Kozimor, S. A.; Yang, P.; Batista, E. R.; Roland, K. S.; Burns, C. J.; Clark, D. L.; Canradson, S. D.; Martin, R. L.; Wilkerson, M. P.; Wolfsberg, L. E. J. Am. Chem. Soc, 131 (2009) 12125-12136.

39. a) Gardner, B. M.; Mcmaster, J.; Lewis, W.; Liddle, S. T.   Chem. Commun. 20 (2009) 2851-2853. b) Napoline, J. W.; Kraft, S. J.; Matson, E. M.; Fanwick, P. E.; Bart, S. C.; Thomas, C. M. Inorg. Chem. 52 (2013) 12170-12177.

40. Rudd, P. A.; Liu, S.; Planas, N.; Bill, E.; Gagliardi, L.; Lu, C. C. Angew. Chem.; Int. Ed. 52 (2013) 4449-4452.

41. a) Day, V. W.; Hoard, J. L. J. Am. Chem. Soc. 92 (1970) 3626-3635. b) Hill, R. J.; Rickard, C. E. F. J. Inorg. Nucl. Chem. 37 (1975) 2481-2485.

42. Hill, R. J.; Rickard, C. E. F. J. Inorg. Nucl. Chem. 34 (1977) 1593-1596.

43. Kepert, D. L. Inorganic Stereochemistry; Springer-Verlag: New York., 1982.

44. Miethke, M.; Marahiel, M. A. Microbiol. Mol. Biol. Rev. 71 (2007) 413-451.

45. Sofen, S. R.; Abu-Dari, K.; Freyberg, D. P.; Raymond, K. N. J. Am. Chem. Soc. 100 (1978) 7882-7887.

46. Lenner, M.; Lindqvist, O. Acta. Cryst. B35 (1979) 600-603.

47. Neliands, J.B. "Microbial Iron Metabolism", Academic Press, New York N.Y., 1974.

48. Smith, W. L.; Raymond, K. N. J. Am. Chem. Soc. 103 (1981) 3341-3349.

49. Weitl, F. L.; Raymond, K. N.; Smith, W. L.; Howard, T. R. J. Am. Chem. Soc. 100 (1978) 1170-1172.

50.   Smith, W. L.; Raymond, K. N. J. Inorg. Nucl. Chem. 41 (1979) 1431-1436.

51. Sofen, S. R.; Cooper, S. R.; Raymond, K. N. Inorg. Chem. 18 (1979) 1611-1616.

52. Blitz, W. Liebig's Ann. Chem. 330 (1904) 334.

53. Reeves, P. J.; A.J. Smith, A. J.   Inorganica Chimica Acta. 139 (1987) 51-53.

54. Lenner, M. Acta Crystallogr. 34 (1978), 3770-3772.

55. Gramer, C. J.; Raymond, K. N. Inorg. Chem. 43 (2004) 6397-6402.

56. Gorden, A. E. V.; Xu, J.; Raymond, K. N.; Durbin, P. W. Chem. Rev. 103 (2003) 4207-4282.

57. Choppin, G. R.; Nash, K. L. Radiochim. Acta. 70/71 (1995) 225-236.

58. Boswell, C. A.; Brechniel, M. W. Nucl. Med. Biol. 34 (2007) 757-778.

59. Pham, T. A.; Xu, J.; Raymond, K. N. J. Am. Chem. Soc. 136 (2014) 9106-9115.

60. a) Clark, D. L.; Frankcom, T. M.; Miller, M. M.; Watkin, J. G. Inorg. Chem. 31 (1992) 1628-1633. b) Travia, N. E.; Monreal, M. J.; Scott, B. L.; Kiplinger, J. L. Dalton Trans. 41 (2012) 14514-14523.

61. Travia, N. E.; Scott, B. L.; Kiplinger J. L. Inorg. Synth. 20 (2014) 16846-16852.

62. Wilson, D. J.; Sebastian, A.; Cloke, F. G. N.; Avent, A. G.; Hitchcock, P. B. Inorg. Chim. Acta. 345 (2003) 89-94.

63. Rogers, R. D.; Bond, A. H.; Witt, M. M. Inorg. Chim. Acta. 182 (1991) 9-17.

64. Gui, D.; Zheng, T.; Chen, L.; Wang, Y.; Li, Y.; Sheng, D.; Diwu, J.; Chai, Z.; Albrecht-Schmitt, T. E.; Wang, S. Inorg. Chem. 55 (2016) 3721-3723.

65. Casellato, U.; Sitran, S.; Tamburini, S.; Vigato, P. A. Inorg. Chim. Acta. 95 (1984) 37-42.

66. Riley, P. E.; Abu-Dari, K.; Raymond, K. N. Inorg. Chem. 22 (1983) 3940-3944.

67. Day, V. W.; Hoard, J. L. J. Am. Chem. Soc. 92 (1970) 3626-3635.

68. Raymond, K. N.; Xu, J.; Siderophore-based Hydroxypyridinone Sequestering Agents. In The Development of Iron Chelators for Clinical Use; Bergeron, R. G., Brittenham, G. M.; Eds.; CRC Press: Boca Raton, FL, 1994; p 307.

69. Xu, J.; Whisenhunt Jr., D. W.; Veeck, A. C.; Uhlir, L. C.; Raymond, K. N. Inorg. Chem. 42 (2003) 2665-2674.

70. a) Cartwright, A. J.; May, C. C.; Worsfold, P. J.; Keith-Roach, M. J. Anal. Chim. Acta. 590 (2007) 125-131. b) Jiang, J.; Sarsfield, M. J.; Renshaw, J. C.; Livens, F. R.; Collison, D.; Charnock, J. M.; Helliwell, M.; Eccles, H. Inorg, Chem. 41 (2002) 2799-2806.

71. Thuèry, P. Inorg, Chem. 50 (2011) 1898-1904.

72. Mikhailov, Y.N.; Lobanova, G.M.; Kanishcheva, A.S.; Sergeev, A.V.; Bolotova, G.T.; Shchelokov, R. N. Koord. Khim. 11 (1985) 545.

73. Dodge, C. J.; Francis, A. J. Environ. Sci. Technol. 36 (2002) 2094-2100.

74. Unruh, D. K.; de Groot, J.; Fairley, M.; Libo, A.; Miller, S.; Forbes, T. Z. Inorg. Chem. 54 (2015) 1395-1404.

75. Li, Y.; Weng, Z.; Wang, Y.; Chen, L.; Sheng, D.; Diwu, J.; Chai, Z.; Albrecht-Schmitt, T. E.; Wang, S. Dalton Trans. 45 (2016) 918-921.

76. Drew, M. G. D. Coord. Chem. Rev. 24 (1977) 179-275.

77. Ruiz-Martinez, A.; Casanova, D.; Alvarez, S. Chem.-Eur. J. 14 (2008) 1291-1303.

78. James, S. L. Chem. Soc. Rev. 32 (2003) 276-288.

79. Valenzano, L.; Civalleri, B.; Chavan, S.; Bordiga, S.; Nilsen, M. H.; Jakobsen, S.; Lillerud, K. P.; Lamberti, C. Chem. Mater. 23 (2011) 1700-1718.

80. Wickleder, M. S.; Fourest, B.; Dorhout, P. K. Thorium. In The Chemistry of the Actinide and Transactinide Elements. Morss, L. R.; Edelstein, N. M.; Fuger, J., Ed.; Springer: The Netherlands, 2006; Vol. 3; p 53.

81. Li, Y.; Weng, Z.; Wang, Y.; Chen, L.; Sheng, D.; Liu, Y.; Diwu, J.; Chai, Z.; Albrecht-Schmitt, T. E.; Wang, S. Dalton Trans. 44 (2015) 20867-20873.

82. Spirlet, M. R.; Rebizant, J.; Apostolidis, C.; Kanellakopulos, B.; Dornberger, E. Acta Cryst. C48 (1992) 1161-1164.

83. Morse, P. T.; Staples, R. J.; Biros, S. M. Polyhedron 114 (2016) 2-12.

84. Grüner, B.; Švec, P. Selucky, P.; Bubeníkova, M. Polyhedron 38 (2012) 103-112.

85. Ruiz- Martinez A.; Alvarez, S. Chem. –Eur. J. 15 (2009) 7470-7480.

86. a) Arora, K.; Agnihotri, S. Asian J. Chem. 19 (2007) 3307-3324. b) Agarwal, R. K.; Agarwal, H.; Arora, K. Inorg. Chem. 20 (2000) 1-55.

Chapter 2: Functionalized Poly(vinyl)Alcohol Resins for Metal Detections

Although uranium occurs naturally in trace amounts in the environment, it is still largely considered an environmental contaminant associated with the nuclear fuel industry.[1] In aqueous media, uranium is found as the dioxy-cation uranyl; a stable, water soluble cation that is relatively mobile and found in soil matrices and water.[2] With its' long half-life and chemical toxicity comparable to lead, uranyl is viewed as an environmental hazard that needs to be identified.[3] In seawater, the concentration of uranyl is approximately 3.3 ppm.[4] With such a low concentration, a highly sensitive means of detection needs to be developed.

Solid-phase extraction is the use of a solid to remove metal from an aqueous phase.[5] These solid phase extractors (abbreviated SPE) are typically comprised of solid matrix with a chelating functional group used to bind the metal. A chelator selective enough to bind low concentrations is ideal to serve as uranyl detector and has application as becoming a real-time detector with minimal sample preparation as required for current methods such as phosphorimetry and surface enhanced Raman scattering.[6] The exploration of SPE to identify metal ions has seen some interest over the years.[7,8,9] Li et al. used benzoylthiourea anchored on activated carbon to serve as an extractor for uranyl.[10] The group found that the maximum sorption was 82 mg of uranium per gram of extractor. With this, the extractor selectively absorbed uranyl ions in the presence of sodium, cobalt, strontium, and lanthanum. Another example of using SPE to detect uranyl was conducted by Shamsipur et al.[11] in which the extraction of ultratrace uranium(VI) in natural water was done with octadecyl silica membrane, OSM, disks modified by tri-*n*-octylphosphine oxide. The authors found that OSM was a suitable extractor, extracting with a limit of detection equal to 10 ppm.[11] These promising results with SPE for detecting low concentrations of uranyl, coupled with the ability of the salen 2-

quinoxalinol, salqu, derived ligands synthesized in the Gorden lab possessing the ability to bind 2+ metal cations via the O-N-N-O tetredentate binding pocket[12] lead us to explore their ability as a SPE.

The initial method of incorporating the salen derived ligand onto a physical substrate involved using a polystyrene aminomethyl resin that resulted in the production of a material that made for a great Cu^{2+} sensor, but was not efficient for uranyl cation.[13] It was then hypothesized that utilizing a resin capable of swelling in water would aide in the recovery of uranyl due to most contaminants occurring in aqueous media.[2] Poly(vinyl) alcohol was chosen due to its ability to be readily functionalized, its relatively low cost, and its ability to swell in water.[14] Following reports of Wang et al.[15], in which, commercially purchased PVA was functionalized to contain a terminal aldehyde functional group that could serve as a site to link the ligand to the resin, thus, a functionalized PVA resin was prepared. Complications arose in effectively quantifying the ability of this functionalized resin to serve as a SPE for uranyl. Overall metal extraction efficacy can be difficult to quantify. The solid removed the ability to use UV-Vis as reliable analytical technique, the difference in degree of functionalization was difficult to determine, therefore making estimation of the correct ratios between ligand and metal for extraction challenging. These issues lead to the utilization of poly-dispersed, magnetic poly(vinyl) alcohol beads, M-PVA, functionalized with a terminal carboxylic acid that can be used as a site for covalently linking the polymer to a hydroxide group of the ligand via a transesterification reaction. The use of the magnetic beads allows for the easy removal of the SPE with a magnet after extraction. Along with this, the ease of synthesizing a variety of salen 2-quinoxalinol ligands via a 5-step solution phase synthesis,[16] made the use of M-PVA

functionalized with the Salqu ligands an attractive and easy means to produce a novel SPE for selective uranyl detection and extraction.

Ligand Selection

The (1 *E*, 1' *E*)-2,2-'-[quinoxaline-6,7-diylbis(azanylidenemethyl)diphenol framework allows for the synthesis of a variety of different salen derived ligands that still offer that tetradentate binding pocket and fluorescent backbone. After synthesizing the fluorescent backbone, 2-qu, it was then reacted with several different salicylaldehydes to afford a series of different salen ligands, scheme 2.1. When deciding which ligand systems to use for characterization and functionalization, the presence of a hydroxyl group to be used to link to resin was needed, therefore, the salqu produced after synthesizing the 2-qu backbone with 2,5-dihydroxybenzaldehyde (DHsalqu) was selected.
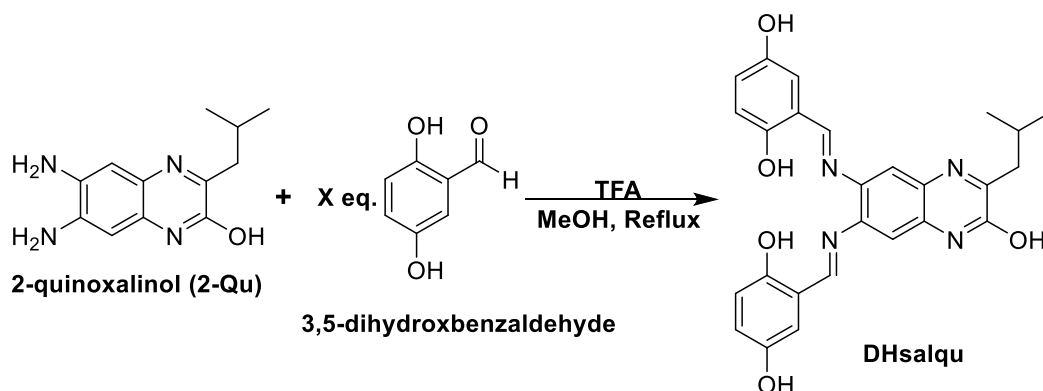
Scheme 2.1. The synthesis of DHsalqu, the di-substituted salen 2-quinoxalinol ligand.

The synthesis of DHsalqu followed the published procedure, in which 2.2 equivalents of salicylaldehyde was reacted with 1 equivalent of 2-qu in ethanol before heating the reaction to reflux temperature. Upon completion of the reaction, after work-up, the product recovered was a

side product known as imidazole, Scheme 2.1. According to the original procedure reported by

Wu et al., the equivalents of salicylaldehyde to 2-qu was 15:1 to get DHsalqu.[13] An increase in

cost of the 2,5-dihydroxybenzaldehyde inspired investigations toward optimization of the

reaction that did not require such a very large excess; Table 2.1 displays the parameters explored.
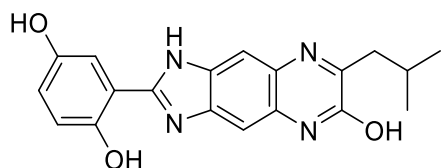
Figure 2.1. Imidazole by-product.

Research has shown that the presence of air aids increases the production of the side

product, imidazole.[17] With this in mind, solvents were degassed and the reaction was performed

under nitrogen. It is likely that activation from the hydroxyl group also plays a role in the

imidazole formation. Until 15 equivalents of 2,5-dihydroxybenzaldehyde were used, the major

product was imidazole in high yields. With 15 equivalents of salicylaldehyde, the reaction does

not have to be performed under an inert atmosphere to produce the di-substituted product, figure

2.2 in good yields (76%).
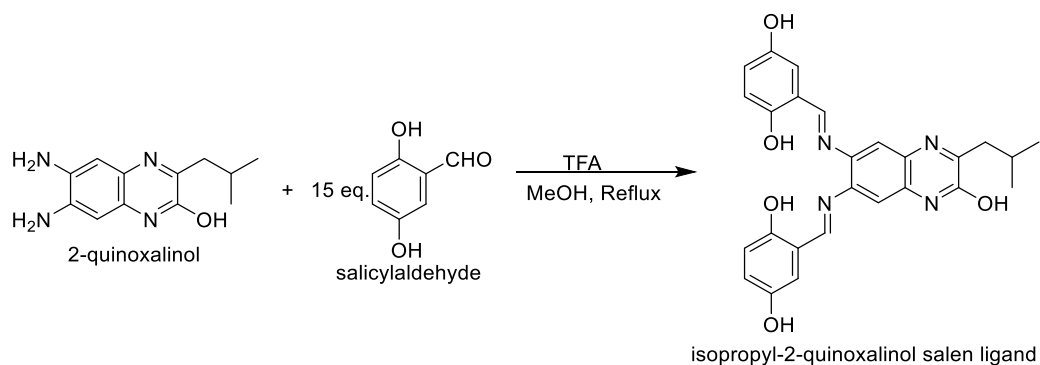
Figure 2.2. Synthesis of DHsalqu.

Table 2.1 Optimization of DHsalqu synthesis.

2-Qu	SA	Solvent	Degassed	Inert	Major Product	Percent Yield
1	2.2	Ethanol	No	No	Imidazole	76
1	2.2	Ethanol	Yes	No	Imidazole	81
1	2.2	Ethanol	Yes	Yes	Imidazole	64
1	2.2	Methanol	Yes	Yes	Imidazole	63
1	5	Methanol	Yes	Yes	Imidazole	60
1	7	Methanol	Yes	Yes	Imidazole	57
1	10	Methanol	Yes	Yes	Imidazole	55
1	15	Methanol	Yes	Yes	Di-Sub	82
1	15	Methanol	Yes	No	Di-sub	76

As previously stated, the presence of a hydroxyl group is needed to link the ligand to polymer. Not wanting to limit our exploration to just one ligand, a new 2-qu was synthesized, in which tyrosine was used as the amino acid methyl ester. The use of tyrosine as the amino acid methylester afforded a hydroxyl group on the phenol ring that could serve as a linker to the M-PVA. This resulted in a poor overall percent yield of 0.8%; however reacting this with 3,5-ditertbutylsalicylaldehyde produced the corresponding salqu, DTBsalqu, in 64% yield, figure

2.3. This affords a hydroxyl group on the phenol ring that can be an additional possible linkage

site. The production of the DTBsalqu in high yields is advantageous if covalently linked to the

resin because the 3,5-ditertbutyl derivative of the (1 *E*, 1' *E*)-2,2-'-[quinoxaline-6,7-

diylbis(azanylidenemethyl)diphenol framework was characterized previously as a metal

scavenger or extraction agent for UO_2^{2+}, Cu^{2+}, and Co^{2+}.[12] Along with a visible color change for

the three metal ions, a hypsochromic shift was observed with the addition of the UO_2^{2+} solutions

and a bathochromic shift was observed with the addition of the Cu^{2+} and Co^{2+} solutions. These

promising results lead to revisiting the idea of incorporating salqu derived ligands onto a solid

phase substrate, such as polymer, to be utilized as a solid-phase extraction agent.
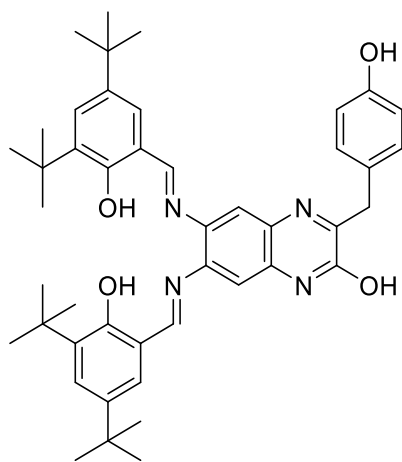
Figure 2.3. DTBsalqu

Loading of Ligand onto Resin

Using the initial reaction conditions as a starting point, the linking of the resin to the

ligand was attempted via the transesterification reaction using 2.2 equivalents of a carbodiimide

and 2.2 equivalents of 4-dimethylaminopyridine(DMAP) in DMF at room temperature for 72

hours. N,N'diisopropylcarbodiimide is a water sensitive carbodiimide that decomposes readily

in the presence of water. This became apparent when these conditions did not work due to the

M-PVA coming suspended in water. To overcome this problem, a water soluble carbodiimide

was employed, 1-ethyl-3-(3-dimethlaminopropyl)carbodiimide, EDC was employed, Scheme

2.2. Upon completion of the reaction, the beads were separated from the solution with a magnet

and the remaining solution was analyzed to determine the ligand amount remaining. For the

DTBsalqu, 98% of the ligand was recovered; however, only 6% of the DHsalqu was recovered in

that preparation. To confirm the covalent linking of the ligand onto the resin, FT-IR was

employed, and the spectra of the ligands, commercially purchased beads, and resin after the

reaction were compared for the presence of the C=O peak at around 1735 cm^{-1} (actual 1734 cm^{-1})

and the C-O stretch at 1050 cm^{-1} (actual 1054 cm^{-1}) in the DHsalqu/M-PVA (HL) spectra to

determine the presence of a new ester functional group. The DTBsalqu/M-PVA did not show

these peaks, suggesting that in this case the ligand did not load the resin. With the successful

formation of the DHsalqu/M-PVA heterogeneous ligand, HL, its ability to detect uranyl as a SPE

was able to be characterized.
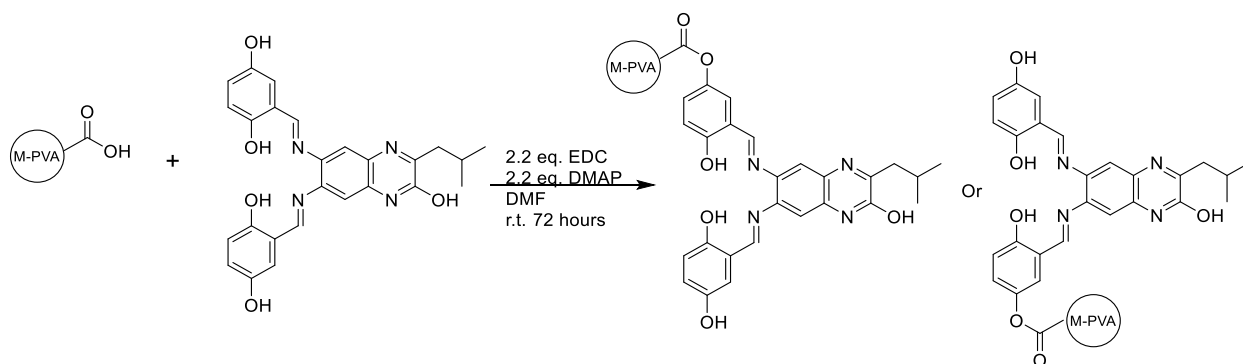
Scheme 2.2. The loading of DHsalqu onto M-PVA (HL).

Results

After the heterogeneous ligand, HL, was successfully synthesized with the DHsalqu ligand covalently bonded to a resin, its capabilities as a solid phase extractor for uranyl were characterized. Due to the metal being coordinated by a solid in this case, UV-Vis as used previously could not be used to analyze the ligand chelation of the metal. Analyzing the concentration of the metal solutions before and after interaction with the heterogeneous ligand was be the best way to determine the ability of the ligand to serve as a solid phase detector. With the low extinction coefficient of uranyl, producing a solution with a high enough concentration to be detected on the UV-Vis requires a fairly large amount of HL to perform any analysis. To solve this problem, ICP-OES was utilized to determine the extraction capabilities of the functionalized resin by measure the before and after concentrations of the metal stock solutions after exposing them to the resin.

To begin, two aqueous stock solutions one of 475 µM of uranyl nitrate and one 475 µM copper nitrate were prepared. From each of these, 7 samples were prepared using serial dilutions with water such that solutions would result with ratios between the ligand HL and metal ion of interest of 1:0.05, 1:0.1, 1:0.5, 1:1, 1:2, 1:5, 1:10. The sample with 0.05 equivalents of metal would aide in determining the limit of detection. All fourteen samples, seven for UO_2^{2+} and seven for Cu^{2+}, were analyzed to measure initial metal ion concentration with ICP-OES before the addition of the resin and agitation with a shaker for the following intervals of time: 5 minutes, 30 minutes, 60 minutes, 90 minutes, 120 minutes, 180 minutes. Three hours was deemed an appropriate stopping point because, as the data would later reveal, that at that point in time, the change in concentration begins to decline. For comparison, another batch of the same solutions was extracted with just the commercially purchased beads, bare resin (BR). In each

case, in order to analyze the samples after the agitation/exposure time, a magnet was used to remove either the extractant HL or the resin BR from the solution.

Uranium Detection

In comparing the sample results of extraction efficacy, the solution containing 0.05 equivalents of uranyl salt, was found to have the greatest extraction as measured by the decrease in effective metal ion concentration measured after 30 to 60 minutes of agitation. The amount of metal ion extracted leveled out after 120 minutes agitation, as shown in figure 2.4. Thus, additional agitation did not further improve efficacy. When compared to just the bare resin, the extraction of metal ion is greater with the presence of the ligand in that HL extracted 51% of the total uranyl and the BR extracted 11% when agitated with the same metal ion concentration; giving an increase of 40% of the total amount of metal ion extracted. The extraction of uranyl in the sample containing 0.05 equivalents of metal ion indicates that the limit of detection for HL is relatively low. Future work will include determining the limit of detection of HL with metal salt solutions of 0.04 equivalents and lower.
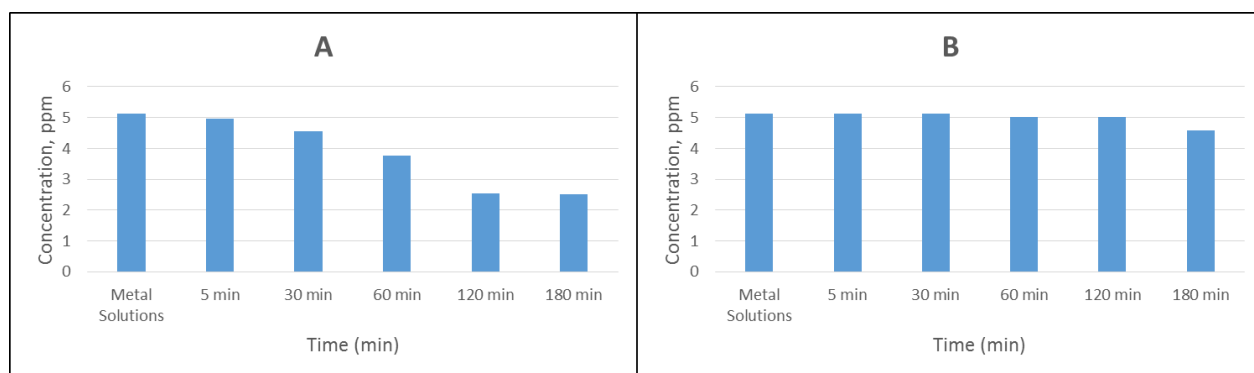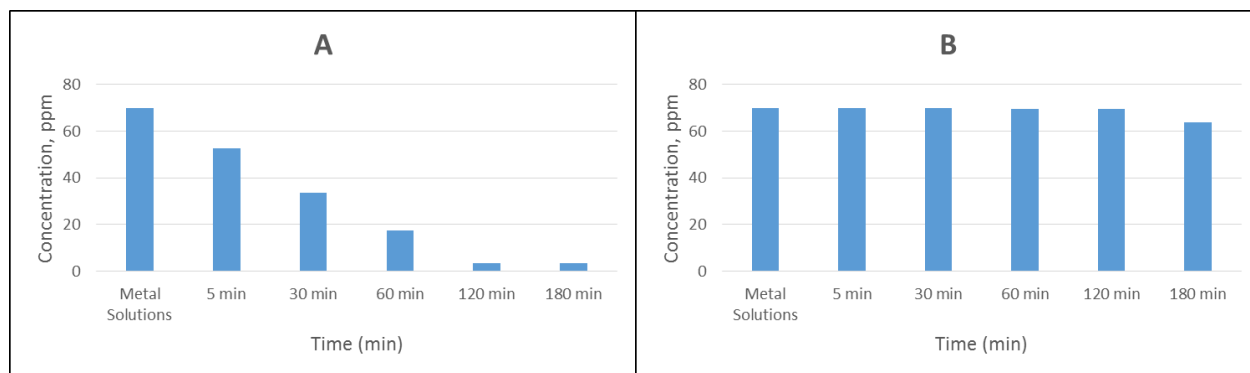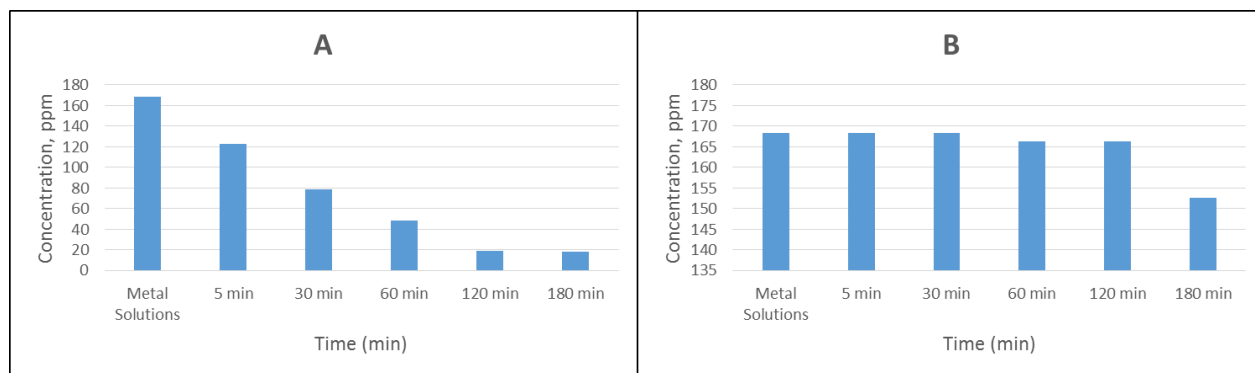

Figure 2.4. The concentration of the Uranium metal remaining from initial solution of 0.05 equivalents of UO_2^{2+} for the A: heterogeneous ligand (HL) and B) the bare resin (BR).

In the solutions containing 0.1 equivalents of metal salt, it was found to have the greatest extraction as measured by the decrease in effective metal ion concentration after 60 to 120 minutes of agitation. The amount of metal ion extracted leveled out after 120 minutes agitation, as shown in figure 2.5. Thus, additional agitation and exposure time did not further improve extraction efficacy. When compared to just the bare (unfunctionalized) resin, the extraction of metal is greater with the presence of the ligand in that HL extracted 53% of the total uranium metal and the BR extracted 11% when agitated with the same uranyl concentration; resulting in an increase of 42% of the total amount of uranyl extracted over the unfunctionalized beads.
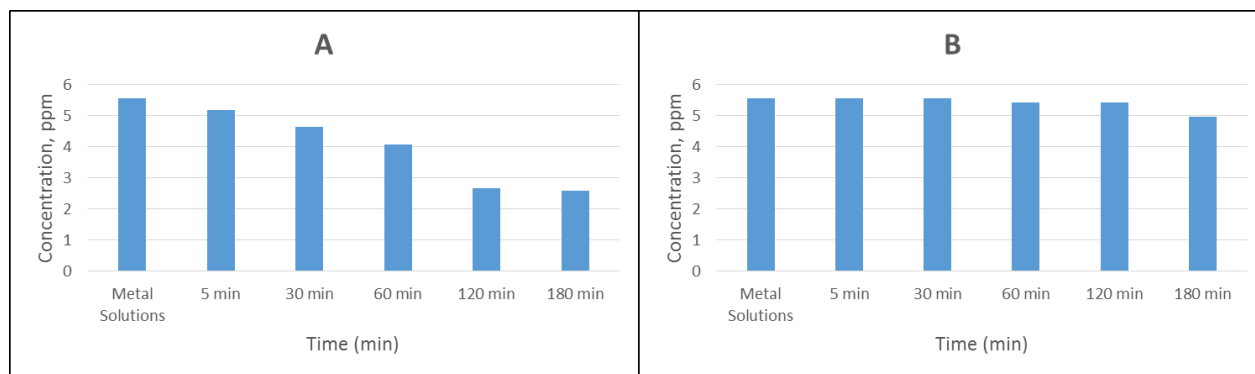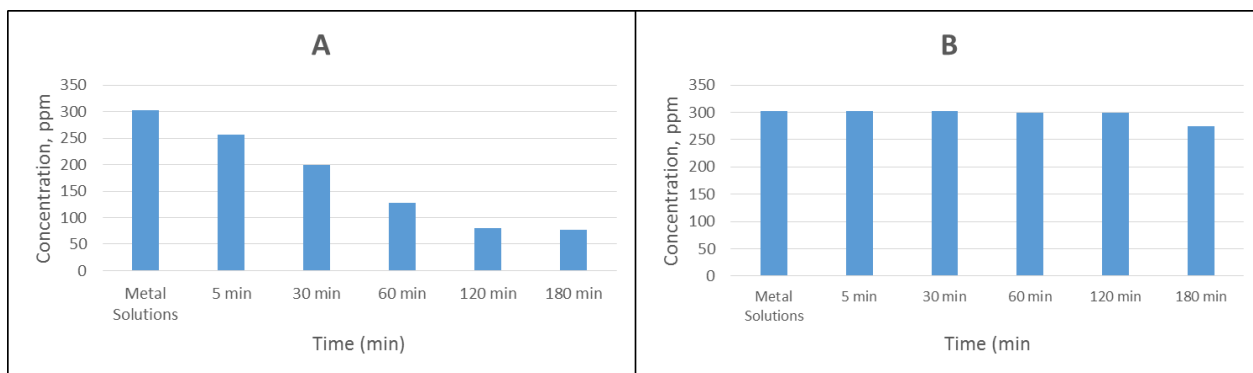

Figure 2.5. The concentration of the Uranium metal remaining from initial solution of 0.1 equivalents of UO_2^{2+} for the A: heterogeneous ligand (HL) and B) the bare resin (BR).

Likewise, in comparing extraction efficacy, the solution containing 0.5 equivalents of uranyl was found to have the greatest extraction as measured by the decrease in effective metal ion concentration after 60 to 120 minutes of agitation. The amount of metal ion extracted leveled out after 120 minutes agitation, as shown in figure 2.6. Thus, additional agitation did not further improve efficacy. When compared to just the bare resin, the extraction of metal is greater with

71

the presence of the ligand in that HL extracted 55% of the total uranyl, and the BR extracted 11% when agitated with the same metal concentration; resulting in an increase of 44% of the total amount of metal ion extracted over the unfunctionalized resin.
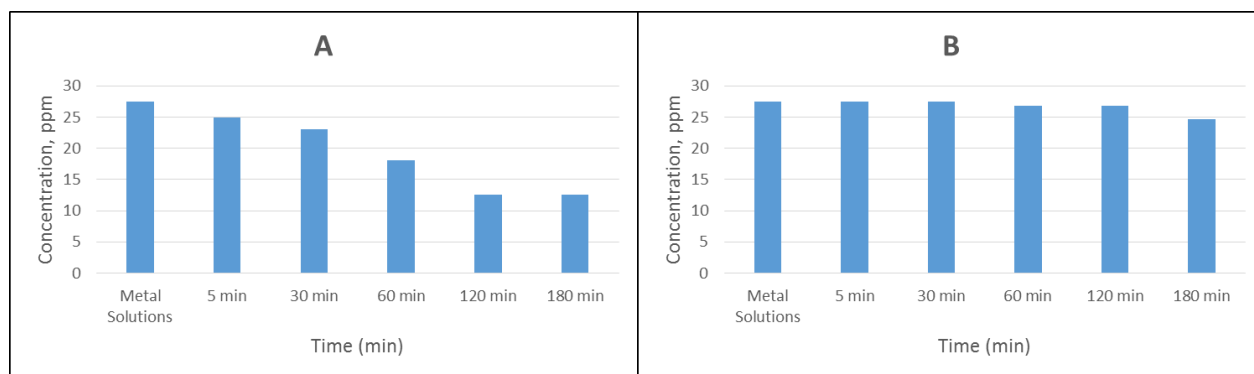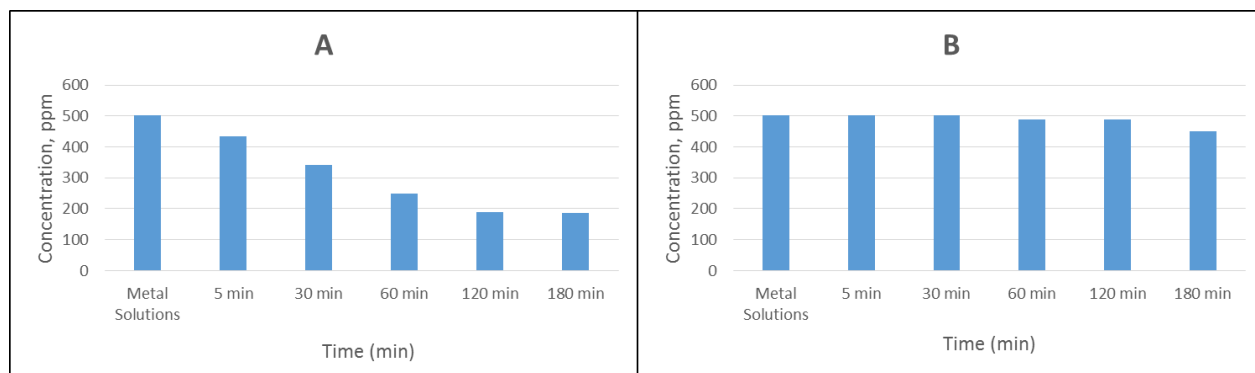

Figure 2.6. The concentration of the Uranium metal remaining from initial solution of 0.5 equivalents of UO_2^{2+} for the A: heterogeneous ligand (HL) and B) the bare resin (BR).

In continuing this comparison, the solution reacted with equivalent amount of functionalized resin to uranyl salt, the greatest decrease of uranyl, was found between 60 and 120 minutes of agitation. Again, the extraction was found the level off with no further increase in extraction if exposure was longer than 120 minutes, as shown in figure 2.7. With this ratio, the concentration of metal left ion after 180 minutes is 4.6% of the starting concentration, suggesting this is the optimum ratio between ligand and metal for this system. When compared to just the bare resin, the extraction of uranyl is greater with the presence of the ligand in that HL extracted 95.4% of the total uranyl, and the BR extracted 8.8% when agitated with the same metal concentration; giving an increase of 86.6% of the total amount of metal ion extracted over the unfunctionalized resin..

Figure 2.7. The concentration of the Uranium metal remaining from initial solution of equal equivalents of UO_2^{2+} and substrate for the A: heterogeneous ligand (HL) and B) the bare resin (BR).

The solution reacted with 2 equivalents of uranyl was found to have the greatest extraction as measured by the decrease in effective metal ion concentration measure after 60 to 120 minutes of agitation. The amount of metal ion extracted leveled out after 120 minutes agitation, as shown in figure 2.8. Thus, additional time of agitation did not further improve efficacy. When compared to just the bare resin, the extraction of metal is greater with the presence of the ligand in that HL extracted 89% of the total uranyl, and the BR extracted 9% when agitated with the same metal concentration; giving an increase of 73% of the total amount of metal extracted for the functionalized resin.
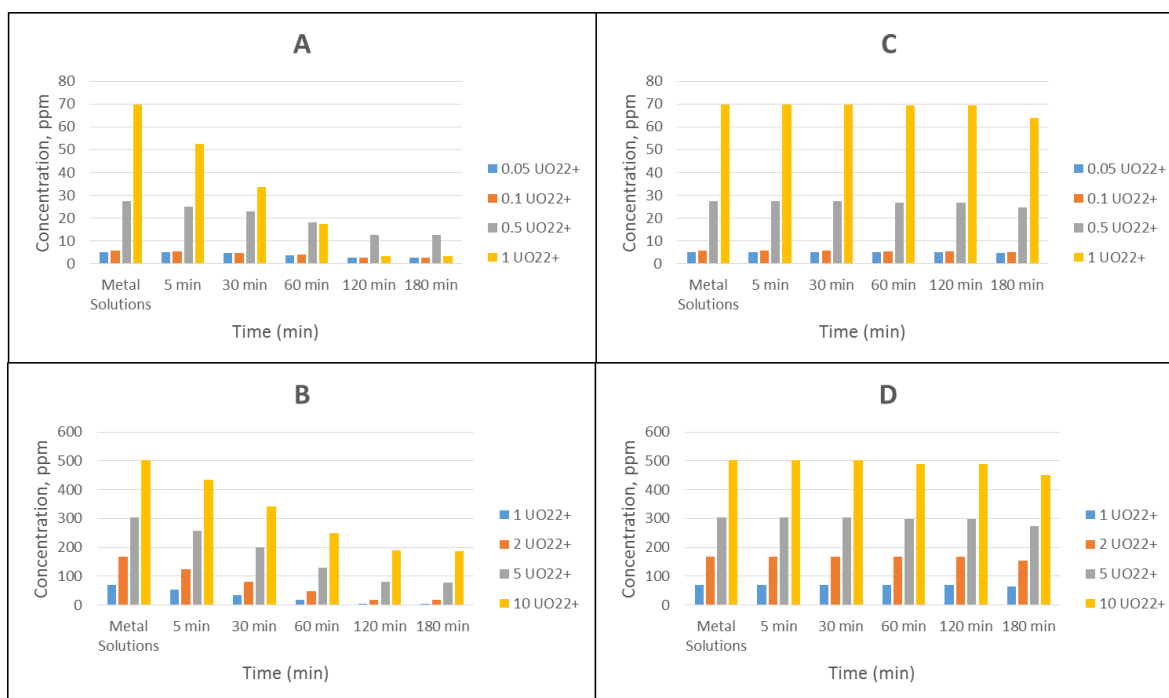
Figure 2.8. The concentration of the Uranium metal remaining from initial solution of 2 equivalents of UO_2^{2+} for the A: heterogeneous ligand (HL) and B) the bare resin (BR).

Investigating further into extraction efficacy, the solution containing 5 equivalents of metal ion, was found to have the greatest extraction as measured by the decrease in effective metal ion concentration measure after 30 to 60 minutes of agitation. The amount of metal ion extracted leveled out after 120 minutes agitation, as shown in figure 2.9. Thus, additional agitation did not further improve extraction efficacy. When compared to just the bare resin, the extraction of metal is greater with the presence of the ligand in that HL extracted 74% of the total uranium metal and the BR extracted 9% when agitated with the same metal concentration; giving an increase of 65% of the total amount of metal extracted over the unfunctionalized resin.

Figure 2.9. The concentration of the Uranium metal remaining from initial solution of 5 equivalents of UO_2^{2+} for the A: heterogeneous ligand (HL) and B) the bare resin (BR).

Finally, in the solution containing 10 equivalents of metal ion, the greatest decrease in concentration occurred between 60 and 120 minutes of agitation and extraction levels out after 120 minutes, as shown in figure 2.10. . Thus, additional agitation did not further improve efficacy. When compared to just the bare resin, the extraction of uranyl is greater with the presence of the ligand in that HL extracted 63% of the total uranium metal and the BR extracted 11% when agitated with the same metal concentration; giving an increase of 52% of the total amount of metal extracted over the bare resin.
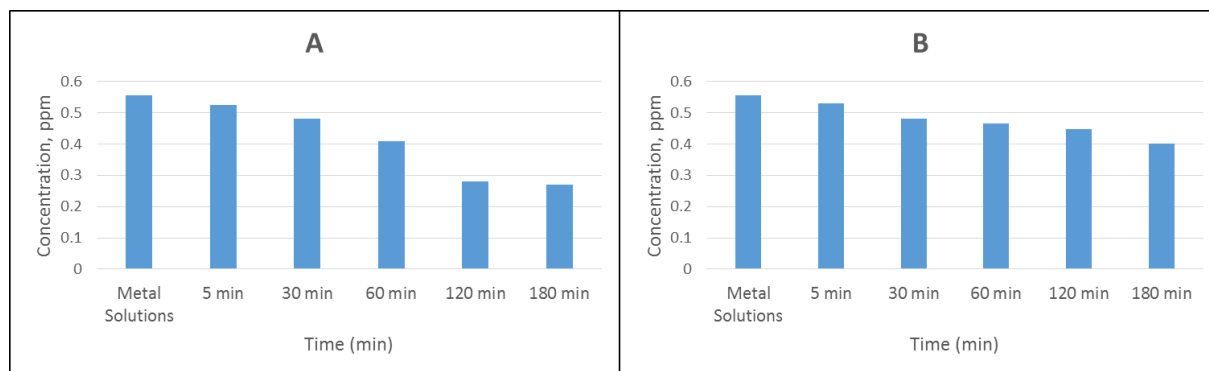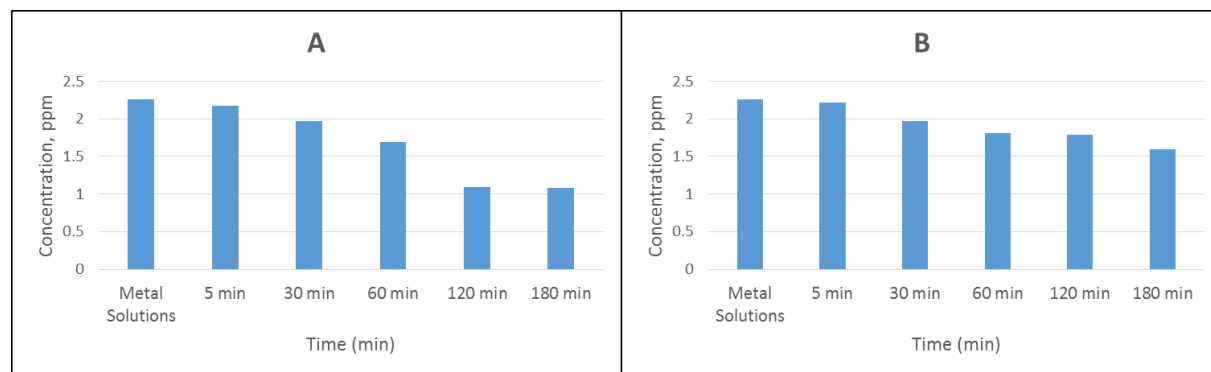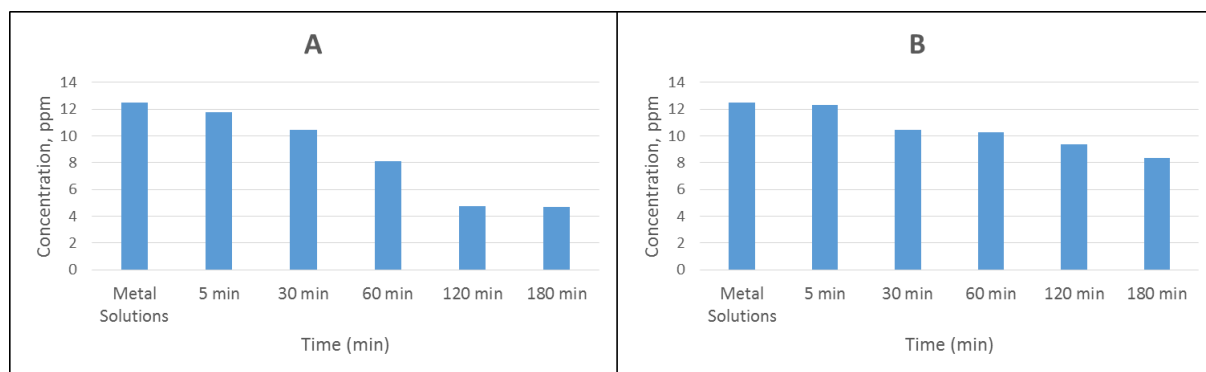
Figure 2.10. The concentration of the Uranium metal remaining from initial solution of 10 equivalents of UO_2^{2+} for the A: heterogeneous ligand (HL) and B) the bare resin (BR).

In combining these results, the greatest rate of extraction was found after exposure and agitation between 60-120 minutes for a majority of the solutions, suggesting the optimum agitation time for uranyl detection or extraction is less than 2 hours. An immediate decrease in the concentration of uranium metal ions, here as uranyl, after less than 5 minutes of agitation with the ligand, was observed in all samples. This small amount of time for detection to begin shows this ligand/resin system could be used as a real-time detector. Comparatively, the samples with the bare resin did not begin to decrease in concentration until well after 60 minutes of agitation. This suggests that although the resin does extract the uranyl somewhat, the ligand functionalized beads are much more efficient in coordination and extraction of the uranyl. Figure 2.11 displays concentrations of uranium metal in the original samples, at the varying metal equivalents and agitation times for every sample.

It was determined that agitating samples or exposing the ligand to the metal containing solution for a longer period of time resulted in more uranyl being extracted, until diminishing returns after 120 minutes. For example, when the 1:0.5 (HL:metal) sample was shaken for 5

minutes, the concentration of metal ion in the solution was found to decrease by 9% (24.88 ppm versus 27.50 ppm); whereas after 60 minutes of shaking, the concentration decreased by 48% (18.04 ppm versus 23.01 ppm). The difference in concentration after 120 minutes of agitation versus 180 minutes decreased by 0.69% (12.498 ppm versus 12.585), indicating that the rate of extraction was slowing down, thus agitation was halted.

Figure 2.11. The concentration of the Uranium metal remaining from initial solutions of UO_2^{2+} for the A: heterogeneous ligand (HL) at lower equivalents, B HL at higher equivalents and C) the bare resin (BR) at lower equivalents, D) BR at higher equivalents.

Copper Detection

The next step was to compare extraction efficacy for copper from solution as copper may be a competing ion and quite common in environmental conditions. The resins were reacted in solutions containing 0.05 equivalents of copper nitrate salt. These were found to have the greatest extraction as measured by the decrease in effective metal ion concentration measure after 60 to 120 minutes of agitation. The amount of metal ion extracted leveled out after 120 minutes agitation, is shown in figure 2.12. Thus, additional agitation did not further improve efficacy. When compared to just the bare unfunctionalized resin, the extraction of metal is greater in the presence of the ligand in that HL extracted 51% of the total uranium metal and the BR extracted 28% when agitated with the same metal concentration; giving an increase of 24% of the total amount of metal extracted.
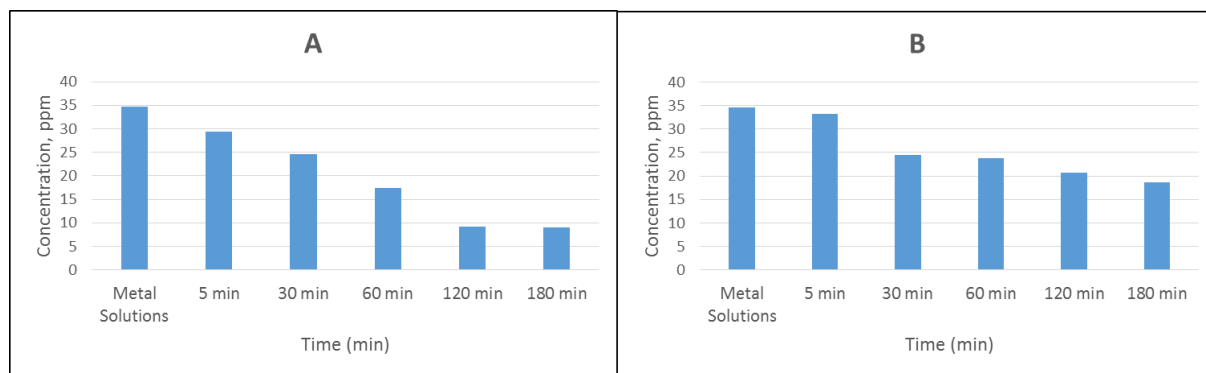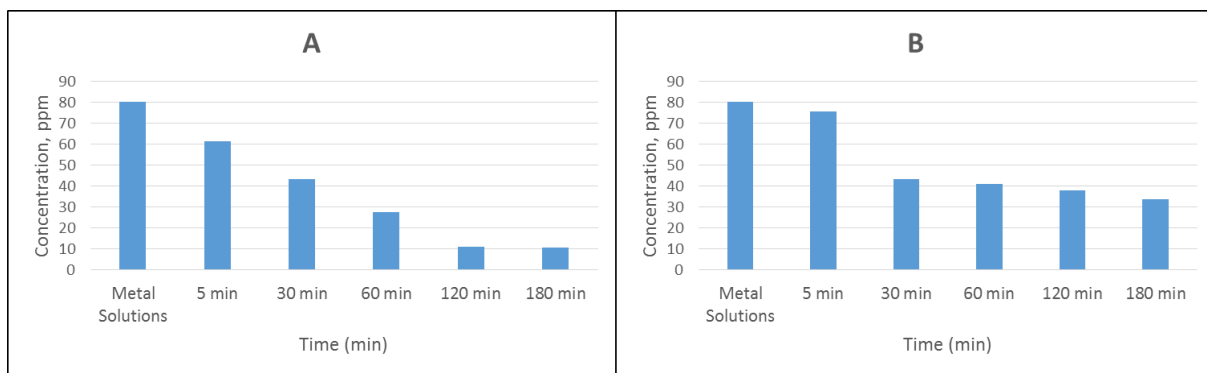

Figure 2.12. The concentration of the Copper metal remaining from initial solution of 0.05 equivalents of Cu^{2+} for the A: heterogeneous ligand (HL) and B) the bare resin (BR).

In the solution reacted with 0.1 equivalents of copper ion, it was found that the greatest extraction as measured by the decrease in effective metal ion concentration measure after 60 to 120 minutes of agitation. The amount of metal ion extracted leveled out after 120 minutes agitation, as shown in figure 2.13. Thus, additional agitation did not further improve efficacy. When compared to just the bare resin, the extraction of metal is greater with the presence of the ligand in that HL extracted 52% of the total uranium metal and the BR extracted 29% when agitated with the same metal concentration; giving an increase of 23% of the total amount of metal extracted.
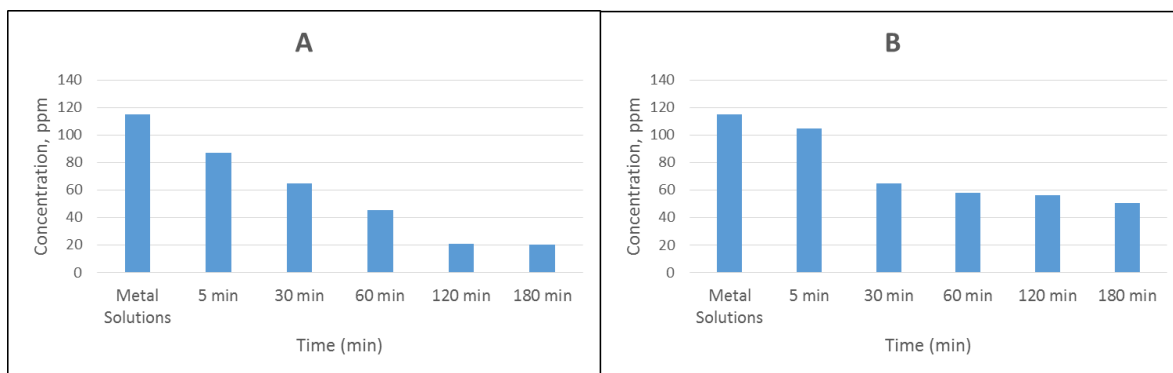

Figure 2.13. The concentration of the Copper metal remaining from initial solution of 0.1 equivalents of Cu^{2+} for the A: heterogeneous ligand (HL) and B) the bare resin (BR).

Comparing the results of extraction efficacy of copper metal, the solution reacted with 0.5 equivalents of metal, was found to have the greatest extraction as measured by the decrease in effective metal ion concentration measure after 60 to 120 minutes of agitation. The amount of extraction leveled out after 120 minutes agitation, as shown in figure 2.14. Thus, additional agitation did not further improve efficacy. When compared to just the bare resin, the extraction

of metal is greater with the presence of the ligand in that HL extracted 62% of the total uranium metal and the BR extracted 33% when agitated with the same metal concentration; giving an increase of 29% of the total amount of metal extracted.
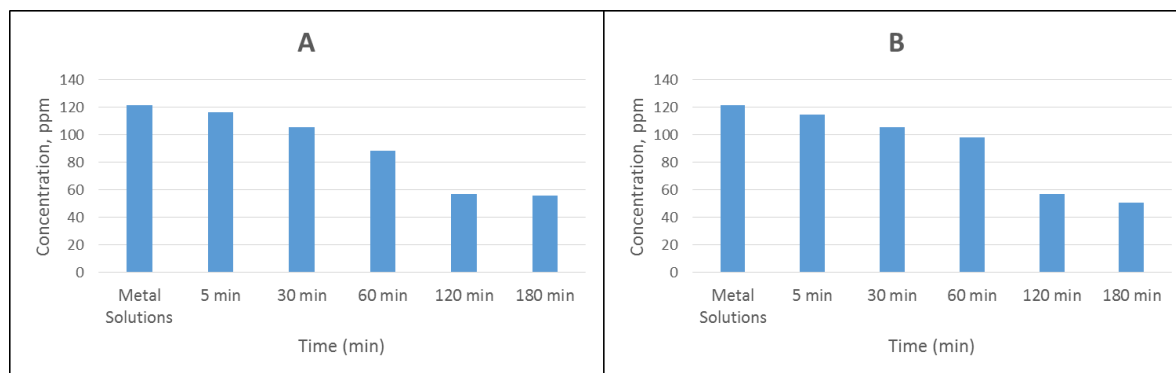

Figure 2.14. The concentration of the Copper metal remaining from initial solution of 0.5 equivalents of Cu^{2+} for the A: heterogeneous ligand (HL) and B) the bare resin (BR).

In further characterization of copper metal ion extraction efficacy, the solution reacted with equivalent amount of functionalized resin and copper metal, was found to have the greatest extraction as measured by the decrease in effective metal ion concentration measure after 60 to 120 minutes of agitation. The amount of metal ion extracted leveled out after 120 minutes agitation, as shown in figure 2.15. Thus, additional agitation did not further improve efficacy. When compared to just the bare resin, the extraction of metal is greater with the presence of the ligand in that HL extracted 74% of the total uranium metal and the BR extracted 46% when agitated with the same metal concentration; giving an increase of 28% of the total amount of metal extracted.

Figure 2.15. The concentration of the Copper metal remaining from initial solution of equal equivalents of Cu^{2+} and substrate for the A: heterogeneous ligand (HL) and B) the bare resin (BR).

In comparing the sample results of copper ion extraction efficacy, the solution reacted with 2 equivalents of metal ion, was found to have the greatest extraction as measured by the decrease in effective metal ion concentration measure after 60 to 120 minutes of agitation. The amount of metal ion extracted leveled out after 120 minutes agitation, as shown in figure 2.16. Thus, additional agitation did not further improve efficacy. When compared to just the bare resin, the extraction of metal is greater with the presence of the ligand in that HL extracted 87% of the total uranium metal and the BR extracted 58% when agitated with the same metal concentration; giving an increase of 29% of the total amount of metal extracted.
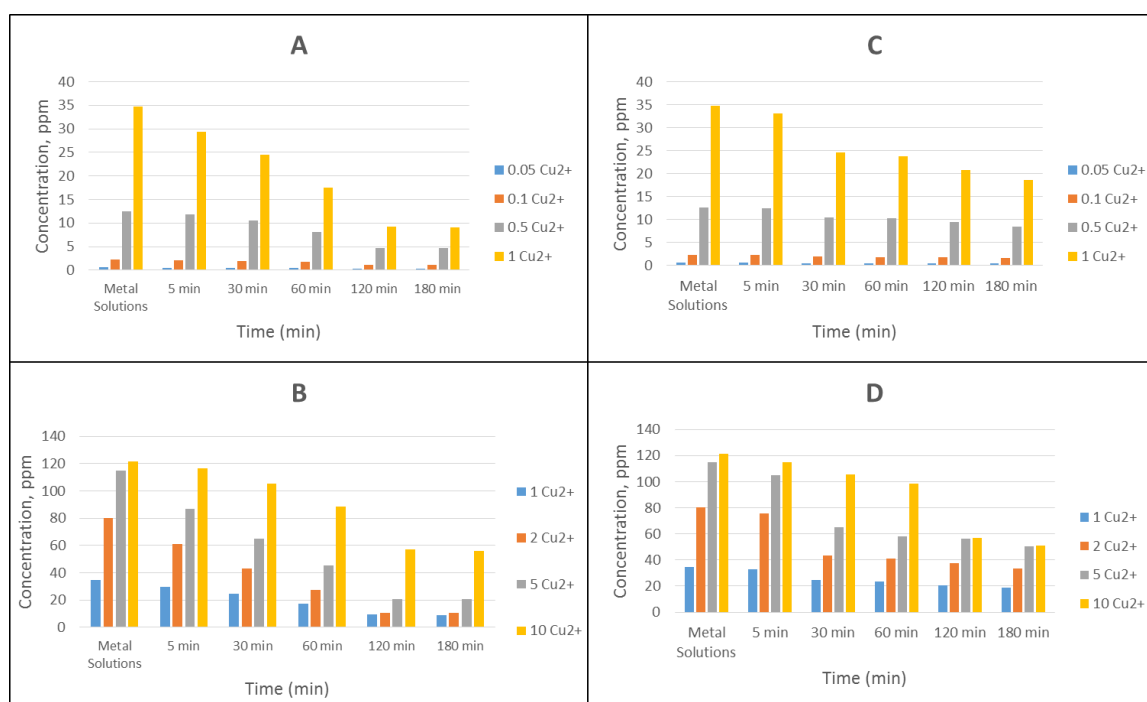
Figure 2.16. The concentration of the Copper metal remaining from initial solution of 2 equivalents of Cu^{2+} for the A: heterogeneous ligand (HL) and B) the bare resin (BR).

Comparing the results of extraction efficacy for copper ions, the solution reacted with 5 equivalents of copper nitrate, was found to have the greatest extraction as measured by the decrease in effective metal ion concentration measure after 60 to 120 minutes of agitation. The amount of metal ion extracted leveled out after 120 minutes agitation, as shown in figure 2.17. Thus, additional agitation did not further improve efficacy. When compared to just the bare resin, the extraction of metal is greater with the presence of the ligand in that HL extracted 82% of the total uranium metal and the BR extracted 56% when agitated with the same metal concentration; giving an increase of 26% of the total amount of metal extracted.

Figure 2.17. The concentration of the Copper metal remaining from initial solution of 5 equivalents of Cu^{2+} for the A: heterogeneous ligand (HL) and B) the bare resin (BR).

In the solutions with 10 equivalents of metal ion demonstrated the greatest decrease in concentration between 60 and 120 minutes of agitation and levels out after 120 minutes, as shown in figure 2.18. Thus, additional agitation did not further improve efficacy. When compared to just the bare resin, the extraction of metal is lower with the presence of the ligand in that HL extracted 53% of the total uranium metal and the BR extracted 58% when agitated with the same metal concentration; giving a decrease of only 5% of the total amount of metal extracted. This can be due to the oversaturation of the SPE with copper.

Figure 2.18. The concentration of the Copper metal remaining from initial solution of 10 equivalents of Cu^{2+} for the A: heterogeneous ligand (HL) and B) the bare resin (BR).

The greatest rate of extraction was found after exposure and agitation between 60-120 minutes for a majority of the solutions, suggesting the optimum agitation time for copper extraction is less than 2 hours. An immediate decrease in the concentration of copper metal ions after less than 5 minutes of agitation with the ligand, was observed in all samples. This small amount of time for detection to begin shows this ligand/resin system could be used as a real-time detector. Comparatively, the samples with the bare resin, unlike with uranyl, began to decrease in metal concentration after 5 minutes. This may be due, in part, to the difference in size of the copper ion versus uranyl, allowing for easier absorption to the surface of the resin. Although the bare resin was able to extract the copper metal ion better than uranyl, the ligand is much more efficient in coordination and extraction of the uranyl. Figure 2.19 displays concentrations of uranium metal in the original samples, at the varying metal equivalents and agitation times for every sample.

It was determined that agitating samples or exposing the ligand to the metal containing solution for a longer period of time resulted in more uranyl being extracted, until diminishing

returns after 120 minutes. For example, when the 1:0.5 (HL:metal) sample was shaken for 5 minutes, the concentration of metal ion in the solution was found to decrease by 6% (12.52 ppm versus 11.75 ppm); whereas after 60 minutes of shaking, the concentration decreased by 22% (8.14 ppm versus 10.49 ppm). Mimicking the conditions of the uranyl samples, the agitation was halted after 180 minutes.

Figure 2.19. The concentration of the Copper metal remaining from initial solutions of Cu^{2+} for the A: heterogeneous ligand (HL) at lower equivalents, B HL at higher equivalents and C) the bare resin (BR) at lower equivalents, D) BR at higher equivalents.

Although the above figures demonstrate that the presence of the ligand covalently bound to the resin increases the amount of metal extracted for both copper and uranyl, this is easier to

understand when the data is combined as in Figure 2.20. Figure 2.20 shows the percent of metal recovered after agitation with HL versus BR per equivalent. For every solution with UO_2^{2+} as the metal, HL demonstrates extraction more effective than BR. This is also true for copper at every equivalent. The ability of the bare resin to extract copper is better than its ability to extract uranyl, but overall, the heterogeneous ligand extracts both metals better than resin alone.
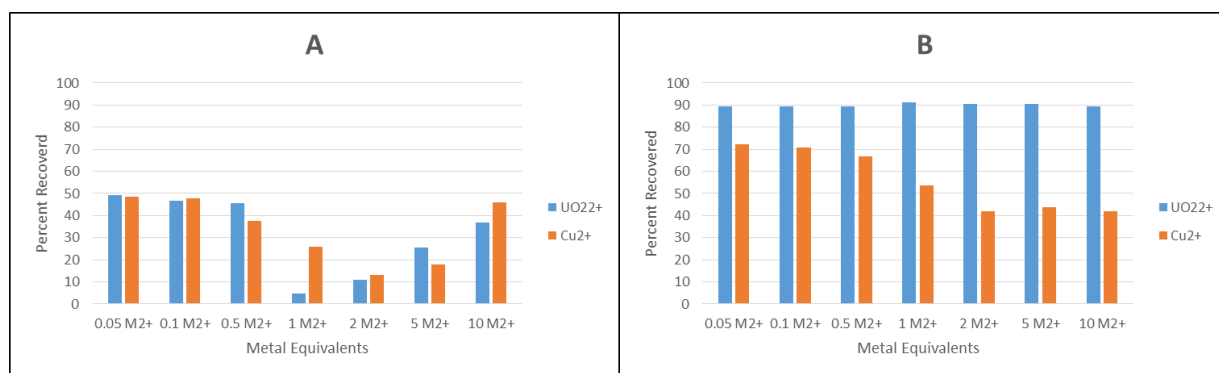
Figure 2.20. Comparison of the changes in concentration of metal remaining after total agitation time for the A) heterogeneous ligand (HL) and B) bare resin (BR).

The ability of the heterogeneous ligand to extract both copper and uranyl could be an issue when considering that the concentration of uranyl is substantially lower than the other naturally occurring metals, such as copper. Taking a closer look at the percentage of uranyl remaining versus copper remaining for each metal equivalents, the amount of copper extracted for every equivalent was higher for every ratio except 0.1, 1, 2, and 10 metal equivalents. At these equivalents, 1%, 20%, 3%, and 10%, respectively, more copper remained after agitation time was complete. These results made it difficult to determine the selectivity of the ligand of

uranyl versus copper. This could possibly be modified by controlling the system with pH. The results can be seen in figure 2.21.
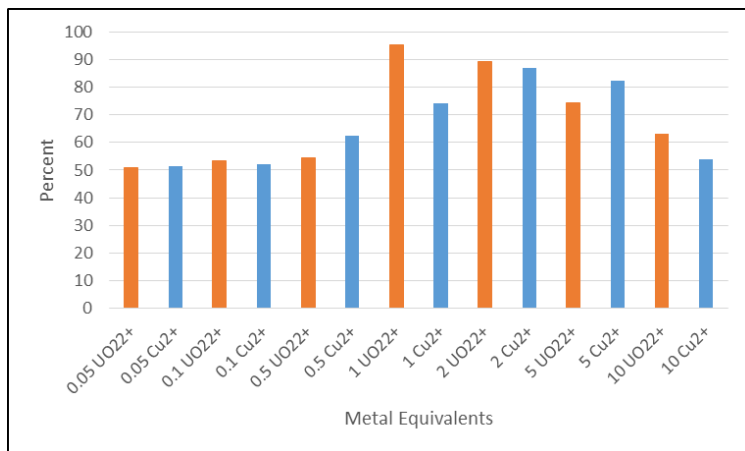
Figure 2.21. The percentage of metal ion extracted at the varying equivalents of HL to metal salt concentration.

To determine if this heterogeneous ligand was a better copper sensor than a uranyl sensor, a short competition study was conducted. A 4.75 µM stock solution, in which both metals were present at the same concentration, was prepared. From the stock solution, dilutions were made to prepare three solutions with the ratios: 1:0.1, 1:0.5 and 1:1 (HL:Metal). The concentration of both metals, in ppm of metal, was determine via ICP-OES before subjecting the samples to agitation with HL for 5 minutes, 60 minutes, and 120 minutes. Figure 2.22 displays the percentage of remaining metal after agitation. With both metals at concentrations of 0.1 equivalents, less than 10% of either metal was extracted. Increasing the metal concentration to one-half of an equivalent, 76% of uranyl and 83% of copper remained. At one equivalent, more

copper was extracted than uranyl, 79% versus 83%, respectively. Overall, the presence of

another metal, decreases the ability of HL to extract uranyl, suggesting the selectivity needs to be

increased to be an efficient detector with minimal sample preparation.
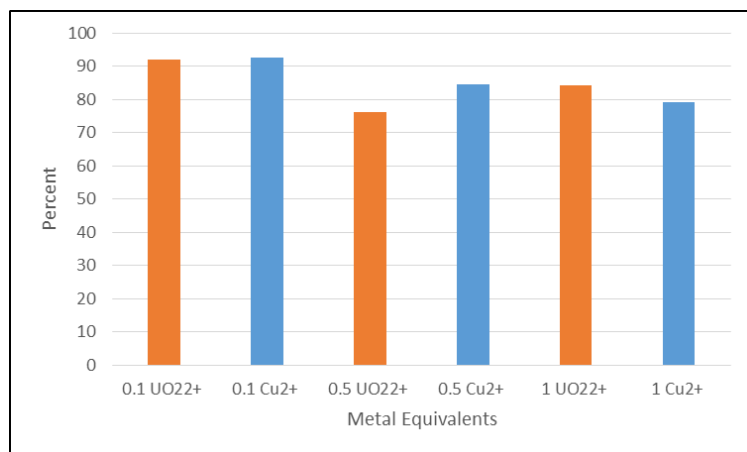
Figure 2.22. The percentage of metal remaining in the competition study at varying equivalents

of HL to metal.

Leaching Study

The utilization of a solid-phase extractor functionalized with a ligand leads to possible

leaching of the ligand into solution or a loss of stability of the covalent linkage of the functional

group over time.. This can occur immediately or over time. Due to this, a leaching study was

conducted to ensure that the ligand remains incorporated into the SPE during agitation and to

determine if the ligand can leach into the aqueous solution. Samples were prepared with an

equivalent amount of heterogeneous ligand and uranyl salt in water at neutral pH of 7, at an

acidic pH of 4.8, and a basic pH = 8.5. To increase the pH for the alkaline solution, 1 M

triethylamine was used and 1 M nitric acid to reduce the pH for the acidic solution after the addition of the metal solution. The UV-Vis absorbance of the samples was measured after 1, 2, and 5 days initially; followed by weekly analysis, Figure 2.23. From the change in UV-Vis spectra, it was determined that the sample with a pH of 7 did not begin leaching until week three and increased from week to week. The acidic sample, pH 4.8, however, appears to have begun leaching after Day 2 of analysis and the changes increased over time. This would suggest that the system would not work well in acidic conditions. The basic sample, pH 8.5, began leaching after week 1 of analysis and leaching continued to increase over time. These results support the neutral conditions to be the optimal conditions of the system and work to identify if buffering could combat leaching and the range of pH stability would be of continuing interest.
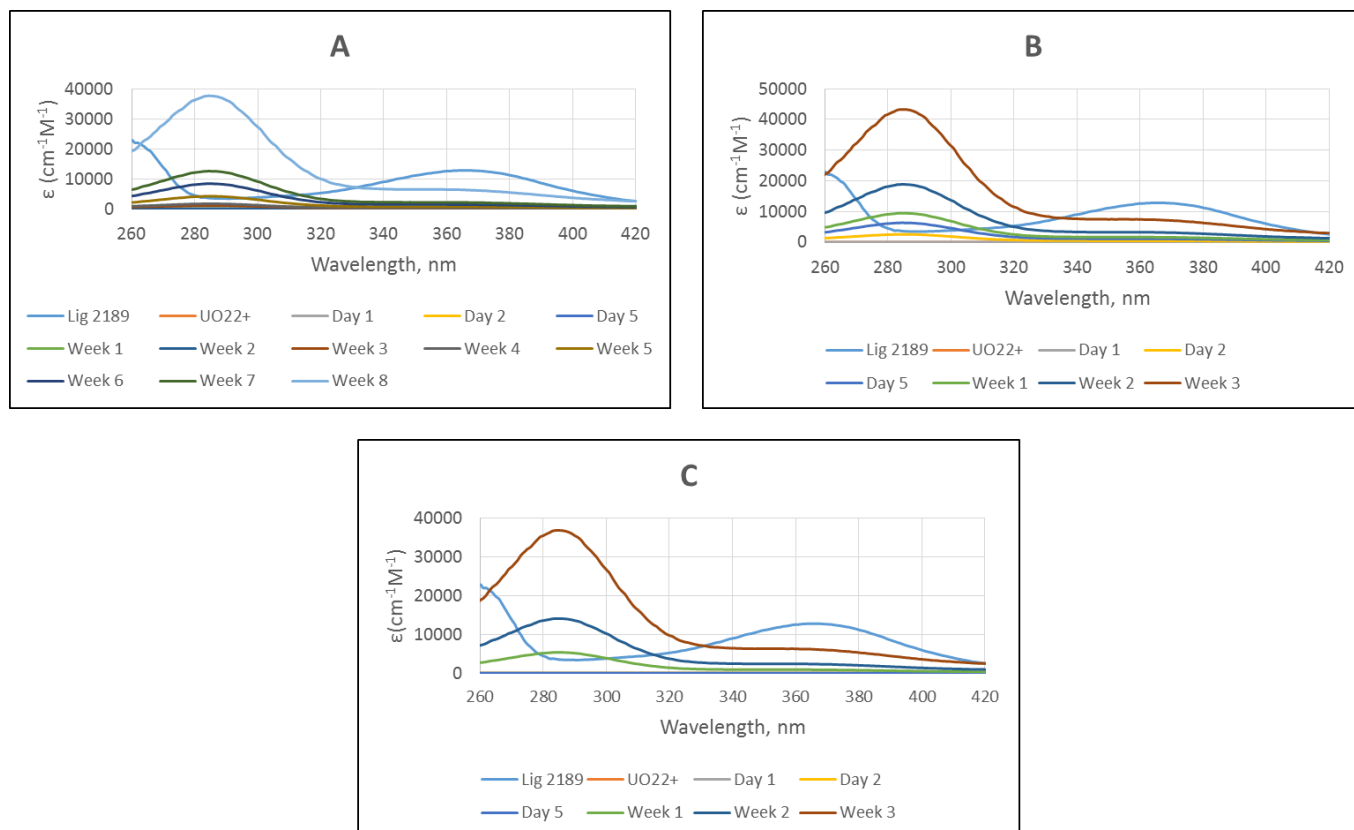
Figure 2.23. The leaching study conducted on HL in aqueous solutions at; A) pH 7, B) pH 4.8, and C) pH 8.5.

Conclusion

The ability of HL to serve as a uranyl detection agent is demonstrated in the above results. Varying the equivalents and time of agitation showed that HL begins working immediately when coordinating uranyl, but best extraction was achieved after a minimum of one hour. For uranyl, although 0.05 equivalents of uranyl to 1 equivalent of HL results in uranyl being extracted, the largest amount of uranyl coordination occurred when the ratio between HL and metal was 1:1. With the presence of copper, the ability of HL to extract uranyl declined substantially; for example, at 0.5 equivalents, 90% of uranyl was detected and removed from the

solution, whereas in the presence of an equivalent amount of copper rather than 45% extracted - only 24% of uranyl was removed from the solution.   These results suggest that a more selective ligand is needed to link to the resin to be able to detect uranyl on-site due to the low concentration of uranyl found in samples of soil and aqueous media and the presence of other naturally occurring metals in higher concentrations. Alternatively, it may be necessary extract copper prior to testing for the uranyl.

References

1. Pestov, D.; Chen, C. C.; Nelson, J. D.; Anderson, J. E.; Tepper, G. Sens. Actuators, B. 2009, 138, 134.

2. Aziz, M.; Beheir, S. G.; Shakin, K. J. Radioanal. Nucl. Chem, 1993, 172, 319.

3. a) Raju, C. S. K.; Subramanian, M. S. A.; J. Hazard. Mater. 2007, 145, 315. b) Merdivan, M. Z.; Duz, C.; Hamamci, C. Talanta, 2001, 55, 639.

4. Miyake, Y. Sugimara, Y.; Mayeda, M. J. Oceanogr. Soc. Jpn. 1970, 26, 123.

5. Rao, T. P.; Metilda, P.; Gladis, J. M.; Talanta 2006, 68, 1047.

6. Ganjali, M. R.; Memari, Z.; Norouzi, P.; Shaabani, B.; Emamalizadeh, M.; Hanifehpour, Y.; Faridbod, F. Anal. Chim. Acta. 1989, 221, 279.

7. Aydin, F. A.; Soylak, M. Talanta 2007, 72, 187.

8. Sadeghi, S.; Sheikhzadeh, E. J. Hazard. Mater. 2009, 163, 861.

9. Sadeghi, S.; Azhdari, H.; Arabi, H.; Moghaddam, A. Z. J. Hazard. Mat. 2012, 215-216, 208.

10. Zhao, Y. Liu, C.; Feng, M.; Chen, Z.; Li, S.; Tian, G.; Wang, L.; Huang, J.; Li, S. J. Hazard. Mater. 2009, 176, 119.

11. Shamsipur, M.; Ghiasvand, A. R.; Yamini, Y. Anal. Chem. 1999, 4892.

12. DeVore, M.; Kerns, S. Gorden, A. E. V. Eur. J. Inorg. Chem. 2015, 34, 5708.

13. Wu, X.; Gorden, A. E. V. Tetrahedron Lett. 2008, 49, 5200.

14. Li, C.; She, M.; She, X.; Dai, J.; Kong, L. J. Appl. Polym. Sci. 2014, 39872.

15. a) Wang, Y.; Huang, W.; Wang, Z.; Zhu, X. X.; Polym. 2004, 45, 71. b) Wang, Z.; Luo, J.; Zhu, X. X. J. Comb. Chem. 2004, 6, 961.

16. Wu, X.; Gorden, A. E. V. J. Comb. Chem. 2007, 9, 601.

17. Poyatos, M.; Sanau, M.; Peris, E. Inorg. Chem. 2003, 42, 2572.

Chapter 3: Use of Imidazole Derivatives for Metal Binding
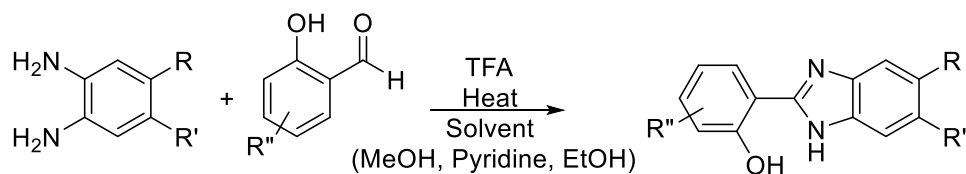
Scheme 3.1. General scheme for formation of imidazole products.

Imidazole a 5-membered 2 nitrogen containing heterocycle can be functionalized with a hydroxyl group to prepare a N-C-C-C-O coordinating pocket in a bidentate ligand.Derivatives, specifically benzimidazole derivatives, are frequently found in nature and have been shown to exhibit anti-inflammatory and anti-tumor activities.[1] Several examples of this type of ligand coordinating transition metals have been reported in literature demonstrating π•••π interactions,[2] reversible iron core-interconversions,[3] polymer enhanced catalysis,[4] and some have been incorporated into fluorescent probes.[5] Maurya et al.[4] prepared cross-linked chloromethylated polystyrene with 5% divinylbenezene to serve as a solid support for the monbasic 2-(2'-hydroxyphenyl)benzimidazole, HBP. This resin was then treated with VO(acac)$_2$, MoO$_2$(acac)$_2$, and Cu(Oac)$_2$, to prepare the corresponding solid supported complexes that were in turn used as heterogenenous catalyst systems in the oxidation reactions. The oxidations of styrene, ethylbenzene, and methyl phenyl sulfide were explored. The VO(acac)$_2$ complex catalyzed the oxidation of methyl phenyl sulfide, Scheme 3.2, into the sulfoxide and sulfone derivatives, with 77.4% selectivity favoring the sulfoxide derivative and a total of 76.5% conversion. The molybdenum complex had 75.1% conversion of the same oxidation; with the copper complex achieving only 44.8% conversion. All three heterogeneous catalysts showed promising catalytic

activity for the oxidation of all three substrates, without the leaching of metals, and were recyclable.[4]
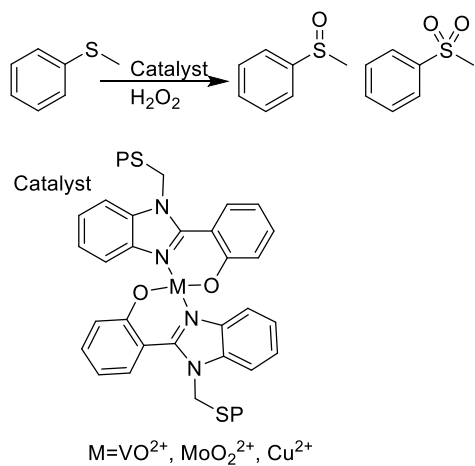
Scheme 3.2. The oxidation of styrene catalyzed by the heterogeneous HBP.

One such example of use of a benzimidazole as a fluorescent detector was published by Srinivan and co-workers, in which they used 2-(1H-benzimidazol-2-yl)phenol (HBYP), Figure 3.1, as a selective fluorescent sensor for the detection of Fe^{3+}.[6] The group found that the HBYP ligand worked best in ethanol, and the presence of the Fe^{3+} cation lead to the formation of the 2HBYP-Fe^{3+} complex. The fluorescence of the HYBP ligand was quenched when bound to Fe^{3+}, a feat not obtained in the presence of common 2+ metal cations, such as Ca^{2+}, Co^{2+}, Ni^{2+}, Cd^{2+}, Pb^{2+}, Zn^{2+}, and Mg^{2+}, all of which had little to no effect on the fluorescence intensity of the ligand. The author's attributed the quenching of the fluorescence to the conversion of the structural charge through tautomerization. Along with serving as a fluorescent sensor for the Fe^{3+} cation, HBYP was found to increase in fluorescence in the presence of H_3PO_4. The

enhancement of fluorescence in the presence of phosphoric acid and the quenching in the presence the Fe^{3+} cation allowed the group to take advantage of the optical properties offered by HBYP and take its sensing capabilities a step further by using it as a cation to anion relay for Fe^{3+} and $H_2PO_4^-$. This relay was based on the displacement approach, in which the fluorescence is turned on with the addition of H_3PO_4 and turned off with the addition of Fe^{3+}.
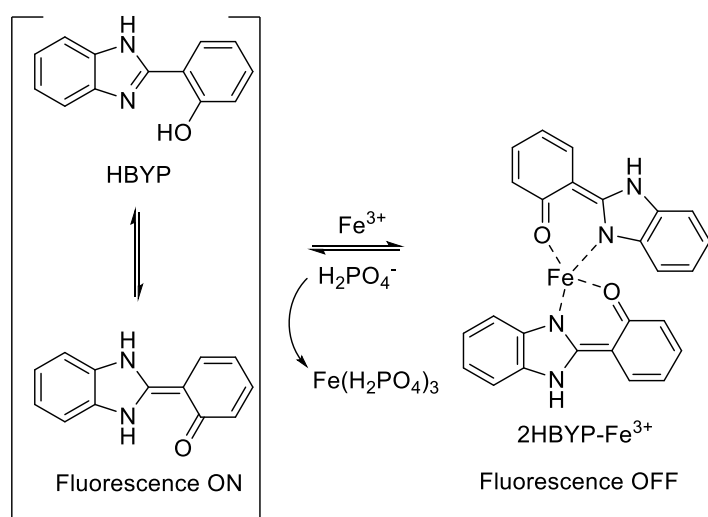
Figure 3.1. The HBYP fluorescent sensor published by Srinivasan et al.

Wang[7] and colleagues synthesized the fluorescent, imidazole-based 4-(trimethyl ammonium chloride)acetamide-2-(1H-naphtho[2,3-d]imidazole-2-yl)phenol, TMAC, and used it as a probe for Cu^{2+}.[7]   The complexation of copper by the TMAC resulted in the quenching of the ligands fluorescence. This fluorescence was recovered after the addition of glutathione to the complex; the authors attribute this to stronger binding force of reduced glutathione and Cu^{2+} versus that of TMAC and Cu^{2+}. This difference in binding interrupts the equilibrium between the TMAC and Cu^{2+} ions, forming the complexation between glutathione and the copper metal

95

center. This, in turn, results in the release of the fluorescent TMAC. As glutathione is a is vital

part of the antioxidant defense system of cells, the authors planned to utilized TMAC as a rapid

glutathione detector.[8]

An interest in organic light-emitting diodes has increased over the years.[9,10,11] Organic

light-emitting diodes, OLEDs, are light emitting diodes that possess an emissive

electroluminescent layer that is comprised of an organic compound capable of emitting light in

response to an electric current, such as imidazoles.[12] Metal complexes of these

electroluminescent materials have been explored to determine their capabilities for OLEDs.[12]

Imidazole complexes in this field, are not solely limited to complexing with transition metals.

Reports of this binding motif with f-elements, mainly the lanthanides, have been published.

Katkova et al. explored imidazole-based 2-(2-hydroxyphenyl)-1*H*-benzimidazole in the presence

of Pr^{3+}, Nd^{3+} and Yb^{3+} to produce near-IR electroluminescent complexes. [13] Suitable crystals of

the neodymium complex were analyzed with X-Ray diffraction. Data collection revealed that

the complex was a centrosymmetric dimer with the Nd^{3+} metal center coordinated by two

terminal and two bridging ligands via N- and exocyclic O-atoms. All three complexes displayed

absorption features similar to previous reports of similar ligands complexed to scandium in their

electronic absorption spectra, suggesting they can be employed in OLEDs.[14] The coupling of

this binding motif with an extended conjugation have not been reported when compared to the

amount of benzimidazole complexes reported, even more, their fluorescent properties of these

systems in the presence of actinide f-elements has not been described.

The intermolecular reaction between the fluorescent backbone 3-secbutyl-diamino-2-

quinoxalinol (2-Qu) and various salicylaldehyde derivatives results in the formation of the mono-

and di-substituted desired salen 2-quinoxalinol (salqu) ligand, as shown in Figure 3.2.
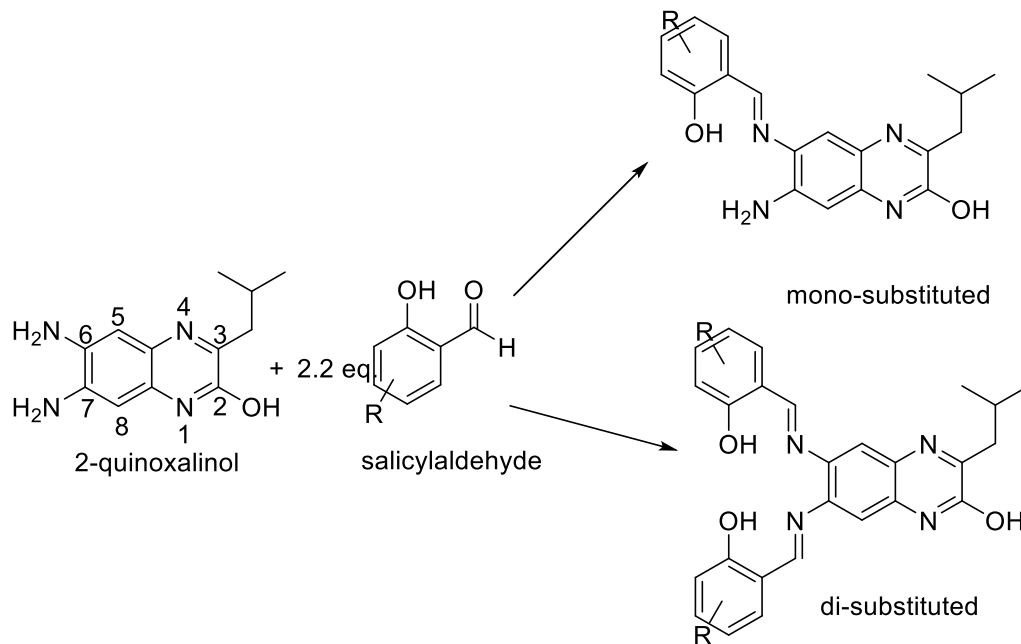
Figure 3.2. The general synthesis of the mono- and di-substituted salen 2-quinoxalinol.

Previous research in the Gorden group, in which the behavior of the two amino nitrogen atoms on the quinoxalinol were observed by labeling one with ^{15}N, demonstrated that the amino group in the 6 position (opposite the hydroxyl group) reacted with the salicylaldehyde first to give the mono-substituted product.[7] With the formation of the mono-substituted salen 2-quinoxalinol, a competition between the intermolecular reaction of the mono-substituted ligand and the salicylaldehyde to produce the desired product, the di-substituted ligand, versus the intramolecular reaction to produce an imidazole derivative occurs, Scheme 3.3. The mechanism, Figure 3.3, begins with the nucleophilic addition of the nitrogen on the carbonyl carbon, pushing the electrons from the double bond to the oxygen and giving it a negative charge. The nucleophilic attack is followed by a proton transfer from the amine, which serves as a weak acid, to the stronger base of the negatively charged oxygen to form a hydroxyl group that can be

protonated to become a good leaving group. Following the deprotonation of the amine by base, an imine is formed and the water leaves, giving the mono-substituted product. From here, the competition begins to achieve the imidazole product, the acid present protonates the imine nitrogen, while the nucleophilic attack of the amine nitrogen on the imine carbon occurs to give the cyclized product. This is followed by the deprotonation of the amine, before oxidation resulting in the imidazole product.
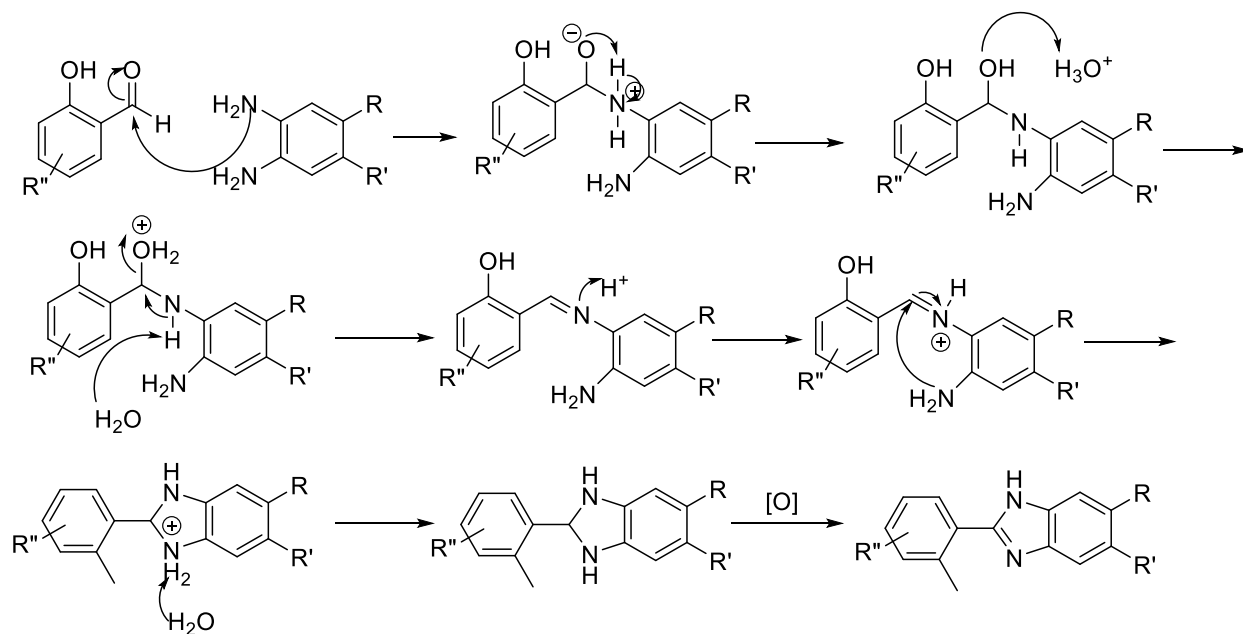
Scheme 3.3. Mechanism of mono-substituted ligand and imidazole formation.

Along with the formation of the imidazole by-product during the salen 2-quinoxalinol synthesis, other members of the group synthesizing salen derived ligands with a 2,3-diaminophenazine backbone, Figure 3.3, also observed the formation of an imidazole product, referred to as salimidizine. The imidazole has been considered a side product and was treated as

waste until a crystal structure of the 2-(1H-imidazo[4,5-b]phenazin-2-yl)phenol (salimidizine) complexed with uranyl was characterized proving the bidentate ligand was a potential ligand of interest.
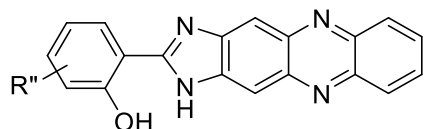
Figure 3.3. The general salimidizine.

During the purification of the desired product, the di-substituted product, via column chromatography, the ease of obtaining the purified imidazole product enabled the collection of this material in large quantities. This led us to analyze explore their chemical abilities to serve as a bidentate chelator for metal cations. Aside from producing imidazole as a side-product during the ligand synthesis, this compound can also be synthesized via an acid catalyzed condensation reaction using a one-to-one molar ratio between the preferred backbone and the chosen salicylaldehyde in the presence of oxygen. Various imidazoles were probed to determine their abilities to bind uranyl and copper cations. A comparison to common transition metals was important because they have been found to commonly cause a false positive in organic coordination ligand systems designed for uranyl sensing.[8] The imidazole derivatives explored possess the 2-quinoxalinol, 2,3-diaminophenazine, and for comparison purposes, a benzene backbone, as shown in Table 3.1.
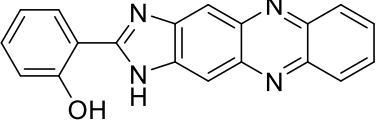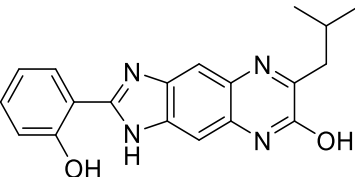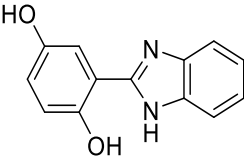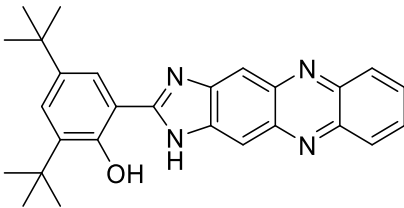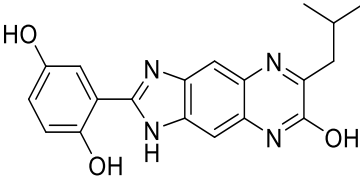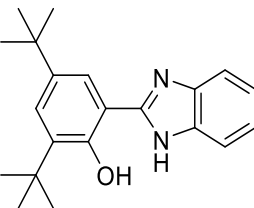
Salimidizine	Salqimidizine	Salphimidizine
Sal1	Salq1	Salph1
Sal2	Salq2	Salph2

Table 3.1. The imidazole derivatives that were explored as bidentate metal chelators.

General Procedure

In a typical procedure, 2 millimoles of the backbone (2,3-diaminophenazine, 2-quinoxalinol, or *ortho*-phenylenediamine) and 2 millimoles of the desired salicylaldehyde were dissolved in a solvent. Methanol was used for 2-quinoxalinol and *ortho*-phenylenediamine; pyridine was used for phenazine derived ligands. For most procedures, 3 microliters of trifluoroacetic acid was added to the reaction before heating to reflux temperature, which was 65 ºC for methanol and 110 ºC allowing the reaction to be open to air for the presence of oxygen. The derivatives were then analyzed using NMR and high-resolution mass spectrometry to confirm its identification.

Results

To determine the efficacy of the imidazole derivatives to coordinate metal cations, ligands were dissolved in *N,N'*-dimethylformamide, DMF, a high temperature basic solvent that would remove the need to account for solvent evaporation and concentration change. DMF is also capable of dissolving all six derivatives. Characterization of the metal complexation was done by following changes in the spectroscopy following a batch titration method for both $UO_2(OAc)_2 \cdot 2H_2O$ and $Cu(OAc)_2 \cdot H_2O$ in water with the ligand to metal ratios ranging from 1:0.1 to 1:5. To account for solvent effects, the total amount of water present in each titration was held constant and did not exceed 20%. Upon introducing the ligand to the metal solutions, the absorbance data was collected and compared to that of the free-base ligand to determine is this would be a means of sensing uranyl. After 24 hours, the fluorescence spectroscopy of the samples was collected to determine the effect of the metal on fluorescent characteristics of the ligand.

2-(1H-imidazo[4,5-b]phenazin-2-yl)phenol (Sal1)

A 20 µM stock solution of the imidazole prepared by the condensation of 2,3-diaminophenazine with salicylaldehyde, Sal1, solution was dissolved in DMF to be analyzed. A 1 mM stock solution of the corresponding metal, uranyl or copper, was prepared and samples in which the ligand concentration was held constant and the concentration of the metal salt was increased from 2 µM (1:0.1 Ligand:Metal ratio) to 100 µM (1:5 Ligand:Metal ration) were prepared. The samples were allowed to sit for 5 minutes before measuring the absorbance, Figure 3.4. This is the "batch titration" method.

For the dilution mixture, a maximum at 433 nm ($\varepsilon = 1.02 \times 10^4$ cm^{-1} M^{-1}), with a small shoulder at 415 nm ($\varepsilon = 9.1 \times 10^3$ cm^{-1} M^{-1}), was observed in the spectrum of the free base ligand. With increasing concentration of $Cu(OAc)_2 \cdot H_2O$, the maxima of 433 nm decreases and becomes quenched completely at a ratio of 1:0.9 Sal1 to ligand. The same is observed for the shoulder at 415 nm. A bathochromic shift of 22 nm to 455 nm of the absorbance maxima is observed starting when the concentration reaches 1:0.9 (Sal1:Cu^{2+}). A maximum extinction coefficient of $\varepsilon = 8.0 \times 10^3$ cm^{-1} M^{-1} at 455 nm is determined once a concentration of 5 times the copper molar equivalent is reached. A small peak at 375 nm is also observed to grow in, and this new feature displayed the highest maximum extinction coefficient in the solution containing 5 times the copper molar equivalent of $\varepsilon = 3.8 \times 10^3$ cm^{-1} M^{-1}. Plotting the metal concentration versus the extinction coefficients at the observed lambda max, it was determined that at the lambda max of 433 nm, between 1:0.0 to 1:0.2 (Sal1:Cu^{2+}) on the lower end metal concentration. With the higher concentrations, 1:3 to 1:5 ligand to metal rations, there is a linear relationship to increasing the amount of metal. The relationship between the metal concentration and extinction coefficient of the ligand at all observed maxima can be seen in figure 3.5. Results show that saturation of the solution occurs at 20 µM of copper metal.
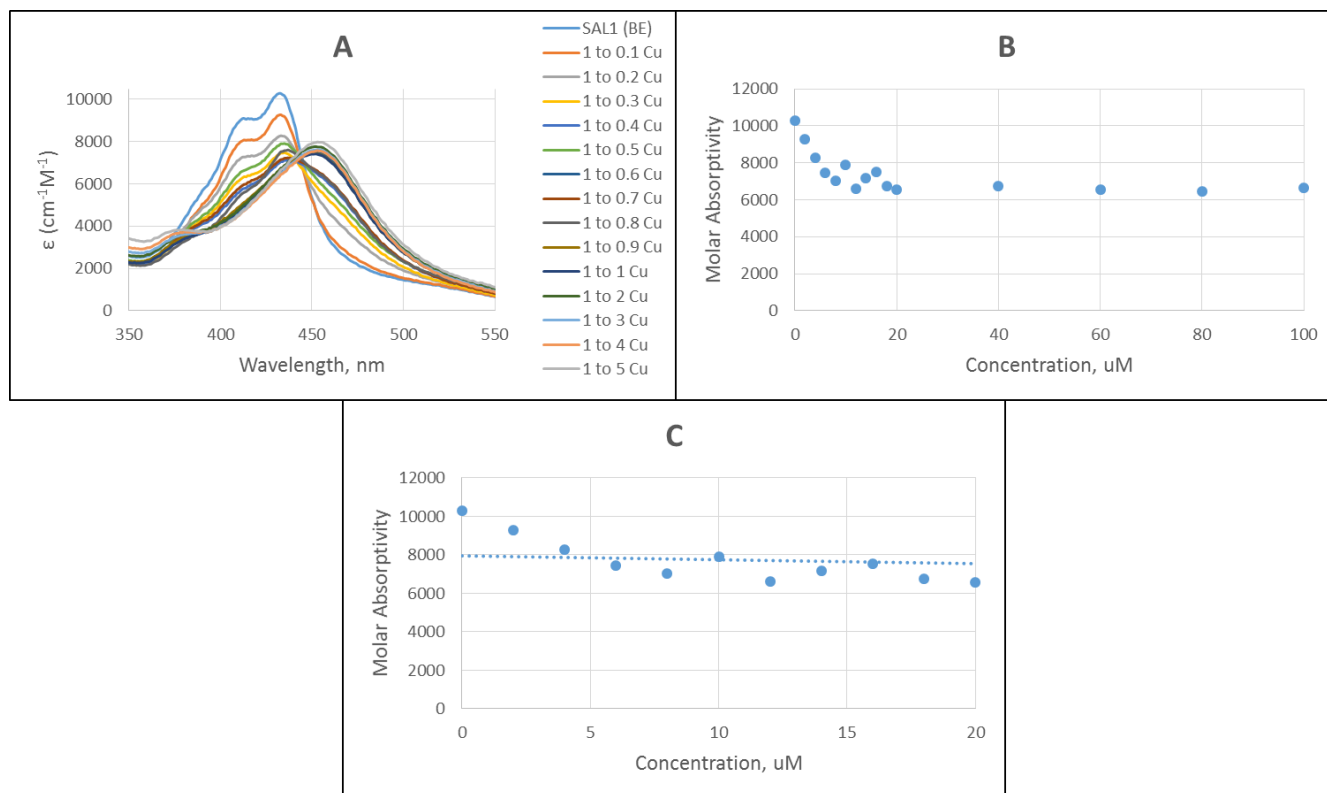
Figure 3.4. A) The change in extinction coefficient of the Sal1 ligand as the solution is titrated with Cu^{2+} solution. B) The molar absorptivity of Sal1 as the concentration of Cu^{2+} increases at 433 nm. C) A closer look at the molar absorptivities of Sal1 in the presence of 0-20 µM of copper.

The extinction coefficient of Sal1/Cu2+ at 375 nm, the line that best fits the molar absorptivities of the lower concentrations of metal intercepts the trend line of the higher concentrations (1-5 equivalents) 15 µM. At 415 nm, the molar absorptivity decreases as the metal concentration increases. This decrease levels out after 1 equivalent of metal was added, the equivalence point occurs at 17 µM. The molar absorptivity increases as the concentration of metal increases, at 18 µM of metal, the interception between the trend line of the higher and

lower metal concentrations occurs, suggesting the equivalence point. An increase in the molar

absorptivity can be seen at 525 nm, the intercept between the lower concentrations and the higher

concentrations occurs at 16 µM of metal.
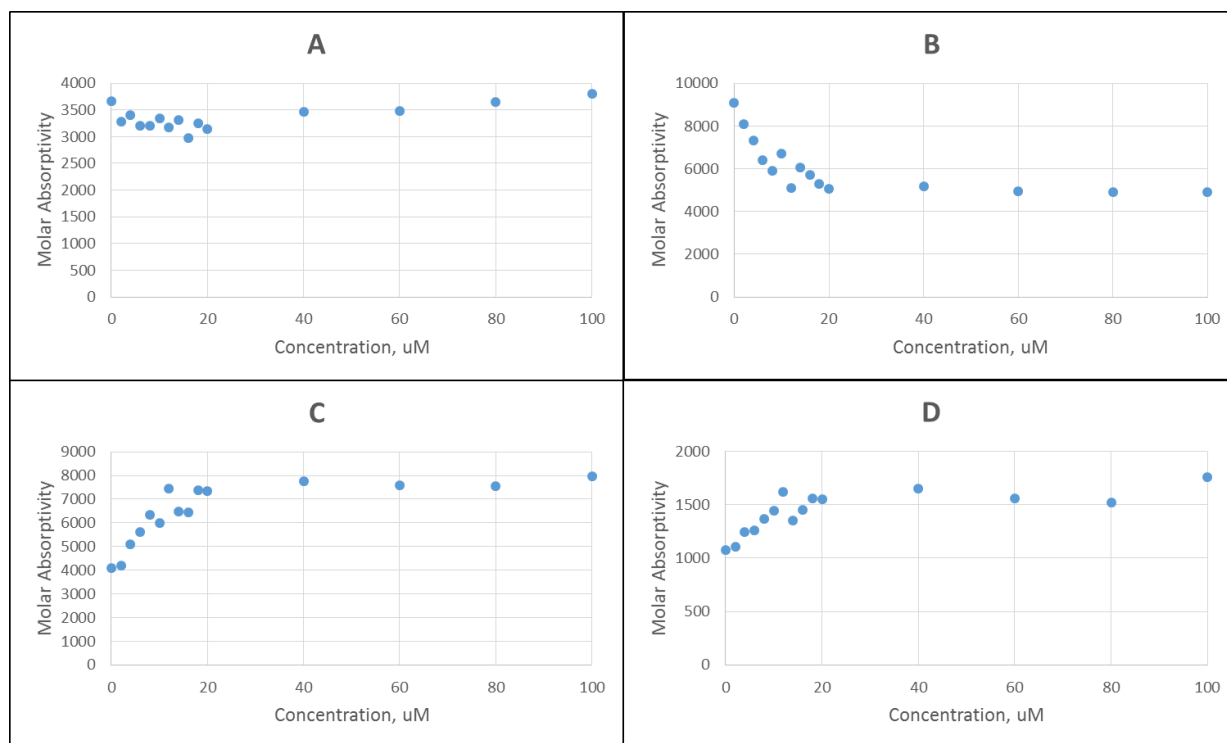
Figure 3.5. The titration curves of extinction coefficient versus metal concentration at A: 375

nm; B: 415 nm; C) 455 nm; and D) 525 nm of Sal1/Cu^{2+}.

The samples were subsequently allowed to sit for 24 hours, and then analyzed using

fluorescence spectroscopy to determine their emission after excitation at the observed maxima.

Upon exciting Sal1 at 433 nm, an emission band at 555 nm, Figure 3.6 was observed. The

addition of the copper solution quenches the fluorescence substantially, suggesting that copper

quenches the ligands fluorescence. The emission for the system at the other observed maxima can be viewed in appendix 1.
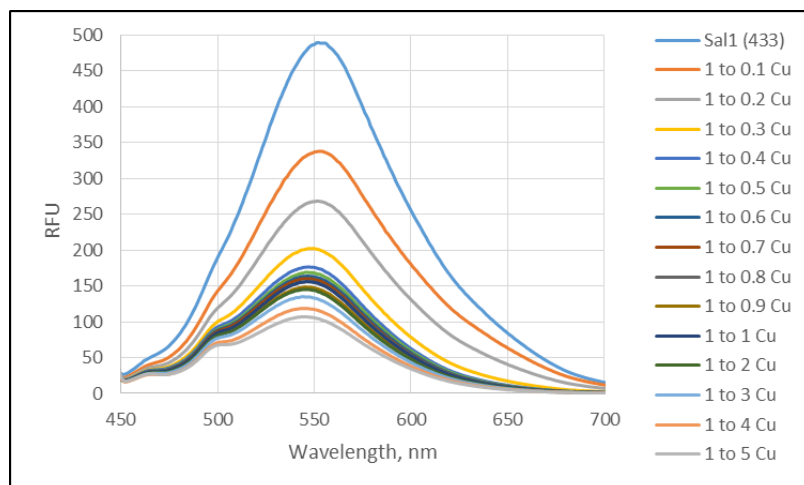
Figure 3.6. The emission spectrum with excitation at 433 nm in the batch titration of Sal1 with Cu(OAc)$_2$·XH$_2$O in 20% H$_2$O in DMF after 24 hours.

When UO$_2$(OAc)$_2$·2H$_2$O was used as the metal ion for complexation an immediate decrease in the maxima at 433 nm on the absorption spectra of Sal1 is observed upon addition. This maxima is extinct in the spectra at a concentration of 1:2 (Sal1:UO$_2^{2+}$). The original shoulder observed at 415 nm in Figure 3.7 shows a very small hypsochromic shift of 5 nm to 410 nm. The maximum extinction coefficient observed at this wavelength is found on the 1:0.1 (Sal1:UO$_2^{2+}$) spectrum ($\varepsilon = 1.0$ x 10^4 cm^{-1} M^{-1}) and decreased until 1:5 ($\varepsilon = 6.0$ x 10^3 cm^{-1} M^{-1}). The titration curve shows an intercept between the low and high concentrations of metal to occur at 42 µM of UO$_2^{2+}$. The relationship between the metal concentration and extinction coefficient of the ligand can be seen in Figure 3.8.
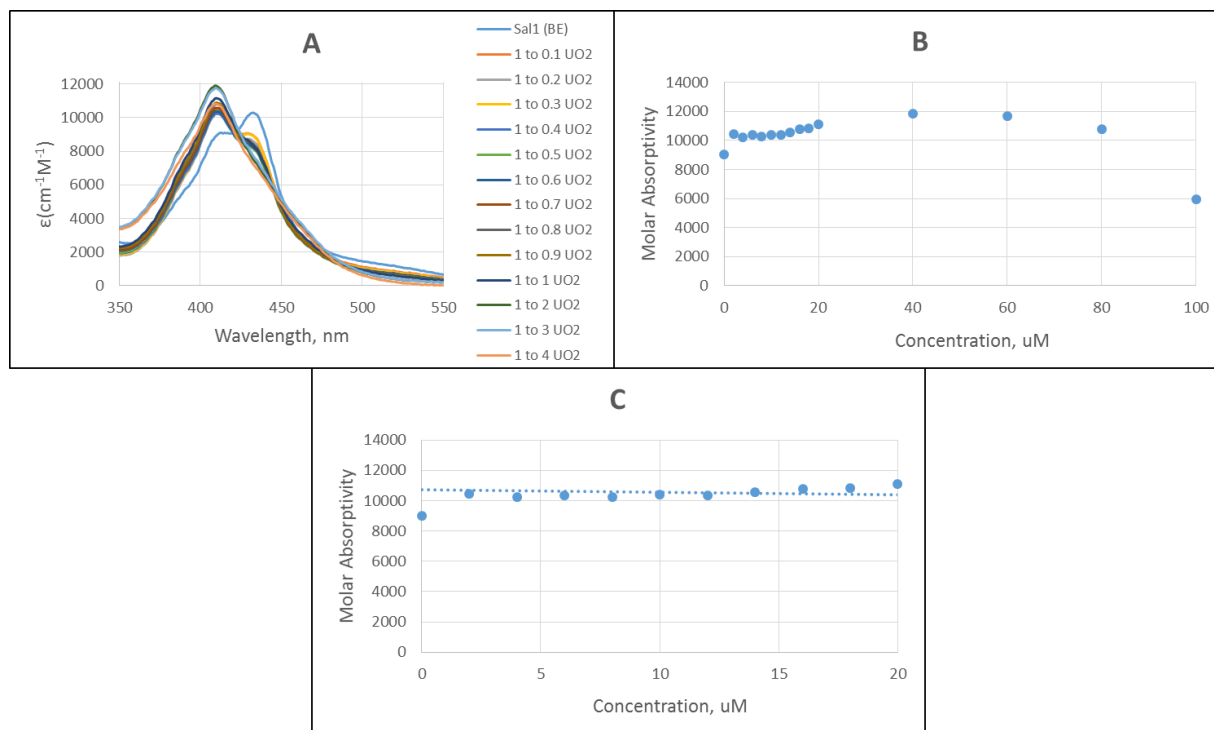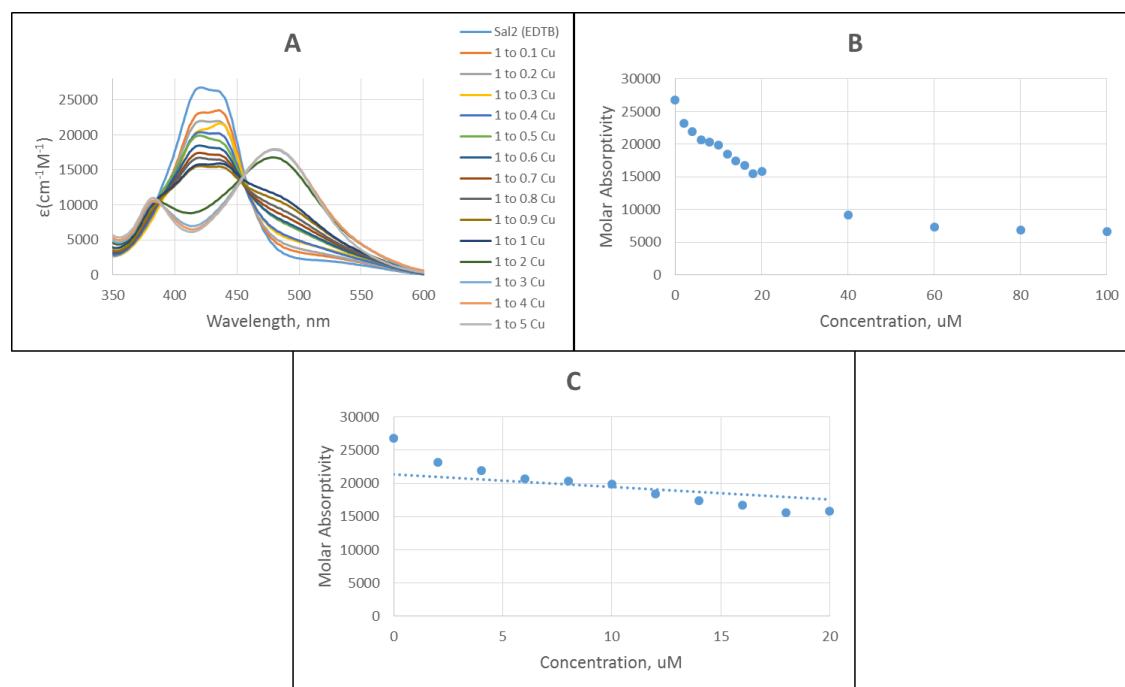
Figure 3.7. A) The change in extinction coefficient of the Sal1 ligand as the solution is titrated with UO_2^{2+} solution. B) The molar absorptivity of Sal1 as the concentration of UO_2^{2+} increases at 410 nm. C) A closer look at the molar absorptivities of Sal1 in the presence of 0-20 µM of uranyl.

The spectra of Sal1/UO_2^{2+} at 415 nm indicates that the molar absorptivity increases, and then after 2 equivalents of metal, it begins to decrease. This results in an equivalence point of 46 µM. At 433 nm, no linear relationship or equivalence point can be determined between the molar absorptivity and the metal concentration. The molar absorptivity decreases at the lower metal concentrations and then increases after 2 equivalents of metal are added. The interception occurs at 32 uM.
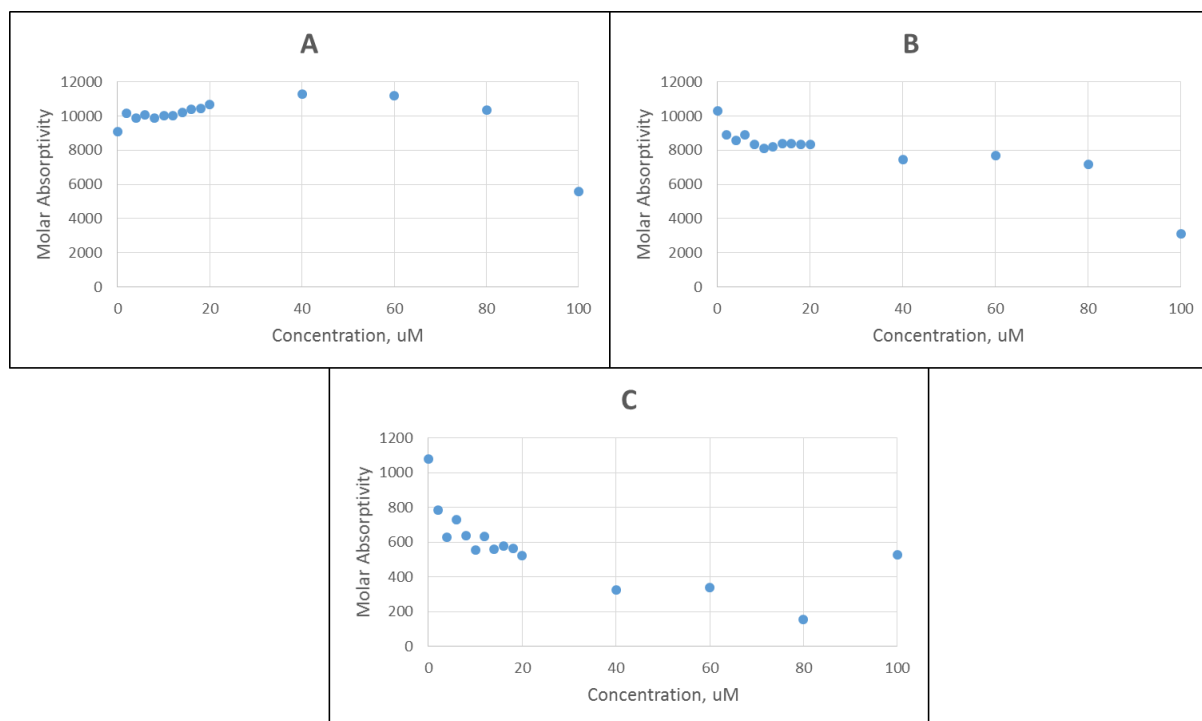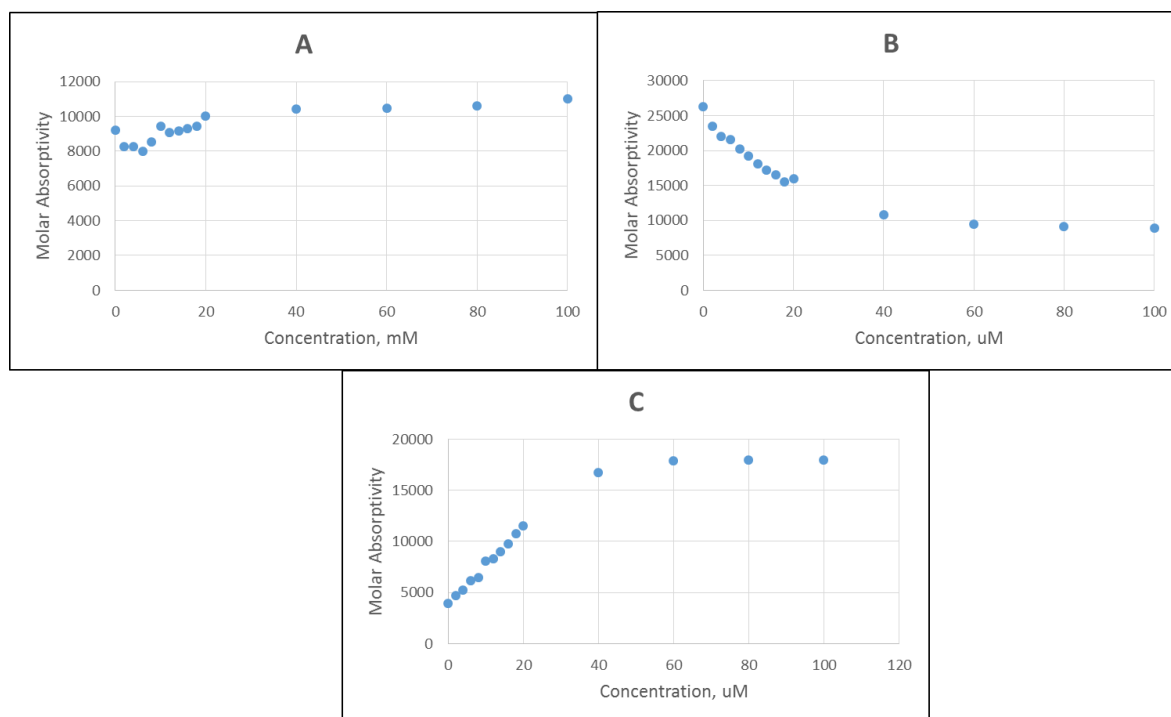
Figure 3.8. The titration curves of extinction coefficient versus metal concentration at A: 415 nm; B: 433 nm; and C) 525 nm of Sal1/UO_2^{2+}.

As with the copper reaction conditions, these samples were subsequently allowed to sit for 24 hours and then characterized by fluorescence spectroscopy to determine their emission after excitation at the observed maxima. An emission band at 547 nm was noticed upon exciting Sal1 at 415 nm, as shown in Figure 3.9. The addition of the uranyl solution greatly decreased the fluorescence of the ligand and the ligand emission intensity; however, when looking solely at the solutions with uranyl, the overall fluorescence of the metal complex increases greatly as the concentration of uranyl increases.   The emission for the system at the other observed maxima can be viewed in appendix 1.
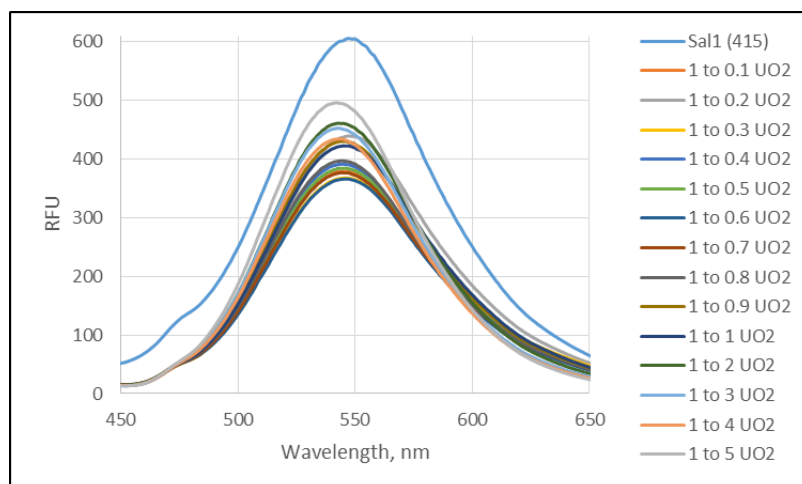
Figure 3.9. The emission spectrum with excitation at 433 nm in the batch titration of Sal1 with UO$_2$(OAc)$_2$·2H$_2$O in 20% H$_2$O in DMF after 24 hours.

2-(1H-imidazo[4,5-b]phenazin-2-yl)phenol (Sal2)

The imidazole obtained through condensation of 2,3-diaminophenazine with 3,5-ditertbutylsalicylaldehyde, Sal2, was dissolved in DMF to a concentration of 20 µM and reacted with Cu(OAc)$_2$·XH$_2$O or UO$_2$(OAc)$_2$·2H$_2$O before measuring the absorption spectrum. Two 1 mM stock solutions 1 of Cu(OAc)$_2$·XH$_2$O and 1 of UO$_2$(OAc)$_2$·2H$_2$O metal were also prepared. A series of samples where prepared from these stock such that the ligand solution was divided such that the ligand concentration was held constant for all of the samples while the concentration of the metal salt added was increased from 2 µM (1:0.1 Ligand:Metal ratio) to 100 µM (1:5 Ligand:Metal ration). The samples were allowed to sit for 5 minutes before being measuring the absorbance spectra. The spectrum for the results from batch titration with the copper solution can be viewed in Figure 3.10. A maximum at 421 nm ($\varepsilon = 2.7$ x 10^4 cm^{-1} M^{-1}), with a small shoulder at 435 nm ($\varepsilon = 2.6$ x 10^3 cm^{-1} M^{-1}), was observed in the spectrum of the

108

free base ligand. With the addition of the $Cu(OAc)_2 \cdot XH_2O$ aqueous solutions, both peaks begin

to decrease and a peak at 481 nm begins to appear on the 1:0.5 spectra. Upon the addition of 2

equivalents of copper, a red shift of 46 nm and lambda max at 481 ($\varepsilon = 4.0$ x 10^3 cm^{-1} M^{-1}) is

observed, as well as a blue shift of 39 nm of the 421 nm peak is observed at 382 nm ($\varepsilon = 9.2$ x

10^3 cm^{-1} M^{-1}). These extinction coefficients increase to 1.8 x 10^4 cm^{-1} M^{-1} and 1.1 x 10^4 cm^{-1} M^{-1}, respectively with the addition of 5 equivalents of the copper metal. Plotting the Cu^{2+}

concentration versus the extinction coefficients at the observed lambda max, it was determined

that at 421 nm, the molar absorptivity decreases overall at the low and high concentrations.

These two lines intercept at 30 µM. The relationship between the Cu^{2+} concentration and

extinction coefficient of the ligand at all observed maxima can be seen in Figure 3.11.

Figure 3.10. A) The change in extinction coefficient of the Sal2 ligand as the solution is titrated with Cu^{2+} solution. B) The molar absorptivity of Sal2 as the concentration of Cu^{2+} increases at 421 nm. C) A closer look at the molar absorptivities of Sal2 in the presence of 0-20 µM of copper.

The extinction coefficient of Sal2/Cu_2^{2+} at 382 nm increases, overall, at both higher and lower Cu^{2+} concentrations. The trend lines for the higher and lower metal concentrations intercept at 29 µM. At 435 nm, as with 382 nm, the interception occurs at 29 µM. The linear relationship can be seen between the molar absorptivity and the metal concentration between 0.4 to 0.9 µM, as well as, 1:3 to 1:5 ratios. The molar absorptivity increases at both the higher and lower concentrations, with the intercept occurring at 36 µM at 481 nm.

Figure 3.11. The titration curves of extinction coefficient versus metal concentration at A: 382 nm; B: 435 nm; and C) 481 nm of Sal2/Cu^{2+}.

After 24 hours, these samples were analyzed with fluorescence spectroscopy to determine their emission after excitation at the observed maxima. Upon exciting Sal1 at 421 nm, an emission band at 538 nm, Figure 3.12, was observed. The addition of the copper solution, unlike Sal1 which contains the same backbone, shows an increase in intensity with addition of the metal salt, with 4 equivalents of copper giving the highest RFU value, suggesting that the addition of copper increases the fluorescence of the ligand. The emission for the system at the other observed maxima can be viewed in appendix 1.
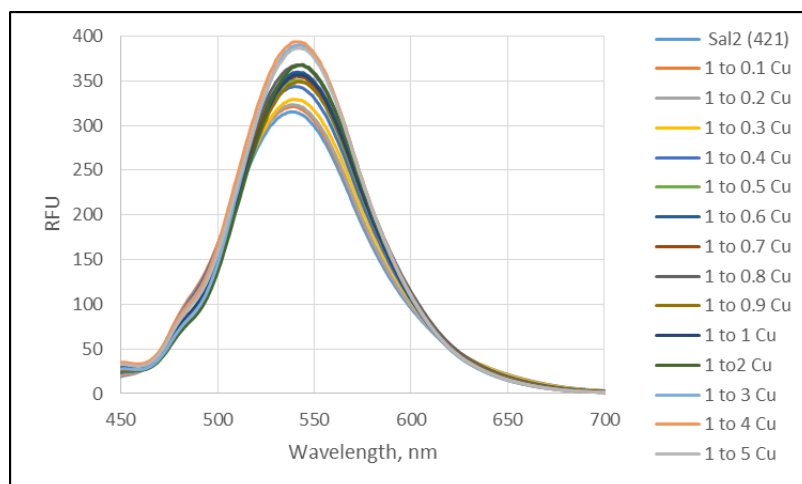
Figure 3.12 The emission spectrum with excitation at 421 nm of the batch titration of Sal2 with Cu(OAc)$_2$·XH$_2$O in 20% H$_2$O in DMF after 24 hours.

An immediate decrease in the maxima at 435 nm is observed when UO$_2$(OAc)$_2$·2H$_2$O and Sal2 interacted. The maxima becomes absent in 1:3 (Sal2:UO$_2^{2+}$) spectra. The original shoulder, Figure 3.13, observed at 421 nm shows only a very small hypsochromic shift of 4 nm to 417 nm. The maximum extinction coefficient observed at the 417 nm wavelength is found on the 1:4 (Sal2:UO$_2^{2+}$) spectra ($\varepsilon = 3.1$ x 10^4 cm^{-1} M^{-1}) and decreased until 1:0.1 ($\varepsilon = 2.5$ x 10^3 cm^{-1} M^{-1}). In the titration curve we observe between 2 and 3 equivalents of UO$_2^{2+}$, there is a linear decrease in the molar absorptivity of the ligand; however, no equivalence point was found. The relationship between the UO$_2^{2+}$ concentration and extinction coefficient of the ligand at all observed maxima can be seen in Figure 3.14.
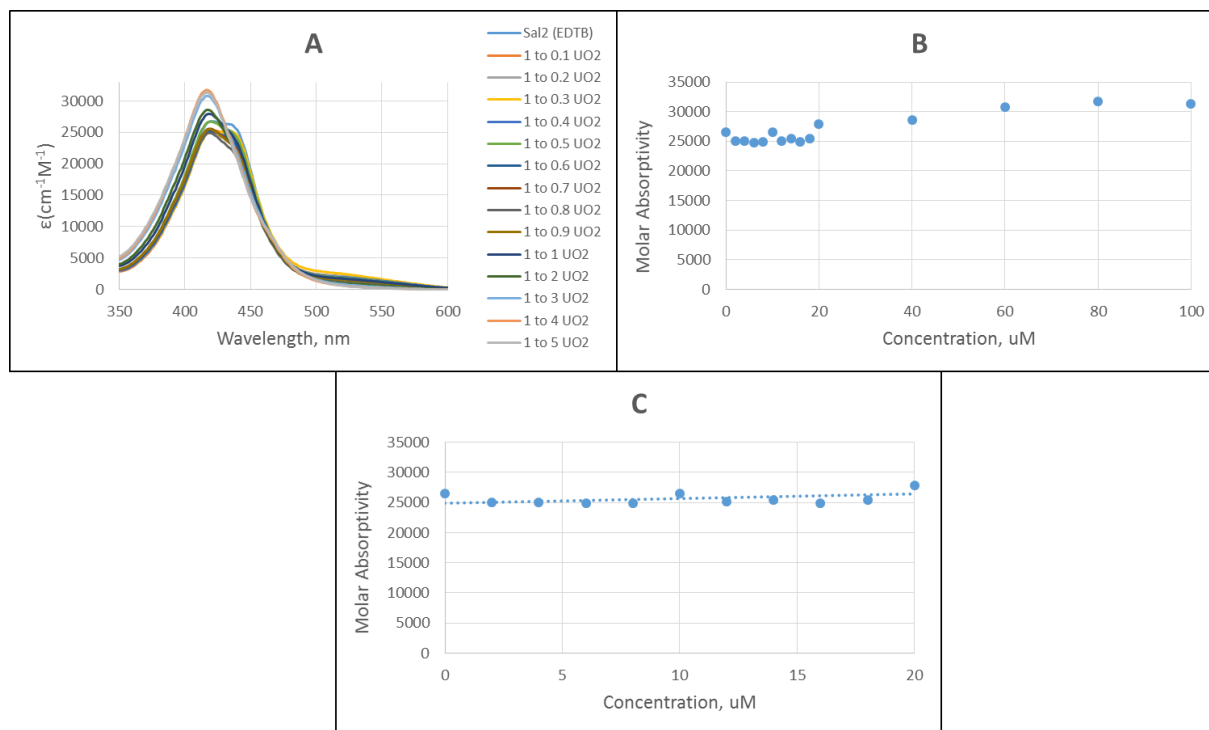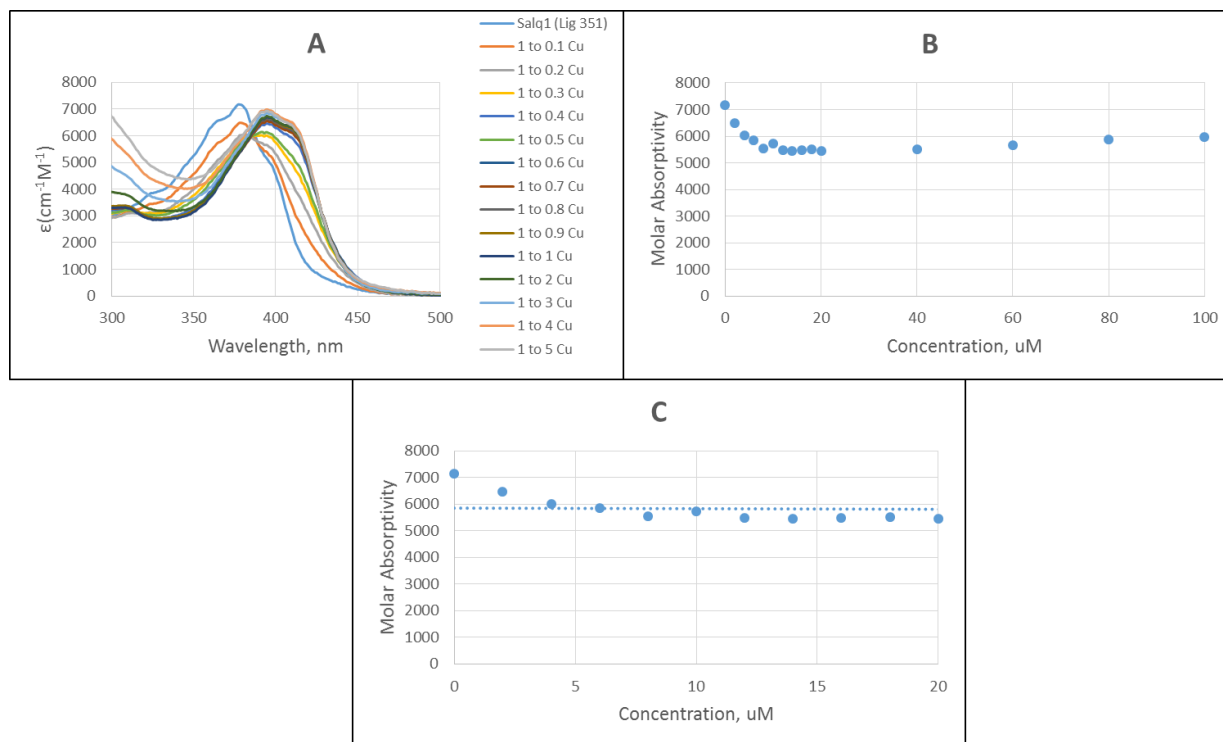
Figure 3.13. A) The change in extinction coefficient of the Sal2 ligand as the solution is titrated with UO_2^{2+} solution. B) The molar absorptivity of Sal2 as the concentration of UO_2^{2+} increases at 417 nm. C) A closer look at the molar absorptivities of Sal2 in the presence of 0-20 µM of uranyl.

The extinction coefficient of Sal2/UO_2^{2+} at 421 nm indicates that the molar absorptivity decreases, except at 10 µM and increases at the higher metal concentrations. An intercept of the lines is not observed. At 435 nm, the molar absorptivity decreases at the lower and higher concentrations of UO_2^{2+}, these trend lines intercept at 9 µM.
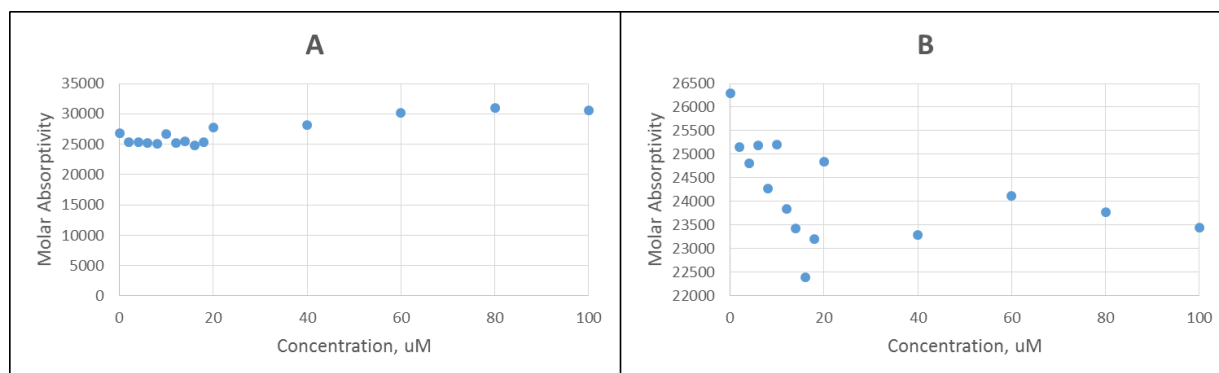
Figure 3.14. The titration curves of extinction coefficient versus metal concentration at A: 421 nm; and B: 435 nm; of Sal2/UO_2^{2+}.

As with the copper batch titration, these samples were then allowed to sit for 24 hours and then analyzed with fluorescence spectroscopy to determine their emission after excitation at the observed maxima. Upon excitation at 421 nm, an emission band at 538 nm was observed, as shown in Figure 3.15. The addition of the uranyl solution decreased the fluorescence of the ligand; however, when looking at the solutions containing uranyl, the fluorescence increases as the concentration of uranyl increases, maxing out at 3 equivalents, suggesting that uranyl increases the fluorescence of the ligand.   The emission for the system at the other observed maxima can be viewed in appendix 1.
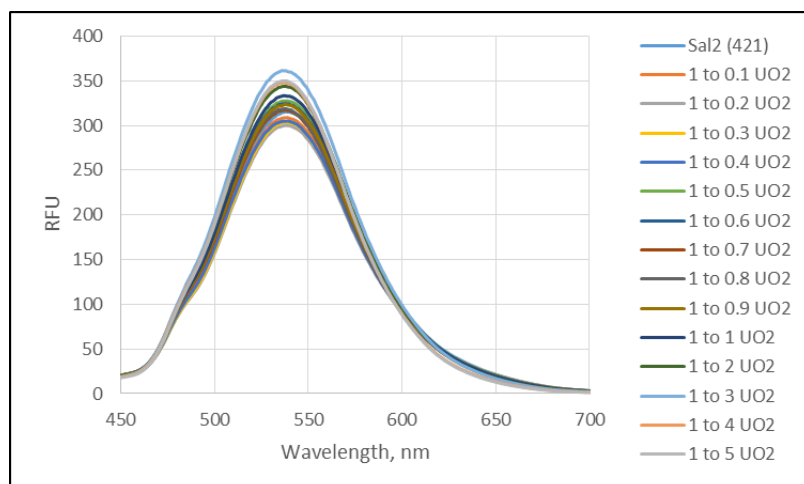
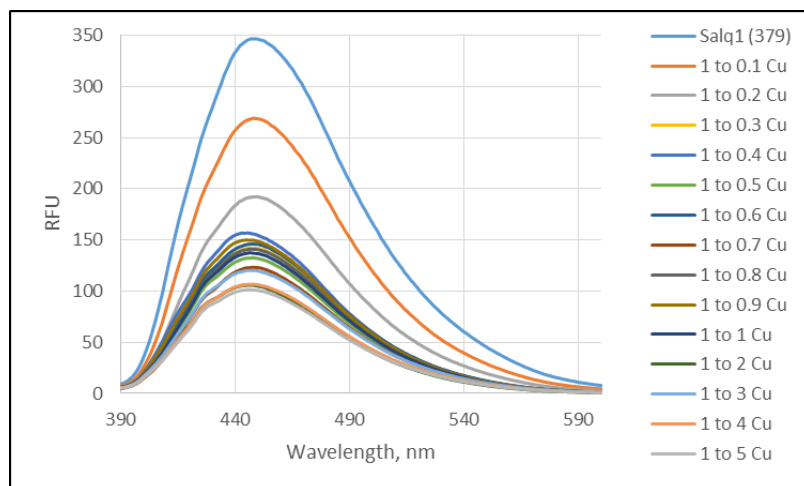Figure 3.15. The emission spectrum with excitation at 421 nm of the batch titration of Sal2 with UO$_2$(OAc)$_2$·2H$_2$O in 20% H$_2$O in DMF after 24 hours.

2-(1H-imidazo[4,5-b]quinoxalin-2-yl)phenol (Salq1)

A 20 µM stock solution of the imidazole obtained from condensing 2-quinoxalinol with salicylaldehyde, Salq1, solution was dissolved in DMF was prepared. As with the prior ligands, a 1 mM stock solution of Cu(OAc)$_2$·XH$_2$O and UO$_2$(OAc)$_2$·2H$_2$O metal was also prepared and 14 samples, in which, the ligand concentration was held constant and the concentration of the metal salt increased from 2 µM (1:0.1 Ligand:Metal ratio) to 100 µM (1:5 Ligand:Metal ration), were prepared. The samples were allowed to sit for 5 minutes before being measuring the absorbance. The spectrum for the batch titration with copper solution can be viewed in Figure 3.16. A maximum at 393 nm (ε = 7.2 x 10^3 cm^{-1} M^{-1}), with a small shoulders at 323 nm (ε = 2.6 x 10^3 cm^{-1} M^{-1}), 362 nm (ε = 3.9 x 10^3 cm^{-1} M^{-1}), and 396 nm (ε = 5.0 x 10^3 cm^{-1} M^{-1}), were observed in the spectrum of the free base ligand. With the addition of the Cu(OAc)$_2$·XH$_2$O aqueous solutions, the lambda max at 379 nm begins to shift with metal amounts as low as 0.1

equivalents, shifting completely to 393 nm after 0.6 equivalents of metal was introduced to the solution. In as small as 0.2 equivalents of metal, the initial peaks of the free base are absent. Along with the new lambda max at 393 nm ($\varepsilon = 6.9$ x 10^3 cm^{-1} M^{-1}), a bathochromic shift of 14 nm, a shoulder at 410 nm ($\varepsilon = 6.5$ x 10^3 cm^{-1} M^{-1}) is also observed. Plotting the metal concentration versus the extinction coefficients at the observed lambda max, it was determined that at 379 nm, the intercept between the lower metal concentrations and the higher metal concentrations occurs at 16 μM of metal. The relationship between the metal concentration and extinction coefficient of the ligand at all observed maxima can be seen in figure 3.17.
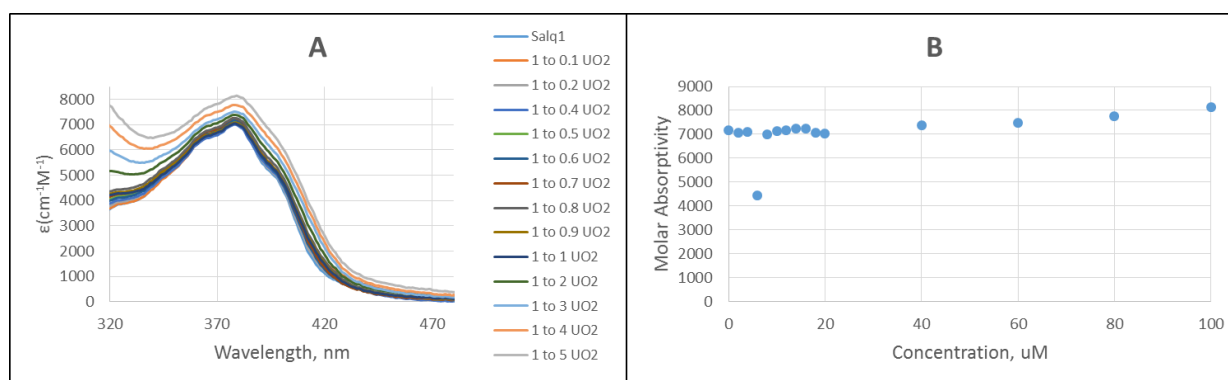
Figure 3.16. A) The change in extinction coefficient of the Salq1 ligand as the solution is titrated with Cu^{2+} solution. B) The molar absorptivity of Salq1 as the concentration of Cu^{2+} increases at 379 nm. C) A closer look at the molar absorptivities of Salq1 in the presence of 0-20 µM of copper.

The spectra of Salq1/Cu^{2+} has a lambda max at 310 nm where the molar absorptivity increases after 6 equivalents of metal added. The intercept between the high and low metal concentrations occurs at 28 µM. At the secondary maxima - 323 nm, this intercept occurs at 18 uM, after decreasing at the lower concentrations and increasing at the higher concentrations. An intercept at 16 µM occurs at 362 nm, after decreasing before 0.9 equivalents and increasing after 1 equivalent of metal was added, similar to 379 nm. For both, 396 nm and 410 nm, the intercept

occurs at 16 uM, however, the molar absorptivity of the lower concentrations increases and continues to increase after the 1 equivalence point.
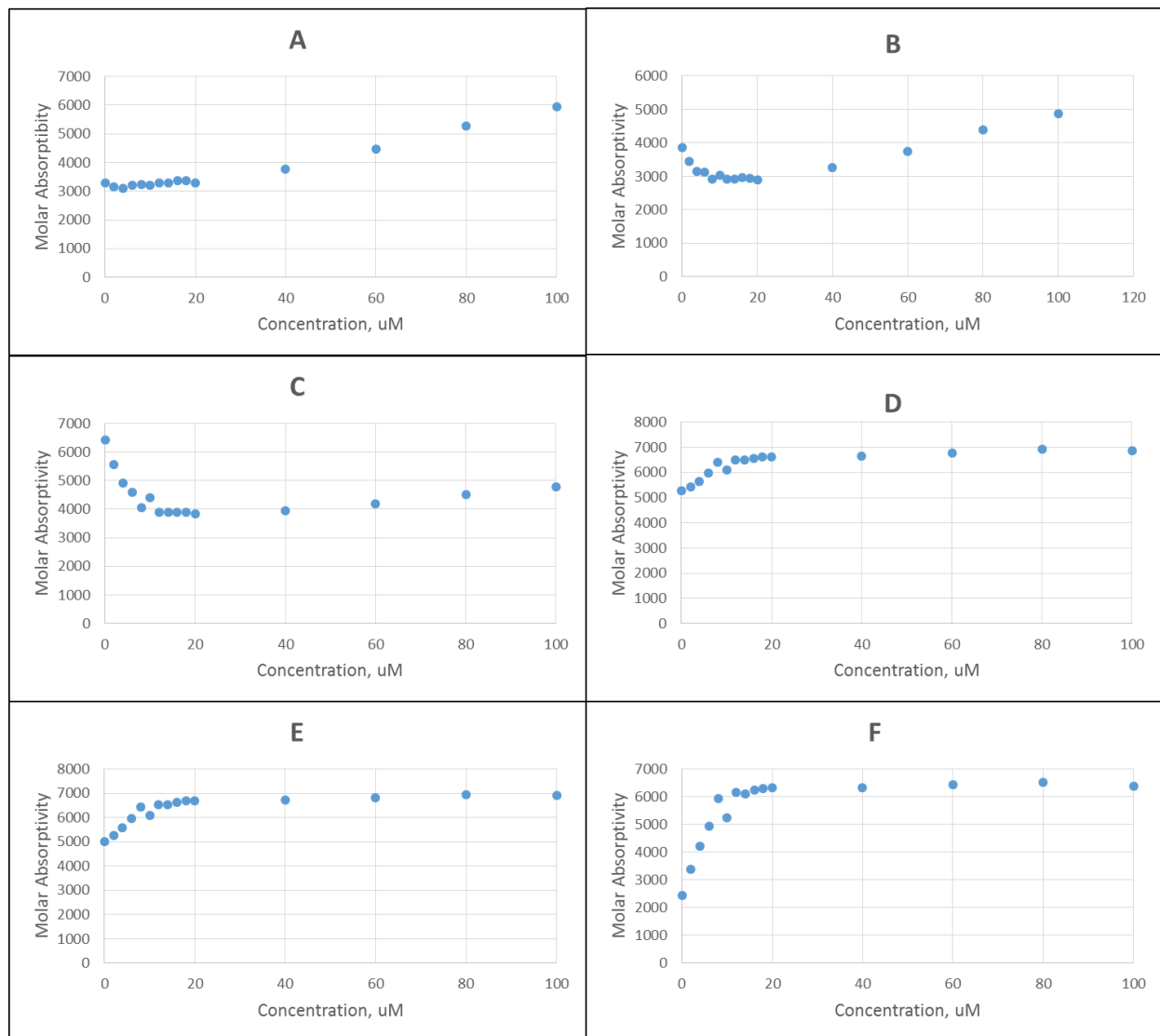
Figure 3.17. The titration curves of extinction coefficient versus metal concentration at A: 310 nm; B: 323 nm; C) 362 nm; D) 393 nm; E) 396 nm; and F) 410nm of Salq1/Cu^{2+}.

After 24 hours, these samples were characterized using fluorescence spectroscopy to determine their emission after excitation at the observed maxima. Upon exciting Salq1 at 379 nm, an emission band at 446 nm, Figure 3.18, was observed. The fluorescence of the ligand at 446 nm decreased as the amount of copper metal increased, proving that copper quenches the fluorescence of the ligand. The emission for the system at the other observed maxima can be viewed in appendix 1.

Figure 3.18. The emission spectrum with excitation at 379 nm of the batch titration of Salq1 with Cu(OAc)$_2$·XH$_2$O in 20% H$_2$O in DMF after 24 hours.

The batch titration method was employed when Salq1 was reacted with UO$_2$(OAc)$_2$·2H$_2$O. A 1 mM stock solution of Cu(OAc)$_2$·XH$_2$O and UO$_2$(OAc)$_2$·2H$_2$O metal were prepared and 14 samples, in which, the ligand concentration was held constant and the concentration of the metal salt increased from 2 µM (1:0.1 Ligand:Metal ratio) to 100 µM (1:5 Ligand:Metal ration), were prepared. The samples were allowed to sit for 5 minutes before

being measuring the UV-Vis absorbance. Although the spectrum, Figure 3.19, observed after

titrating with uranyl acetate did not show any shifts in the lambda max values seen in the spectra

of the free base, the initial addition of 0.1 until 0.7 equivalents of metal a decrease in extinction

coefficient is observed, with the lowest of 4.5 x 10^3 cm^{-1} M^{-1} versus 7.2 x 10^3 cm^{-1} M^{-1} of the

free-base; however, after 0.8 equivalents, an increase in the absorption spectra is observed and

achieves a maximum with 5 equivalents of uranyl for every one equivalent of metal (8.1 x 10^3

cm^{-1} M^{-1}). The titration curve, at 379 nm, shows that the lower concentrations, where the molar

absorptivity increases from 8 µM to 16 µM of metal, intercepts the higher concentrations at 10

µM. The relationship between the metal concentration and extinction coefficient of the ligand at
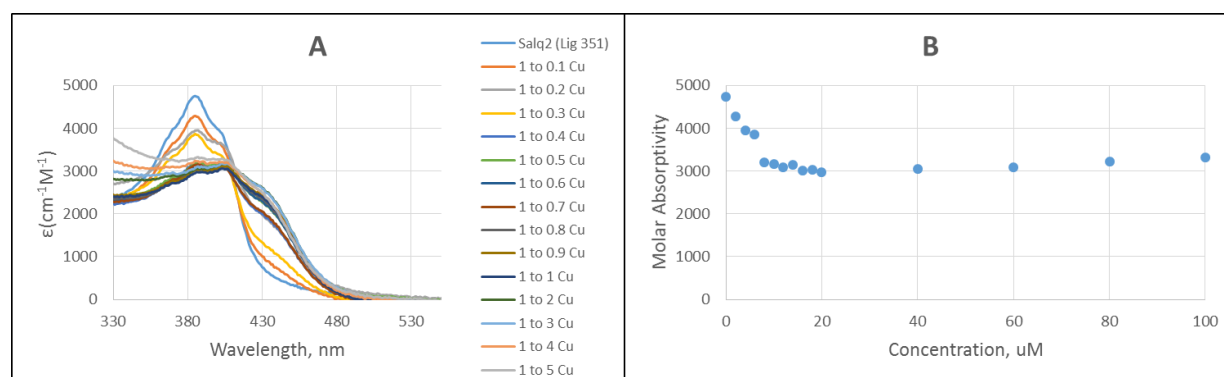
all observed maxima can be seen in figure 3.20.

Figure 3.19. A) The change in extinction coefficient of the Salq1 ligand as the solution is

titrated with UO$_2^{2+}$ solution. B) The molar absorptivity of Salq1 as the concentration of UO$_2^{2+}$

increases at 379 nm.

According to the titration curve, at 323 nm, the intercept between the lower and higher

concentrations of metal occurs at 0 µM. For 362 nm and 396 nm, the equivalents point occurs at

12 µM of metal.
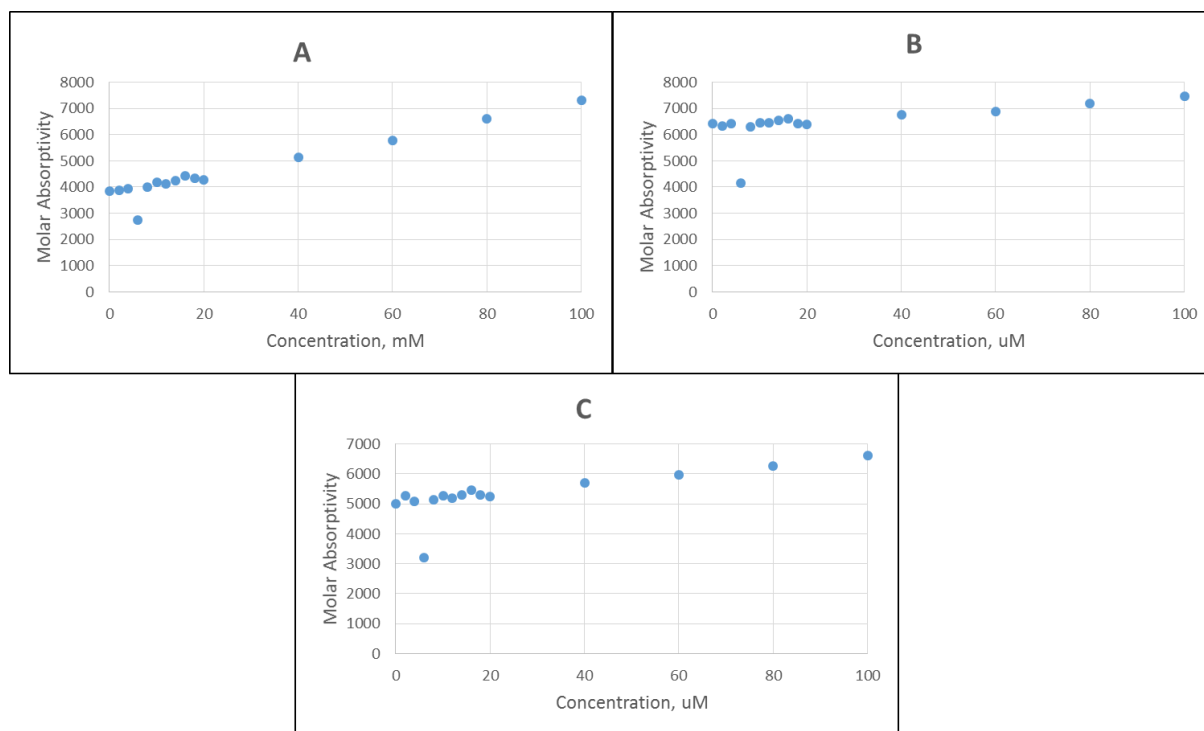
Figure 3.20. The titration curves of extinction coefficient versus metal concentration at A: 323

nm; B: 362 nm; and C) 396 nm of Salq1/UO_2^{2+}.

As with the copper batch titration, these samples were then allowed to sit for 24 hours

and observed with fluorescence spectroscopy to determine their emission after excitation at the

observed maxima. Upon excitation at 379 nm, an emission band at 449 nm was observed, as

shown in Figure 3.21. The addition of the uranyl solution decreased the fluorescence of the

ligand. Taking a closer look at the solutions with uranyl, the fluorescence quenches as the

addition of the equivalents of uranyl increases, showing that for this particular ligand, uranyl

quenches the fluorescence. The emission for the system at the other observed maxima can be
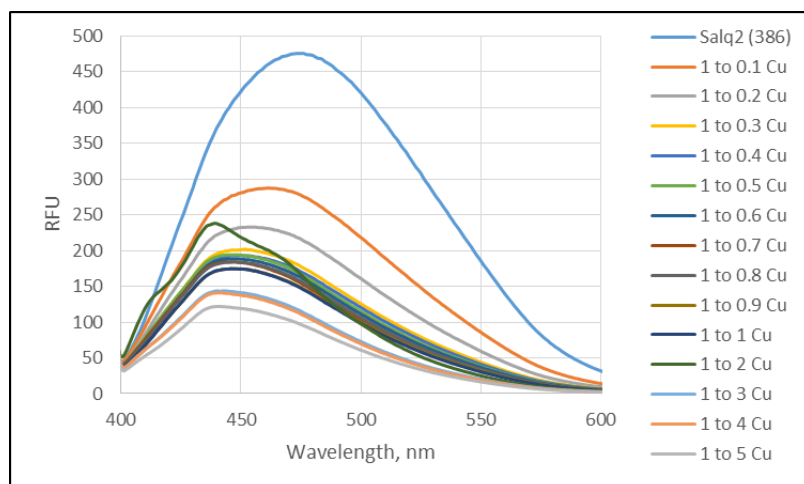
viewed in appendix 1.
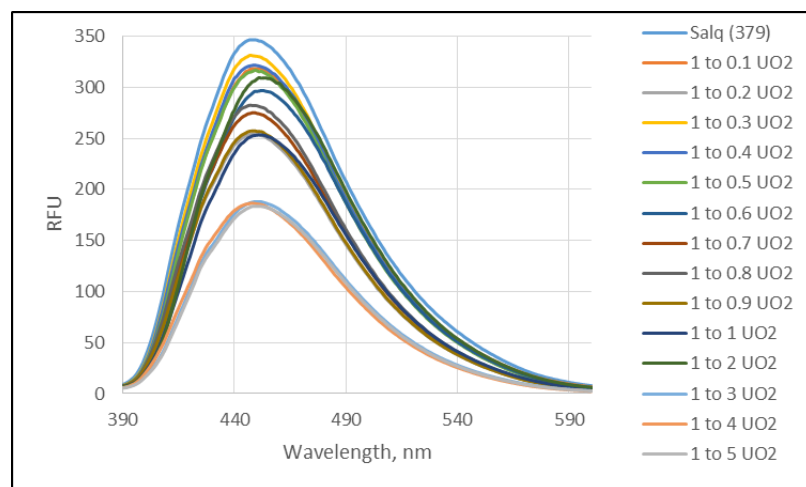
Figure 3.21. The emission spectrum with excitation at 379 nm of the batch titration of Salq1 with

$UO_2(OAc)_2 \cdot 2H_2O$ in 20% H_2O in DMF after 24 hours.

2-(1H-imidazo[4,5-b]quinoxalin-2-yl)phenol (Salq2)

The imidazole obtained from condensing 2-quinoxalinol with 3,5-ditertbutyl

salicylaldehyde, Salq2, was dissolved in DMF and a 20 µM stock solution was prepared. As

with the prior ligands, a 1 mM stock solution of $Cu(OAc)_2 \cdot XH_2O$ and a 1mM $UO_2(OAc)_2 \cdot 2H_2O$

stock solution was prepared and 14 samples, in which, the ligand concentration was held

constant and the concentration of the metal salt increased from 2 µM (1:0.1 Ligand:Metal ratio)

to 100 µM (1:5 Ligand:Metal ration). The samples were allowed to sit for 5 minutes before

being measuring the absorbance, figure 3.22. A maximum at 386 nm ($\varepsilon = 4.7$ x 10^3 cm^{-1} M^{-1})

was observed in the spectrum of the free base ligand. The addition of the $Cu(OAc)_2 \cdot XH_2O$

aqueous solutions results in the immediate decrease in the absorbance of the lambda max at 386

nm, before becoming quenched completely after 0.3 equivalents of metal is added. A

hypsochromic shift of 17 nm is observed beginning with the addition of 0.4 equivalents of metal

with a maximum reached with the addition of 5 equivalents at 403 nm ($\varepsilon = 3.3$ x 10^3 cm^{-1} M^{-1}),

with a shoulder at 430 nm. Plotting the metal concentration versus the extinction coefficient at

the observed lambda max, it was determined that the lower concentrations, in which 0.1

equivalents of metal were added at a time, the emission decreases overall. At the higher

concentrations of metal, after 1 equivalent of metal was added, increases overall. The lines

intercept at 18 µM.   The relationship between the metal concentration and extinction coefficient

of the ligand at all observed maxima can be seen in figure 3.23.

Figure 3.22. A) The change in extinction coefficient of the Salq2 ligand as the solution is

titrated with Cu^{2+} solution. B) The molar absorptivity of Salq2 as the concentration of Cu^{2+}

increases at 386 nm.

The titration curve of Salq2/Cu^{2+} shows that at 403 nm, the molar absorptivity increases overall as the metal concentration increases. The molar absorptivity than decreases as 1 equivalent of metal is added at a time. The interception of both lines occurs 17 µM. At 430 nm, an interception at 20 uM, or 1:1 ligand to metal, occurs.
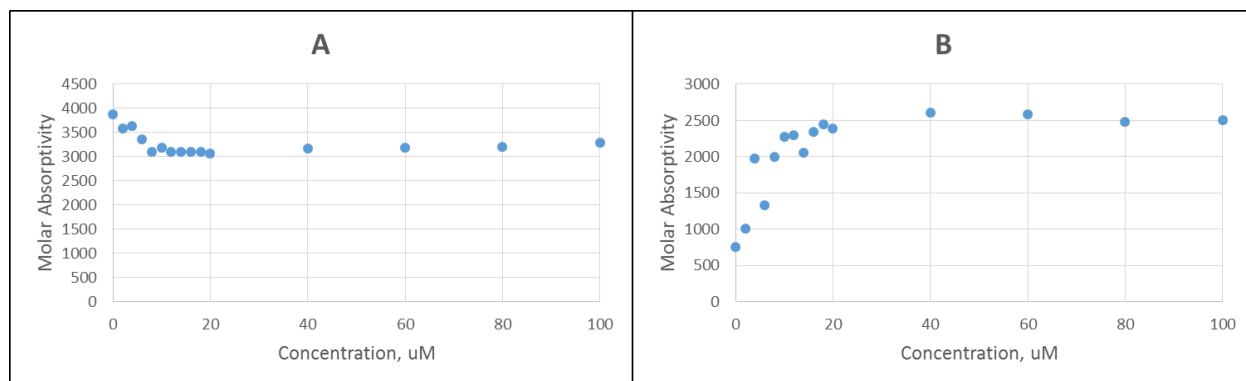
Figure 3.23. The titration curves of extinction coefficient versus metal concentration at A: 403 nm; and B) 430 nm of Salq2/Cu^{2+}.

These samples were allowed to sit for 24 hours and analyzed using fluorescence spectroscopy to determine their emission after excitation at the observed maxima. Upon exciting Salq2 at 386 nm, an emission band at 476 nm, Figure 3.24, was observed. An increase in the concentration of copper metal added to solution resulted in a decrease in the over fluorescence of the ligand at this wavelength. This proves that copper quenches the ligands fluorescence. The emission for the system at the other observed maxima can be viewed in appendix 1.

Figure 3.24 The emission spectrum with excitation at 386 nm of the batch titration of Salq2 with Cu(OAc)$_2$·XH$_2$O in 20% H$_2$O in DMF after 24 hours.

Using a batch titration method, Salq2 was reacted with UO$_2$(OAc)$_2$·2H$_2$O and the UV-Vis absorbance measured. As with Salq1, when introduced to uranyl, no significant absorbance shifts were observed in the spectrum of Salq2 as compared to the free base (Figure 3.25). A maxima at 386 nm (4.7 x 10^3 cm^{-1} M^{-1}) was observed and this was observed to decrease upon the addition of up to 0.3 equivalents of metal; however, after the addition of 0.5 equivalents, an increase in the absorption spectra is observed.   This reaches a maxima with 3 equivalents of uranyl added to every one equivalent of metal (5.3 x 10^3 cm^{-1} M^{-1}). The titration curve shows an increase in molar absorptivity as the metal increases, after an initial decrease in the first 3 additions of equivalents of metal, followed be an overall decrease in molar absorptivity after 2 equivalents. The higher and lower concentration trend lines intercept at 36 µM.
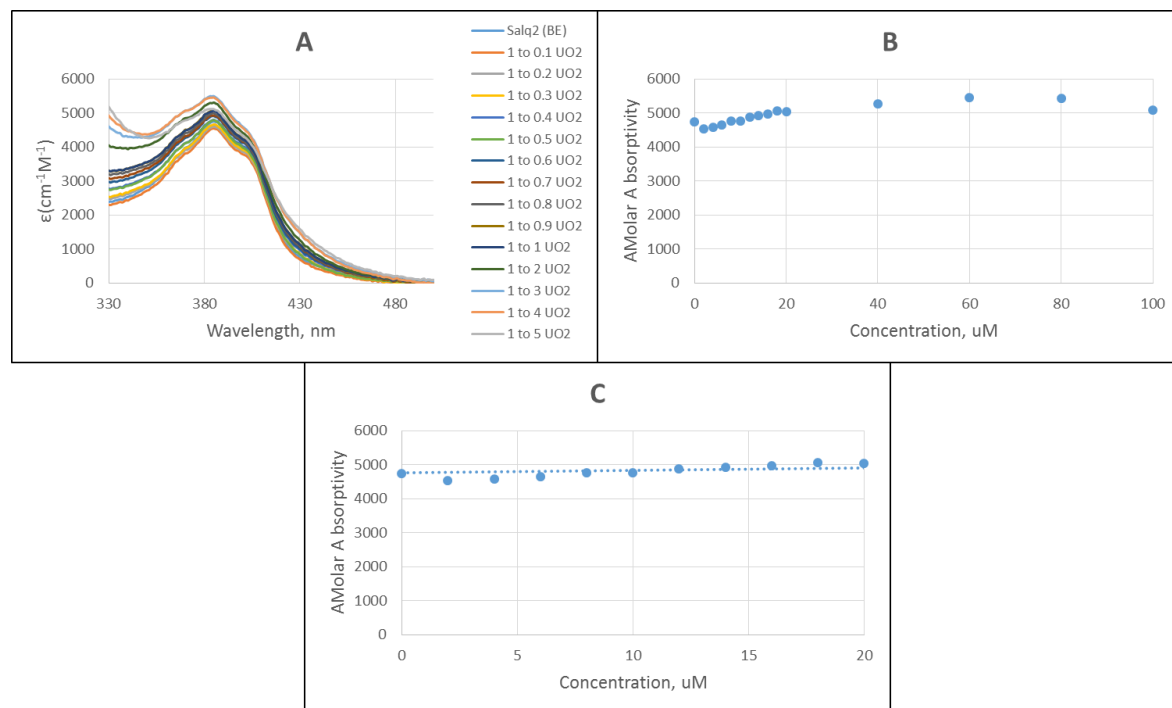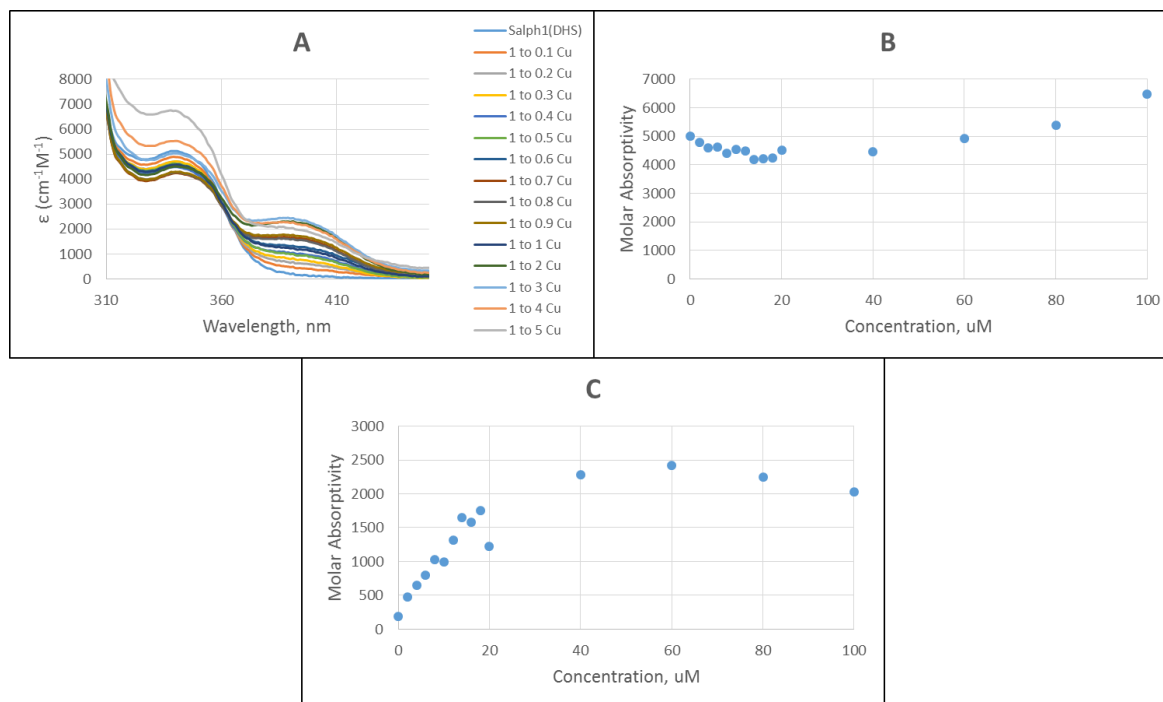
Figure 3.25. A) The change in extinction coefficient of the Salq2 ligand as the solution is titrated with UO_2^{2+} solution. B) The molar absorptivity of Salq2 as the concentration of UO_2^{2+} increases at 386 nm. C) A closer look at the molar absorptivities of Salq2 in the presence of 0-20 μM of uranyl.

These samples were subsequently allowed to sit for 24 hours and subjected to fluorescence spectroscopy to determine their emission after excitation at the observed maxima. An emission band at 476 nm was observed upon exciting Salq2 at 386 nm, as shown in Figure 3.26. The addition of the uranyl solution decreased the fluorescence of the ligand when compared to the free base ligand. When looking at the emission of the solutions containing the uranyl metal solutions, aside from decreasing the fluorescence, there is no direct relationship

between the metal concentration and the amount of fluorescence measured. The emission for the system at the other observed maxima can be viewed in appendix 1.
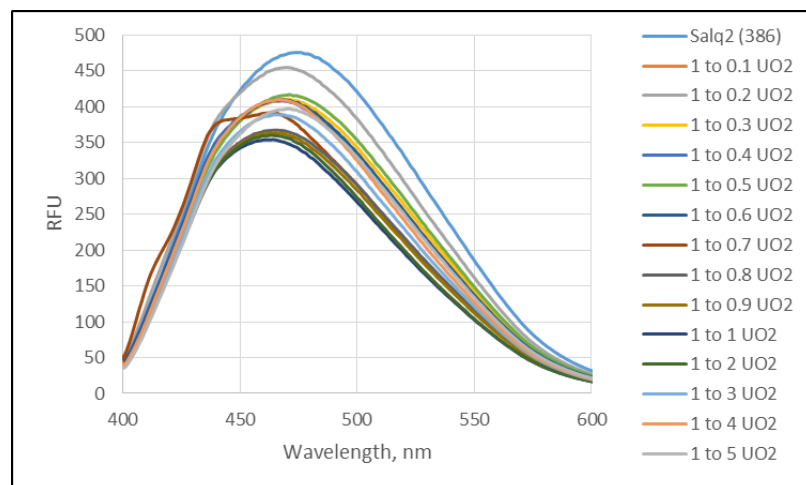
Figure 3.26. The emission spectrum with excitation at 386 nm of the batch titration of Salq2 with $UO_2(OAc)_2 \cdot 2H_2O$ in 20% H_2O in DMF after 24 hours.

2-(1H-imidazo[4,5-b]phenazine-2-yl)phenol (Salph1)

The imidazole obtained from condensing *ortho*-phenylenediamine with 2,5-dihydroxy benzaldehyde, Salph1, was dissolved in DMF, preparing a 20 µM stock solution. A 1 mM stock solution of $Cu(OAc)_2 \cdot XH_2O$ and $UO_2(OAc)_2 \cdot 2H_2O$ metal was also prepared and 14 samples, in which, the ligand concentration was held constant and the concentration of the metal salt increased from 2 µM (1:0.1 Ligand:Metal ratio) to 100 µM (1:5 Ligand:Metal ration), were prepared. The samples were allowed to sit for 5 minutes before being measuring the absorbance. The spectrum for the batch titration with copper solution can be viewed in Figure 3.27. A maximum at 345 nm ($\varepsilon = 5.0 \times 10^3$ cm^{-1} M^{-1}) was observed in the spectra of the free base ligand.

With the addition of the $Cu(OAc)_2 \cdot XH_2O$ aqueous solutions, the lambda max at 345 nm begins to decrease in absorbance, except when 4 and 5 equivalents are added. Along with this decrease, the growth of a peak at 390 nm is observed with the maximum extinction coefficient, $\varepsilon = 2.4 \times 10^3$ cm^{-1} M^{-1}, once 3 equivalents of metal was added. This is a bathochromic shift of 45 nm and is observed in as small 0.1 equivalents of metal ($\varepsilon = 4.7 \times 10^2$ cm^{-1} M^{-1}). Plotting the metal concentration versus the extinction coefficients at the observed lambda max, the molar absorptivity decreases as the concentration of the metal increases. After 1 equivalent of metal is added, the molar absorptivity begins to increase, with an equivalents point occurring at 19.5 μM. At 390 nm, the lambda max of the complex, an increase in molar absorptivity occurs up to 0.9 equivalents of metal. The molar absorptivity of 1 equivalent drops low, before increasing up to 3 equivalents and decreasing again. The interception of the lines occurs at 17 μM of metal.

Figure 3.27. A) The change in extinction coefficient of the Salph1 ligand as the solution is titrated with Cu^{2+} solution. B) The molar absorptivity of Salph1 as the concentration of Cu^{2+} increases at 345 nm. C) The molar absorptivity of Salph1 as the concentration of Cu^{2+} increases at 390 nm.

After 24 hours, the emissions were measured with fluorescence spectroscopy to determine their emission after excitation at the observed maxima. Upon exciting Salph1 at 345 nm, an emission band at 511 nm and 385 nm, Figure 3.28, was observed. Both emission bands decreased with addition of the metal solution, with band at 511 nm becoming completely obsolete after the addition of 0.7 equivalents of copper acetate solution. The band at 385 nm decreases overall, when compared to the free base, but does not display a direct relationship metal concentration and the observed fluorescence. This would suggest that the peak at 385 is

independent to the metal concentration. The emission for the system at the other observed

maxima can be viewed in appendix 1.
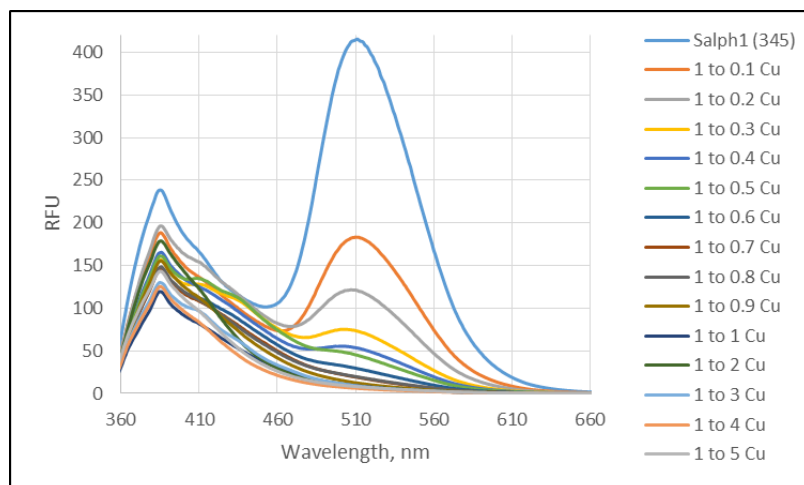
Figure 3.28. The emission spectrum with excitation at 345 nm of the batch titration of Salph1

with $Cu(OAc)_2 \cdot XH_2O$ in 20% H_2O in DMF after 24 hours.

Following the same batch titration method, Salph1 and $UO_2(OAc)_2 \cdot 2H_2O$ were reacted.

Although the spectrum, Figure 3.29, observed after titrating with uranyl acetate did not show any

shifts in the lambda max value of seen in the spectra of the free base, the addition of the uranyl

metal solution increases the absorbance of the system in every concentration except that of the

1:1 solution (4.7×10^3 cm^{-1} M^{-1}) with a maximum found 7.5×10^3 cm^{-1} M^{-1} when 5 equivalents

of metal was added. The titration curve shows a linear relationship between the extinction

coefficient and concentration between 3 and 5 equivalents of metal, which increases with the

increase of the metal concentration; however, no intercept between the trend line of the higher

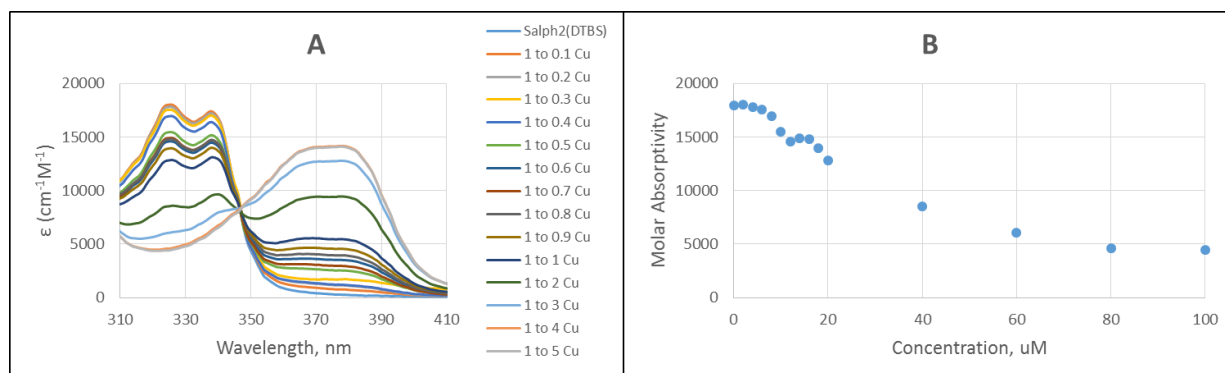and lower concentrations occurred.
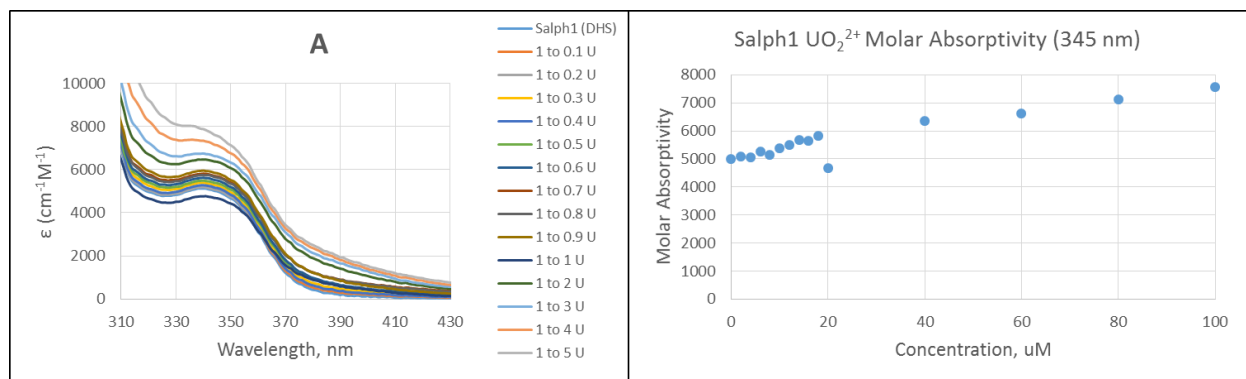
Figure 3.29. A) The change in extinction coefficient of the Salph1 ligand as the solution is titrated with UO_2^{2+} solution. B) The molar absorptivity of Salph1 as the concentration of UO_2^{2+} increases at 345 nm.

As with the other ligands, these samples were then allowed to sit for 24 hours before being characterized using fluorescence spectroscopy to determine their emission after excitation at the observed maxima. Upon excitation at 345 nm, an emission band at 511 nm and 385 nm was observed, as shown in Figure 3.30, the same as the copper spectrum. Unlike the copper reaction, the peak at 511 nm does not quench completely, but does decrease as the concentration of metal increases. As with the copper reaction, the band at 385 nm appears to have no direct relationship between metal concentration and fluorescence ability. The emission for the system at the other observed maxima can be viewed in appendix 1.
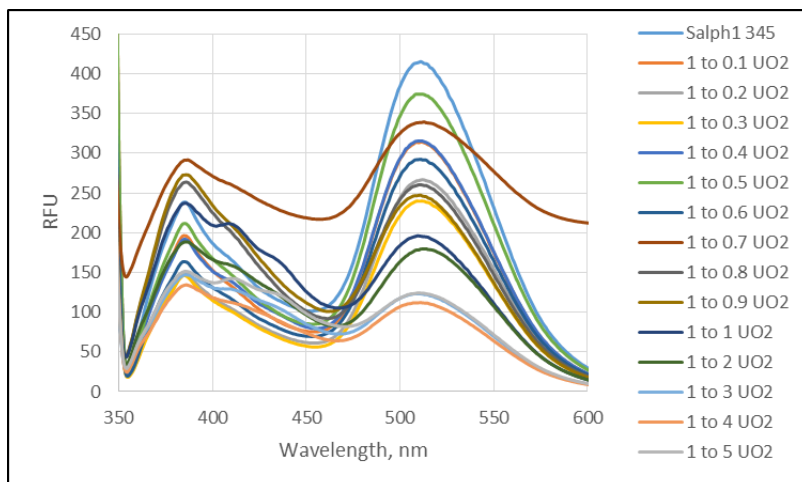
Figure 3.30 The emission spectrum with excitation at 349 nm of the batch titration of Salph1 with $UO_2(OAc)_2 \cdot 2H_2O$ in 20% H_2O in DMF after 24 hours.

2-(1H-imidazo[4,5-b]phenazine-2-yl)phenol (Salph2)

A 20 µM stock solution of the imidazole obtained from condensing *ortho*-phenylenediamine with 3,5-ditertbutylsalicylaldehyde, Salph2, was dissolved in DMF. As with the prior ligands, a 1 mM stock solution of $Cu(OAc)_2 \cdot XH_2O$ and a 1mM $UO_2(OAc)_2 \cdot 2H_2O$ stock solution were prepared and 14 samples, in which, the ligand concentration was held constant and the concentration of the metal salt increased from 2 µM (1:0.1 Ligand:Metal ratio) to 100 µM (1:5 Ligand:Metal ration), were prepared. The samples were allowed to sit for 5 minutes before being measuring the absorbance. The spectrum resultant from this reaction with the copper solution can be viewed in Figure 3.31. A maximum at 325 nm ($\varepsilon = 1.8$ x 10^4 cm^{-1} M^{-1}), with a shoulder at 338 nm ($\varepsilon = 1.7$ x 10^4 cm^{-1} M^{-1}), was observed in the spectrum of the free base ligand. With the addition of the $Cu(OAc)_2 \cdot H_2O$ aqueous solutions, both peaks begin to decrease and become absent on the spectra of 4 equivalents of metal. A bathochromic shift 44

132

and 42 nm is observed in the spectra with as low as 0.3 equivalence results in peaks at 369 and 380 nm and begin appearing on the 1:0.2 spectra. These extinction coefficients increase to 1.4 x 10^4 cm^{-1} M^{-1} at both wavelengths with the addition of 5 equivalents of the copper metal solution. Plotting the metal concentration versus the extinction coefficients at the observed lambda max, it was determined that at 325 nm, an intercept between the high concentrations of metal and the low concentrations occurs at 32 µM metal. This concentration is the intercept for all observed lambda max.

Figure 3.31. A) The change in extinction coefficient of the Salph2 ligand as the solution is titrated with Cu^{2+} solution. B) The molar absorptivity of Salph2 as the concentration of Cu^{2+} increases at 325 nm.

The resulting spectra of Sal2/UO$_2$$^{2+}$ at 382 nm shows that molar absorptivity increased in a linear fashion at the lower end of the metal concentration measurements. Ratios 1:0.6 to 1:0.9 between the ligand and metal increase linearly. At 435 nm, the linear relationship can be seen between the molar absorptivity and the metal concentration between 0.4 to 0.9 uM, as well as,

1:3 to 1:5 ratios. The molar absorptivity decreases in a linear fashion between 1:0.6 and 1:1 at 481 nm.
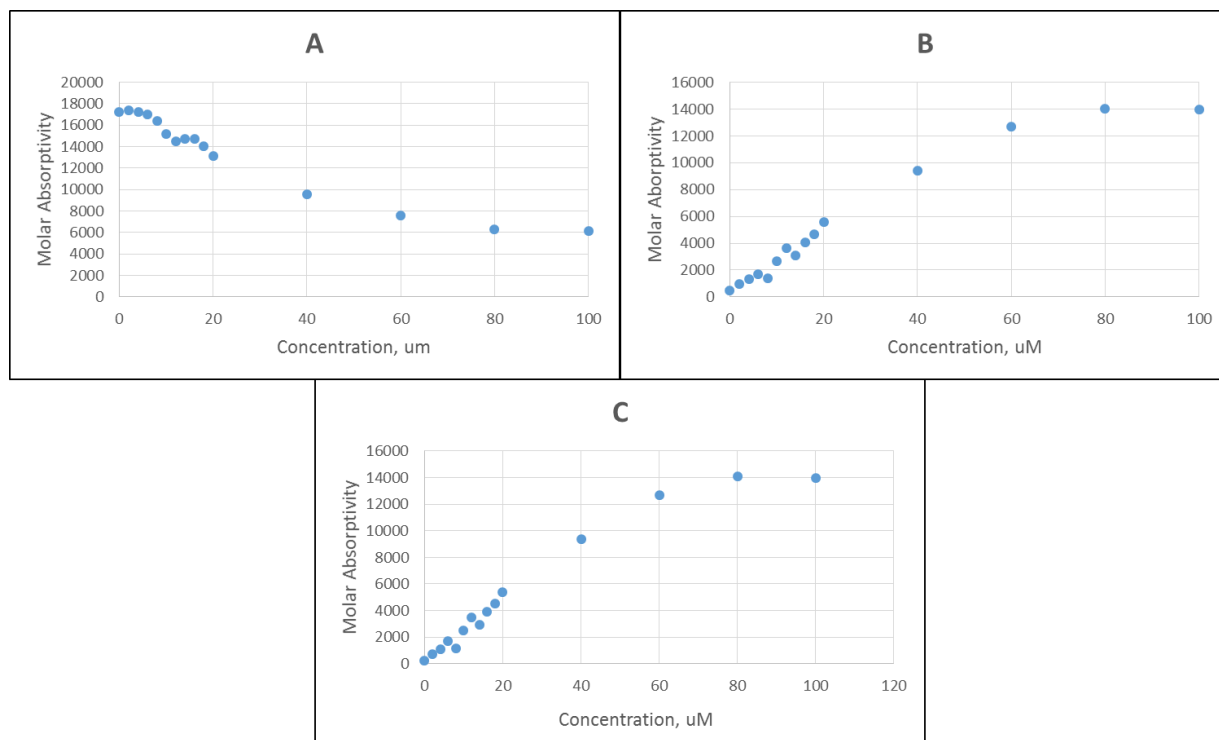
Figure 3.32. Figure 3.34. The titration curves of Salph2 ligand titrated with Cu^{2+} at A) 338 nm; B) 369 nm and C) 380 nm.

After 24 hours, these samples were characterized with fluorescence spectroscopy to determine their emission after excitation at the observed maxima. Upon exciting Salph1 at 325 nm, an emission band at 486 nm, Figure 3.33, was observed. Upon the addition of the copper solution, the emission quenches substantially as the amount of copper concentration increases. The emission for the system at the other observed maxima can be viewed in appendix 1.
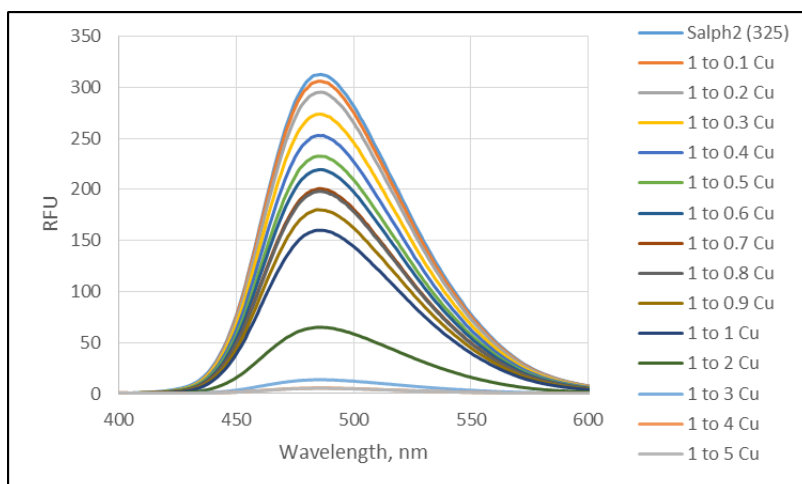
Figure 3.33 The emission spectrum with excitation at 325 nm of the batch titration of Salph2 with Cu(OAc)$_2$·XH$_2$O in 20% H$_2$O in DMF after 24 hours.

When UO$_2$(OAc)$_2$·2H$_2$O was the metal salt added, an immediate decrease in the maxima at 325 and 338 nm is observed in the spectra of Salph2, figure 3.34. Upon increasing the metal concentration, the extinction coefficient begins to increase and maxes out with the addition of 5 metal equivalents at both wavelengths. The titration curve, although an intercept between the lower and higher concentrations was not found, shows that between 3 and 5 equivalents of metal, there is a linear increase in the molar absorptivity of the ligand. The relationship between the metal concentration and extinction coefficient of the ligand at all observed maxima can be seen in the same figure. The extinction coefficient of Salph2/UO$_2^{2+}$ at 338 nm indicated that molar absorptivity increased in a linear fashion at the higher end of the metal concentration, 1:3 to 1:5 (ligand to metal).
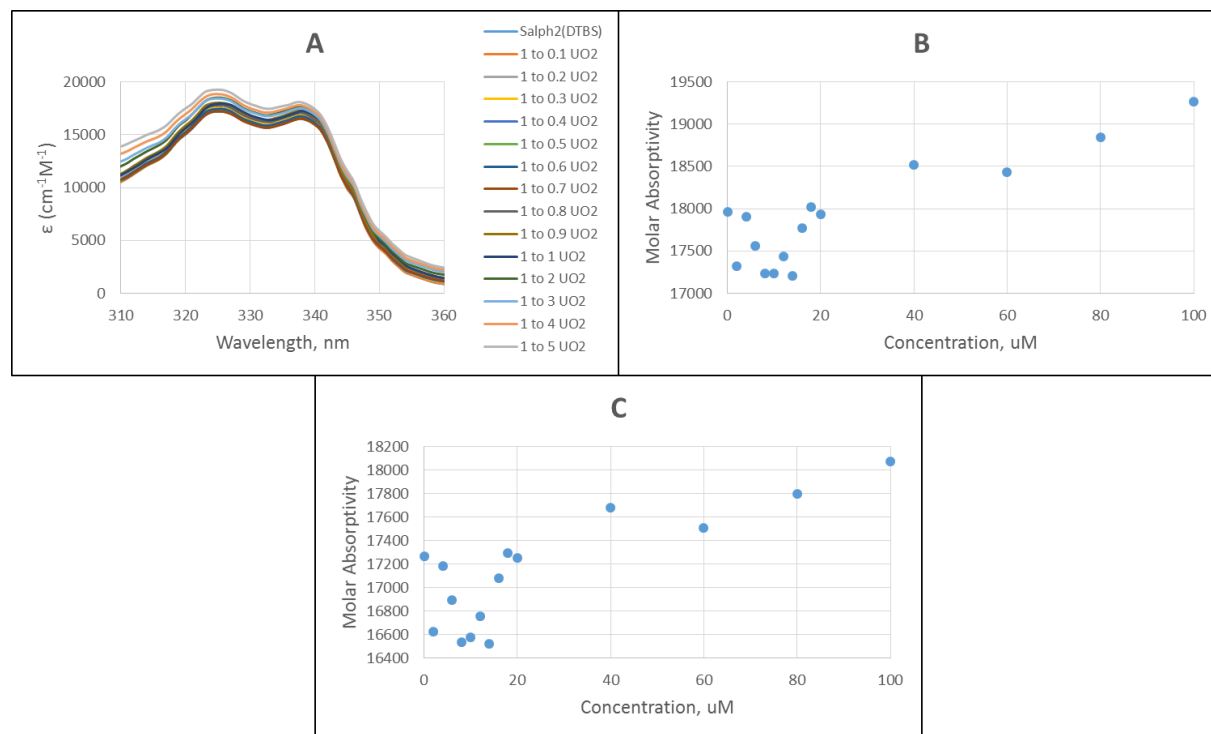
Figure 3.34. A) The change in extinction coefficient of the Salph2 ligand as the solution is titrated with UO_2^{2+} solution. B) The molar absorptivity of Salph2 as the concentration of UO_2^{2+} increases at 325 nm. C) The molar absorptivity of Salph2 as the concentration of UO_2^{2+} increases at 338 nm.

As with the copper reactions, these samples were then allowed to sit for 24 hours and characterized with fluorescence spectroscopy to determine their emission after excitation at the observed maxima. Upon excitation at 325 nm, an emission band at 486 nm was observed, as shown in Figure 3.35. The addition of the uranyl solution quenches the fluorescence of the ligand. This was also observed when looking solely at the solutions with uranyl present, although a total quenching of the ligand may not be obtained. The emission for the system at the other observed maxima can be viewed in appendix 1.
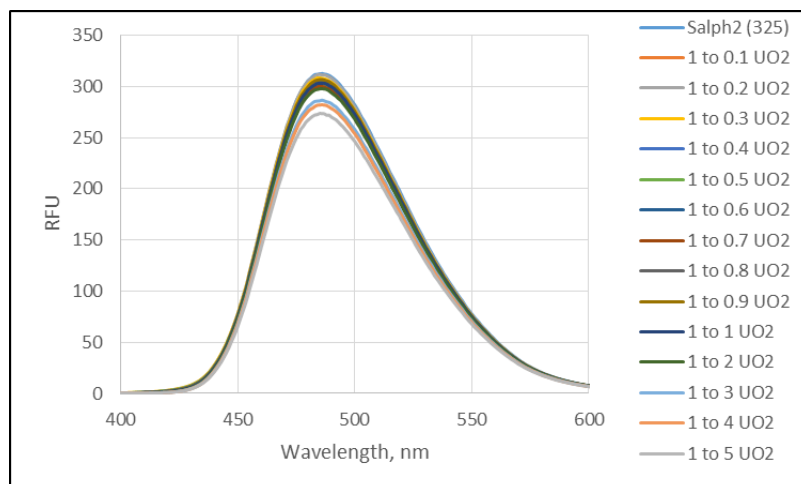
Figure 3.35 The emission spectrum with excitation at 325 nm of the batch titration of Salph2 with $UO_2(OAc)_2 \cdot 2H_2O$ in 20% H_2O in DMF after 24 hours.

Conclusions

The development of a rapid detection method for uranyl was the ultimate goal of this project. In our search for developing an organic ligand that is easily synthesized and readily detects uranyl, giving an indication via a color change or shift in the spectra, the phenazine derived imidazoles are the only two ligands that granted these specifications. Both ligands had observed shifts in their absorbance spectra when titrated with uranyl, these shifts were different from those of the batch titration with copper acetate, making them distinguishable. Sal1, the ligand in which no R-groups are present on the aryl substituent of the imidazole, had the lowest detection in regards to uranyl, with spectral changes occurring in solutions with as low as 0.1 uranyl metal equivalents. With the ease of preparing the ligand in one step with commercially produced chemicals, this ligand could very well be used as a uranyl detector. In the future,

incorporating these ligands onto a solid substrate will allow them to be employed as a solid phase

extractor. Overall, it was observed that both ligands could serve as rapid detectors for uranyl.

References

1. Sondhi, S. M.; Singh, J.; Roy, P.; Agrawal, S. K.; Saxena, A. K. Med. Chem. Res. 2010, 20, 887; Sondhi, S. M.; Arya, S.; Rani, R.; Kumar, N.; Roy, P. Med. Chem. Res. 2011, 21, 3620.

2. Tong, Y.-P.; Zheng, S.-L.; Chen, X.-M. Eur. J. Inorg. Chem. 2005, 2005, 3734.

3. Boudalis, A. K.; Clemente-Juan, J. M.; Dahan, F.; Psycharis, V.; Raptopoulou, C. P.; Donnadieu, B.; Sanakis, Y.; Tuchagues, J.-P. Inorg. Chem. 2008, 47, 11314.

4. Maurya, M. R.; Kumar, M.; Kumar, U. J. Mol. Catal. A: Chem. 2007, 273, 133.

5. Ouyang, J.; Hong, H.; Shen, C.; Zhao, Y.; Ouyang, C.; Dong, L.; Zhu, J.; Guo, Z.; Zeng, K.; Chen, J.; Zhang, C.; Zhang, J. Free Radical Biol. Med. 2008, 45, 1426; Gao, G.-y.; Qu, W.-j.; Shi, B.-b.; Zhang, P.; Lin, Q.; Yao, H.; Yang, W.-l.; Zhang, Y.-m.; Wei, T.-b. Spectrochimica Acta Part A: Molecular and Biomolecular Spectroscopy 2014, 121, 514.

6. Prakash, S. M.; Jayamoorthy, K.; Srinivasan, N.; Dhanalekshmi, K. I. J. Lumin. 2016, 172, 304.

7. Liang, W.; Zhao, Z.; Zhang, Y.; Wang, Q.; Zhao, X.; Ouyang, J. J. Lumin. 2012, 132, 1160-1165.

8. Zhang, S. Y.; Ong, C. N. Shen, H. M. Cancer Lett. 2004, 208, 143.

9. Kamtekar, K. T.; Monkman, A. P.; Bryce, M. R. Adv. Mat. 2010, 5, 572.

10. Chang, Y-L.; Lu, Z-H. J. Disp. Tech. 2013, 99, 1.

11. Evans, R. C.; Douglas, P.; Winscom, C. J. Coord. Chem. Rev. 2006, 250, 2093.

12. Sutton, C.; Risko, C.; Bredas, J-L. Chem. Mater. 2016, 28, 3.

13. Katkova, M. A.; Balashova, T. V.; Ilichev, V. A.; Konev, A. N.; Isachenkov, N. A.; Fukin, G. K.; Ketkov, S. Y.; Bochkarev, M. N. Inorg. Chem. 2010, 49, 5094; Katkova, M. A.; Pushkarev, A. P.; Balashova, T. V.; Konev, A. N.; Fukin, G. K.; Ketkov, S. Y.; Bochkarev, M. N. J. Mater. Chem. 2011, 21, 16611.

14. Katkova, M. A.; Balashova, T. V.; Ilichev, V. A.; Konev, N. A.; Isachenkov, G. K.; Fukin, S. Y.; Bochkarev, M. N. Inorg. Chem. 2010, 49, 5094.

15. Wu, X.; Gorden, A. E. V.; Tonks, S. A.; Vilseck, J. Z. J. Org. Chem. 2007, 72, 8691.

16. Mosquera, M.; Penedo, J. C.; Ríos Rodríguez, M. C.; Rodríguez-Prieto, F. The Journal of Physical Chemistry 1996, 100, 5398; Chipem, F. A. S.; Krishnamoorthy, G. J. Phys. Chem. B 2013, 117, 14079.

Chapter 4: Simple Thorium Salts for Catalysis

This work was published in part previously in Maynard, B. A.; Tutson, C. D.; Lynn, K. S.; Pugh, C. W.; Gorden, A. E. V. *Tetrahedron Lett.* **2016**, *57*, 472-475.

Introduction

Interest in the early 5f elements has recently had a resurgence thanks in part for their use in catalysis or metal mediated synthesis.[1-6] The large ionic radii and 5f valence orbitals of actinides offers distinguishing chemical characteristics, for example, large coordination numbers and unique coordination geometries[7], that can be of unique use in applications in catalysis.[8] The exploration of synthetic methods[3,4,9,10] or catalytic reactions[2,5,11,12] reported that incorporate actinide metals are becoming more common as new starting materials have been developed.[13-15] One example of this is the use of thorium catalysts in the cyclization and hydroalkoxylation of alkynyl alcohols,[2] and also the use of thorium or uranium Cp* complexes for ring-opening metathesis in the polymerization of cyclic esters.[12] Most of this work is focused on the use of an actinide center saddled with sterically hindered ligands (such as cyclopentadiene,[14] pentamethyl cyclopentadienyl, or N-ethylmethylamine[12,16]), although Collin et al. has reported the use of UI_3 to catalyze Diels-Alder reactions and Mukaiyama aldol reactions.[17,18] The ligand and metal are covalently bound to some degree, and the reactivity of these ligand-actinide complexes and their mechanisms of action have not been fully explained.[12,16] For example, Arnold and coworkers have used an organothorium metallacycle precatalyst, $[(Me_3Si)_2N]Th[k_2-(N,C)-CH_2Si(CH_3)N(SiMe_3)]$, to regioselectively oligomerize terminal alkynes and produce organic enynes. This is remarkable, and demonstrates the first example of using a Th(IV) catalyst such as this in C-C bond formation.[19] The development of these methods has aided in the understanding of the chemistry of the actinides; however, as catalysts, they require laborious preparation and,

being either air or moisture sensitive, have short shelf-lives. In contrast to these organometallic type catalysts, simple actinide salts offer longer shelf-lives, lower sensitivity, and increased ease of use. They are commercially available, and still have as yet to be characterized.

The aromatic 2,3-diaminophenazine (DAP) is a heterocycle that is of interest due to its application in the self-assembly of nanobelts,[12] and has typically been prepared through the use of H_2O_2 catalysis with horseradish peroxidase and fungal laccase enzymes.[21] Li and co-workers took advantage of the electroactivity of DAP when using the rapid oxidation of OPD to DAP by cupric ion-catalysis to synthesize electroactive nanoparticles that were then able to be used to dope a graphene nanolabel. This graphene nanolabel was subsequently coupled with a peptide-based probe to target SMO, a protein connected to metastatic tumor cells that is used as a biomarker, to determine the metastatic activity of tumor cells.[22]   Non-biological synthetic pathways are known, including catalysis by Fe(III), Co(II), and Cu(II) metal salts.[20,24,25] We noted that the unencumbered 5f orbitals of actinide salts offers another non-biological pathway to catalyze this synthesis. Previous work in conducted in the Gorden lab proved that simple actinide salts were capable of oxidizing OPD into DAP. Here, we describe the thorium nitrate, uranyl nitrate, and oxygen mediated synthesis of 2,3-diaminophenazine from *ortho*-phenylenediamine (OPD), Scheme 4.1. Of note, simple, sterically unencumbered actinide centers have rarely been reported in the literature.[18,19] Few reactions have been reported with simple actinide salts,[18,19] most of these are based on using the metal salt as a strong Lewis acid, and no catalytic reactions have been reported using simple thorium salts prior to date.

In continuing with the exploration of 5f elements to better elucidate additional information about their chemical characteristics and capabilities, thorium nitrate was employed as a catalyst in the coupling of *ortho*-phenylenediamine (OPD) to produce 2,3-diaminophenazine

(DAP). This chapter will explore the optimization of conditions and mechanistic exploration of the roles reagents played in the reaction.
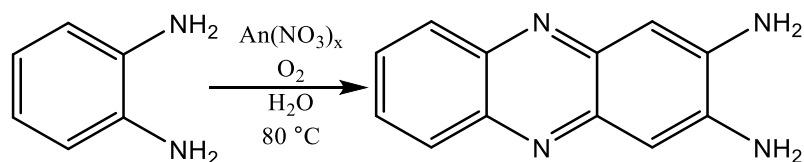
Scheme 4.1. The oxidative coupling of *ortho*-phenylenediamine

Caution! The U and Th are radioactive, heavy metals and require special precautions and waste handling.

General Procedure for 2,3-Diaminophenazine

Ortho-phenylenediamine (OPD), 0.4324 g (4 mmol), was heated at 80° C in a 100 ml round bottom flask containing a stir bar and 100 ml of deionized H_2O as solvent. Once the OPD dissolved, an appropriate volume of a stock actinide starting material solution was added to the mixture to allow a 1% catalyst loading (Th(NO$_3$)$_4$:OPD). The reaction was allowed to stir and heat at 80° C. Once the experiment time had lapsed; the solution was filtered, the solid was washed with hexanes, and dried in a vacuum oven. Mass spectrometry M+1 211.0961 (found) 210.0905 (calculated) was obtained 1H NMR (400 MHz, C2D6OS) δ7.90-7.86 (2H, m) δ7.57-7.52 (2H, m) δ6.8987 (2H, s) δ6.26 (4H, s)

General Procedure for Aromatic Derivatives

In a typical procedure, 4 mmol of substrate(s) was heated at 80° C in a 250 ml round bottom flask with a stir bar and 100 ml of deionized H_2O as solvent. Once the substrate was dissolved, 1 mol% of Th(NO$_3$)$_3$ was added to the mixture. The reaction was allowed to stir and

heated to 80° C. When the experiment time had lapsed; the solution was filtered, the solid was washed with hexanes, and dried in a vacuum oven.

Results and Discussion

While probing the oxidation of OPD to DAP, it was found that the reaction can proceed solely in the presence of oxygen to produce 2,3-diaminophenazine, as shown in Figure 4.1. With the addition of uranyl nitrate ($UO_2(NO_3)_2$) or thorium nitrate ($Th(NO_3)_4$) as simple salt catalyst, the oxidation of OPD to DAP increases by a factor of 1.5 and 2, respectively, while still in the presence of oxygen. When compared to the same oxidation in which $FeCl_3$ was employed as the catalyst, the reaction proceeds at a much slower rate, however the simple actinide salts require a 1% catalyst loading and the $FeCl_3$ demands an 80% loading.[20] The addition of the actinide salts allow for metal mediation for the oxidative generation of DAP, which increases with a higher concentration of Th^{4+}. The oxidation of OPD to produce DAP in the presence of oxygen, coupled with the increase yield when both the actinide and oxygen are present proves that there is a synergistic behavior between the two reagents.
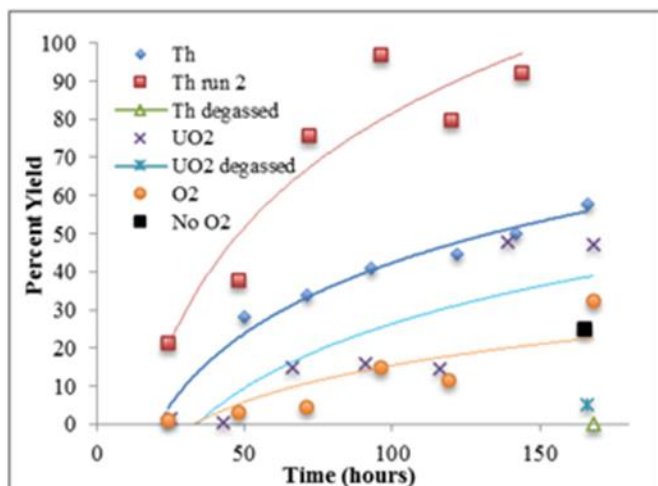
Figure 4.1. Percent yield of the oxidative coupling of *ortho*-pheynlenediamine.

The influence of dioxygen in the mechanism of the oxidation reaction was explored using two reactions that were prepared and allowed to react for seven days, Figure 4.2. The first reaction was performed in a Schlenk flask containing the reagents and $Th(NO_3)_4$ as the actinide source, but the solution was degassed. The reaction solution was bubbled with Argon for two hours before undergoing three cycles of freeze-pump-thaw to remove all possible traces of O_2. This removes as much dioxygen as possible. In the second reaction, utilizing the same parameters and degassing the solvent, $UO_2(NO_3)_2$ was the actinide source. After 7 days, no observable precipitate was present in the reaction flask containing the $Th(NO_3)_4$ in the degassed solution, and no color change was observed. Upon workup and analysis, no phenazine was detected. The reaction flask with $UO_2(NO_3)_2$ was found to contain 5.2 % yield of isolable 2,3-diaminophenazine. These results indicate that the presence of dioxygen, is indeed required for the efficient oxidation.[17]

To get a greater understanding of just how vital oxygen was to the reaction, a third reaction was explored. In this case, a Schlenk flask was set up containing only an aqueous

145

solution of *ortho*-phenylenediamine and not actinide source. This reaction was then bubbled

with Argon for two hours before undergoing three cycles of freeze-pump-thaw to remove all

possible traces of O_2. Upon the completion of the 96 hours and work up, a 25% yield of 2,3-

diaminophenazine was produced. This relatively low yield without the presence of O_2 is

evidence that an oxygen donor in the reaction participates in the reaction pathway. In this case,

the oxygen in the solvent served as the oxidant. It is important to point out that the only two

reagents present in this reaction were water and OPD, in which a thorough literature search

resulted in us being unable to find any previous reports on the temperature induced oxidation of

ortho-phenylenediamine in an inert atmosphere.
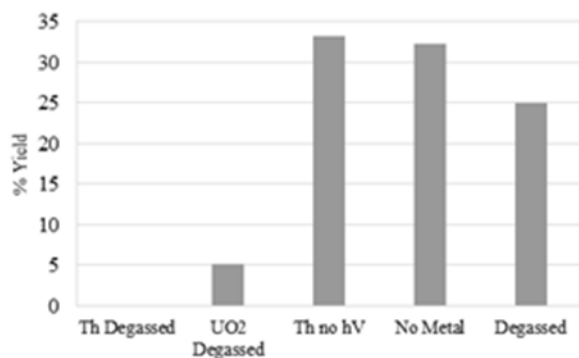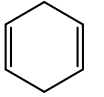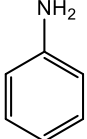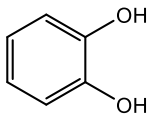
Figure 4.2. Percent yield of oxidative *ortho*-phenylenediamine coupling with varying conditions.

Without any prior reports of the oxidative coupling of *ortho*-phenylenediamine to

produce 2,3-diaminophenazine to compare our findings to, a deeper look into the roles of the

reagents was taken. A few questions remained to be explored include: 1) does the reaction

proceed through interactions with pi orbitals of *ortho*-phenylenediamine? Or 2) does it proceed

through interaction with the lone pairs of the amines that are present on the *ortho*-

phenylenediamine? Or 3) does it proceed through interaction of both the pi orbitals and lone

pairs?

To determine this, various substrates were subjected to the same reaction parameters of

the highest yielding actinide catalyzed reaction. The parameters included using $Th(NO_3)_4$ as the

actinide source, water as the solvent, and allowing the reaction to react for 96 hours at room

temperature, as shown in Table 4.1. In exploring the importance of the pi orbitals, the substrates

employed were cyclohexene, benzene, and 1,4-cyclohexadiene. To demonstrate the importance

of lone pairs, the substrates utilized were aniline and catechol. The substrates were subjected to

oxidative coupling conditions to see if the conditions could facilitate the coupling of substrates.

After the 96 hours were complete, results show that thorium (IV) nitrate was proven to be of

little use as a catalyst in the oxidative coupling of the substrates under these conditions. Nuclear

magnetic resonance and mass spectrometry confirmed only the presence of the starting materials.
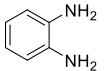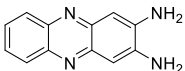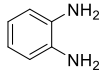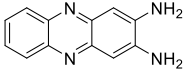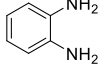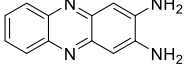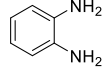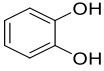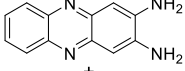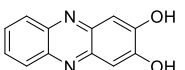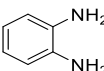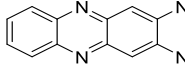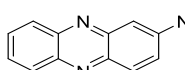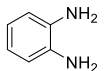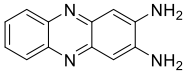
Table 4.1. Metal catalyzed oxidative coupling of various substrates to test the scope of the reaction.

Entry	Reagent	Catalyst	Time(hrs)	Product Recovered
1	(cyclohexene structure)	$Th(NO_3)_2$	96	Starting Material
2	(benzene structure)	$Th(NO_3)_2$	96	Starting Material
3	(cyclohexadiene structure)	$Th(NO_3)_2$	96	Starting Material
4	(aniline structure, NH₂)	$Th(NO_3)_2$	96	Starting Material
5	(catechol structure, OH OH)	$Th(NO_3)_2$	96	Starting Material

Along with exploring the scope of the reaction and thorium (IV) nitrate's ability to oxidatively couple other substrates, determining if the oxidative coupling of *ortho*-phenylenediamine is favored was explored. To do this, the substrates were reacted with OPD under the same conditions and the results can be viewed in Table 4.2. The reactions involving For a majority of the reactions in which *ortho*-phenylenediamine was present, the only product detected was 2,3-diaminophenazine in yields up to 64%. Mass spec analysis supported the reaction between *ortho*-phenylenediamine with aniline and *ortho*-phenylenediamine with catechol were catalyzed. In both cases, however, 2,3-diaminophenazine was also synthesized and NMR analysis did not support the presence of the aniline/*ortho*-phenylenediamine product.

Thus, for thorium (IV) nitrate reactions, what was observed is better suited to electron rich environments.

Table 4.2. Metal catalyzed oxidative coupling of varying benzene derivatives with *ortho*-phenylenediamine.

Entry	Substrate A	Substrate B	Catalyst	Catalyst Loading	Temp	Time	Product	Isolated Yield(%)
1	(o-phenylenediamine, NH₂/NH₂)	(cyclohexene)	Th(NO₃)₄	0.04 mmol	80	96	(phenazine-NH₂/NH₂)	39.52
2	(o-phenylenediamine, NH₂/NH₂)	(benzene)	Th(NO₃)₄	0.04 mmol	80	96	(phenazine-NH₂/NH₂)	57.38
3	(o-phenylenediamine, NH₂/NH₂)	(cyclohexadiene)	Th(NO₃)₄	0.04 mmol	80	96	(phenazine-NH₂/NH₂)	64.29
4	(o-phenylenediamine, NH₂/NH₂)	(catechol, OH/OH)	Th(NO₃)₄	0.04 mmol	80	96	(phenazine-NH₂/NH₂) + (phenazine-OH/OH)	29.76*
5	(aniline, NH₂)	(o-phenylenediamine, NH₂/NH₂)	Th(NO₃)₄	0.04 mmol	80	96	(phenazine-NH₂/NH₂) + (phenazine-NH₂)	38.1
6	(o-phenylenediamine, NH₂/NH₂)	(cyclohexene)	Fe(NO₃)₃	0.04 mmol	80	96	(phenazine-NH₂/NH₂)	15.95

Conclusion

In an age where green chemistry is highly sought after, it is difficult to argue that incorporating actinide ions into reaction pathways might result in reaction conditions that allow for mild reaction conditions, safer solvents, and catalysis with good turnover as outlined by in the principles of Green Chemistry as outlined so well by Anastas and Warner.[28] These observations do engage the idea of using the depleted actinide reserve, such as depleted ^{238}U, as a source for new routes of metal mediation. Previous reports in the literature of phenazine

149

prepared in this fashion feature metals that are able to go through one electron oxidations [Cu(II) and Co(II)], and the proposed mechanisms involved μ-dioxygen with hydrogen peroxide evolution, the Cu(II) does not clearly report the catalyst loading and the Co(II) catalyst loading was much higher, 50%.[20] In our reaction 40% loading is required for that same yield with the Cu(II) salts. The mechanism observed in that reaction would be highly unlikely here for either the Th^{4+} or the UO_2^{2+} ions, as both metal centers contain complete electronic shells (K, L, M and N); also neither ion possess paired or unpaired electrons in the O shell. Future work will pursue computation analyses to determine what might be a more reasonable mechanism.

References

1. Barnea, E.; Eisen, M. S. Coord. Chem. Rev. 2006, 250, 855.

2. Wobser, S. D.; Marks, T. J. Organometallics 2013, 32, 2517.

3. Weiss, C. J.; Marks, T. J. Dalton Trans. 2010, 39, 6576.

4. Weiss, C. J.; Wobser, S. D.; Marks, T. J. Organometallics 2010, 29, 6308.

5. Stubbert, B. D.; Marks, T. J. J. Am. Chem. Soc. 2007, 129, 4253.

6. Fox, A. R.; Bart, S. C.; Meyer, K.; Cummins, C. C. Nature (London, U. K.) 2008, 455, 341.

7. Tutson, C. Gorden, A. E. V. Chem. Coor. Rev. 2017, 333, 27.

8. Andrea, T.; Eisen, M.S. Chem. Soc. Rev., 2008, 37, 550-567.

9. Schelter, E. J.; Morris, D. E.; Scott, B. L.; Kiplinger, J. L. Chem. Commun. (Cambridge, U. K.) 2007, 1029.

10. Kiplinger, J. L.; Pool, J. A.; Schelter, E. J.; Thompson, J. D.; Scott, B. L.; Morris, D. E. Angew. Chem., Int. Ed. 2006, 45, 2036.

11. Hayes, C. E.; Platel, R. H.; Schafer, L. L.; Leznoff, D. B. Organometallics 2012, 31, 6732.

12. Barnea, E.; Moradove, D.; Berthet, J.-C.; Ephritikhine, M.; Eisen, M. S. Organometallics 2006, 25, 320.

13. Foyentin, M.; Folcher, G.; Ephritikhine, M. J. Chem. Soc., Chem. Commun. 1987, 494.

14. Kiplinger, J. L.; Morris, D. E.; Scott, B. L.; Burns, C. J. Organometallics 2002, 21, 5978.

15. Eisen, M. S.; Marks, T. J. J. Mol. Catal. 1994, 86, 23.

16. Andrea, T.; Barnea, E.; Eisen, M. S. J. Am. Chem. Soc. 2008, 130, 2454.

17. Collin, J.; Maria, L.; Santos, I. J. Mol. Catal. A: Chem. 2000, 160, 263.

18. Giuseppone, N.; Van De Weghe, P.; Mellah, M.; Collin, J. Tetrahedron 1998, 54, 13129.

19. Batrice, R.J.; McKniven, J.; Arnold, P.L.; Eisen, M.S. Organometallics 2015, 34, 4039.

20. He, D.; Wu, Y.; Xu, B.-Q. Eur. Polym. J. 2007, 43, 3703.

21. Niu, S.Y.; Zhang, S.S.; Ma, L.B.; Jiao, K. Bull. Korean Chem. Soc. 2004, 25, 829.

22. Li, H.; Huang, Y.; Yu, Y.; Li, W.; Yin, Y.; Li, G. Anal. Chem. 2015, Ahead of Print, DOI: 10.1021/acs.analchem.5b01750

23. Zhou, P.; Liu, H.; Chen, S.; Lucia, L.; Zhan, H.; Fu, S. Molbank 2011, M730.

24. Nemeth, S.; Simandi, L. I.; Argay, G.; Kalman, A. Inorg. Chim. Acta 1989, 166, 31.

25. Peng, S. M.; Liaw, D. S. Inorg. Chim. Acta 1986, 113, L11.

26. Rosso, N. D.; Szpoganicz, B.; Martell, A. E. Inorg. Chim. Acta 1999, 287, 193.

27. Morss, L.; Edelstein, N. M.; Fuger, J. The Chemistry of the Actinide and Transactinide Elements Springer, 2006; Vol. 1.

28. Anastas, P. T.; Warner, J. C. Green Chemistry: Theory and Practice; Oxford University Press: New York, 1998.

Chapter 5: Conclusions and Future Work

Functionalized M-PVA for Metal Detection
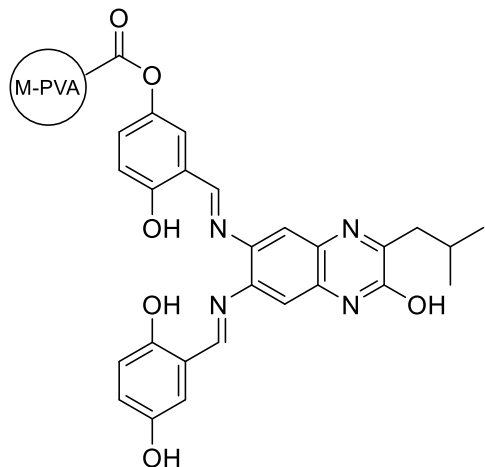
Figure 5.1. The heterogeneous ligand, HL.

The ease of preparing HL, figure 5.1, has made it a viable option to serve as a solid phase extractor for uranyl. Replacing the water sensitive DIC with water-soluble EDC removed the need to use dry DMF and aided in the ease of HL preparation. Along with this, the ability to use a magnet to remove (figure 5.2) HL from the extraction solution allows for the use of a mono-phase system, water in this case. In the past, bi-phase systems have typically been used, with an organic solvent serving as the second solvent. No longer requiring a bi-phase system allows for aqueous solutions that are closer to mimicking uranyl in the environment, as well as, a greener approach without the need for organic solvents.
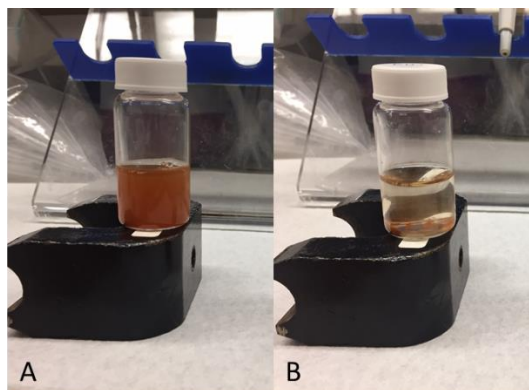
Figure 5.2. Removal of HL from uranyl metal solution with ligand. The time difference between A and B is 12 seconds.

Results presented here demonstrate that the optimum ligand:metal (HL to UO_2^{2+}) ratio was 1:1 to remove uranyl from the solution and an agitation time of 60-120 minutes. In the presence of another metal, copper as copper nitrate in this case, the ability of HL to extract uranyl declined. This is an issue considering the presence of other naturally occurring metals, in higher concentrations, is inevitable with environmental samples and the one goal was to keep sample preparation to a minimum. To our knowledge, this is the first example of utilizing M-PVA functionalized with a salen ligand for uranyl detection.

The future direction of this project should begin with optimizing the conditions to load DTBsalqu onto the M-PVA to determine its ability to serve as a SPE. Furthermore, and most importantly, developing a more uranyl selective ligand, that is capable of being loaded onto the magnetic poly(vinyl)alcohol beads, needs to be done. One idea was to design a ligand with two binding pockets, allowing for two sites of binding for one ligand, which may decrease the limit of detection for the ligand. Preliminary work was conducted to synthesize 2,3,6,7-

tetraaminophenazine, TAP, figure 5.3, a possible backbone of that offers two diamines to react with salicylaldehydes to produce the two tetradentate binding pockets.
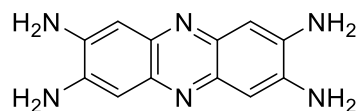
Figure 5.3. Tetraaminophenazine

After a search of the literature, the synthesis of all published TAP followed work published by Gajiwala et al.[1], in which commercially available 1,3-diamino-4,6-dinitrobenzene underwent reduction to give TAP in quantitative yields. This method requires the use of a Zn/HCl reduction and gaseous HCl. The starting material used in the synthesis of 2-qu, 1,3-difluoro-4,6-dinitrobenzene (DFDNB), already possess the two nitro-groups needed for the starting point of the Gajiwala synthesis. When synthesizing 2-qu, the first step results in the substitution of the fluoride with the amino acid, by passing this step and dissolving the DFDNB in 8 equivalents of ammonium hydroxide resulted in the production of 1,3-tetraamino-4,6-dinitro-benzenein 98% yield. From this, palladium on carbon and ammonium formate in THF resulted in the production of 1,3,4,6-tetraaminobenzene (47% yield;TAB). This method gets rid of the need to perform the Zn/HCl reduction. TAB was then dissolved in water and sodium acetate was added to the reaction before heating for 5 hours producing TAP(56%). From here, TAP needs to be explored as the backbone for a poly-tetradentate binding ligand.

Imidazole Metal Extractions

The ability of the salphenzine derived imidazole ligands to bind uranyl and copper, while giving two distinct identifying absorbance spectra, leads one to believe that these ligands can serve as chemosensors for uranyl. The ease of preparation and purification associated with these ligands make it an attractive option as a chemosensor, especially the ligand without the presence of R-groups since it had a detectable change in concentrations as low as 0.1 equivalents of uranyl. The extended conjugation, when compared to 2-qu and benzene, of the backbone seems to play a role in the efficiency of the ligand as a uranyl detector. Elucidating the structure of one of the imidazole ligands bound to a metal with x-ray crystallography is needed to complete this paper. Along with that, performing a competition study between copper and uranyl would aide in determining the selectivity of the ligands.

Thorium Catalysis

The need to increase our fundamental knowledge of the 5-f elements, the use of exploring the simple actinide salt, thorium nitrate, $Th(NO_3)_4$, to oxidatively couple *ortho*-phenylenediamine (OPD) gave a broader knowledge of the catalytic abilities of thorium. Although the use of an actinide as a catalyst is far cry from the highly sought after green chemistry, the 1% catalyst loading required to oxidize OPD shows that the presence of the 5-f thorium aides in production of the product and is lower than previously reported approaches with 50% catalyst loading of Co(II). Future directions of this project should begin with computational analysis to elucidate a reasonable mechanism. Also, increasing the knowledge of what reactions

this simple actinide salt can catalyze may offer a greater understanding of its role in the

mechanism.

References

1. Gajiwala, H. M.; Zand, R. Polym. 1999, 41, 2009.

Chapter 6: Experimental Procedures and Materials

Materials

The L-Leucine methylester·HCl(98%) and 3,5-ditertbutyl-salicylaldehyde(>98%) were purchased from TCI. From Alfa Aesar, the following chemicals were purchased: N,N-diisopropylethylamine(99%), palladium on carbon (dry, 5%), salicylaldehyde(99%), trifluoroacetic acid(99%), filter aid, Celite hyflo super-cel, and 2-(N-morpholino)ethansulfonic acid monohydrate (MES·monohydrate, 985). Ammonium hydroxide(28-30%) and Silica gel(60-200 um) was purchased from BDH. L-tyrosine methylester·HCl(98%), ammonium formate(97%), 2,5-dihydroxy-benzaldehyde(98%), copper (II) nitrate(99.999%), 1,4-cyclohexadiene, 2,3-diaminophenazine, cyclohexene, N,N'-diisopropylcarbodiimide(98%), 4-dimethylaminopyridine, sodium acetate(99%), and pyridine(98%) were purchased from Sigma-Aldrich. The 1,3-difluoro-4,6-dinitrobenzene(97%) was purchased from Matrix Scientific. *Ortho*-phenylenediamine(98%) aniline, catechol, copper (II) acetate monohydrate(98%), N,N-were purchased from Acros Organic. The phenol and benzene were purchased from Fisher Scientific. The 1-ethyl-3-(3-dimethylaminopropyl)carbodiimide(EDC, premium grade) was purchased from Thermo Scientific. The $UO_2(NO_3)_2$ and $UO_2(OAc)_2$ were purchased from Fischer and Polysciences, Inc., respectively. The thorium nitrate was purchased from Fluka. The THF and ethyl acetate was purchased from Macron. The 200 proof ethanol was purchased from PharmCo-Aaper. The methanol (HPLC grade), dimethylformamide(dry solvent) and hexanes(ACS grade) were purchased from EMD. The magnetic poly(vinyl)alcohol beads (950 umol COOH/g) were purchased from Perkin Elmer. The ^{1}H NMR solvents, d-DMSO and chloroform-d, were purchased from Cambridge Isotope. Starting materials were used as received. All Solvents were purchased from and used as received, unless otherwise stated.

Instruments

The ^{1}H NMR analysis was conducted on a Bruker AC 400 spectrometer with shift values given as δ values (ppm). Unless otherwise stated, DMSO-d[6] was the solvent used to dissolve the samples for NMR analysis. Mass spectrometry analysis was conducted using a Micromass Q-TOF mass spectrometer from the Waters Corp (Miliford, MA). A Cary 50 UV-Vis spectrophotometer with a xenon lamp was used for all absorbance data measured. A Shimsdzu Inc. IR, Prestige-21 Fourier Transform Infrared Spectrophotometer was used for all IR data collected and the samples were prepared using KBr. Fluorescence spectroscopy was performed on a Shimadzu RF-5301 PF fluorospectrophotometer. ICP-OES, Microfluorimeter.

Synthesis

Salen 2-quinoxalinol derivatives

2-Quinoxalinol

10 mmol of 1,5-difluoro-2,4-dinitrobenzene (2.041 g), DFDNB, 10 mmol of the corresponding amino acid methyl ester, and 2.2 equivalents of diisopropylethylamine, DIPEA were mixed in a 1:1 mixture of ethanol and THF. The reaction mixture was stirred at room temperature for 12 hours before 5 equivalents of ammonium hydroxide was added to the reaction. This solution was then allowed to stir at room temperature for 8 hours or until TLC confirmed the reaction was complete. The reaction mixture was then concentrated by means of a rotary evaporator, before dissolving the yellow solid in 100 mL of ethanol. The addition of 20 equivalents of ammonium formate, $HCOONH_4$, and 1 g of 5% dry palladium on carbon occurred before heating the mixture to reflux temperature, which was 76 ºC, for 4 hours. Upon completion of the reaction, the remaining starting materials were filtered off utilizing a vacuum filtration. The remaining

mixture was concentrated by means of a rotatory evaporator; then purified using column chromatography in an 8:2:1 mobile phase of ethyl acetate:hexanes:ethanol, in which the product was dissolved in the mobile phase. The resulting bright yellow solution concentrated to dryness using the rotatory evaporator. The yield for leucine 2-Qu was 72% and tyrosine 2-Qu was 8%.

Leucine 2-Qu Mass spectrometry M+1 233 (found) 232 (calculated) was obtained

^{1}H NMR: δ0.90 (2H, d), δ2.15-2.29 (1H, m), δ2.47 (2H, d), δ 4.62 (2H, bs), δ5.39 (2H, bs), δ6.35 (1H, s), δ6.79 (1H, s), δ11.98 (1H, bs).

Tyrosine 2-Qu Mass spectrometry M+1 283.2846 (found) 282.30 (calculated) was obtained

^{1}H NMR: δ3.85 (2H, s), δ4.57 (2H, bs), δ5.42 (2H, s), δ6.34 (1H, s), δ6.63-6.65 (1H, d), δ6.78 (1H, s), δ7.07-7.09 (1H, d), δ9.14 (1H, s), δ11.78 (1H, bs).

DHSalqu

To synthesize DHsalqu, 2 mmol of 2-qu was dissolved in 50 mL of degassed MeOH (degassed by the freeze, pump, thaw method) and 15 equivalents of 2,5-dihydroxybenzaldehyde was added to the round bottom flask. The reaction was allowed to reflux for 24 hours, before cooling and removing the solvent with rotary evaporation. Percent yield: 84%

Mass spectrometry M+1 473.1832 (found) 472.18 (calculated) was obtained

^{1}H NMR: δ0.98 (6H, d), δ2.27-2.31 (1H, m), δ2.71 (2H, d), δ6.77-6.91 (4H, m), δ7.06 (2H, s), δ7.14 (1H, s), δ7.92 (1H, s), δ8.77 (1H, s), δ 9.01 (1H, s), δ9.12 (1H, bs), δ9.15 (1H, bs), δ11.49 (1H, bs), δ12.36 (1H, bs), δ12.45 (1H, bs).

DTBSalqu

To synthesize DTBsalqu, 2 mmol of tyrosine 2-qu was dissolved in 50 mL of MeOH and 2.2 equivalents of 3,5-ditertbutylsalicylaldehyde was added to the round bottom flask. The reaction was allowed to reflux for 8 hours, before cooling and removing the solvent with rotary evaporation. The product was then purified with a silica gel column with 5:1 DCM:MeOH as the mobile phase. Percent yield: 64%

Mass spectrometry M+1 715.1943 (found) 715.18 (calculated) was obtained

^{1}H NMR: δ1.35 (10H, s), δ1.40 (12H, s), δ2.19 (12H, s), δ4.13 (2H, s), δ6.68 (2H, d), δ7.18 (2H, d), δ7.39 (2H, d), δ7.51 (2H, s), δ7.91 (1H, s), δ8.84 (1H, s), δ9.19 (1H, s), δ9.23 (1H, s), δ13.49 (1H, s), δ13.67 (1H, s).

Heterogeneous Ligand

1.494 mL (7.097×10^{-3} mmol of COOH) of M-PVA was washed with 0.1 M MES buffer (pH 5.0) to activate the beads. EDC, 0.1561 mmol (0.02993 g) in 2 mL of water was added to 50 mL round bottom of activated M-PVA. Separately, 7.097×10^{-3} mmol of DHsalqu (0.0335 g) and 0.156 mmol (0.0193 g) of DMAP were dissolved in 30 mL of DMF before being added to the round bottom of M-PVA. The reaction mixture was then agitated using a shaker for 72 hours, at room temperature. After 72 hours, the beads were immobilized using a magnet and the solvent was decanted off, dried, and then analyzed for ligand content. A small amount of beads (20 µL) was dried using a lyophillizer before being analyzed by FTIR. Ligand major peaks (1279, 1489, 1577, 1622, 1658, and 3381 cm^{-1}); HL major peaks (1054, 1251, 1489, 1577, 1622, 1658, 1734, and 3381 cm^{-1})

Imidazole derivatives

For the synthesis of the imidazole derivatives with the 2-quinoxalinol and salophen backbones, 2 mmol of desired backbone, 2.4 mmol of salicylaldehyde, and 20 uL of TFA were dissolved in 20 mL of methanol before heating to reflux temperature, which was 65 ℃ for methanol and 110 ℃ for pyridine, for 8 hours. The reaction was allowed to cool before removing the solvent using a rotary evaporator.

Salq1: Mass spectrometry M+1 334.4098 (found) 334.37 (calculated) was obtained

^{1}H NMR: δ0.93 (6H, s), δ2.47 (1H, m), δ2.91 (1H, s), δ5.91 (1H, s), δ7.24 (1H, d), δ7.38 (1H, m), δ7.42 (1H, m), δ7.78 (1H, s), δ7.95 (1H, s), δ9.54 (1H, bs), δ9.98 (1H, s).

Salq2: Mass spectrometry M+1 351.4018 (found) 350.37 (calculated) was obtained

^{1}H NMR: δ0.95 (6H, s), δ2.49 (1H, m), δ2.82 (2H, s), δ6.31 (1H, s), δ6.92 (1H, d), δ7.03 (1H, d), δ7.37 (1H, s), δ7.72 (1H, s), δ7.74 (1H, s), δ9.31 (1H, bs), δ10.16 (1H, s), δ10.24 (1H, s).

*Salph1*DH: Mass spectrometry M+1 227.3008 (found) 226.23 (calculated) was obtained

^{1}H NMR: δ5.43 (1H, s), δ6.86 (1H, d), δ6.95 (1H, d), δ7.10 (1H, m), δ7.31 (1H, s), δ7.36 (1H, m), δ7.77 (1H, s), δ7.90 (1H, s), δ9.13 (1H, bs), δ9.31 (1H, s).

*Salph2*DTB: Mass spectrometry M+1 339.4398 (found) 338.44 (calculated) was obtained

^{1}H NMR: δ1.25 (9H, s), δ1.26 (9H, d), δ5.38 (1H, s), δ7.06 (1H, m), δ7.09 (1H, s), δ7.31 (1H, m), δ7.75 (1H, d), δ7.78 (1H, d), δ8.00 (1H, s), δ9.15 (1H, bs).

Sal1 was synthesized by dissolving 0.24 mmol (0.05052g) of DAP in 20 mL of salicylaldehyde and was allowed to stir at 80 ℃ for 24 hours. Upon completion of the reaction, a yellow product was recovered after filtering and washing with ethanol. Percent Yield: 61%

Sal1: Mass spectrometry M+1 313.3401 (found) 312.32 (calculated) was obtained

^{1}H NMR: δ5.21 (1H, s), δ7.21 (1H, d), δ7.67 (1H, m), δ7.71 (1H, m), δ7.86 (1H, m), δ7.89 (1H, m), δ8.14 (1H, s), δ8.19 (1H, d), δ8.20 (1H, s), δ8.23 (1H, d), δ8.84 (1H, s), δ8.41 (1H, d), δ9.43 (1H, bs).

Sal2 was synthesized by dissolving 1.13 mmol (0.2371 g) of DAP in 25 mL of pyridine and allowed to stir while heating at 110 ℃ to dissolve all the DAP. To this, 1.12 mmol (0.2630 g) of 3,5-ditertbutyl-salicylaldehyde was added and the reaction was allowed to reflux for 24 hours. Upon completion of the reaction, the solution was filtered and washed with hexane to retrieve the crude brown product. To purify, a silica column was ran with ethyl acetate mobile phase to retrieve the yellow product. Percent Yield: 72%

Sal2: Mass spectrometry M+1 425.5517 (found) 424.54 (calculated) was obtained

^{1}H NMR: δ1.55 (9H, s), δ1.62 (9H, s), δ6.32 (1H, s), δ7.73 (1H, s), δ7.77 (1H, m), δ7.78 (1H, m), δ7.97 (1H, s), δ8.12 (1H, d), δ8.15 (1H, s), δ8.16 (1H, d), δ8.69 (1H, s), δ9.64 (1H, bs).

Thorium Catalysis

2,3-diaminophenazine

Ortho-phenylenediamine (OPD), 0.4324 g (4 mmol), of was heated at 80° C in a 100 ml round bottom flask with a stir bar and 100 ml of deionized H_2O as solvent. Once the OPD dissolved, an appropriate volume of a stock actinide starting material solution was added to the mixture to allow a 1% catalyst loading ($Th(NO_3)_4$:OPD). The reaction was allowed to stir and heat at 80° C. When the experiment time had lapsed; the solution was filtered, the solid was washed with hexanes, and dried in a vacuum oven.

Mass spectrometry M+1 211.0961 (found) 210.0905 (calculated) was obtained

^{1}H NMR (400 MHz, C2D6OS) δ7.90-7.86 (2H, m) δ7.57-7.52 (2H, m) δ6.8987 (2H, s) δ6.26 (4H, s)

Aromatic Derivatives

In a typical procedure, 4 mmol of substrate(s) was heated at 80° C in a 250 ml round bottom flask with a stir bar and 100 ml of deionized H_2O as solvent. Once the dissolved, 1 mol% of Th(NO3)3 was added to the mixture. The reaction was allowed to stir and heated to 80° C. When the experiment time had passed; the solution was filtered, the solid was washed with hexanes, and dried in a vacuum oven.

1,4-Cyclohexadiene OPD reaction Mass spectrometry M+1 211.0961 (found) 210.0905 (calculated) was obtained ^{1}H NMR (400 MHz, C_2D_6OS) δ7.90-7.86 (2H, m) δ7.56-7.51 (2H, m) δ6.8978 (2H, s) δ6.2380 (4H, s).

Aniline OPD reaction Mass spectrometry M+1 211.0961 (found) 210.0905 (calculated) was obtained ^{1}H NMR (400 MHz, C_2D_6OS) δ7.90-7.86 (2H, m) δ7.56-7.52 (2H, m) δ6.8984 (2H, s) δ6.2412 (4H, s).

Benzene OPD reaction Mass spectrometry M+1 211.0961 (found) 210.0905 (calculated) was obtained ^{1}H NMR (400 MHz, C_2D_6OS) δ7.90-7.86 (2H, m) δ7.56-7.51 (2H, m) δ6.8970 (2H, s) δ 6.369 (4H, s).

Catechol OPD reaction Mass spectrometry M+1 211.0961 (found) 210.0905 (calculated) was obtained ^{1}H NMR (400 MHz, C_2D_6OS) δ7.90-7.86 (2H, m) δ7.57-7.52 (2H, m) δ 6.8969 (2H,

s) δ6.2443 (4H, s); Mass spectrometry M+1 213.0773 (found) 212.0905 (calculated) was

obtained δ8.58-8.54 (2H, m) δ8.15-8.11 (2H, m) δ 7.7309 (2H, s).

Cyclohexene OPD reaction Mass spectrometry M+1 211.0961 (found) 210.0905 (calculated)

was obtained ^{1}H NMR (400 MHz, C_2D_6OS) δ7.90-7.86 (2H, m) δ7.56-7.51 (2H, m) δ 6.8976

(2H, s) δ6.2376 (4H, s).

Phenol OPD reaction Mass spectrometry M+1 211.0961 (found) 210.0905 (calculated) was

obtained ^{1}H NMR (400 MHz, C_2D_6OS) δ7.90-7.86 (2H, m) δ7.57-7.52 (2H, m) δ6.8985 (2H, s)

δ6.2388 (4H, s).

2,3,6,7-Tetraaminophenazine

1,3-diamino-4,6-dinitrobenzene

1,3-difluoro-4,6-dinitrobenzene (DFDNB), 3 mmol (0.6121 g) was dissolved in 24 mL (8

equivalents) of $NH_3 \cdot H_2O$/ethanol and allowed to stir at room temperature for 72 hours. The

bright yellow product crashes out of the solution and was filtered before being placed into a

vacuum oven over night to dry. Percent yield: 98%.

Mass spectrometry M+1 198.14 (found) 199.1509 (calculated)

^{1}H NMR (400 MHz, d^6-DMSO): δ8.95 (1H, s) δ7.62 (4H, s) δ6.13 (1H, s).

1,3,4,6-tetraaminobenzene (TAB)

1,3-diamino-4,6-dinitrobenzene, 1.82 mmol (0.2143 g), palladium on carbon (0.24 g) and

ammonium formate, 39.94 mmol (2.52 g) was dissolved in 30 mL THF and brought to reflux for

5 hours before being filtered and allowing the brown solid to dry in the vacuum oven over night.

Percent yield: 47%.

Mass spectrometry M+1 139.11689 (found) 138.17 (calculated)

^{1}H NMR (400 MHz, d^6-DMSO): δ6.97 (8H, s) δ5.44 (2H, s).

2,3,6,7-Tetraaminophenazine

TAB, 0.3601 mmol (0.0497 g) and sodium acetate, 4.433 mmol (0.3637 g) was dissolved in 2.5 mL of deionized water and heated to reflux temperature for 5 hours. The brown solid obtained upon cooling was allowed to dry in the vacuum overnight. Percent yield: 56%.

Mass spectrometry M+1 241.2701 (found) 240.26 (calculated)

^{1}H NMR (400 MHz, d^6-DMSO): δ6.78 (8H, s) δ5.47 (4H, s).

Appendix

Chapter 1: Functionalized Poly (Vinyl)Alcohol Resins for Metal Detection
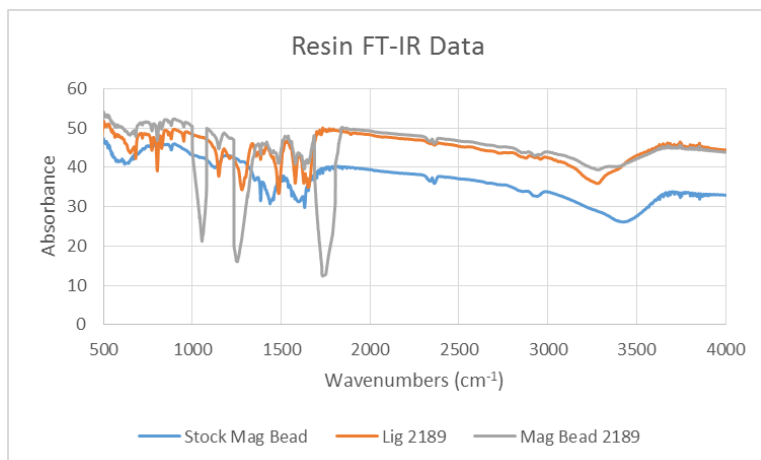
A1.1 FT-IR overlap of ligand, BR, and HL.
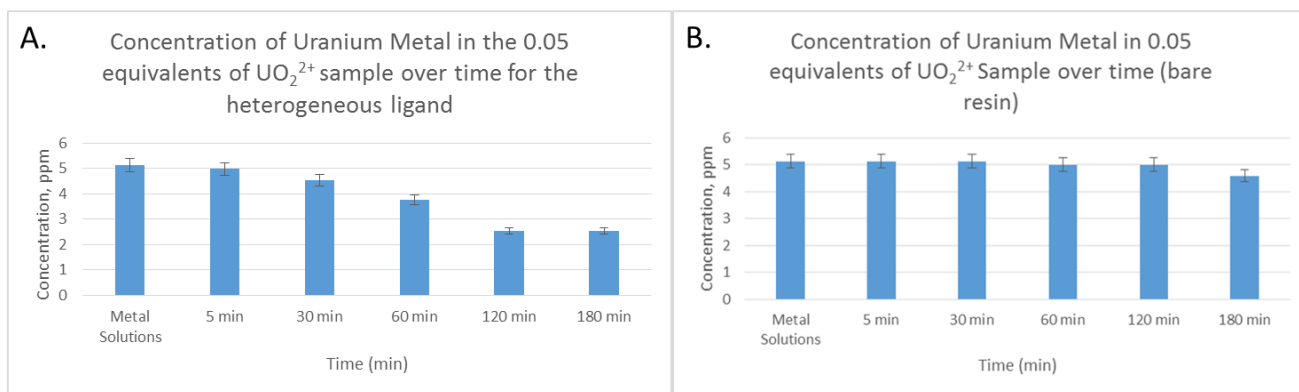
Figure A1.2. The change in concentration of uranium metal in the 0.05 equivalents of uranyl sample over time for the: A) heterogeneous ligand (HL) and B) bare resin (BR).
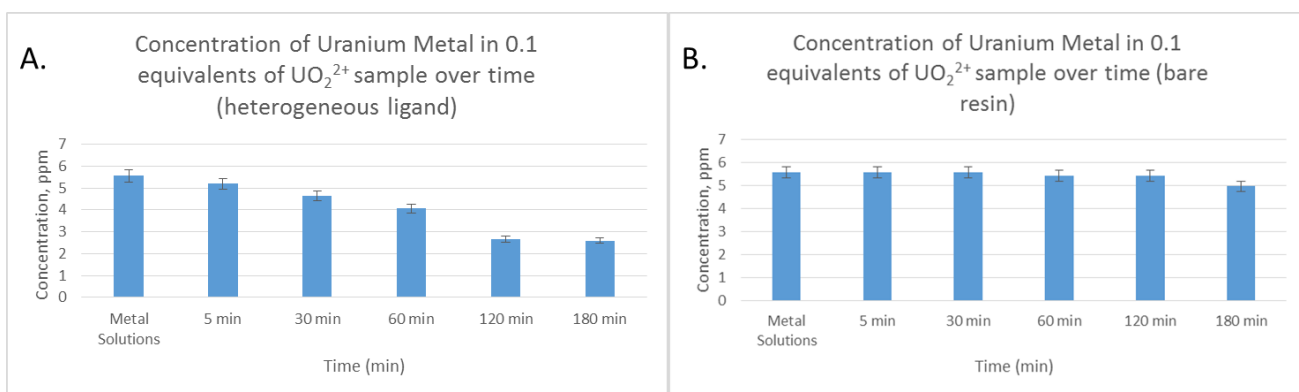
Figure A1.3. The change in concentration of uranium metal in the 0.1 equivalents of uranyl sample over time for the: A) heterogeneous ligand (HL) and B) bare resin (BR).
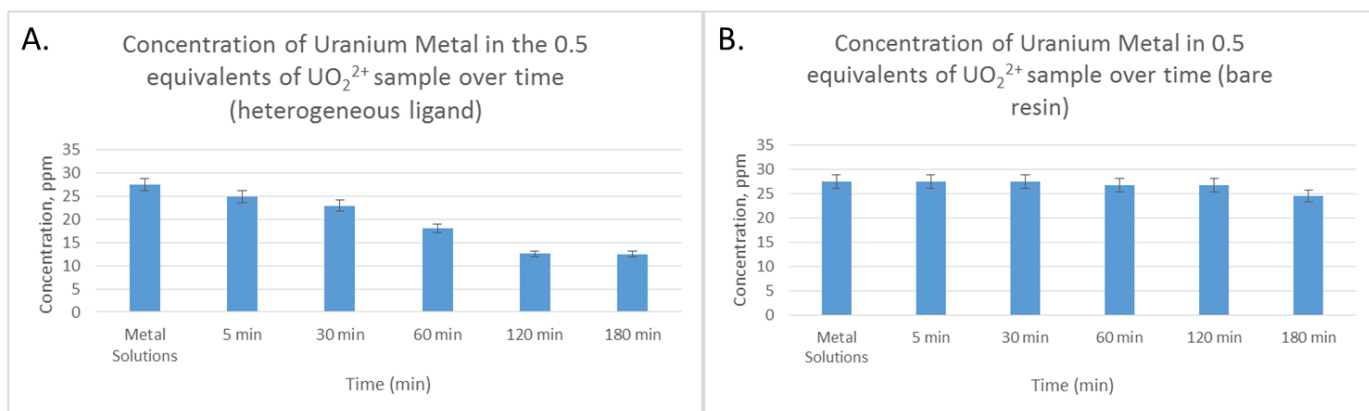
Figure A1.4. The change in concentration of uranium metal in the 0.5 equivalents of uranyl sample over time for the: A) heterogeneous ligand (HL) and B) bare resin (BR).
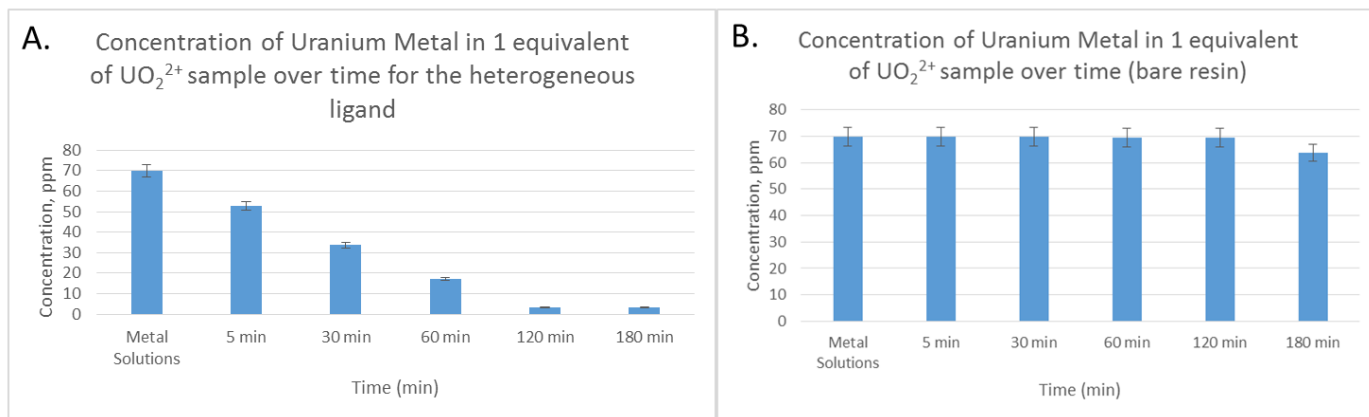
Figure A1.5. The change in concentration of uranium metal in the 1 equivalent of uranyl sample over time for the: A) heterogeneous ligand (HL) and B) bare resin (BR).
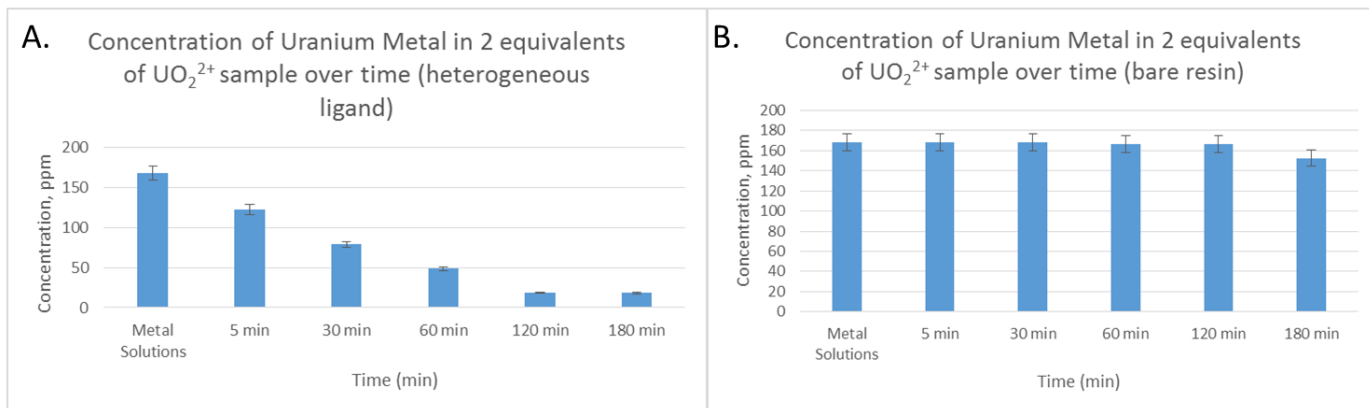
Figure A1.6. The change in concentration of uranium metal in the 2 equivalents of uranyl sample over time for the: A) heterogeneous ligand (HL) and B) bare resin (BR).
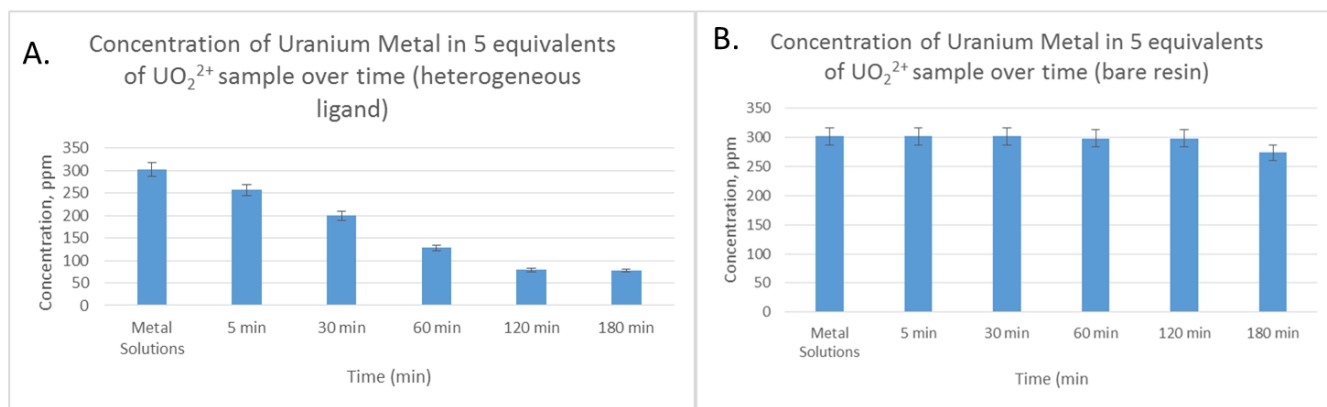
Figure A1.7. The change in concentration of uranium metal in the 5 equivalents of uranyl sample over time for the: A) heterogeneous ligand (HL) and B) bare resin (BR).
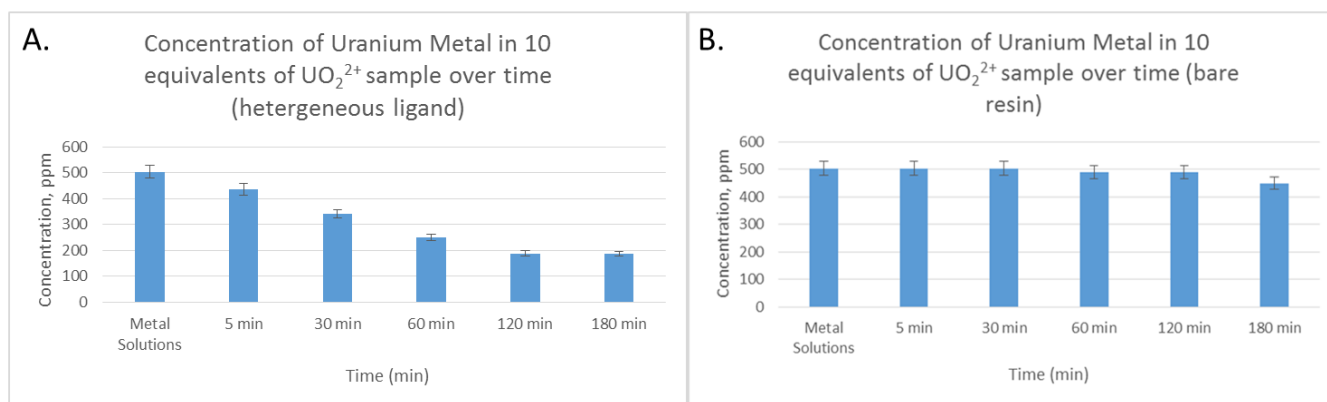
Figure A1.8. The change in concentration of uranium metal in the 10 equivalents of uranyl sample over time for the: A) heterogeneous ligand (HL) and B) bare resin (BR).
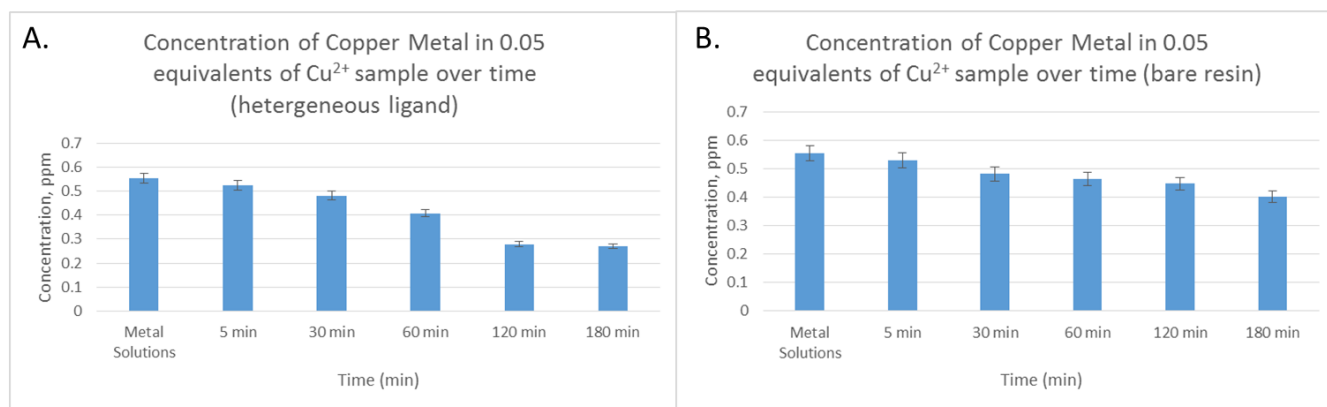
Figure A1.9. The change in concentration of copper metal in the 0.05 equivalents of uranyl sample over time for the: A) heterogeneous ligand (HL) and B) bare resin (BR).
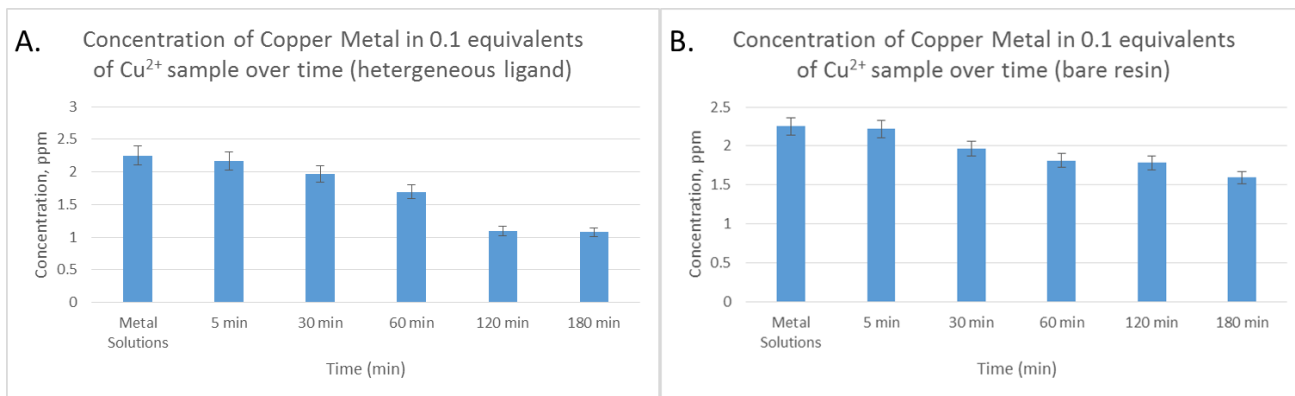
Figure A1.10. The change in concentration of copper metal in the 0.1 equivalents of uranyl sample over time for the: A) heterogeneous ligand (HL) and B) bare resin (BR).
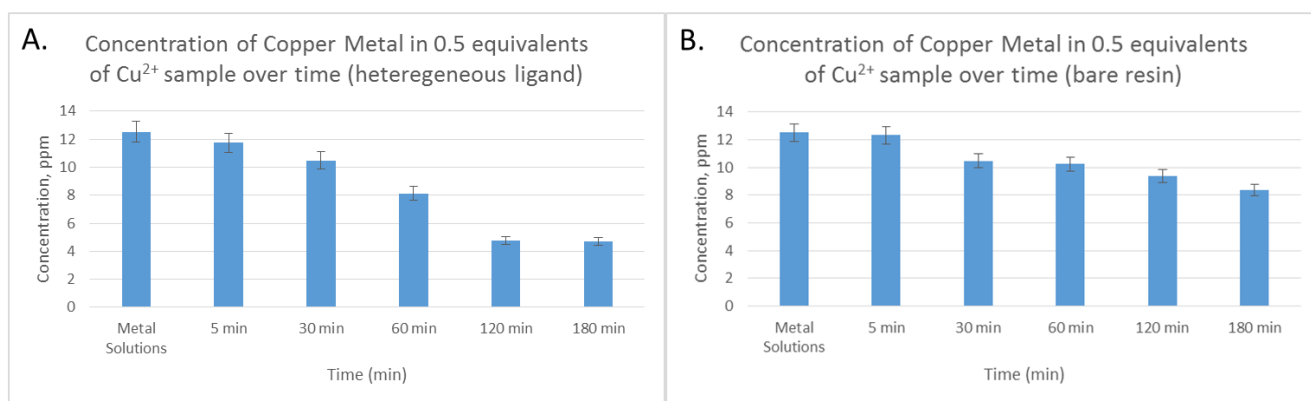
Figure A1.11. The change in concentration of copper metal in the 0.5 equivalents of uranyl sample over time for the: A) heterogeneous ligand (HL) and B) bare resin (BR).
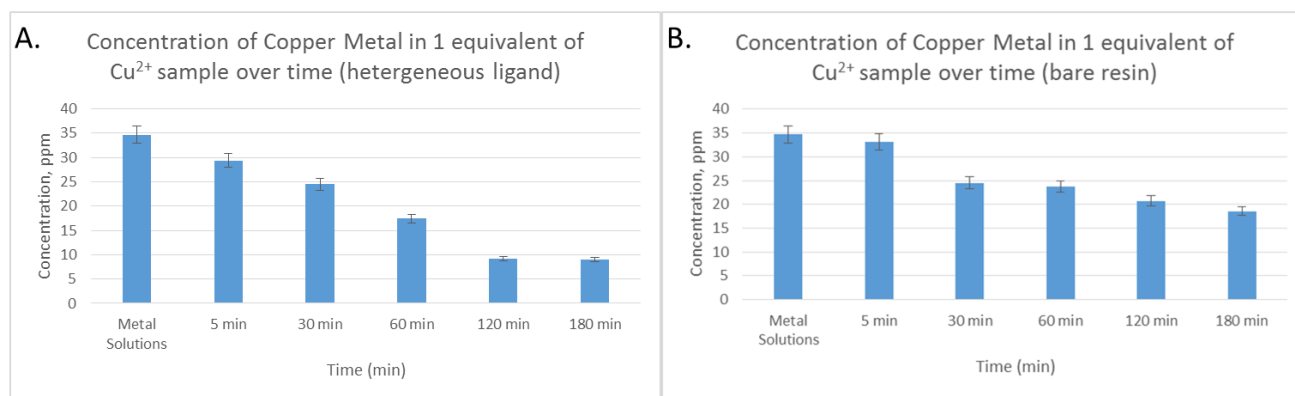
Figure A1.12. The change in concentration of copper metal in the 1 equivalent of uranyl sample over time for the: A) heterogeneous ligand (HL) and B) bare resin (BR).
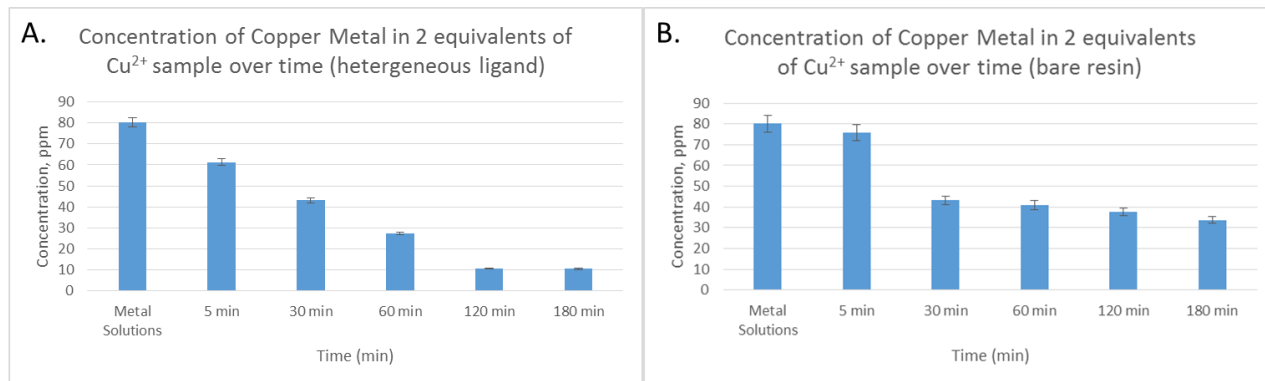
Figure A1.13. The change in concentration of copper metal in the 2 equivalents of uranyl sample over time for the: A) heterogeneous ligand (HL) and B) bare resin (BR).
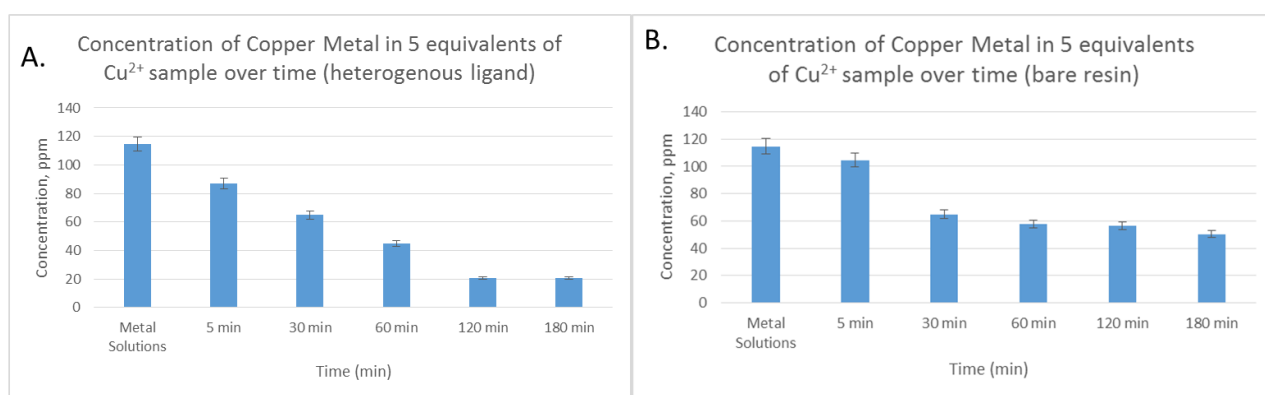
Figure A1.14. The change in concentration of copper metal in the 5 equivalents of uranyl sample over time for the: A) heterogeneous ligand (HL) and B) bare resin (BR).
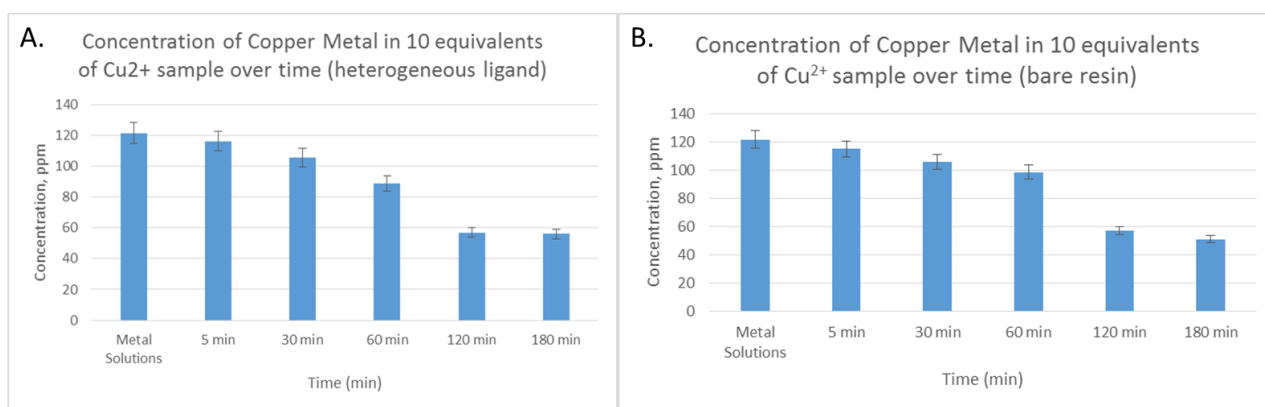
Figure A1.15. The change in concentration of copper metal in the 10 equivalents of uranyl sample over time for the: A) heterogeneous ligand (HL) and B) bare resin (BR).
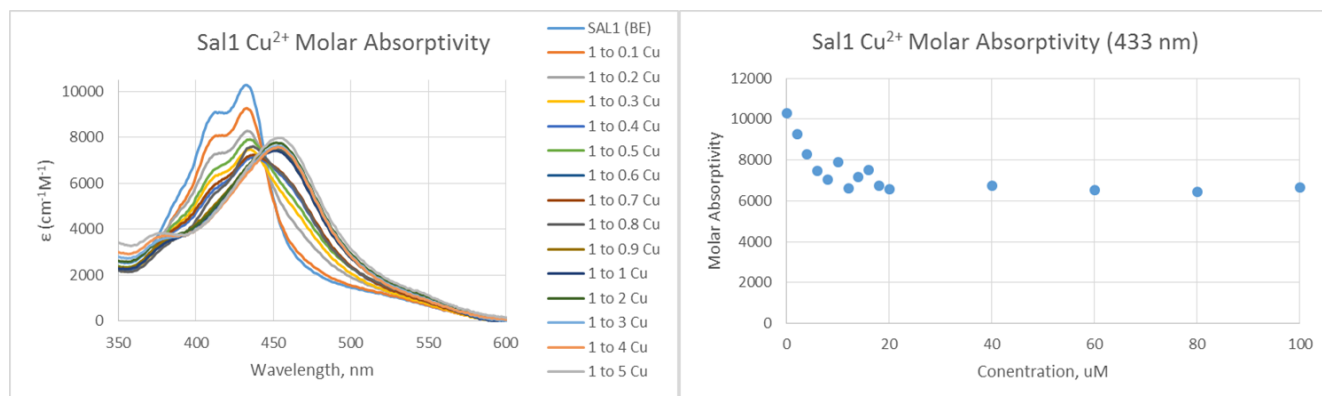
Figure B1.1. The absorbance spectra for the Sal1 ligand titrated with Cu^{2+} and the titration curve.
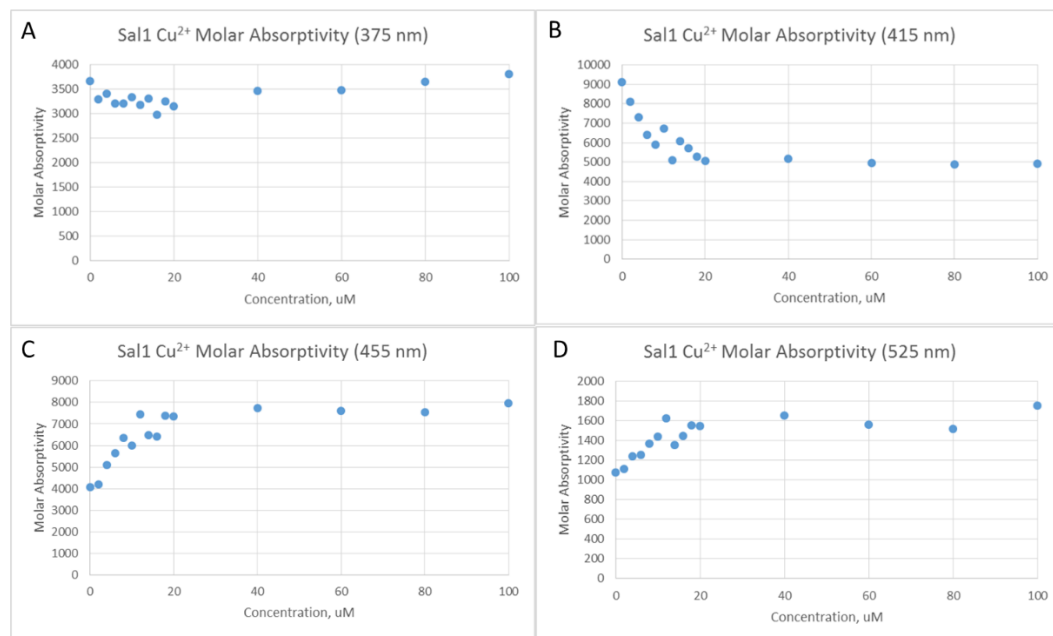
Figure B1.2. The titration curves of extinction coefficient versus metal concentration at A: 375 nm; B: 415 nm; C) 455 nm; and D) 525 nm of Sal1/Cu^{2+}.
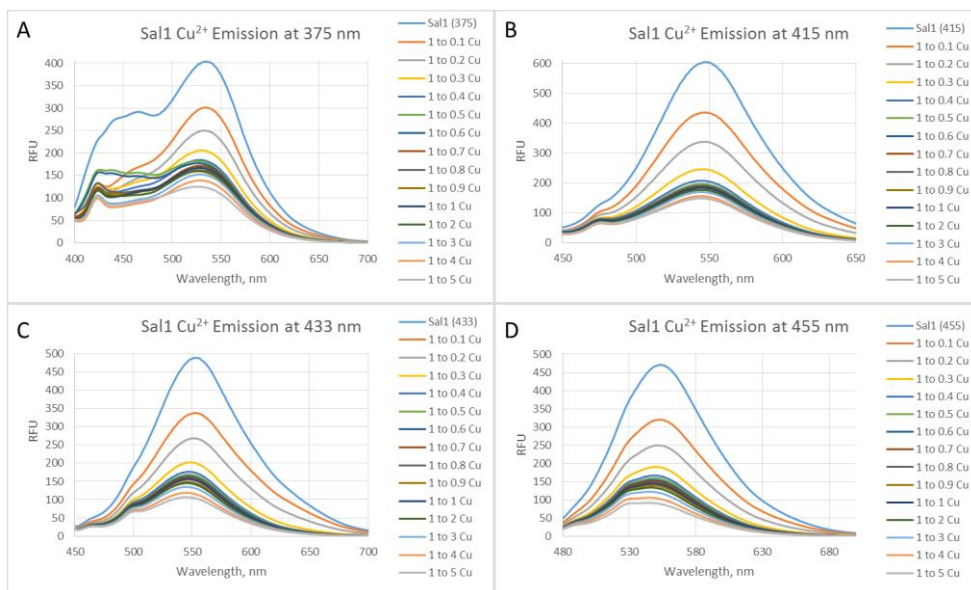
Figure B1.3. The emission spectrum with excitation at A) 375, B) 415, C) 433, and D) 455 nm in the batch titration of Sal1 with $Cu(OAc)_2 \cdot XH_2O$ in 20% H_2O in DMF after 24 hours.
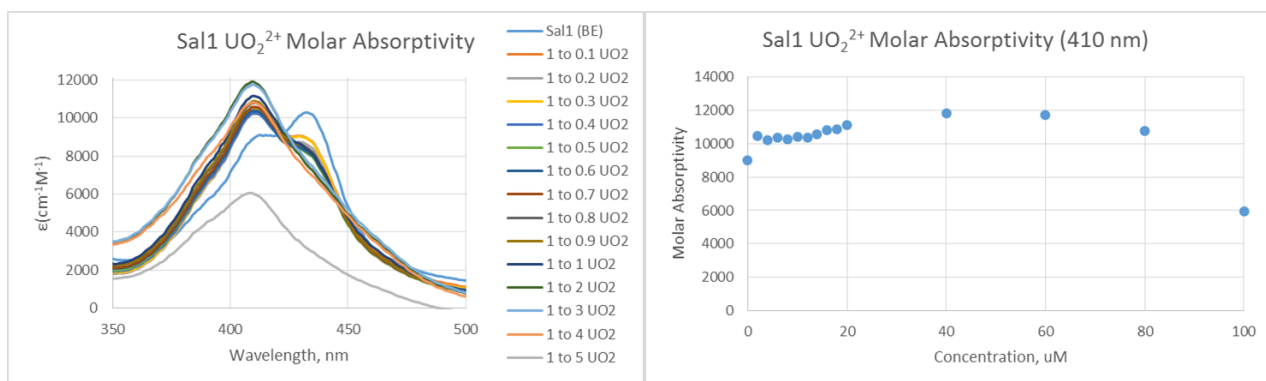
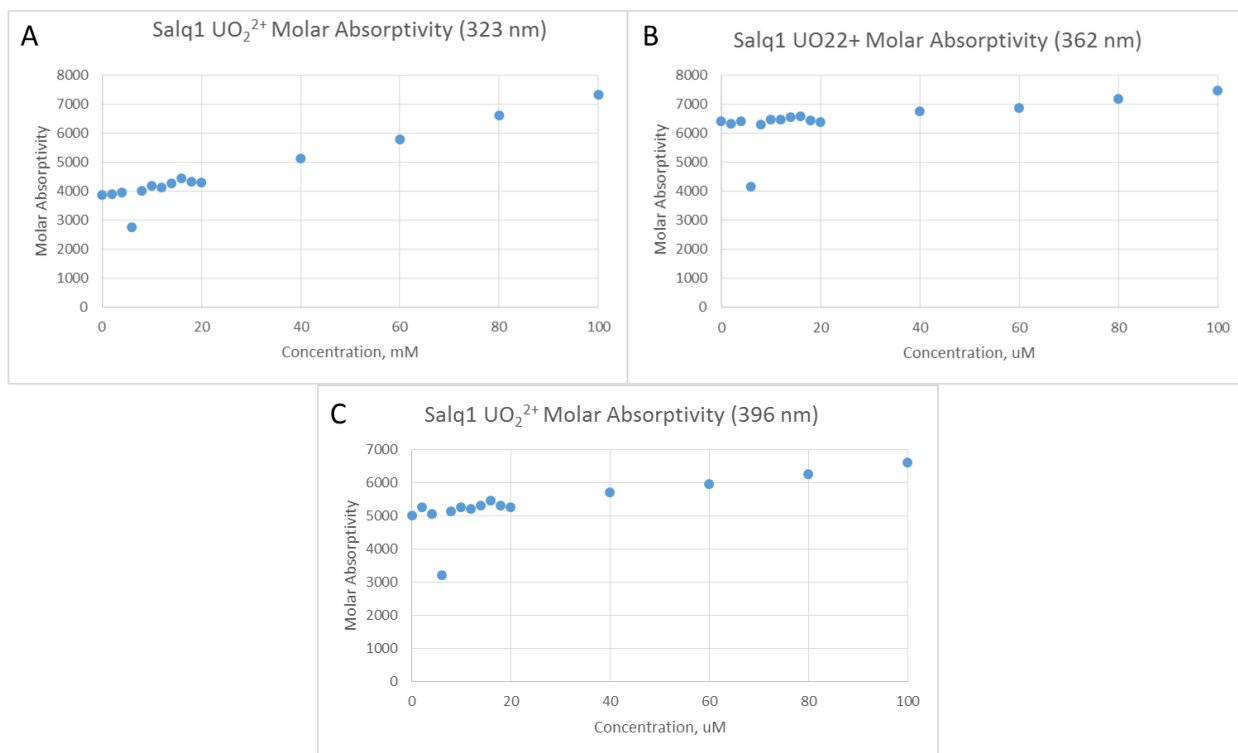Figure B1.4. The absorbance spectra for the Sal1 ligand titrated with UO_2^{2+} and the titration curve.
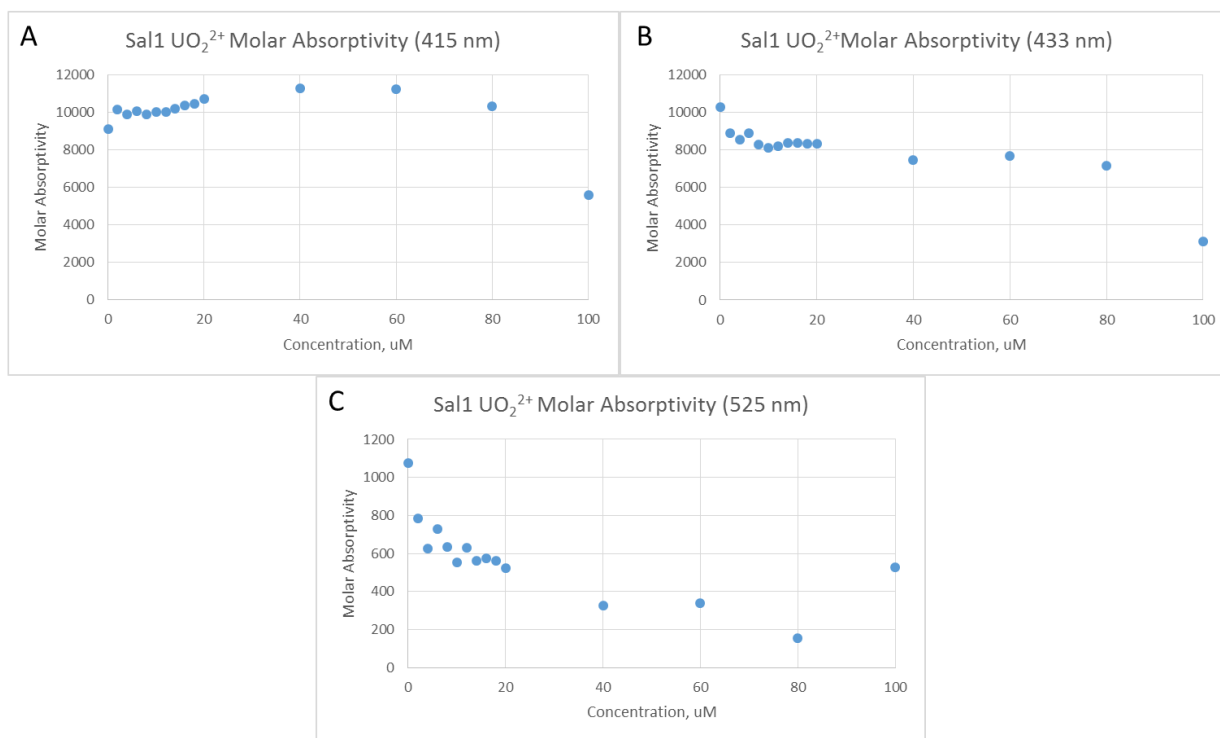
Figure B1.5. The titration curves of extinction coefficient versus metal concentration at A: 415 nm; B: 433 nm; and C) 525 nm of Sal1/UO_2^{2+}.
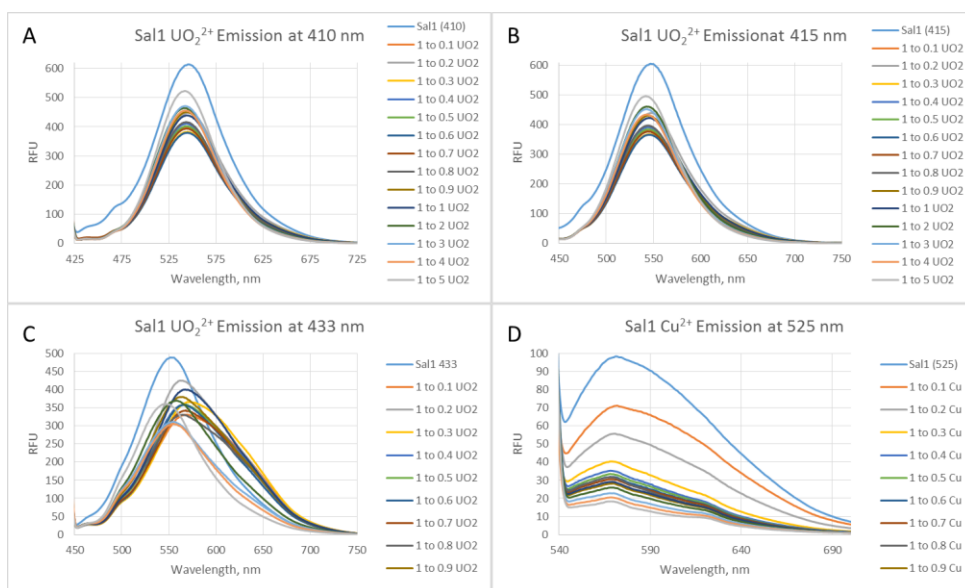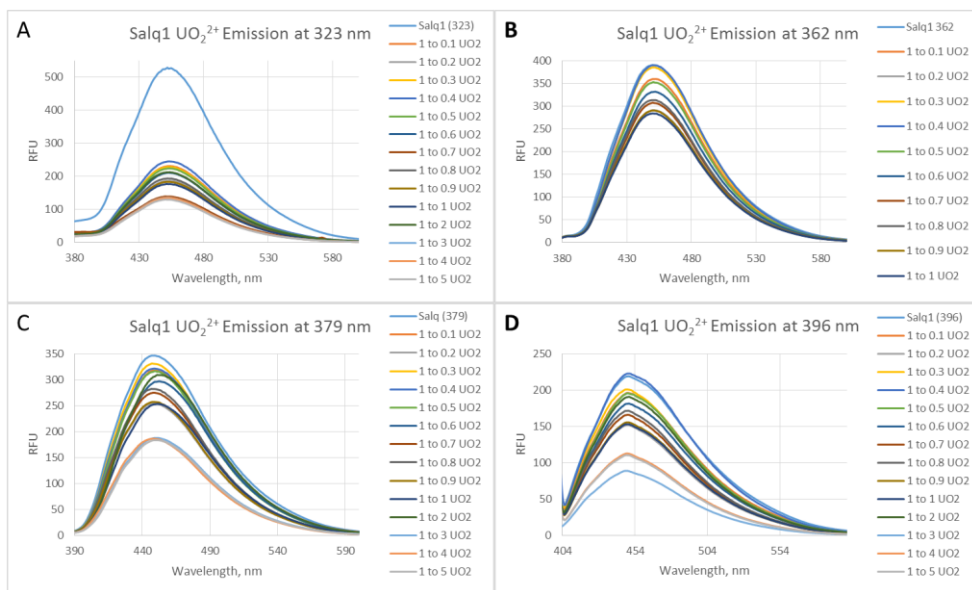

Figure B1.6. The emission spectrum with excitation at A) 410 nm, B) 415 nm, C) 433 nm, and D) 525 nm in the batch titration of Sal1 with $UO_2(OAc)_2 \cdot 2H_2O$ in 20% H_2O in DMF after 24 hours.
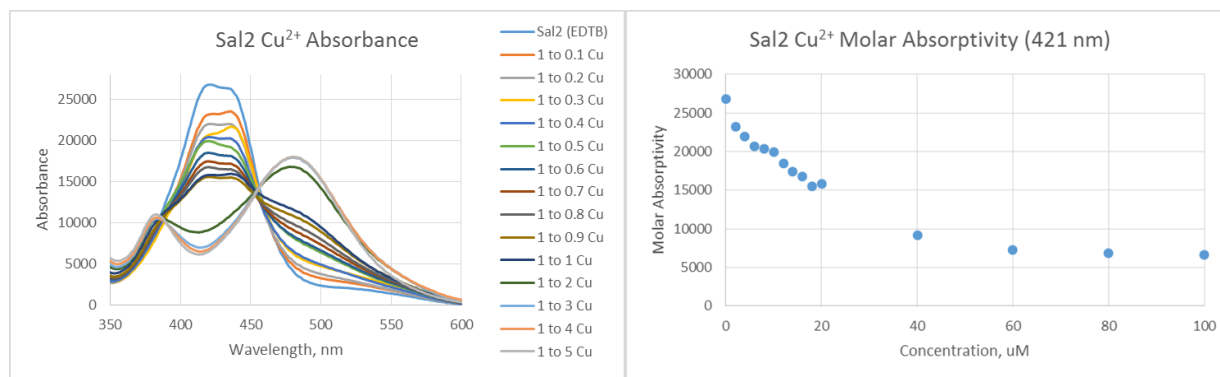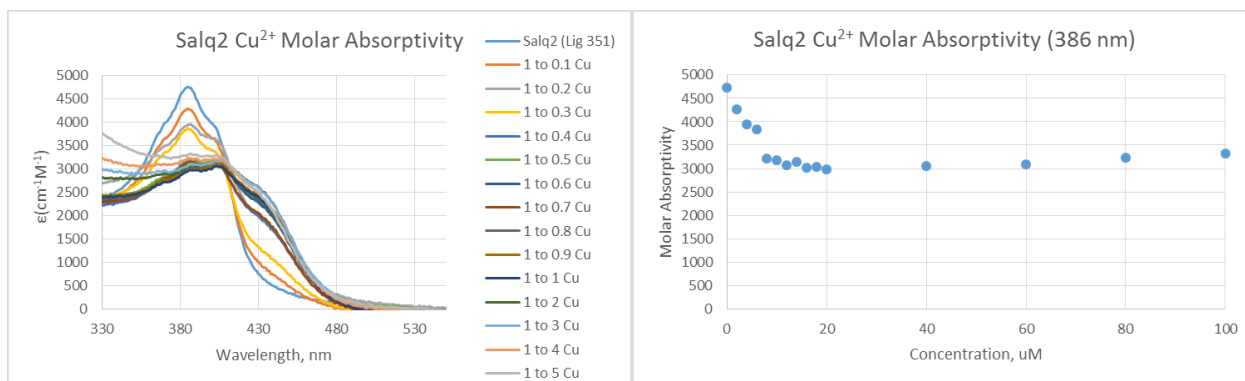
Figure B1.7. The absorbance spectra for the Sal2 ligand titrated with Cu^{2+} and the titration curve.
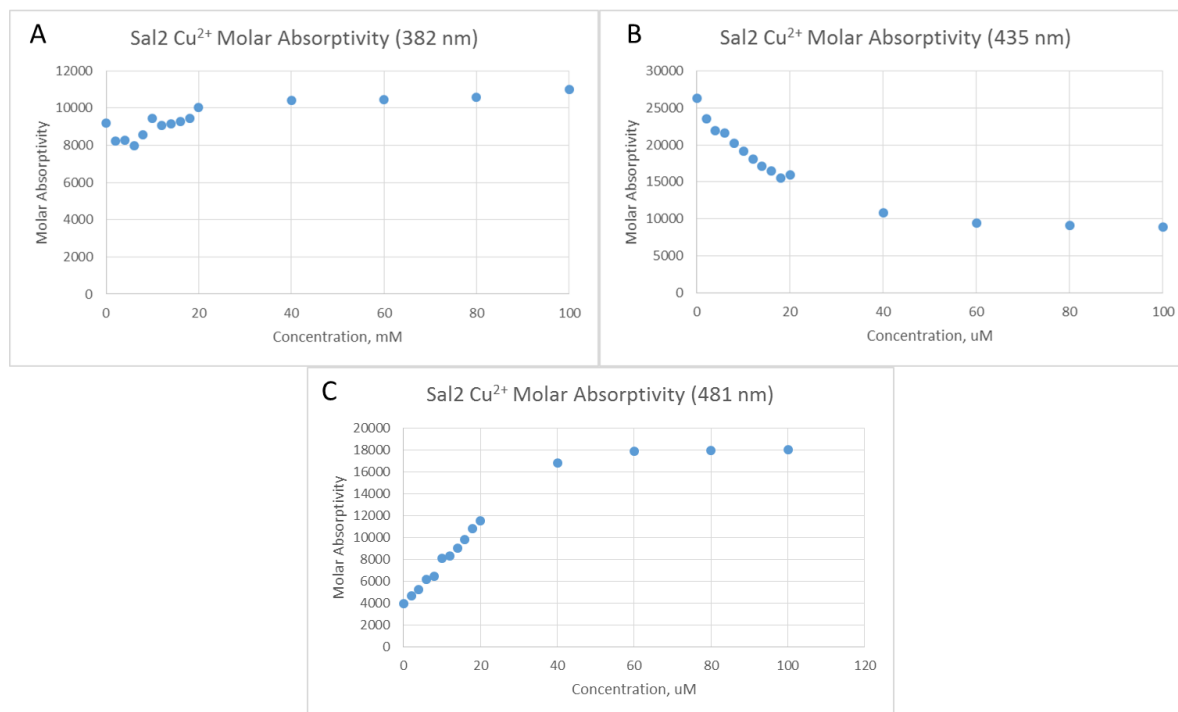
Figure B1.8. The titration curves of extinction coefficient versus metal concentration at A: 382 nm; B: 435 nm; and C) 481 nm of Sal2/Cu^{2+}.
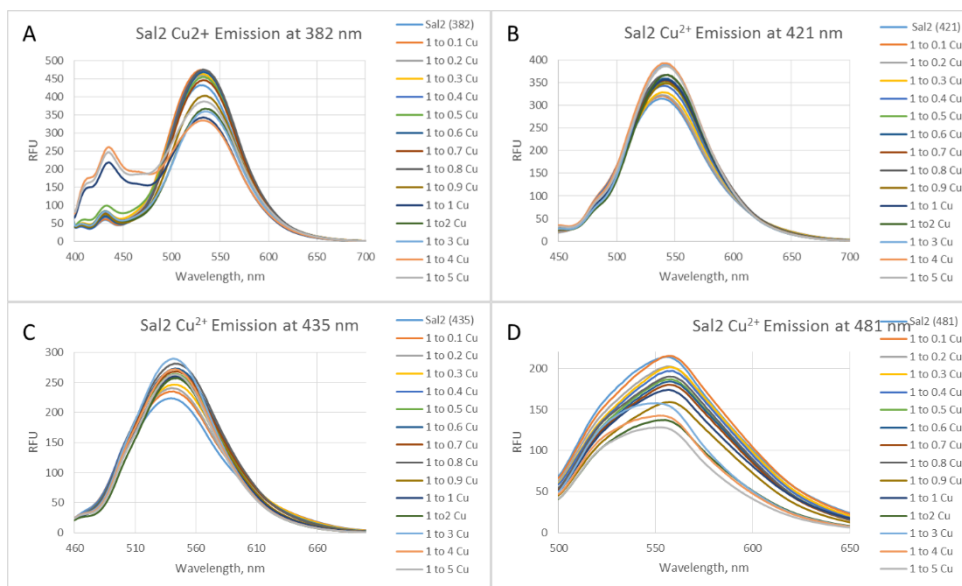
Figure B1.9. The emission spectrum with excitation at A) 382 nm, B) 421 nm, C) 435 nm, and D) 481 nm of the batch titration of Sal2 with Cu(OAc)$_2$·XH$_2$O in 20% H$_2$O in DMF after 24 hours.
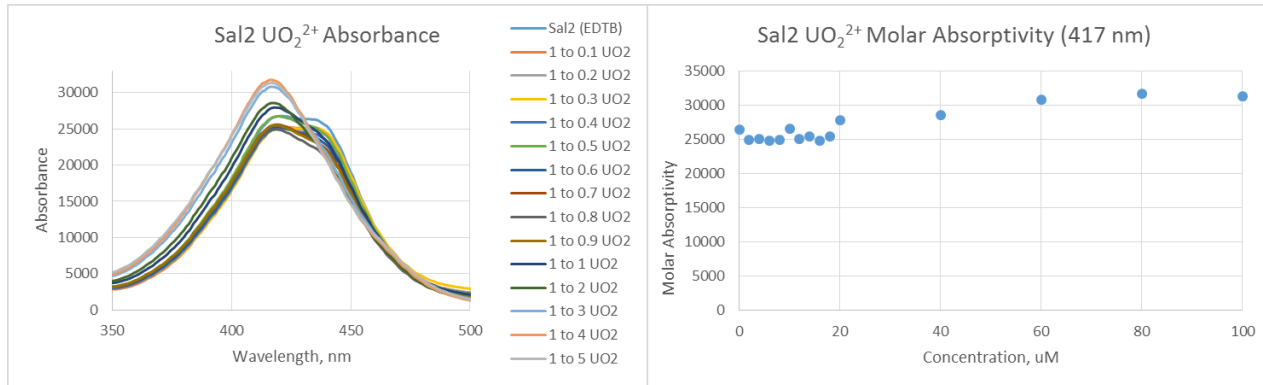
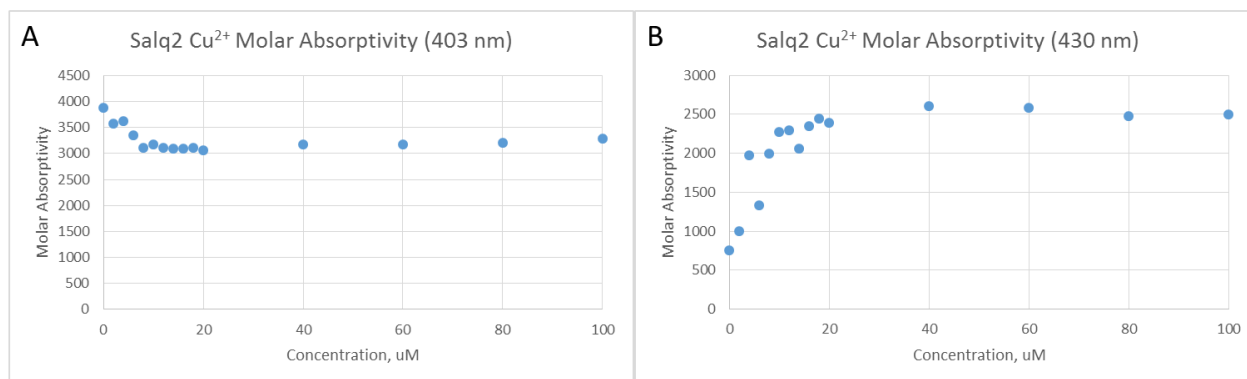Figure B1.10. The absorbance spectra for the Sal2 ligand titrated with UO$_2^{2+}$ and the titration curve.
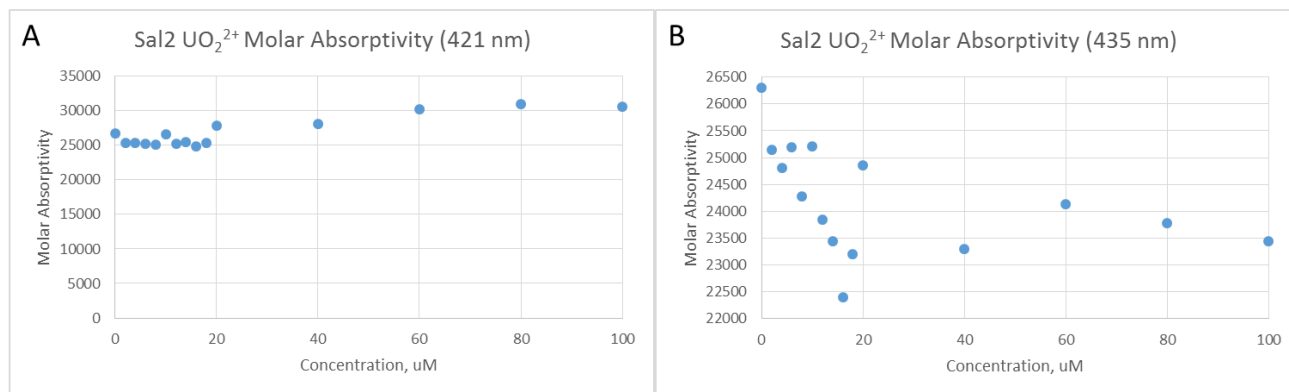
Figure B1.11. The titration curves of extinction coefficient versus metal concentration at A: 421 nm; and B: 435 nm; of Sal2/UO_2^{2+}.
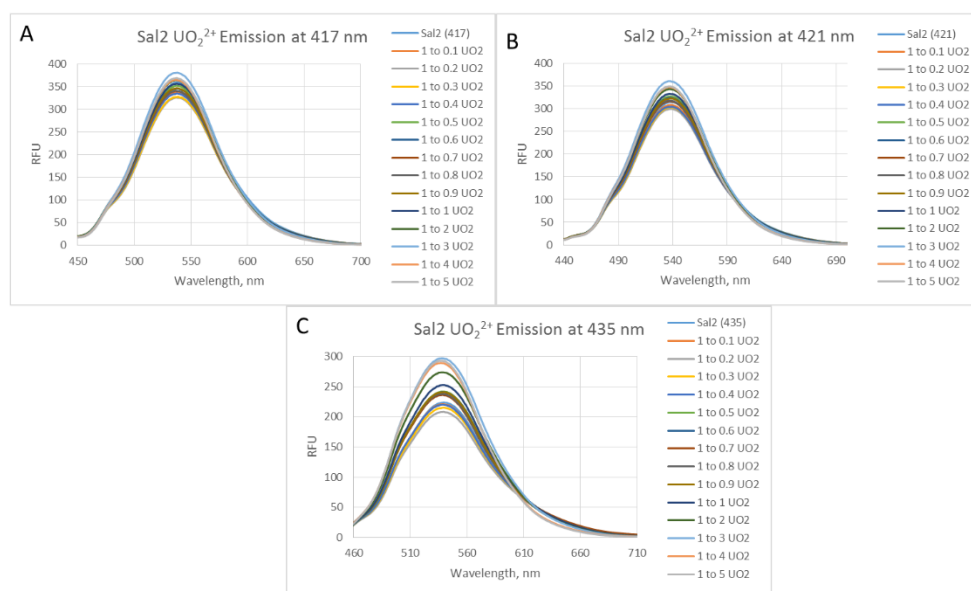
Figure B1.12. The emission spectrum with excitation at A) 417 nm, B) 421 nm, and C) 435 nm of the batch titration of Sal2 with $UO_2(OAc)_2 \cdot 2H_2O$ in 20% H_2O in DMF after 24 hours.
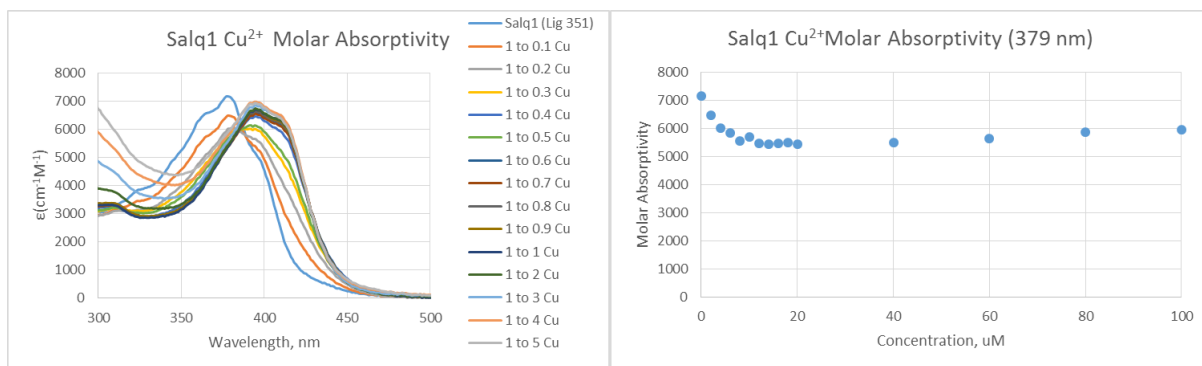
Figure B1.13. The absorbance spectra for the Salq1 ligand titrated with Cu^{2+} and the titration curve.
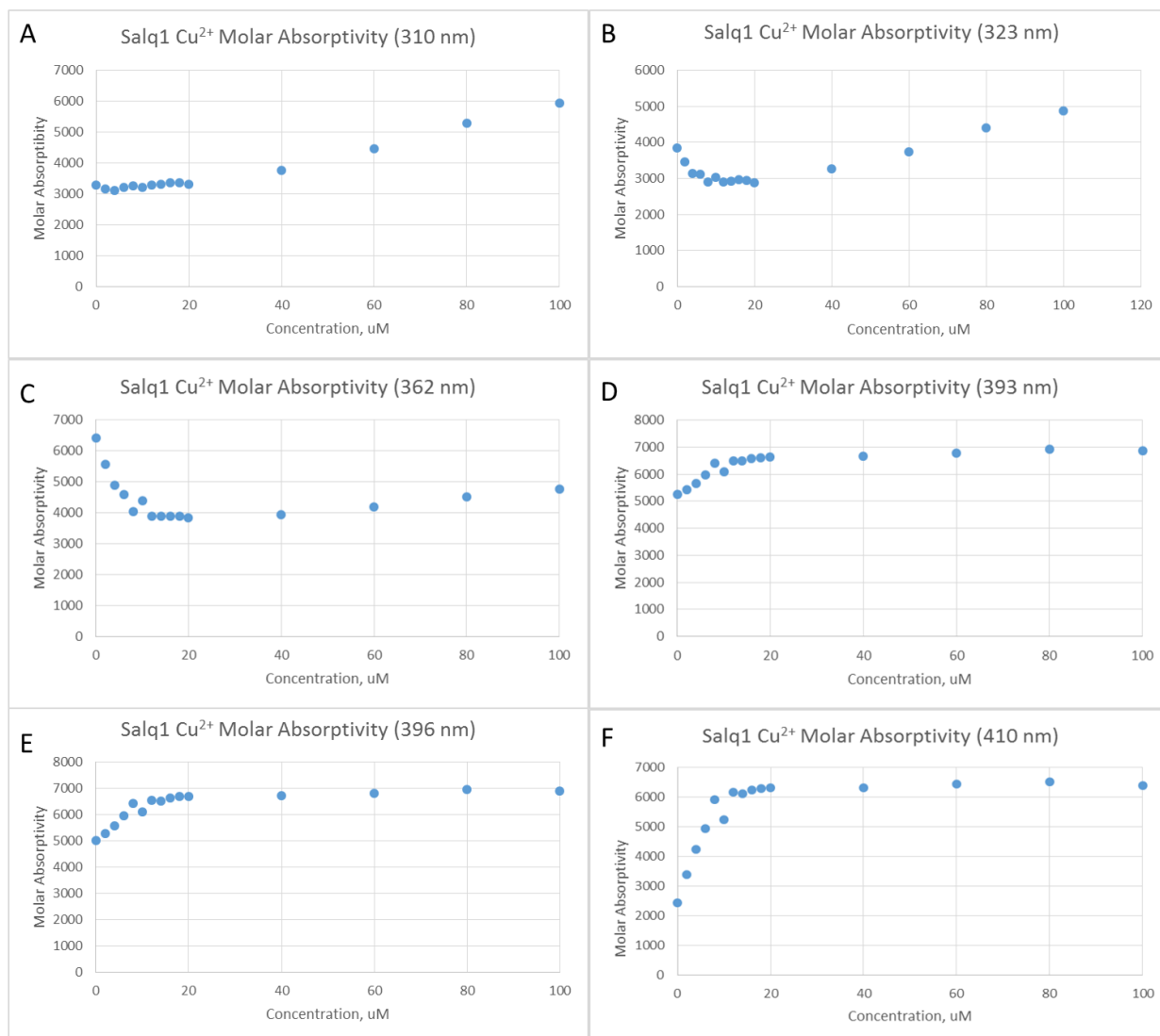
Figure B1.14. The titration curves of extinction coefficient versus metal concentration at A: 310 nm; B: 323 nm; C) 362 nm; D) 393 nm; E) 396 nm; and F) 410nm of Salq1/Cu^{2+}.
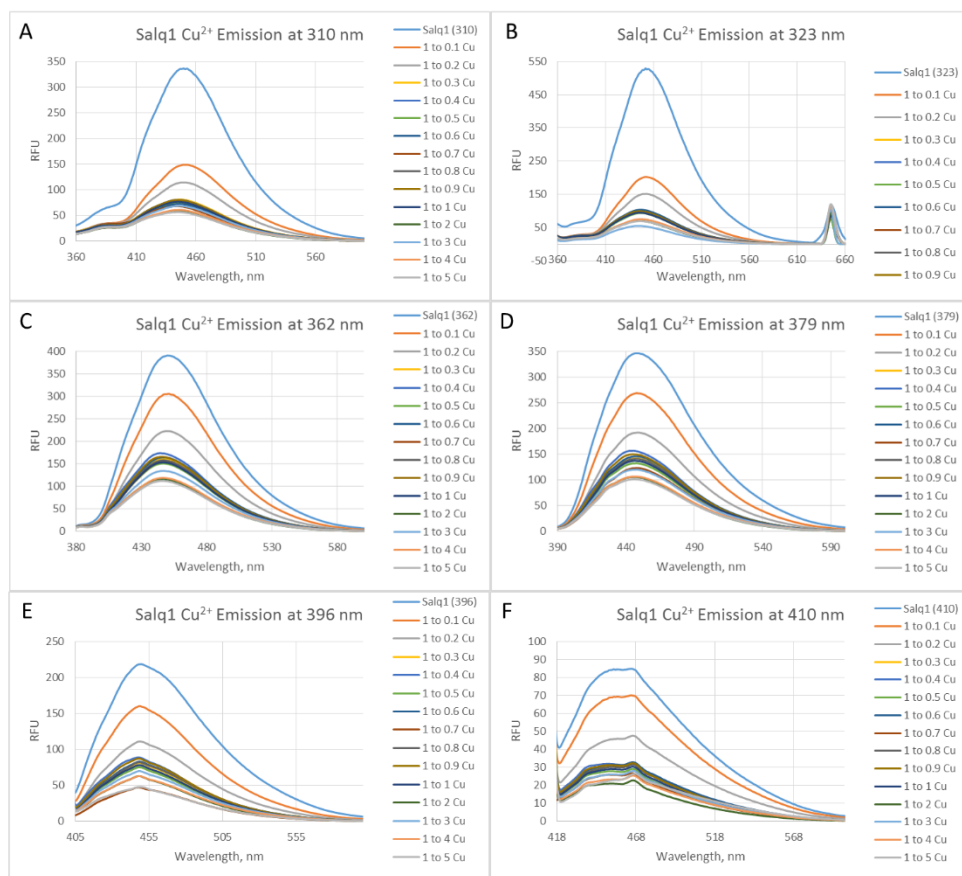
Figure B1.15. The emission spectrum with excitation at A) 310, nm B) 323 nm, C) 362 nm, D) 379 nm, E) 396 nm, and F) 410 nm of the batch titration of Salq1 with Cu(OAc)$_2$·XH$_2$O in 20% H$_2$O in DMF after 24 hours.
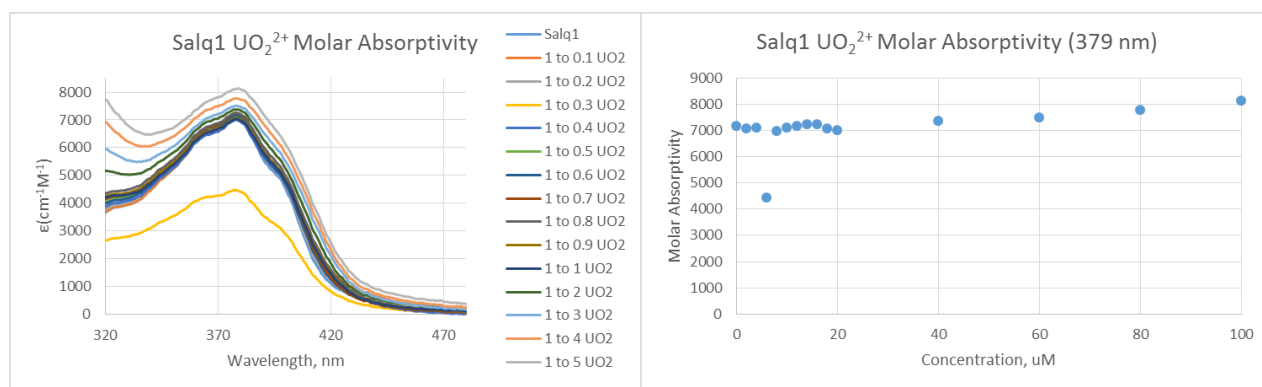
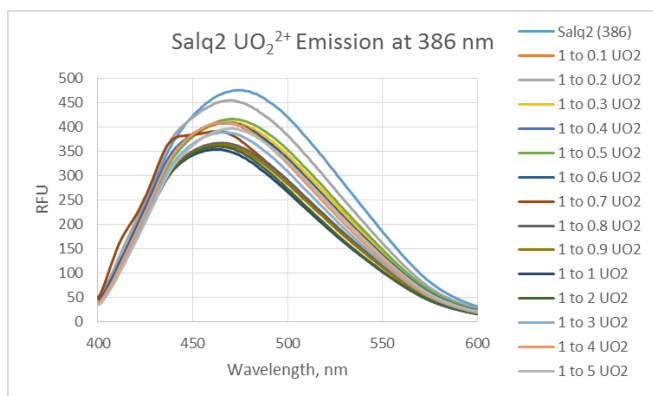Figure B1.16. The absorbance spectra for the Salq1 ligand titrated with UO$_2^{2+}$ and the titration curves at the respective wavelengths.

Figure B1.17. The titration curves of extinction coefficient versus metal concentration at A: 323 nm; B: 362 nm; and C) 396 nm of Salq1/UO$_2^{2+}$.

Figure B1.18. The emission spectrum with excitation at A) 323 nm, B) 362 nm, C) 379 nm, and D) 396 nm of the batch titration of Salq1 with UO$_2$(OAc)$_2$·2H$_2$O in 20% H$_2$O in DMF after 24 hours.

Figure B1.19. The absorbance spectra for the Salq2 ligand titrated with Cu^{2+} and the titration curve.

Figure B1.20. The titration curves of extinction coefficient versus metal concentration at A: 403 nm; and B) 430 nm of Salq2/Cu^{2+}.
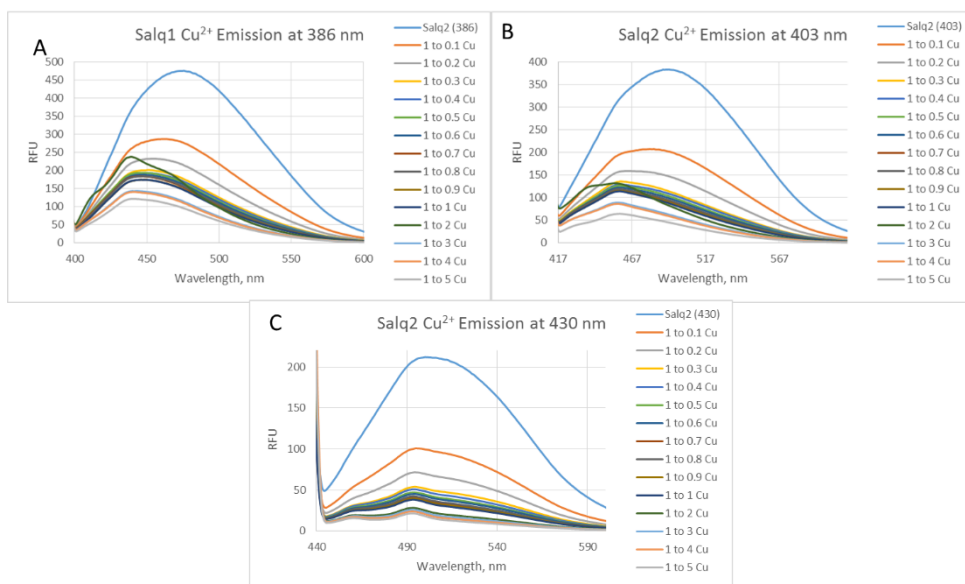
Figure B1.21 The emission spectrum with excitation at A) 386 nm, B) 403 nm, and C) 430 nm of the batch titration of Salq2 with $Cu(OAc)_2 \cdot XH_2O$ in 20% H_2O in DMF after 24 hours.
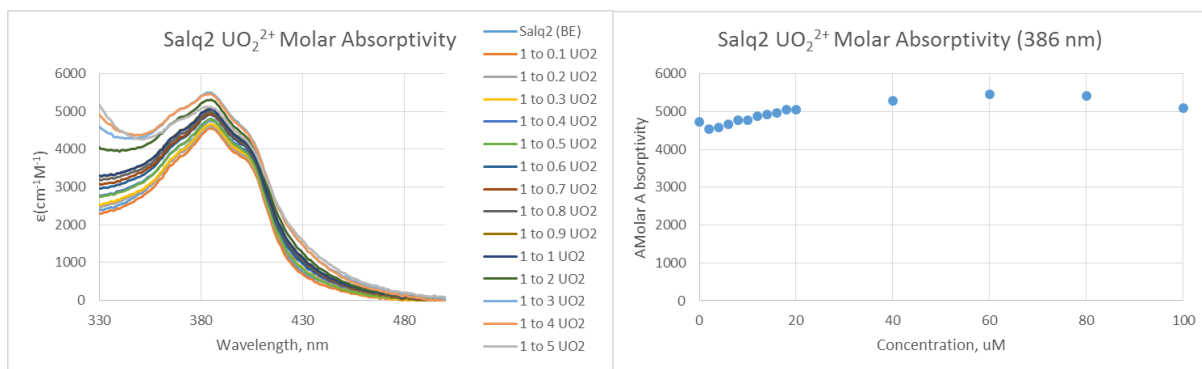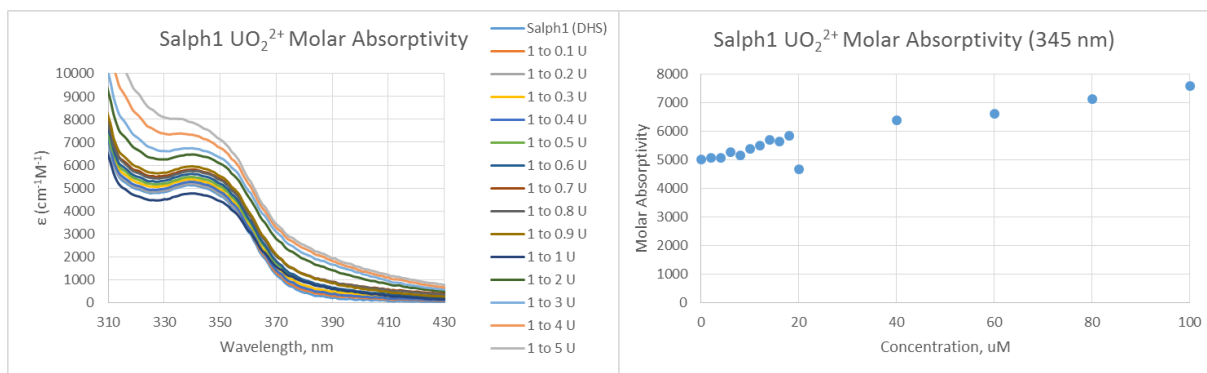

Figure B1.22. The absorbance spectra for the Salq2 ligand titrated with UO_2^{2+} and the titration curve.
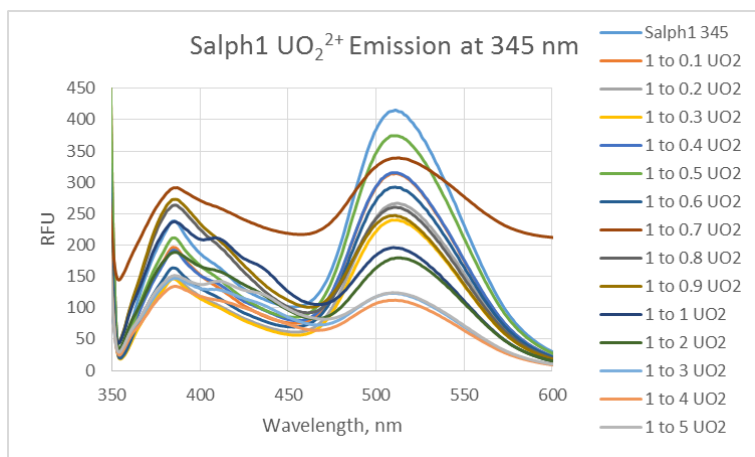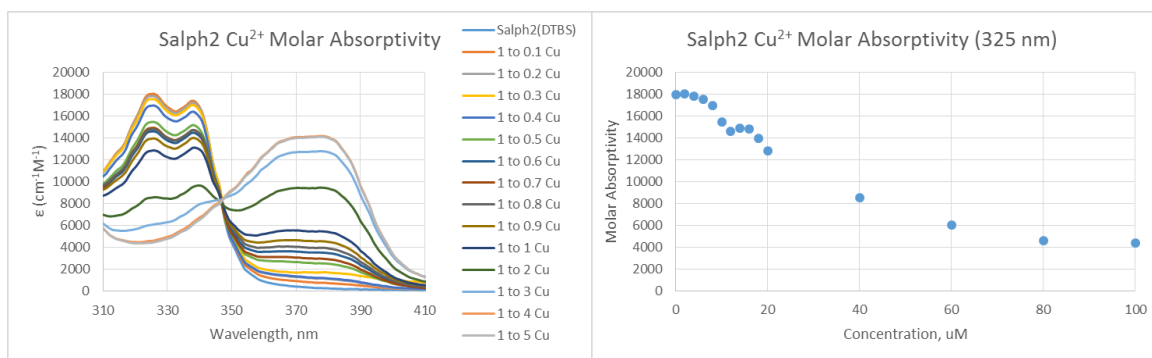
Figure B1.23. The emission spectrum with excitation at 386 nm of the batch titration of Salq2 with $UO_2(OAc)_2 \cdot 2H_2O$ in 20% H_2O in DMF after 24 hours.
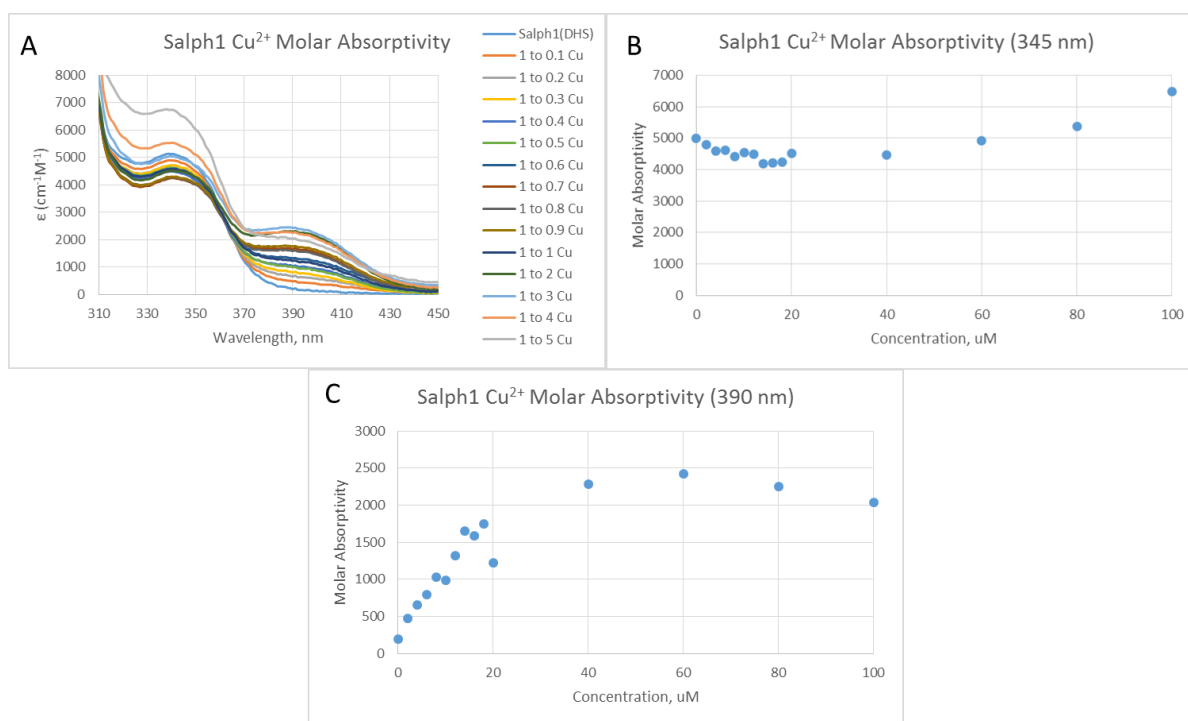
Figure B1.24. A) The absorbance spectra for the Salph1 ligand titrated with Cu^{2+} and the titration curves at B) 345 nm and C) 390 nm.
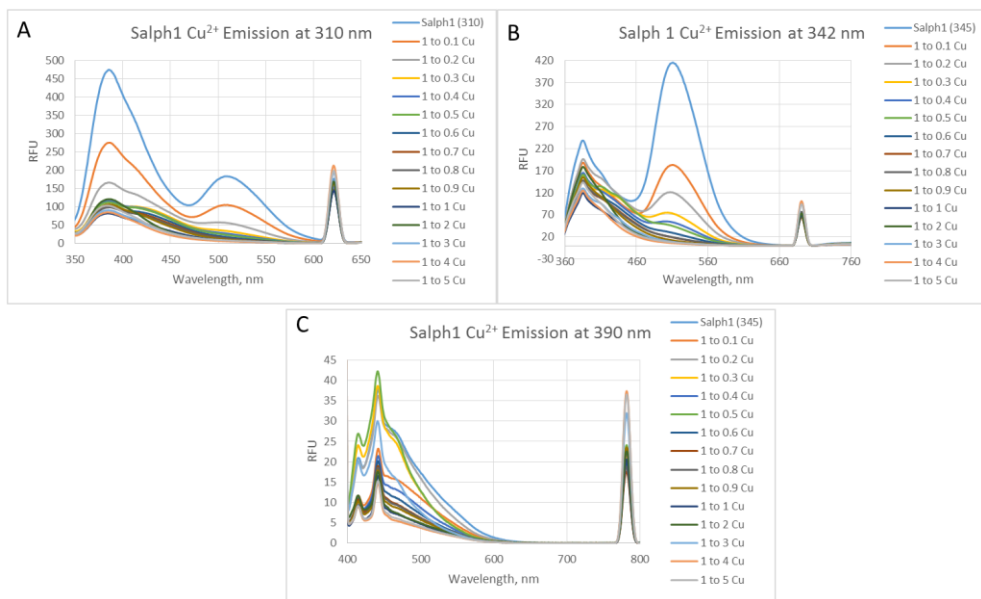
Figure B1.25. The emission spectrum with excitation at A) 310 nm, B) 345 nm, and C) 390 nm of the batch titration of Salph1 with $Cu(OAc)_2 \cdot XH_2O$ in 20% H_2O in DMF after 24 hours.

Figure B1.26. The absorbance spectra for the Salph1 ligand titrated with UO_2^{2+} and the titration curves at the respective wavelengths.

Figure B1.27. The emission spectrum with excitation at 349 nm of the batch titration of Salph1 with $UO_2(OAc)_2 \cdot 2H_2O$ in 20% H_2O in DMF after 24 hours.

Figure B1.28. The absorbance spectra for the Salph2 ligand titrated with Cu^{2+} and the titration curve.
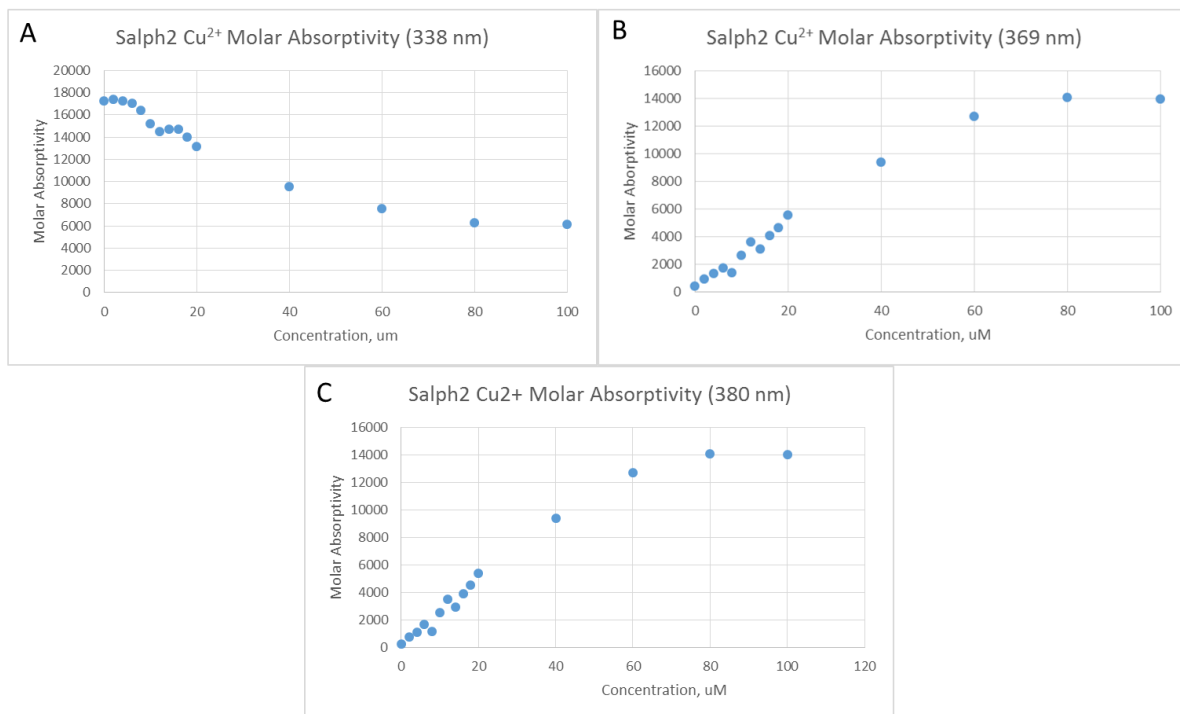
Figure B1.29. Figure 3.34. The titration curves of Salph2 ligand titrated with Cu^{2+} at A) 338 nm; B) 369 nm and C) 380 nm.
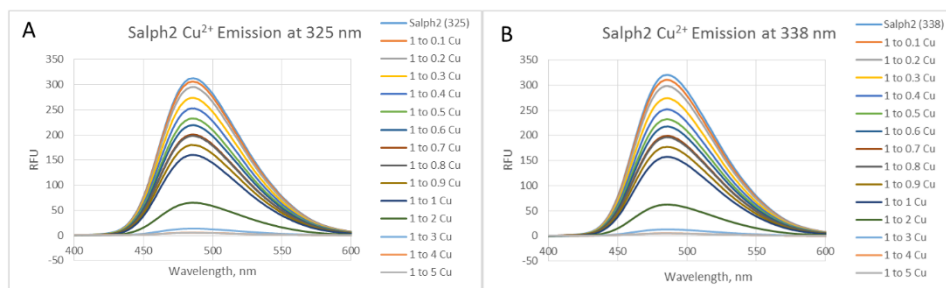

Figure B1.30. The emission spectrum with excitation at A) 325 nm and B) 338 nm of the batch titration of Salph2 with $Cu(OAc)_2 \cdot XH_2O$ in 20% H_2O in DMF after 24 hours.
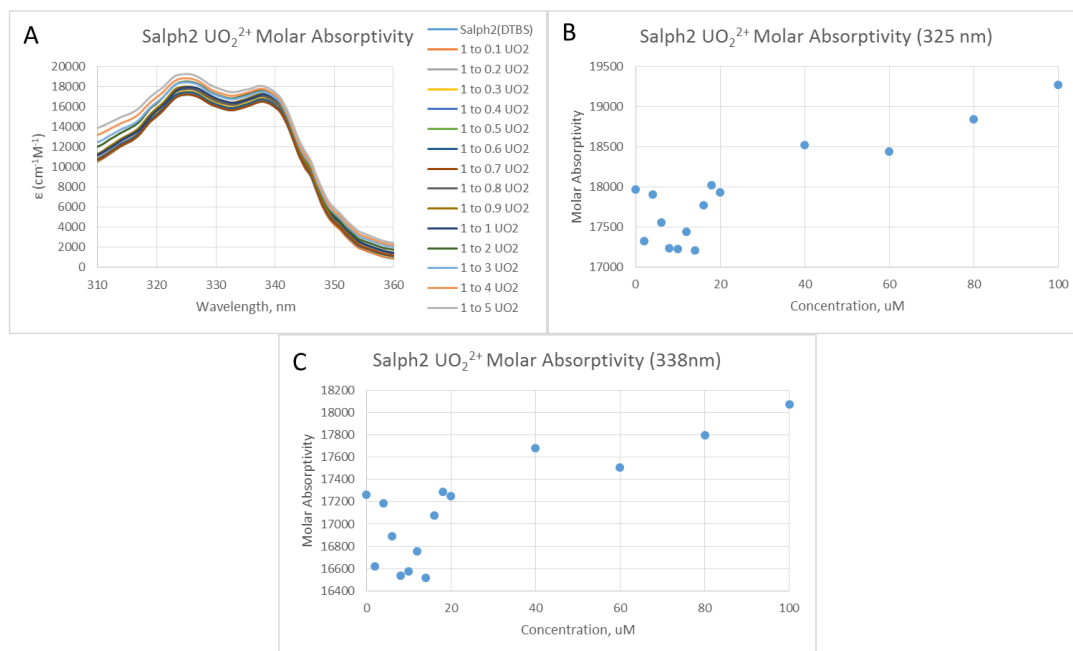
Figure B1.31. The A) absorbance spectra for the Salph2 ligand titrated with UO_2^{2+} and the titration curves B) at 325 nm and C) 338 nm.
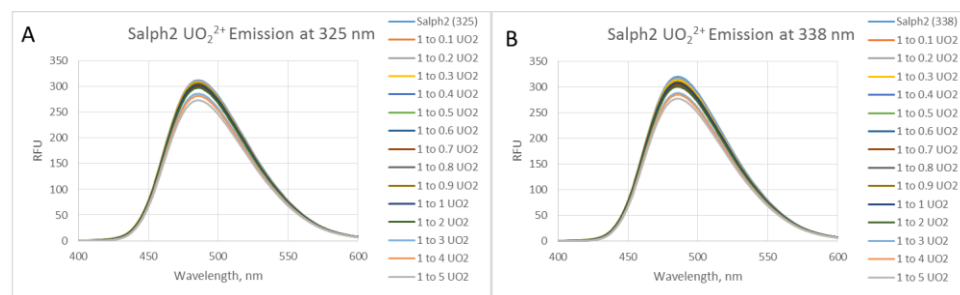

Figure B1.32. The emission spectrum with excitation at A) 325 nm and B) 338 nm of the batch titration of Salph2 with $UO_2(OAc)_2 \cdot 2H_2O$ in 20% H_2O in DMF after 24 hours.